PROCEEDINGS OF THE 1992 ANTENNA APPLICATIONS SYMPOSIUM

Paul Mayes, et al

DTIC
ELECTE
AUG 10 1993
S B D

93-18364

3 8 9 0 3 2

This report has been reviewed by the Rome Laboratory Public Affairs Office (PA) and is releasable to the National Technical Information Service (NTIS). At NTIS it will be releasable to the general public, including foreign nations.

RL-TR-93-119, Vol I , (of two) has been reviewed and is approved for publication.

APPROVED:

DANIEL J. JACAVANCO, Chief
Antennas and Components Division
Electromagnetics and Reliability Directorate

FOR THE COMMANDER:

JOHN K. SCHINDLER
Director of Electromagnetics and Reliability

If your address has changed or if you wish to be removed from the Rome Laboratory mailing list, or if the addressee is no longer employed by your organization, please notify RL (ERAS) Hanscom AFB MA 01731-5000. This will assist us in maintaining a current mailing list.

Do not return copies of this report unless contractual obligations or notices on a specific document require that it be returned.

DISCLAIMER NOTICE
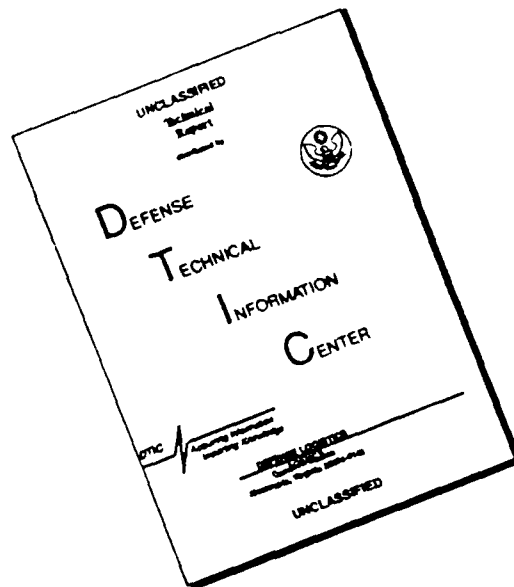
THIS DOCUMENT IS BEST QUALITY AVAILABLE. THE COPY FURNISHED TO DTIC CONTAINED A SIGNIFICANT NUMBER OF PAGES WHICH DO NOT REPRODUCE LEGIBLY.

REPORT DOCUMENTATION PAGE

1. AGENCY USE ONLY (Leave blank)	2. REPORT DATE	3. REPORT TYPE AND DATES COVERED
	June 1993	In-house Volume I

4. TITLE AND SUBTITLE	5. FUNDING NUMBERS
Proceedings of the 1992 Antenna Applications Symposium	PE 62702F
	PR 4600 TA 14 WU PH

6. AUTHOR(S)

Paul Mayes, et al

7. PERFORMING ORGANIZATION NAME(S) AND ADDRESS(ES)	8. PERFORMING ORGANIZATION REPORT NUMBER
Rome Laboratory/ERAS	
31 Grenier Street	
Hanscom AFB, MA 01731-3010	RL-TR-93-119(I)
Project Engineer: John Antonucci/ERAS	

9. SPONSORING/MONITORING AGENCY NAME(S) AND ADDRESS(ES)	10. SPONSORING/MONITORING AGENCY REPORT NUMBER

11. SUPPLEMENTARY NOTES

Volume I consists of pages 1 through 336
Volume II consists of pages 337 through 644

12a. DISTRIBUTION/AVAILABILITY STATEMENT	12b. DISTRIBUTION CODE
Approved for public release; distribution unlimited	

13. ABSTRACT (Maximum 200 words)

The Proceedings of the 1992 Antenna Applications Symposium is a collection of state-of-the-art papers relating to phased array antennas, multibeam antennas, satellite antennas, microstrip antennas, reflector antennas, HF, VHF, UHF and various other antennas.

14. SUBJECT TERMS			15. NUMBER OF PAGES
Antennas	Microstrip	Multibeam antennas	342
Satellite antennas	Reflector	Array antennas	16. PRICE CODE
Broadband antennas	HF, VHF, UHF		

17. SECURITY CLASSIFICATION OF REPORT	18. SECURITY CLASSIFICATION OF THIS PAGE	19. SECURITY CLASSIFICATION OF ABSTRACT	20. LIMITATION OF ABSTRACT
Unclassified	Unclassified	Unclassified	SAR

CONTENTS

WEDNESDAY, 23 SEPTEMBER 1992

OPTOELECTRONIC ARRAYS

PHASED ARRAYS

* NOT INCLUDED IN THIS VOLUME

THURSDAY, 24 SEPTEMBER 1992

BROADBAND AND/OR LOW PROFILE ELEMENTS

COMPUTATIONAL ELECTROMAGNETICS

* NOT INCLUDED IN THIS VOLUME

FRIDAY,25 SEPTEMBER 1992

BROADBAND AND OTHERS

* NOT INCLUDED IN THIS VOLUME

Accession For

NTIS GRA&I	☑
DTIC TAB	☐
Unannounced	☐
Justification	

By_____
Distribution/

Availability Codes

| Dist | Avail and/or Special |

A-1

v

OPTICALLY FED AND CONTROLLED PHASED ARRAY ANTENNAS -
A DREAM OR A REAL POSSIBILITY?

P. R. Herczfeld

Drexel University / F & H Applied Science Associates, Inc.

ABSTRACT

Experimental results are presented demonstrating an optically fed phased array antenna operating at C-band in the 5.5 to 5.8GHz frequency range. The present system consists of two optically fed 1x4 subarrays with MMIC based active T/R modules. Custom designed fiber optic links have been employed to provide distribution of data and frequency reference signals to phased array antenna. The paper will also describe recent research of optical beamforming using an optical processing scheme.

1. INTRODUCTION

Phased array antennas play an important role in military and civilian applications. They are used in radar, communications, surveillance, electronic warfare (EW) and guidance systems. With the trend toward more agile, higher frequency and larger arrays that use monolithic microwave and millimeter wave integrated circuit components, finding the available space for signal distribution becomes a serious problem. Therefore, the use of fiber optic cables for signal distribution in the antenna represents an attractive alternative to conventional coaxial cables or waveguide structures. Fiber optic links are also attractive because of their immunity to interference (EMI and EMP), excellent crosstalk isolation, small size and weight, and inherently wide bandwidth. Furthermore, the use of optical links provides for novel beam forming techniques based on true-time delay phase shifters and parallel optical processors.

The elusive dream of an optically fed and controlled phased array antenna has been pursued by a number of researchers. In this paper two alternate approaches using optical beamforming techniques are discussed.

2. OPTICALLY FED PHASED ARRAY ANTENNA

System Layout. The overall optically fed phased array system under consideration is shown in Fig. 1. It consists of a central processing unit (CPU), the planar array comprised of optically fed subarrays, the fiberoptic distribution system for the control, carrier and intelligence signals and the true time delay units between the CPU and the individual subarrays. The present demonstration model employs C-band MMIC T/R modules fabricated by GE Electronics laboratory.
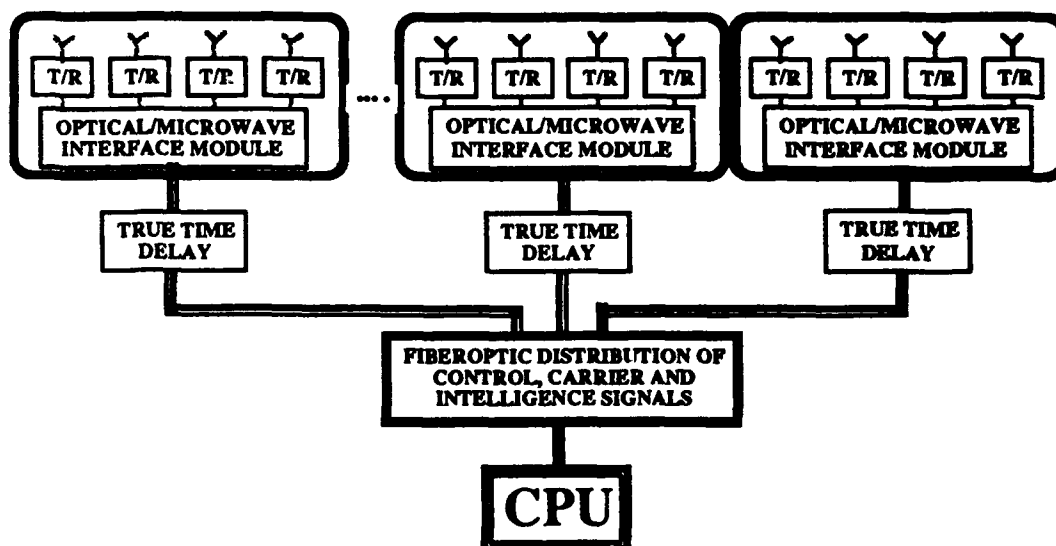
Fig.1. Entire system diagram for the phased array antenna, showing layout of optically fed four element C-band subarrays.

The function of the control distribution network is to carry the appropriate control signals from the CPU to the T/R modules. The T/R modules contain the digital phase shifters and driving circuits. Beam steering at the subarray clusters is

achieved via this phase shifters. The true time delayers are used to set the time delays between the CPU and the subarray. The combination of the time delay units and phase shifters provide for beam steering with minimal squint at an acceptable cost.

At each subarray, a modulated carrier is obtained by mixing a coding/data (intelligence) signal with a stabilized local oscillator (LO). Two separate fiberoptic (FO) links are used; one for the distribution of the frequency reference to synchronize the remotely located local oscillators (one at each subarray) and one for the coding/data signals distribution. In the receive mode of operation the detected signals are down-converted at the subarrays with the same stabilized LO and routed to the CPU for further processing, using the coding/data FO link. This approach is called *T/R Level Data Mixing* architecture [1] and has a better system performance over the standard *CPU Level Data Mixing* architecture.
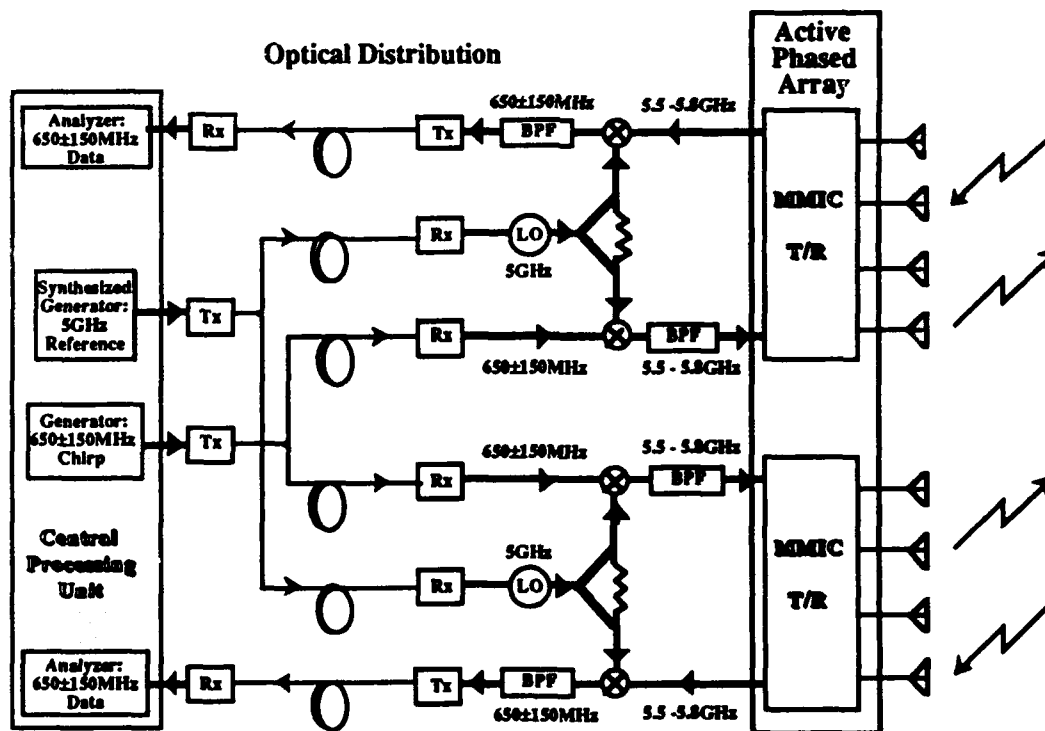
Fig. 2. Optical feed network of 2x4 MMIC active phased array antenna.

3

The Experimental setup for the optically fed antenna is shown in Fig.2. The MMIC T/R modules operated optimally from 5.5 to 5.8GHz, therefore fiber optic links at 5GHz (for frequency reference) and at 650±150 MHz (for coding/data signals) were designed. The narrow band fiber optic links at 5GHz provide for the distribution of the frequency reference by synchronizing the two isolated, subarray based local oscillators. The reference FO link is designed for low FM noise degradation characteristics. The coding/data signals are provided to and from subarrays using 650±150MHz FO links, designed for low loss and high dynamic range. In the following sections the various subsystems are described.

Frequency Synchronization — Optically Injection Locked Local Oscillator. The block diagram of the local oscillator at 5GHz, based on the design of Berceli et. al. [2], is shown in Fig. 3. The spectra of the free running oscillators are depicted in Figs. 4 and 5, indicating high close-in FM noise and instability, at output power levels of ~10dBm. To synchronize the two local oscillators, a reference signal at 5GHz has been optically distributed to the subarrays (cf. Fig. 2), and electrically injected to the two local oscillators to provide stabilized oscillations at 5GHz. Note that with the present design of the oscillators no circulator is required for electrical injection locking; hence this design is quite compatible with MMIC techniques.
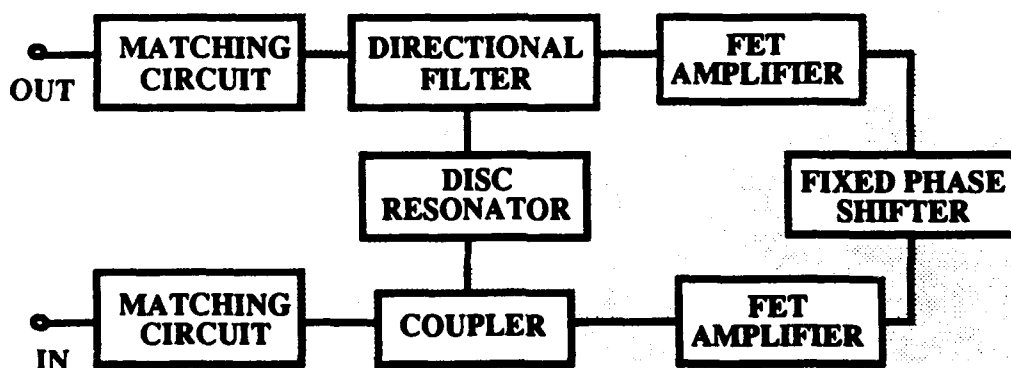
Fig.3. Block diagram of the local oscillator designed for optically controlled injection locking.
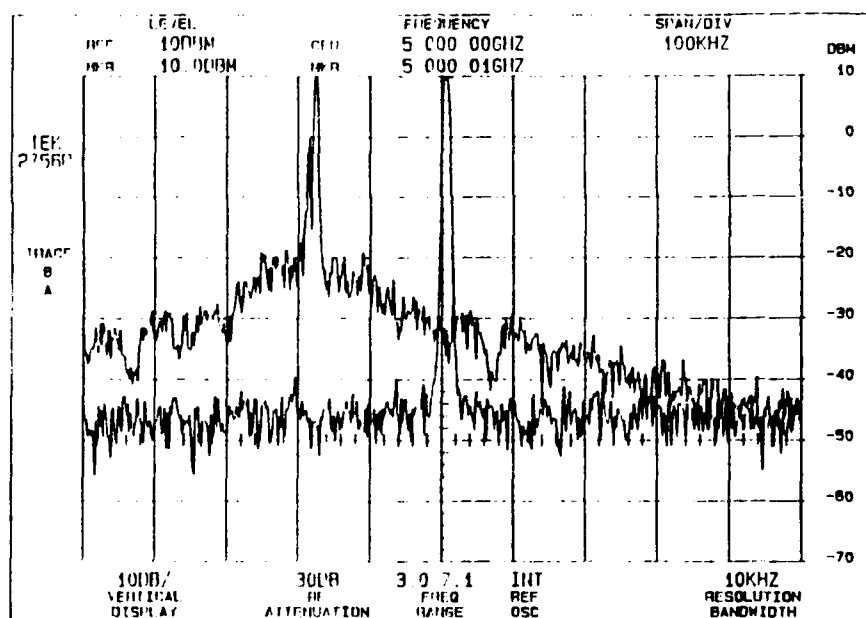
Fig.4. Spectra of oscillator #1 when it is free running at 4.99983GHz and injection locked at 5.00001GHz. (Horizontal scale of 100kHz/division, vertical scale of 10dB/division and reference level of 10dBm.)
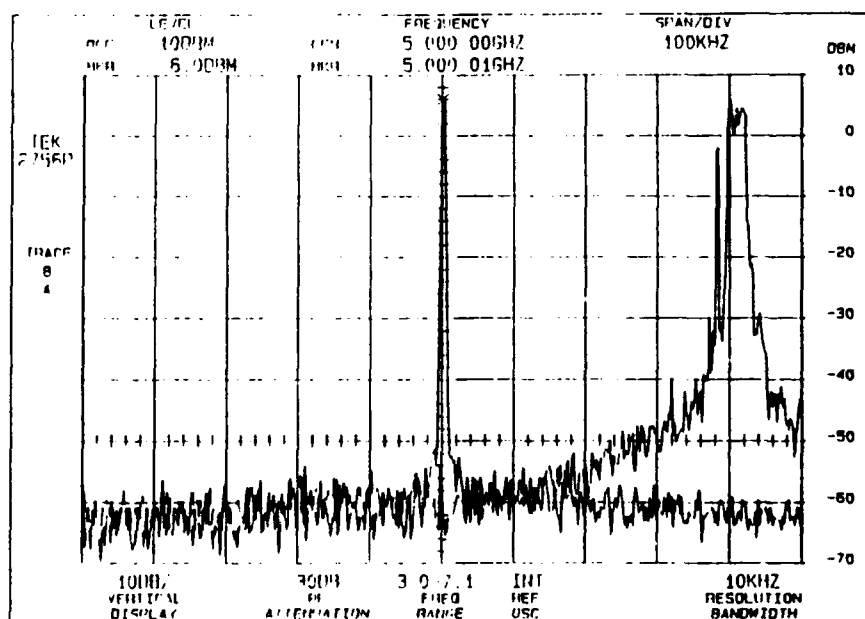
Fig.5. Spectra of oscillator #2 when it is free running at 5.00040GHz and injection locked at 5.00001GHz. (Horizontal scale of 100kHz/division, vertical scale of 10dB/division and reference level of 10dBm.)

5

The optical distribution of 5GHz reference signal has been accomplished using custom designed optical transmitter and receiver modules and a 3dB optical coupler from Canstar (Model PC3-C-050). The optical transmitter and receivers are based on the reactively matched AlGaAs laser diode (Ortel's SL1000H) and AlGaAs pin photodiodes (Ortel's PDO-25C). The link gains in the respective branches of the distribution network are measured to be -28dB and -38dB.

Injection locking, as shown in Figs. 4 and 5, considerably improves the spectral purity of the oscillators. Furthermore, these figures reveal the synchronization of the two local oscillators to the desired 5GHz reference. The locking range increases with injected power level and is measured to be as high as 5MHz for a power gain of 22dB.

Intelligence Signal Distribution. To achieve low loss, low noise, and high dynamic range fiberoptic data links, custom designed optical transmitter and receiver modules were developed. Since our long range goal is to integrate optical T/R modules with GaAs MMICs, lasers and detectors operating at 850nm (Ortel's SL300H and PDO50C) have been selected. To develop efficient optical/microwave interfaces over the required 500-800MHz frequency range, reactive and active impedance matching techniques have been utilized for the laser and pin photodiode, respectively [3]. Return losses of the optical transmitter and receiver modules are measured to be 11dB and 4dB respectively. The optical transmitter and receiver were coupled using straight cleaved fibers. Gain of the complete link has been measured to be -27dB as shown in Fig. 6.

Much higher link gains of -9dB and -15dB have been measured for custom designed single mode lensed fibers and are also shown in Fig. 6. However, use of a lensed fiber has two disadvantages. First, the amount of light coupling from the laser to the lensed fiber is very position sensitive. (Position tolerances for lateral and transverse movements of the fiber are ±0.6μm and ±0.5μm, respectively, for a 1dB power drop). Second, the large coupling factor from the laser to the fiber makes the laser performance sensitive to the coherent light feedback from any

scattering point. Strong reflections back into the laser result in large induced peaks in the noise spectrum of the link. This source of noise can be made minimized by inserting an optical isolator between the laser and the lensed fiber.
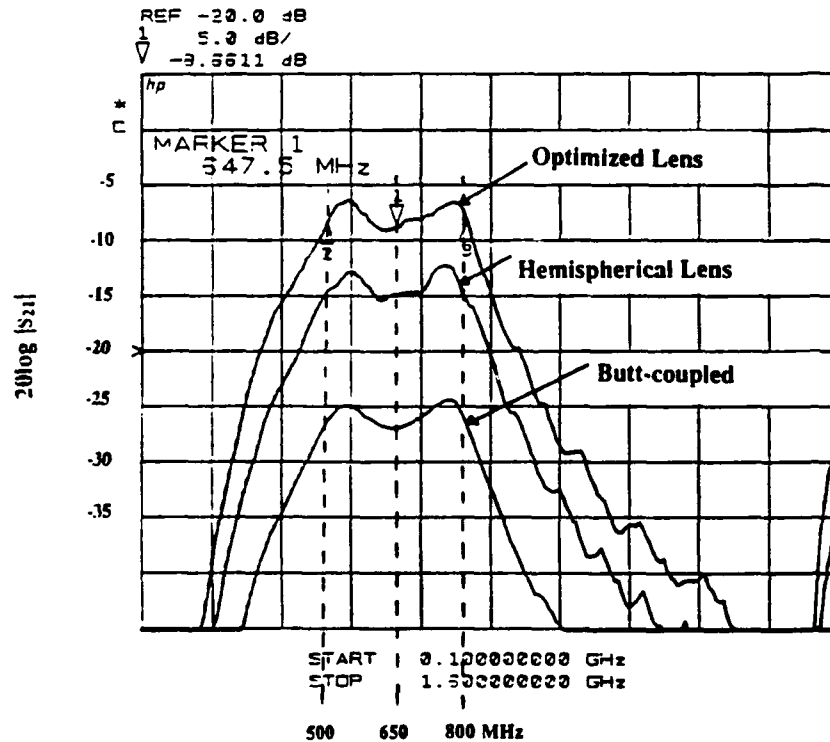
Fig. 6. Measurements of the 650±150MHz intelligence FO link using three different coupling factors of lensed single mode optical fibers coupled to the laser [4].

From the above discussion we can observe that by using a straight cleaved multi-mode fiber, to couple the laser's light to the detector, results in a lower gain, but a much reduced noise level and consequently a more acceptable dynamic range can be obtained. We have performed noise figure and two tone intermodulation distortion measurements for the link. The measured noise figure of the FO link at 650MHz is 45dB. The link exhibits a 1dB compression dynamic range of 65dB over a 1MHz bandwidth and a spurious-free dynamic range of about 50dB•MHz$^{2/3}$.

7

Transmit Mode of Operation. An experimental setup similar to Fig. 2, has been established to examine the fiber optic distribution performance for the transmit mode of operation. A modulated carrier over 5.5 to 5.8GHz has been achieved by mixing signals from the data and the synchronizing FO links. In our experiment this up-conversion has been achieved by mixing the power conditioned coding/data signal from the 650±150MHz link with the stabilized 5GHz output of the injection locked local oscillator using a commercial balanced mixer (Avantek DBX-72L).
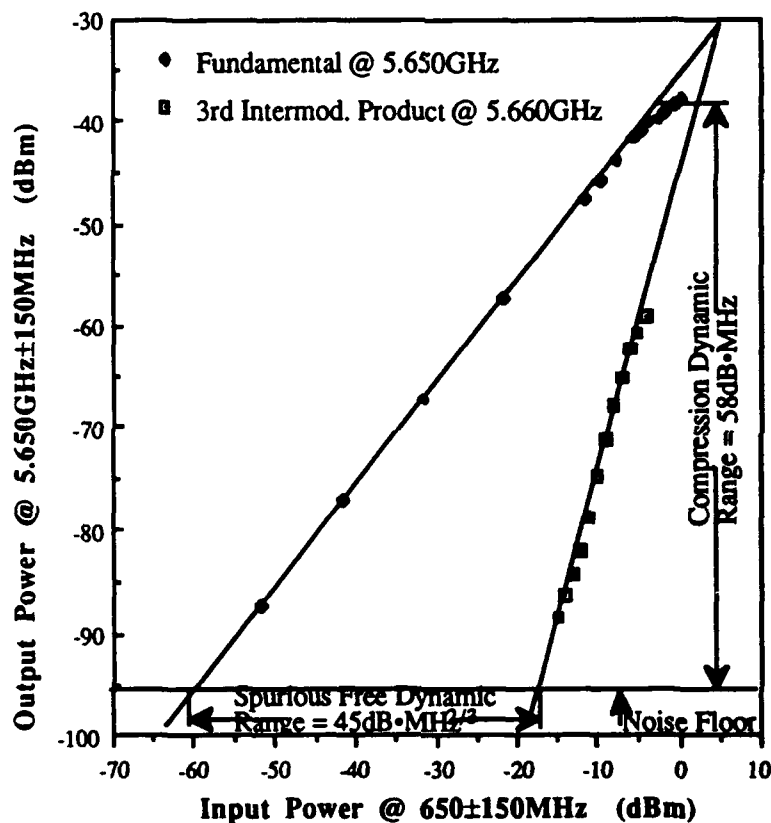
Fig.7. Measurement of two tone intermodulation distortion showing gain, third order intermodulation product, noise figure, compression and spurious free dynamic ranges over a 1MHz bandwidth in the transmit mode of operation. Input IF powers are at f_1=650MHz and f_2=655MHz and RF output powers are at the fundamental frequency of 5.65GHz and at the third order intermodulation product frequency of 5.66GHz.

8

The dynamic range of the transmit mode of operation has been measured using two tone intermodulation and noise figure measurements at carrier frequency of 5.650GHz. Results of these measurements are depicted in Fig. 7. The measured compression dynamic range (CDR) of the system is 58dB in a 1MHz bandwidth and the measured spurious free dynamic range (SFDR) is $45dB \cdot MHz^{2/3}$. The dynamic range is almost the same as that of the coding/data link. This is due to the fact that the mixer has a higher third order intercept point than the FO link. In comparison with the two tone intermodulation measurements of the coding/data FO link, it has been observed that for the transmit mode the fundamental signal, the third order intermodulation product, and the noise floor of the system are scaled by the conversion gain of the mixer, which is measured to be about -7dB.

Receive Mode of Operation. In the receive mode of operation, shown in Fig. 2, a signal from the MMIC sub-array is down-converted to IF frequency. This procedure is the reverse of the transmit mode technique. To simulate receive mode of operation, a signal of 5.5 to 5.8GHz from generator has been down-converted by the stabilized LO and the coding/data signal at IF frequency of 500 - 800MHz has been extracted. The IF signals from 500 - 800MHz are returned to the analyzers using the coding/data FO links. A high gain, low noise and high dynamic range MMIC based amplifier (LNA) is used at the input of the mixer to increase the sensitivity of the receive mode.

The dynamic range of the system without the LNA has been measured using two tone intermodulation and noise figure measurements, which are shown in Fig. 8. The measured compression dynamic range of the receive system is $64dB \cdot MHz$ whereas a spurious free dynamic range of $50dB \cdot MHz^{2/3}$ has been measured. Dynamic range in the receive mode, is also limited by the coding/data FO link performance.
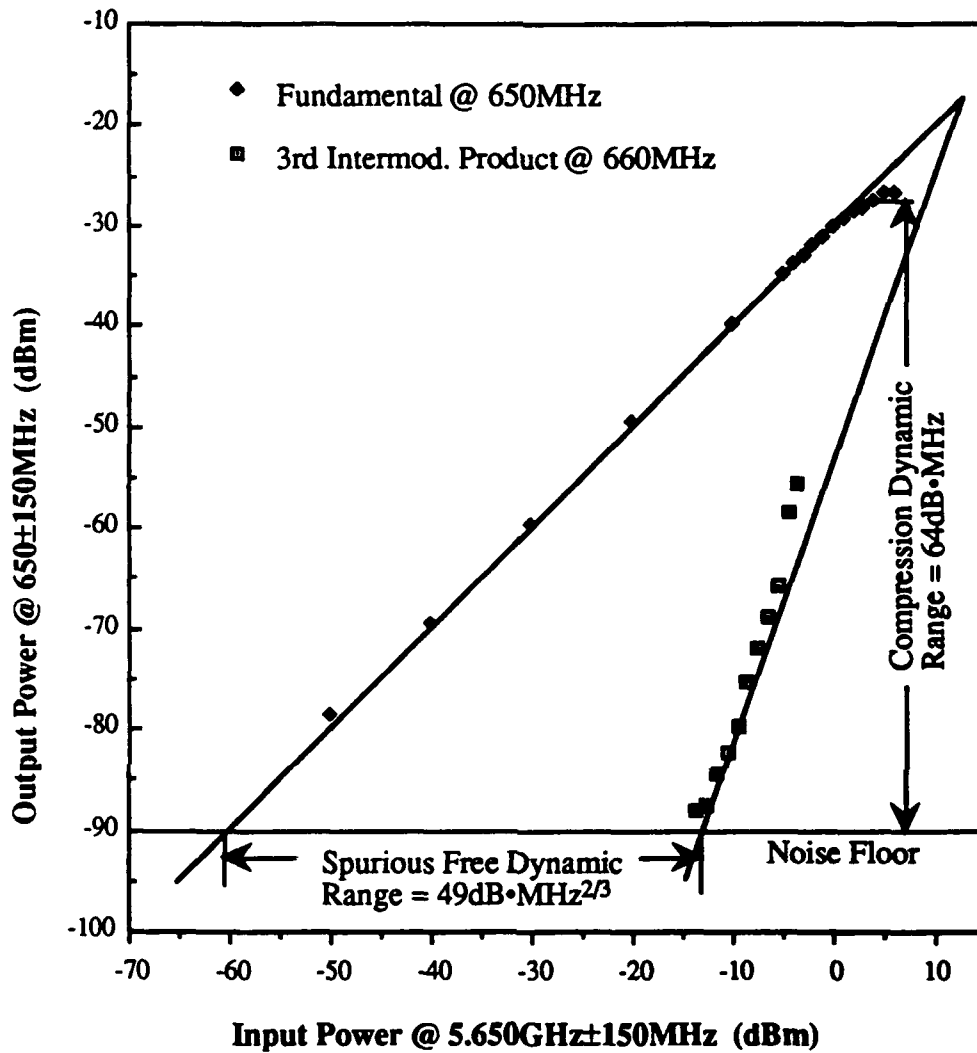
Fig. 8. Measurement of two tone intermodulation distortion showing gain, third order intermodulation product, noise figure, compression and spurious free dynamic ranges over a 1MHz bandwidth in the receive mode of operation. Input rf powers are at f_1=5.650GHz and f_2=5.655GHz and the output IF powers are at the fundamental frequency of 650MHz and at the third order intermodulation product frequency of 660MHz.

Discussion. Experimental results of T/R level data mixing for a C-band active phased array antenna are presented. The mixing of the data and reference signal are achieved using fiber optic links in each stage. In the actual receive mode operation

10

of the system the LNA plays the critical role of increasing the sensitivity of the receiver. The high gain and low noise figure of the MMIC LNA reduce the overall noise figure of the system. If the third order intercept of the LNA is higher than that of the data FO link, then receive mode of operation of the system with the amplifier will have an enhanced sensitivity without any degradation to the overall receive mode system dynamic range. The entire antenna system was assembled and tested at a GE test facility.

3. ACOUSTO-OPTIC BEAMSTEERING

Phased array beamsteering control is typically accomplished using digital computers to calculate and distribute the amplitude and phase control commands to MMIC T/R modules. These control commands must be provided in a reliable, efficient, timely, and cost effective manner. However, the beamsteering controller design becomes more difficult for large arrays which may incorporate thousands of active radiating elements with four to seven bits of phase and/or gain control. In addition, the beamsteering controller design becomes more difficult as the array operating frequency increases, which results in reduced inter-element spacing to maintain grating lobe suppression. In this case, the beamsteering controller must distribute the phase and gain commands in a much smaller size, while avoiding both electrical and physical interference with the other array subsystems such and the DC, microwave, and cooling manifolds. An alternative technique to digital control schemes is described below which uses parallel optical signal processing to control digital phase shifters and/or gain controllers within a MMIC-based phased array architecture. This technique is compatible with existing MMIC phase shifter designs, may be applied to a wide range of phased array systems, and offers compatibility with the rapidly growing field of optical signal processing.

System Layout. The basic system concept utilizing parallel optical signal processing for controlling MMIC phase shifters is shown in Fig.9. In this approach, the laser illuminates a spatial light modulator, or spatial filter, which is regulated by the control unit. The spatial filter generates a spatially varying optical

11

intensity distribution, which is sampled by a fiber optic bundle and the control signals are then routed to the individual T/R module. An interface circuit between the fiber outputs and the T/R module phase shifters and gain controllers then decodes the optical intensity to set these devices to their required states thereby establishing the appropriate amplitude and phase tapers of the antenna array. In this manner, the spatial light modulator controls the beamsteering. Advantages include a reduced data rate to the array face, immunity to EMI, and a small, light weight control signal distribution medium.
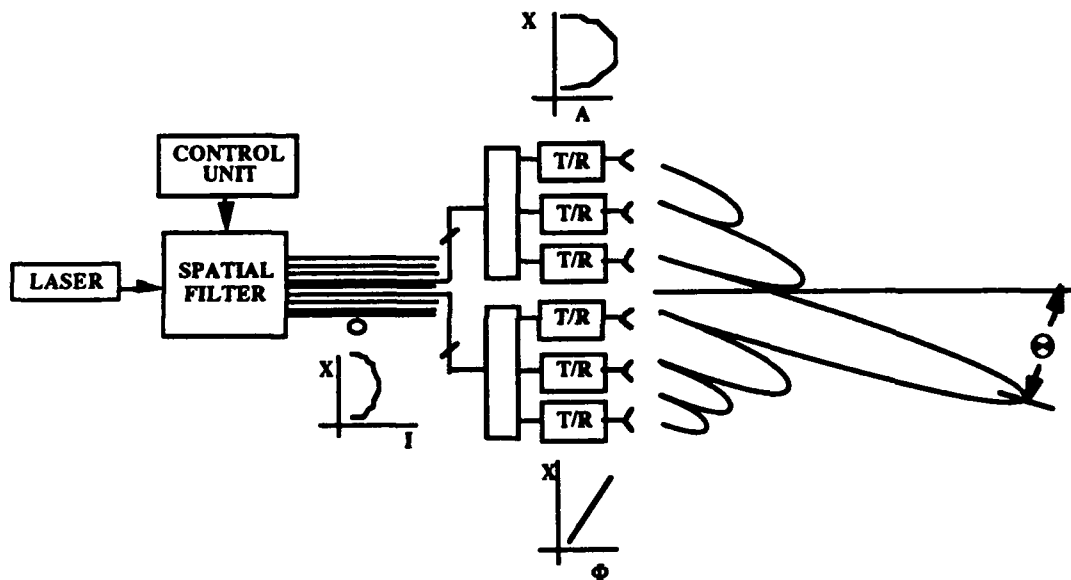
Fig. 9. Conceptual block diagram. The spatial filter generates the spatially
dependent light intensity (I vs X), which in turn produces the desired phase
and or gain taper (F vs X or A vs X).

Experimental set-up. This approach is being demonstrated experimentally using an acousto-optic (AO) cell as the spatial light modulator. The AO cell is driven by a multi-tone RF signal which results in multiple first order diffracted beams at the AO cell output. The intensity of each beam may be individually controlled by adjusting the power of RF tone corresponding to the given beam. The AO cell output beams are then coupled into optical fibers which distribute the intensity information to an

interface circuit at the T/R module. The interface circuit consists of an optical detector driving an A/D converter [5]. The A/D converts the photodetector output voltage to a parallel digital command which is interfaced to the MMIC digital phase shifter control circuitry input. In this manner the optical intensity controls the microwave phase shift. A block diagram of the experimental set-up is given below.
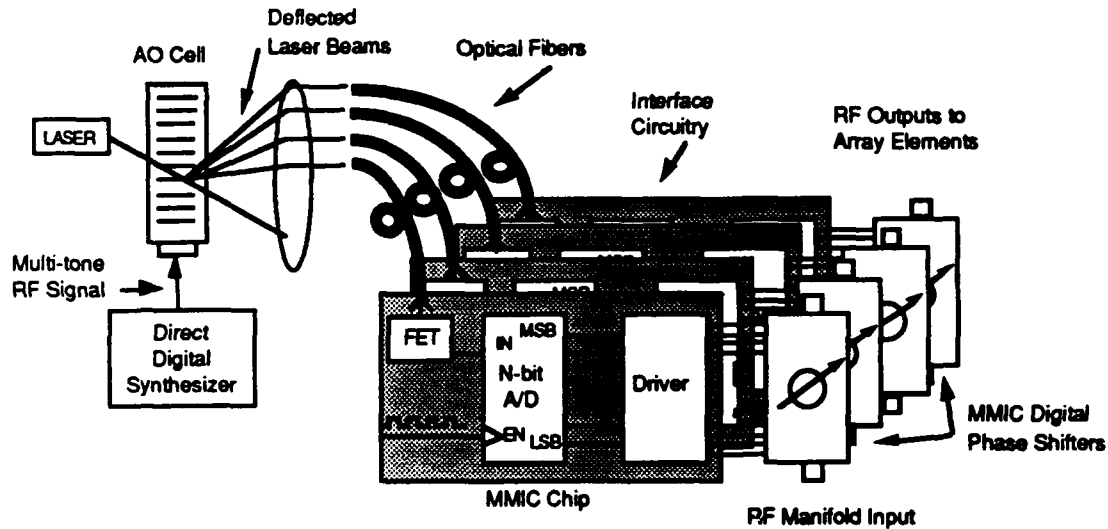
Fig. 10. Optical control of a digital phase shifter

Results. Preliminary experimental results have been taken on a single 3-bit L-band phase shifter driven by the acousto-optic system without fiber coupling. The phase shift results, Fig. 11, show the eight possible phase states as a function of AO cell drive power. The measured results are indicated by the diamonds while the solid line highlights the linearity of the system. Deviations from exact linear response are due to phase errors intrinsic to the phase shifter itself.

Phase Shift vs. AO Cell RF Drive Power
(fo = 1300MHz)
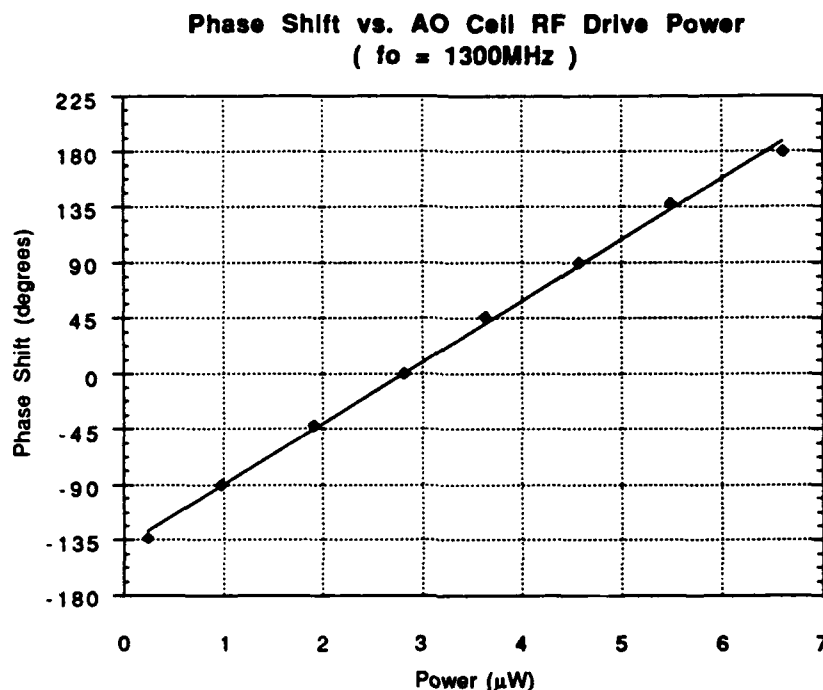
Fig. 11. Experimental result, phase shift versus optical intensity.

Discussion. A novel acousto-optic beamsteering system is described which is compatible with existing MMIC phase shifter design and parallel optical signal processing techniques. Preliminary results are presented for a single phase shifter 3-bit L-band phase shifter and current efforts are in progress to demonstrate a four channel beamsteering system.

4. CONCLUSION

Optically fed and controlled phased array antennas with MMIC T/R modules have been demonstrated. New concepts emphasizing fast, efficient optical processing schemes are emerging. For the full scale implementation of the optically controlled phased array antenna three research areas need to be addressed. First, we need better, more reliable and substantially lower cost electrooptic devices. Second, we need more design work at the interface of the optical and microwave subsystem.

Finally, we need more system level experimentation. Optically fed and controlled phased array antenna, once a dream, now represent a realistic possibility.

5. ACKNOWLEDGEMENT

6. REFERENCES

[1] A.S. Daryoush et. al., "Fiberoptic Links for Millimeter wave Communication Satellites," *IEEE International Microwave Symp*. Digest, June 1988, New York, NY.

[2] T. Berceli, W. Jemison, P. R. Herczfeld, A.S. Daryoush, A. Paolella, " A Double-Stage Injection-Locked Oscillator for Optically Fed Phased Array Antennas, *IEEE Trans. Microwave Theory Tech.,* vol. 39, no. 2, pp. 201-208, Feb. 1991.

[3] A.S. Daryoush et. al., "High-speed fiberoptic links for satellite traffic," *IEEE Trans. Microwave Theory Tech.,* vol. 38, no. 5, pp. 510-517, May 1990.

[4] S. Malone, Fiber Lensing Techniques for Light Coupling to Single Mode and Multi-mode Optical Fibers, Master's thesis, Drexel University, Philadelphia, June 1991.

[5] W. D. Jemison, et al., "Optical Control of a Digital Phase Shifter," IEEE MTT-S International Microwave Symposium Digest, May 1990.

AN ULTRAFAST OPTOELECTRONIC THz BEAM SYSTEM

N. Katzenellenbogen and D. Grischkowsky

IBM Watson Research Center, Yorktown Heights, NY 10598

1. ABSTRACT

This paper describes the optoelectronic generation and detection of freely-propagating fsec pulses of THz electromagnetic radiation. Via optoelectronic excitation, a transient point source of THz radiation is generated at the focus of a dielectric collimating lens, followed by an additional paraboloidal focusing and collimating mirror. This sources produces well collimated beams of subpicosecond pulses of THz radiation. Matched to an identical receiver, the resulting system has extremely high collection efficiency. With a demonstrated signal-to-noise ratio of 1000, a time resolution of less than 150 fsec and a frequency range from 0.2 THz to more than 6 THz, the performance of this optoelectronic THz system is limited only by the ballistic acceleration of the photocarriers.

2. INTRODUCTION

Recently, there has been a great deal of work demonstrating the generation of THz radiation via the photoconductive excitation of semiconducting and semi-insulating materials by ultrashort laser pulses. Modern inte-

1

grated circuit techniques have made possible the precise fabrication of micron-sized dipoles, which when photoconductively driven by fsec laser pulses can radiate well into the THz regime[1,2]. An alternative and complimentary approach has been to extend radio and microwave techniques into the THz regime through the use of optoelectronic antennas[3][12]. Most recently, radiation has been generated by photoconductively driving the surface field of semiconductors with ultrafast laser pulses[13]. A new and quite efficient source of broadband THz radiation involves the generation of photocarriers in trap-enhanced electric fields with ultrafast laser pulses[14-16].

Some of these sources are based on an optical type approach whereby a transient point source of THz radiation is located at the focus of a dielectric collimating lens, followed by an additional paraboloidal focusing and collimating mirror[2,9-11]. This type of source produces well collimated beams of THz radiation. Matched to an identical receiver, the resulting system has extremely high collection efficiency. With a demonstrated signal-to-noise ratio of 1000, a time resolution of less than 150 fsec and a frequency range from 0.2 THz to more than 6 THz, this optoelectronic THz system is presently the most highly developed and will be the one described in this article. One of the most useful versions of the system is based on repetitive, subpicosecond optical excitation of a Hertzian dipole antenna imbedded in a charged coplanar transmission line structure[2,9-11]. The burst of radiation emitted by the resulting transient dipole is collimated by a THz optical system into a diffraction limited beam and

2

focused onto a similar receiver structure, where it induces a transient voltage and is detected. The THz optical system gives exceptionally tight coupling between the transmitter and receiver, while the excellent focusing properties preserves the sub-picosecond time dependence of the source.

The combination of THz optics with the synchronously-gated, optoelectronic detection process has exceptional sensitivity for repetitively pulsed beams of THz radiation. Via two stages of collimation a THz beam with a frequency independent divergence is obtained from the THz transmitter. The THz receiver with identical optical properties collects essentially all of this beam. The resulting tightly coupled system of the THz transmitter and receiver can give strong reception of the transmitted pulses of THz radiation after many meters of propagation. Another reason for the exceptional sensitivity is that the THz receiver is gated. The gating window of approximately 0.6 psec is determined by the laser pulsewidth and the carrier lifetime in ion-implanted silicon-on-sapphire SOS. Thus, the noise in the comparatively long time interval (10 nsec) between the repetitive THz pulses is not seen by the receiver. A final important feature of the detection method is that it is a coherent process; the electric field of a repetitive pulse of THz radiation is directly measured. Because a repetitive signal is synchronously detected, the total charge (current) from the signal increases linearly with the number of sampling pulses, while the charge (current) from noise increases only as the square root of the number of pulses.

3

3. THE OPTOELECTRONIC THz BEAM SYSTEM

3.1 The Experimental Set-Up.

The setup used to generate and detect beams of short pulses of THz radiation is presented in Fig.1. For this example, the transmitting and receiving antennas are identical, each consisting of the antenna imbedded in a coplanar transmission line[2,9-11], as shown in Fig. 1a. The antenna is fabricated on an ion-implanted silicon-on-sapphire (SOS) wafer. The 20-μm-wide antenna structure is located in the middle of a 20-mm-long coplanar transmission line consisting of two parallel 10-μm-wide, 1-μm-thick, 5 Ω/mm, aluminum lines separated from each other by 30 μm. A colliding-pulse mode-locked (CPM) dye laser, produces 623 nm, 70 fsec pulses at a 100 MHz repetition rate in a beam with 5 mW average power. This beam is focused onto the 5-μm-wide photoconductive silicon gap between the two antenna arms. The 70 fsec laser creation of photocarriers causes subpsec changes in the conductivity of the antenna gap. When a DC bias voltage of typically 10 V is applied to the transmitting antenna, these changes in conductivity result in pulses of electrical current through the antenna, and consequently bursts of electromagnetic radiation are produced. A large fraction of this radiation is emitted into the sapphire substrate in a cone normal to the interface; the radiation pattern is presented in Ref. (10). The radiation is then collected and collimated by a dielectric lens attached to the backside (sapphire side) of

4

the SOS wafer[2,9-11]. For the work reported here, the dielectric lenses were made of high-resistivity (10 kΩcm) crystalline silicon with a measured absorption of less than 0.05 cm^{-1} in our frequency range. The silicon lens is a truncated sphere of 10 mm diameter with a focal point located at the antenna gap when attached to the back side of the chip. As shown in Fig. 1b, after collimation by the silicon lens, the beam diffracts and propagates to a paraboloidal mirror, where the THz radiation is recollimated into a highly directional beam. Although the 70 mm aperture paraboloidal mirrors have a 12 cm focal length, a 16 cm distance was used between the silicon lenses and the mirrors to optimize the response of the system at the peak of the measured spectrum. After recollimation by the paraboloidal mirror, beam diameters (10-70mm) proportional to the wavelength were obtained; thereafter, all of the frequencies propagated with the same 25 mrad divergence. The combination of the paraboloidal mirror and silicon lens (THz optics) and the antenna chip comprise the transmitter, the source of a highly-directional freely-propagating beam of subpicosecond THz pulses. After a 50 cm propagation distance this THz beam is detected by an identical combination, the THz receiver, where the paraboloidal mirror focuses the beam onto a silicon lens, which focuses it onto a SOS antenna chip, similar to the one used in the emission process. The electric field of the focused incoming THz radiation induces a transient bias voltage across the 5 μm gap between the two arms of this receiving antenna, directly connected to a low-noise current amplifier. The amplitude and time dependence of this transient voltage is obtained by measuring the

5
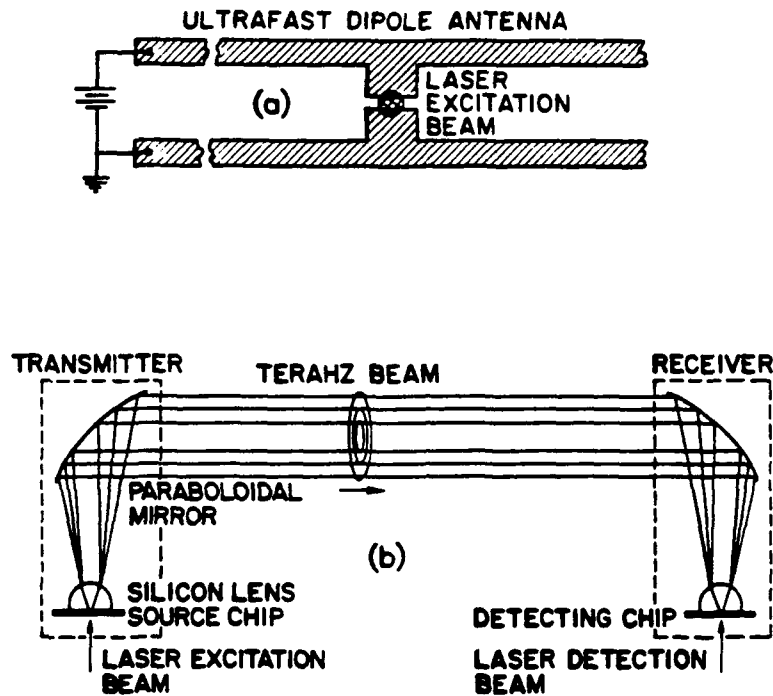
Fig.1 (a) Ultrafast dipolar antenna. (b) THz transmitter and receiver.

collected charge (average current) versus the time delay between the THz pulses and the delayed CPM laser pulses in the 5 mW detection beam. These pulses synchronously gate the receiver, by driving the photoconductive switch defined by the 5 μm antenna gap. The detection process with gated integration can be considered as a sub-picosecond boxcar integrator.

3.2 Measurements of Signal-to-Noise

A typical time-resolved measurement[11] is shown in Fig.2a. The clean pulseshape is a result of the fast action of the photoconductive switch at

6
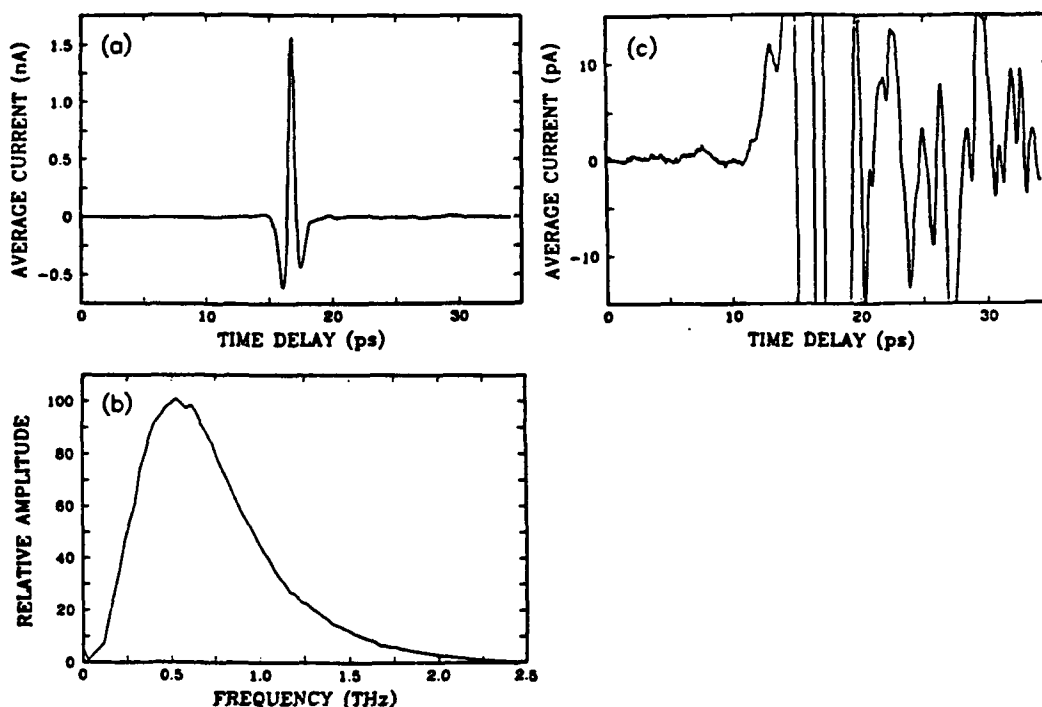
Fig.2 (a) THz pulse measured to 35 psec by scanning the time delay between the optical gating pulses and the incident THz pulses, while monitoring the current induced in the THz receiver. (b) Amplitude spectrum to 2.5 THz of the measured pulse shape. (c) THz pulse on a 100 times expanded vertical scale.

the antenna gap, the broadband response of the ultrafast antennas, the broadband THz optical transfer function of the lenses and paraboloidal mirrors, and the very low absorption and dispersion of the silicon lenses. The measured pulsewidth of 0.54 psec (FWHM) is only an upper limit to the true pulsewidth, because no deconvolution has been applied to the

7

measurement to take out the response time of the antenna gap. This time-response will be determined in the next section of this article.

In Fig. 2b, the Fourier transform of the measured signal (Fig. 2a) is shown to stretch from about 0.1 to 2.0 THz. This represents only a lower limit to the true extent of the emitted radiation as it contains the frequency response of the receiver. At the low frequency end, the efficiency of both emitter and receiver has been shown to be proportional to the length of the antenna, i.e., proportional to the separation between the two lines of the coplanar transmission line. For extremely low frequencies the size of the paraboloidal mirrors will also limit the efficiency. For the high frequency limit the efficiency of the antenna is strongly reduced when 1/2 the wavelength (in the dielectric) of the emitted radiation is no longer small compared to the antenna length. The high frequency part of the spectrum is also limited by the finite risetime of the current transient and the non-ideal imaging properties of the THz optics.

In Fig. 2c, the time-resolved signal is shown on a hundred times expanded vertical scale. The structure observable after the main pulse is reproducible and is due to reflections of the electrical pulse on the transmission line, reflections of the THz pulse from the various dielectric interfaces, and absorption and dispersion of water vapor in the 1 cm path outside the vapor-tight box placed around most of the setup. The signal-to-noise ratio in this 4 minute scan is more than 10,000:1. Another 4 minute scan is shown in Fig. 3, for which the intensity of the pump laser beam was reduced from the 6 mW normally used to only 15 μW. This

8

400-fold reduction in laser power led to a reduction in the transient photocurrent of 320, instead of the expected 400. The discrepancy indicates a slight nonlinearity due to the onset of saturation, related to the fact that the electrical pulses generated on the transmission line are quite strong (almost 1 V in either direction). This 320-fold reduction in photocurrent led to a reduction in the power of the THz beam by the factor 1/100,000. However, despite this enormous reduction in power, the peak amplitude is still more than 30 times larger than the rms noise. Based on previous calculations[11], the average power in the THz beam during this measurement was about 10^{-13} W. If the power of the THz beam were even further reduced, the detection limit of the THz receiver would be reached at 1×10^{-16} W, for a signal-to-noise-ratio of unity and a 125 ms integration time. Because the generation and detection of the THz (far-infrared)
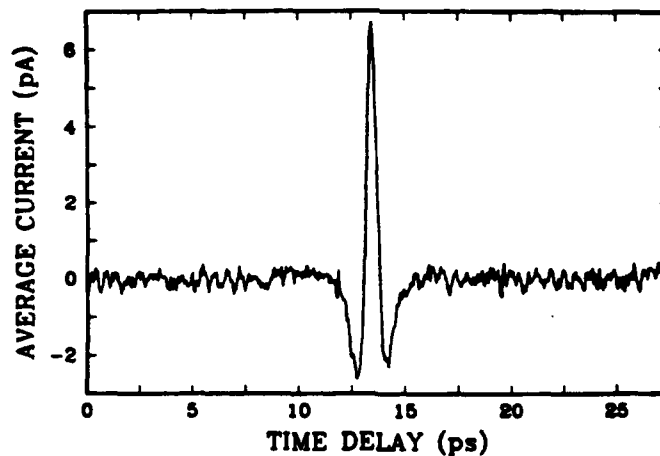
Fig.3 Measured THz pulse to 27.5 psec with a 100,000 times reduction (compared to Fig. 2a) of the THz beam power.

9

radiation is coherent, the THz receiver is intrinsically much more sensitive than the incoherent bolometer. The above receiver is approximately 1000 times more sensitive than a helium cooled bolometer[17].

3.3 Measurements of the Time-Dependent Response Function

In this section the experimental study of the THz beam system is extended to smaller 10 μm-long antennas, which have a frequency response extending to 6 THz. From the calculated THz optical transfer function together with the known THz absorption, the limiting bandwidth of the system is extracted following the procedure of Ref. (18). Because the transmitter and receiver are identical, identical transmitter and receiver bandwidths are obtained. This result is compared to the calculated radiation spectrum from a Hertzian dipole driven by the current pulse determined by the laser pulsewidth, the current risetime, and the carrier lifetime. From this comparison, the time-domain response function for the antenna current is obtained.

The optoelectronic THz beam system is the same as previously described and as shown in Fig. 1, except that here smaller antennas are used. The antenna structure, again fabricated on ion-implanted SOS, is located in the middle of a 20-mm-long coplanar transmission line consisting of two parallel 5-μm-wide aluminum lines separated from each other by 10 μm. The performance of the colliding-pulse, mode-locked (CPM) dye laser was im-

10

proved to provide 60 fsec excitation pulses in a beam with an average power of 7 mW on the excitation spot.

For these 10-μm-long antennas the measured transmitted THz pulse is shown in Fig. 4a. This pulse is shown on an expanded time scale in Fig. 4b, where the measured FWHM pulsewidth of 420 fsec (with no deconvolution) is indicated. This pulsewidth is significantly shorter than the 540
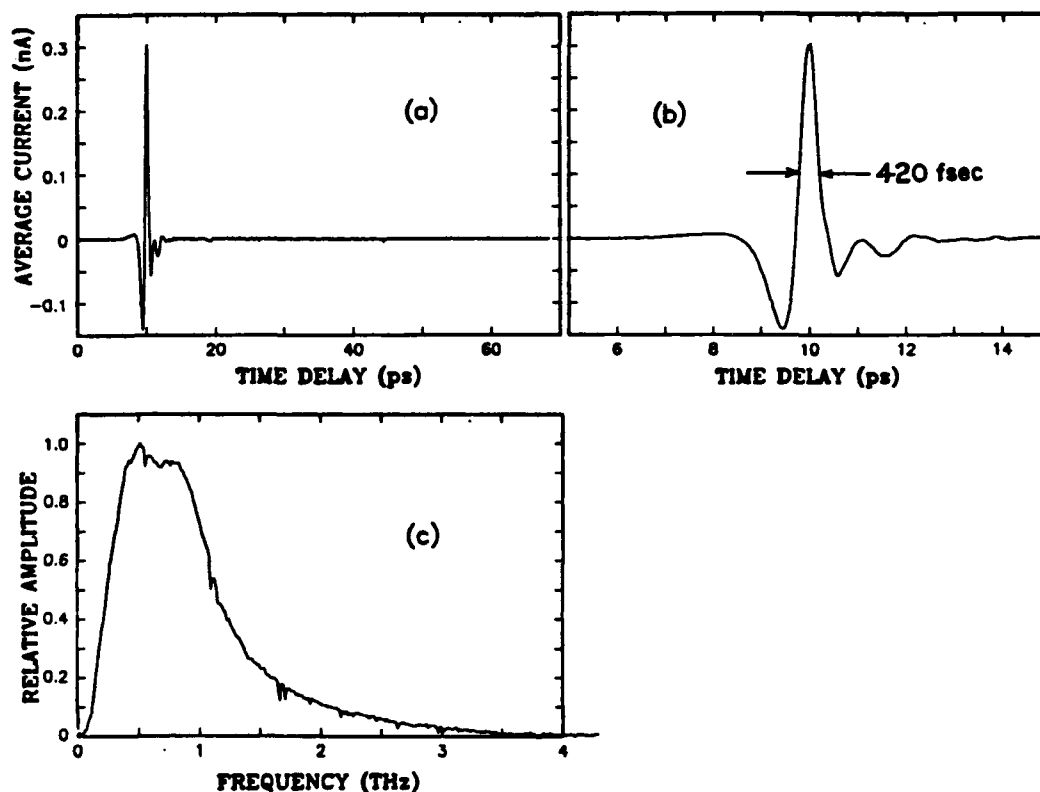
Fig.4 (a) Measured THz pulse to 70 psec. (b) Measured THz pulse on expanded 10 psec time scale. (c) Amplitude spectrum to 4 THz of Fig. 4b.

11

fsec pulse (Fig. 2a) obtained from the same experimental arrangement, but with the 30-μm-long antennas described in the previous section. The use of even still smaller antennas did not significantly shorten the THz pulses. The numerical Fourier transform of Fig. 4a is shown in Fig. 4c, where the amplitude spectrum is seen to extend beyond 3 THz. The sharp spectral features are water lines, from the residual water vapor present in the apparatus.
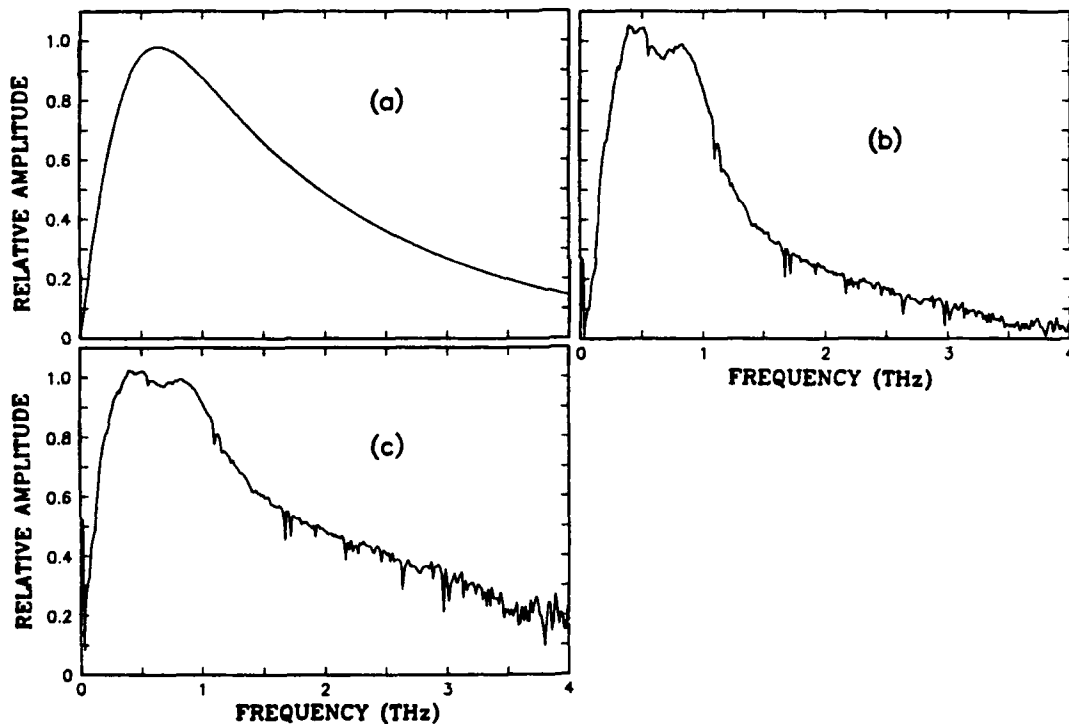
Fig.5 (a) Transmission function to 4 THz. (b) Amplitude spectrum of Fig. 4c divided by transmission function. (c) Amplitude spectral response of transmitter and receiver.

12

Two effects reduce the spectral extent of the measured pulse (Fig. 4c). These are the frequency-dependent transfer function[19] of the THz optical system (Fig. 1b) and the THz absorption in the sapphire (SOS) chips. The absorption of sapphire has been previously measured[20]. The transmission function describing these two effects is presented in Fig. 5a, for our focusing geometry and the SOS chip thickness of 0.46 mm. Dividing the measured spectrum in Fig. 4c by this transmission function we obtain Fig. 5b. Here, the spectral extent is determined only by the product of the receiver response and the transmitted spectrum. Because the transmitter and receiver are identical, by the reciprocity theorem[21] the transmitted spectrum is identical to the receiver response, and is given by the square root of Fig. 5b shown in Fig. 5c.

3.4 The Semiconductor Time-Dependent Response Function

In the small antenna limit corresponding to the Hertzian dipole, the generated radiation field is proportional to the time-derivative of the current pulse. Based on our study we conclude that the current in the antenna is mainly determined by the intrinsic response of the semiconductor itself. The intrinsic time-domain response function will now be derived for a semiconductor described by the simple Drude formalism. For this case the free carriers are considered as classical point charges subject to random collisions. Here the simplest version of this model is assumed, for which

13

the collision damping is independent of the carrier energy and for which the frequency dependent complex conductivity $\sigma(\omega)$ is given by

$$\sigma(\omega) = \sigma_{dc}\frac{i\Gamma}{\omega + i\Gamma},$$ (1)

where $\Gamma = 1/\tau$ is the damping rate and τ is the average collision time. The dc conductivity is given by $\sigma_{dc} = e\mu_{dc}N$, where e is the electron charge, μ_{dc} is the dc mobility and N is the carrier density. This relationship is in good agreement with recent time-domain spectroscopy measurements[22], on lightly doped silicon from low frequencies to beyond 2 THz. The following procedure is similar to that of Ref. (18). It is helpful to recast the formalism into a frequency dependent mobility as

$$\mu(\omega) = \mu_{dc}\frac{i\Gamma}{\omega + i\Gamma}.$$ (2)

The dc current density is given by $J_{dc} = \sigma_{dc}E$, or equivalently $J_{dc} = eE\mu_{dc}N$, where E is a constant electric field for the simple case considered here. Because of the linearity of the current in N, for a time dependent carrier density N(t), the time dependent current density can be written as

$$J(t) = eE\int_{-\infty}^{t} \mu(t - t')N(t')dt',$$ (3)

14

where μ(t-t') is the time-domain response function for the mobility. This function is determined by the inverse transform of the frequency dependent mobility to be the causal function

$$\mu(t - t') = \mu_{dc}\Gamma e^{-\Gamma(t - t')} \tag{4}$$

which vanishes for negative (t-t').

In order to facilitate the understanding of the photoconductive switch it is useful to rewrite the basic Eq. (3) in the equivalent form,

$$J(t) = eEA\int_{-\infty}^{t} \mu(t - t')\int_{-\infty}^{t'} R_c(t' - t'')I(t'')dt''dt', \tag{5}$$

where $I(t'')$ is the normalized intensity envelope function of the laser pulse, A is a constant giving the conversion to absorbed photons/volume and R_c is the response function describing the decay of the photogenerated carriers. By defining a new photocurrent response function j_{pc}(t-t'), we can rewrite Eq.(5) in the following way

$$J(t) = \int_{-\infty}^{t} j_{pc}(t - t')I(t')dt', \tag{6}$$

15

where $j_{pc}(t\text{-}t')$ is obtained by evaluating Eq.(5) with a delta function $\delta(t'')$ laser pulse. Assuming the causal function $R_c(t'\text{-}t'') = \exp\text{-}(t'\text{-}t'')/\tau_c$, describing a simple exponential decay of the carriers with the carrier lifetime τ_c (significantly longer than the average collision time τ) for positive $(t'\text{-}t'')$ and vanishing for negative $(t'\text{-}t'')$, and that $\mu(t\text{-}t')$ is given by the Drude response of Eq. (4), the causal response function $j_{pc}(t^*)$ is then evaluated to be

$$j_{pc}(t^*) = \frac{\mu_{dc} eEA\Gamma}{\Gamma - 1/\tau_c} \left(e^{-t^*/\tau_c} - e^{-t^*/\tau} \right) \tag{7}$$

for positive $t^* = (t\text{-}t')$ and shown to vanish for negative t^*. In the short pulse limit of the ultrafast excitation pulses, the time dependence of the photocurrent $J(t)$ is approximately equal to that of the photocurrent response function $j_{pc}(t^*)$ for positive t^*. For a long carrier lifetime, the time dependence of $j_{pc}(t^*)$ is described by a simple exponential rise with a risetime of the order of $\tau = 1/\Gamma$, which is equal to 270 fsec and 150 fsec for the electrons and holes, respectively, in lightly doped silicon as previously measured[22]. As these results show, the material response can be slow compared to the duration of the ultrafast laser excitation pulses which can be as short as 10 fsec, but is more typically of the order of 60 fsec.

16
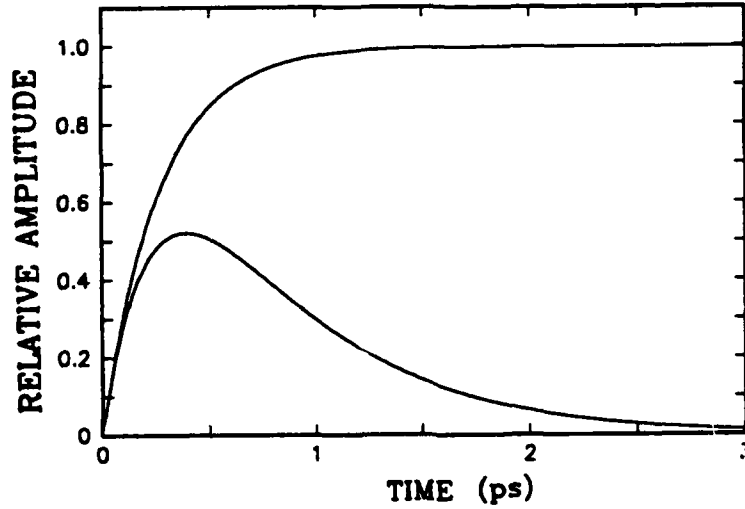
Fig.6 Calculated photoconductive response function to 3 psec with the scattering time $\tau = 270$ fsec and infinite carrier lifetime τ_c (upper curve) and with $\tau_c = 600$ fsec (lower curve).

The time-dependent response function described by Eq. (7) is calculated in Fig. 6 for the two cases; $\tau = 270$ fsec and $\tau_c = \infty$, and $\tau = 270$ fsec and $\tau_c = 600$ fsec. The result for infinite carrier lifetime has the following intuitive interpretation. After the instantaneous creation of carriers, the initial current and mobility is zero. The carriers then accelerate ballistically, as determined by the applied electric field, their charge and effective mass. This acceleration continues for approximately a time equal to the scattering time τ, after which the velocity and current equilibrate to their steady-state value. This discussion will now be shown to accurately describe the mathematical dependence of Eq. (7). With $\tau_c = \infty$, Eq. (7) is equal to

17

$$j_{pc}(t^*) = \mu_{dc} eEA(1 - e^{-t^*/\tau}), \qquad (8)$$

which for times short compared to τ reduces to
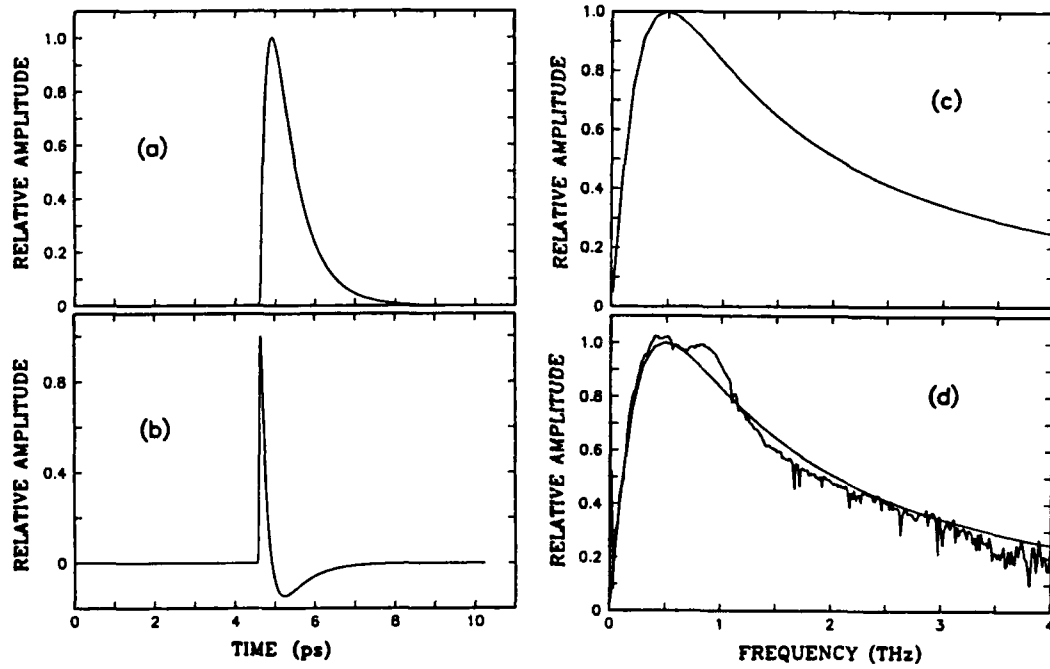
Fig.7 (a) Calculated current pulse (11 psec timescale) in semiconductor and antenna. (b) Time-derivative of current pulse. (c) Amplitude spectrum to 4 THz of Fig. 7b. (d) Comparison of Figs. 5c and 7c.

18

$$j_{pc}(t^*) = \mu_{dc} eEAt^*/\tau. \qquad (9)$$

Remembering that for Drude theory $\mu_{dc} = e/(m^*\Gamma)$, Eq. (9) is equivalent to

$$j_{pc}(t^*) = Aet^*(eE/m^*), \qquad (10)$$

which describes the ballistic acceleration eE/m^*.

For the photoconductive switches considered here, we assume the time-domain response function $j_{pc}(t^*)$ to be given by Eq. (7). This response function is then convolved with a Gaussian shaped laser pulse with a FWHM of 60 fsec, as prescribed by Eq. (6). The carrier lifetime τ_c has been measured[23] to be 600 fsec for ion-implanted SOS. As demonstrated in Fig. 7, good agreement with experiment is obtained with the average collision time $\tau = 190$ fsec. With these parameters the calculated shape of the current pulse in the photoconductive switch and the Hertzian dipole antenna is presented in Fig. 7a. The time derivative of this pulse is given in Fig. 7b, where an extremely fast transient, corresponding to the rising edge of the current pulse, is seen. The numerical Fourier transform of Fig. 7b, presented in Fig. 7c, is the predicted amplitude spectrum of the transmitter. In Fig. 7d, this spectrum is compared with the amplitude spectrum of the transmitter from Fig. 5c; the agreement is excellent. Thus, we have determined an experimentally self-consistent time-domain response function describing the current in the Hertzian dipole antenna. For longer

19

antennas for which the radiated pulse is no longer the time-derivative of the current pulse, the calculated current pulse is Fourier analysed and the resulting spectral amplitudes are put into the antenna response to determine the emitted pulse.

In summary, we have shown that the 10-μm-long antenna imbedded in the coplanar transmission line has electrical properties much faster than the semiconductor itself. Consequently, the performance is completely determined (and limited) by the intrinsic response time of the semiconductor. With the 10-μm-long antennas, it is now possible to directly study the dynamical response of free carriers in a variety of semiconductors.

3.5 A High-Performance GaAs THz Source

A different-type, high-performance optoelectronic source chip[14], used to generate pulses of freely propagating THz electromagnetic radiation, is shown in Fig. 8d. The simple coplanar transmission line structure consists of two 10-μm-wide metal lines separated by 80 μm fabricated on high-resistivity GaAs. Irradiating the metal-semiconductor interface (edge) of the positively biased line with focused ultrafast laser pulses produces synchronous bursts of THz radiation. This occurs because each laser pulse creates a spot of photocarriers in a region of extremely high electric field, the trap enhanced field[15]. The consequent acceleration of the carriers generates the burst of radiation. The CPM dye laser provides 60 fsec excitation pulses with an average power of 5 mW at the 5μm diameter

20

excitation spot. The major fraction of the laser generated burst of THz radiation is emitted into the GaAs substrate in a cone normal to the interface and as before is collected and collimated by the crystalline silicon lens attached to the back side of the chip. This GaAs trap-enhanced field (TEF) source chip is completely compatible with the previously described
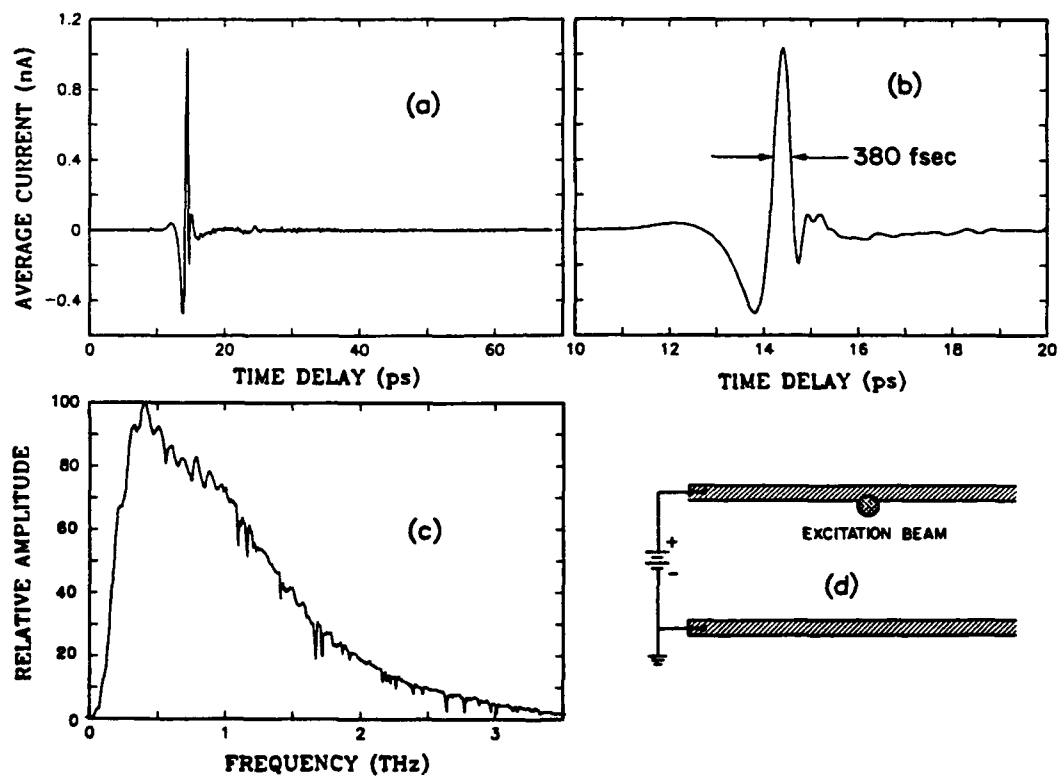
Fig.8 (a) Measured THz pulse to 70 psec. (b) Measured THz pulse on an expanded 10 psec time scale. (c) Amplitude spectrum to 3.5 THz of the THz pulse of Fig. 8a. (d) Source chip configuration used to generate the freely propagating pulses of THz radiation.

21

optoelectronic THz beam system. However this chip is limited only to the transmitter, because of its long carrier lifetime.

Our receiver operates in conjunction with a current amplifier, whose output signal-to-noise ratio is determined by the ratio of the on-time of the photoconductive switch to its off-time. Stated more precisely the noise on the current amplifier is determined by the average resistance of the photoconductive switch. Upon illumination by the laser pulse this resistance typically changes from MegOhms to a few hundred Ohms and recovers with the carrier lifetime. Therefore, the switch must reopen relatively rapidly, otherwise the average resistance is lowered and the system noise increases. For intrinsic GaAs the carrier lifetime is too long to allow for any measurement capability, resulting in an effective signal-to-noise ratio of zero. Thus, again the THz radiation detector of choice is the ion-implanted SOS detection chip with the antenna geometry shown in Fig. 1a, but with the smaller and thus faster 10-μm-long antenna.

The measured THz pulse emitted from the laser excited GaAs TEF source chip with +60V bias across the transmission line is shown in Fig. 8a, and on an expanded time scale in Fig. 8b. The measured pulsewidth with no deconvolution is seen to be 380 fsec. At the time these results were obtained[14], they were the shortest directly measured THz pulses; the dip on the falling edge was the sharpest feature ever observed with an ion-implanted detector and indicated a response time faster than 190 fsec. The numerical Fourier transform of the pulse of Fig. 8a, as presented in Fig.

22

8c, extends to beyond 3 THz; the sharp line structure is due to residual water vapor present in the system.

Using a newly developed receiver together with the same GaAs TEF source chip described above, we now measure a GaAs TEF source spectrum with a FWHM bandwidth almost twice as broad as the initial characterization[14], and even exceeding that obtained by a recent interferometric characterization of this same TEF source[16]. The system changes enabling the doubling of the measured bandwidth will now be described. Firstly, the positions of the paraboloidal mirrors were set to have a unity transfer function for the THz radiation[19]. Secondly, exceptional care was taken to match the focus of the silicon lens to the antenna position. A series of observations were made using lenses of the same curvature, but with thicknesses varying in steps of 50 μm. Thirdly, a new sandwich chip (flip-chip) arrangement was used to eliminate the absorption of the incoming THz radiation by the sapphire substrate of the SOS detection chip. For the sandwich chip the antenna on the SOS chip is covered by contacting a 0.5 mm thick polished plate of high-resistivity (10kΩcm) silicon. The collimating silicon lens is then contacted to this silicon plate. In contrast to the previous approach, the antenna is now driven by the ultrashort laser sampling pulses entering the sapphire side (back-side) of the chip and focusing onto the antenna on the Si layer.

The THz pulse measured with this ultrafast flip-chip receiver is shown in Fig. 9a. The feature at 17 psec is a reflection of the measured THz pulse from the sapphire/air interface. On the trailing edge of the pulse, rise and

23
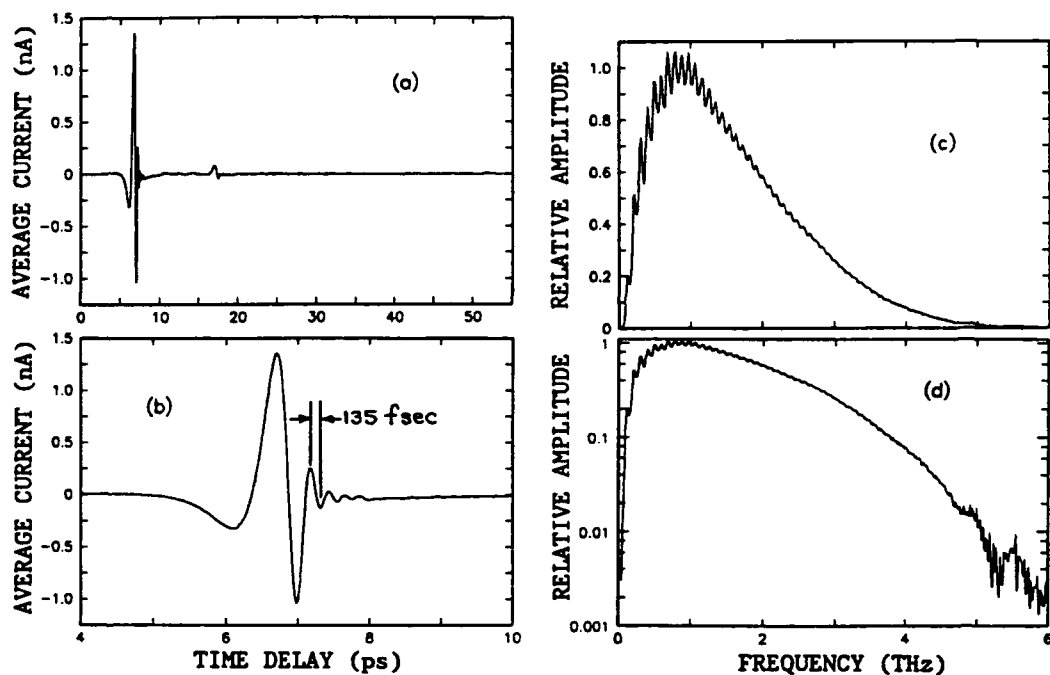
Fig.9 (a) THz pulse measured by the ultrafast flip-chip receiver. (b) Measured THz pulse on an expanded time scale. (c) Numerical Fourier transform of Fig. 9a. (d) Logarithmic presentation of Fig. 9c.

fall times faster than 135 fsec are observed, as shown in the expanded view of Fig. 9b. This exceptional time resolution demonstrates that the ion-implanted SOS photoconductive receiver can be much faster than is generally realized, but is consistent with the earlier prediction of a 150 fsec time resolution[18]. The numerical Fourier transform of this pulse peaks at approximately 1 THz and extends to 6 THz, as shown in Figs. 9c and 9d. The spectral oscillations are caused by the reflection at 17 psec.

24

The earlier characterization of the THz receiver[18] compared theory with measurements for which the THz optical transfer function peaked at 0.6 THz and significantly attenuated the higher frequency components. In addition, THz absorption by the sapphire substrate further attenuated the higher frequency components. When these effects were factored out of the data, reasonable agreement between the measured and the calculated spectrum was obtained. This factorization is now unnecessary, because for the results presented in Fig. 9, the transfer function is unity and independent of frequency, and the absorption in the sapphire substrate of the receiver has been eliminated by the flip-chip geometry. Therefore, in the following analysis we can take the actual calculated ballistic receiver response to describe the receiver.

As determined by the previous characterization[18] described above, the photocurrent response function is given by Eq. (7) with the average collision time $\tau = 190$ fsec and the carrier lifetime $\tau_c = 600$ fsec. The response function with these parameters is shown as the lower curve in Fig. 10a. The upper curve is calculated with the parameters describing unimplanted silicon. The THz radiation pulse is given by the time derivative of the photocurrent pulse, which is equal to the convolution of the photocurrent response function and the laser intensity pulse, Eq. (6). The amplitude spectrum describing the THz radiation pulse is the upper smooth curve in Fig. 10b; the power spectrum, equal to the square of this curve, is the lower curve. Because the measured spectrum is the product of the transmitter and receiver amplitude spectra, it is meaningful to compare the

25
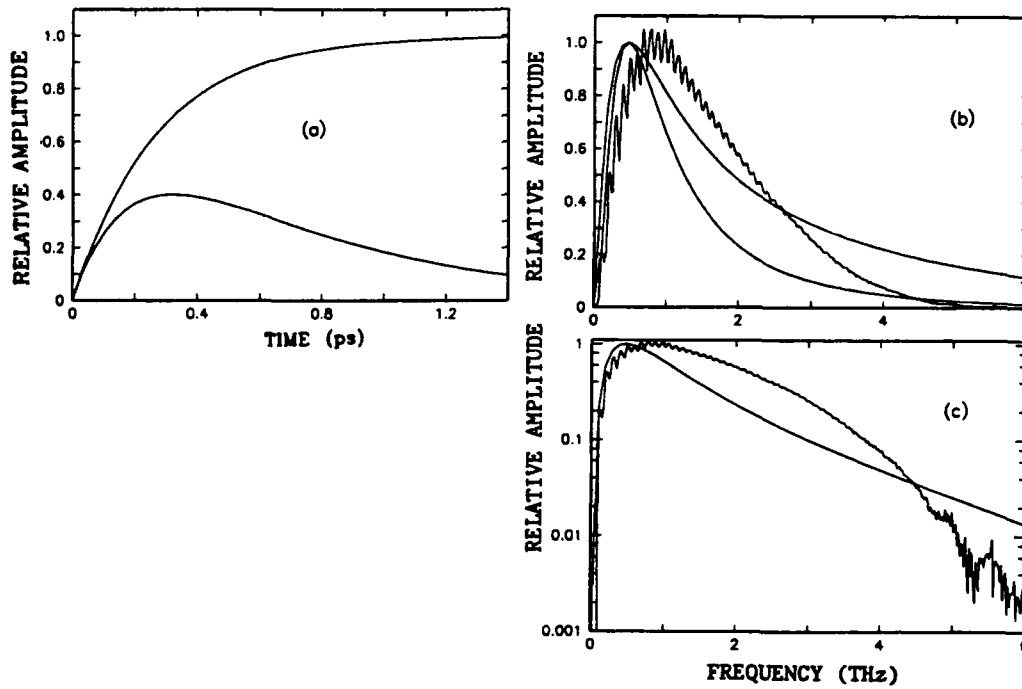
Fig.10 (a) Calculated photoconductive response functions with τ = 270 fsec, and τ_c = ∞ (upper curve) and with τ = 190 fsec and τ_c = 600 fsec (lower curve). (b). Calculated ballistic receiver amplitude spectrum (upper curve) and power spectrum (lower curve), together with the measured spectrum. (c) Logarithmic presentation of Fig. 10b.

measured spectrum with the ballistic receiver power spectrum shown in Figs. 10b and 10c. It is quite significant that the (FWHM) measured spectrum is broader than the ballistic power spectrum, and that it is higher than the power spectrum until 4.5 THz, after which it drops significantly with increasing frequency. Two contributions to this high frequency drop-off are the increasing THz absorption of the 0.5mm-thick GaAs

26

source chip, and that at the highest frequencies the antenna may be too large to be in the Hertzian dipole limit. The broad measured bandwidth demonstrates the high performance of the entire THz system and experimentally confirms the predicted broadband response of the ballistic photoconductive receiver. The fact that the measured spectrum exceeds the ballistic power spectrum indicates that the frequency response of the GaAs TEF source is broader and the time dependence is faster than that of the ion-implanted SOS ballistic receiver. A possible explanation for the extremely rapid time dependence of the photocurrent for the GaAs TEF source could be the rapid and large changes in the mobility of the photocarriers associated with intervalley scattering and carrier cooling. In summary, we have experimentally confirmed the broad-band response of the SOS ballistic photoconductive receiver, and we have used the receiver to infer even faster carrier dynamics in GaAs.

4. REFERENCES

1. Auston, D.H., Cheung, K.P. and Smith, P.R. (1984) Picosecond photoconducting Hertzian dipoles, Appl. Phys. Lett. Vol. 45, 284-286.
2. Fattinger, Ch. and Grischkowsky, D. (1988) Point source THz

27

Optics, Appl. Phys. Lett., Vol.53, 1480-1482; (1989) THz beams, Appl. Phys. Lett., Vol.54, 490-492.

3. Mourou, G., Stancampiano, C.V., Antonetti, A. and Orszag, A. (1981) Picosecond microwave pulses generated with a subpico-second laser-driven semiconductor switch, Appl. Phys. Lett., Vol.39, 295-297.

4. Heidemann, R., Pfeiffer, Th. and Jager, D. (1983) Optoelectron-ically pulsed slot-line antennas, Electronics Lett., Vol.19, 317.

5. DeFonzo, A.P., Jarwala, M. and Lutz, C.R. (1987) Transient response of planar integrated optoelectronic antennas, Appl. Phys. Lett., Vol.50, 1155-1157; (1987) Optoelectronic trans-mission and reception of ultrashort electrical pulses, Appl. Phys. Lett., Vol.51, 212-214 (1987).

6. Pastol, Y., Arjavalingam, G., Halbout, J-M and Kopcsay, G.V. (1988) Characterization of an optoelectronically pulsed broad-band microwave antenna, Electron. Lett. Vol.24, 1318.

7. Pastol, Y., Arjavalingam, G., Halbout, J-M. (1990) Characteri-zation of an optoelectronically pulsed equiangular spiral antenna, Electron. Lett., Vol. 26, 133.

8. Smith, P.R., Auston, D.H. and Nuss, M.C. (1988) Subpicosecond photoconducting dipole antennas, IEEE J. Quantum Elect. Vol. 24, 255-260.

9. van Exter, M., Fattinger, Ch. and Grischkowsky, D. (1989) High brightness THz beams characterized with an ultrafast detector,

28

Appl. Phys. Lett., Vol.55, 337-339.

10. Fattinger, Ch. and Grischkowsky, D. (1989) Beams of Terahertz electromagnetic pulses, OSA Proc. on Psec. Elect. and Optoelect., T.C.L. Gerhard Sollner and D.M. Bloom, Eds. (Optical Society of America, Washington, DC), Vol.4.

11. van Exter, M. and Grischkowsky, D. (1990) Characterization of an optoelectronic teraHz beam system, IEEE Trans. Microwave Theory and Techniques, Vol. 38, 1684.

12. Dykaar, D.R., Greene, B.I., Federici, J.F., Levi, A.F.J., Pfeiffer, L.N. and Kopf, R.F. (1991) Log-periodic antennas for pulsed terahertz radiation, Appl. Phys. Lett., Vol.59, 262-264.

13. Zhang, X.-C., Hu, B.B., Darrow, J.T. and Auston, D.H. (1990) Generation of femtosecond electromagnetic pulses from semiconductor surfaces, Appl. Phys. Lett., Vol.56, 1011-1013.

14. Katzenellenbogen, N. and Grischkowsky, D. (1991) Efficient generation of 380 fs pulses of THz radiation by ultrafast laser pulse excitation of a biased metal-semiconductor interface, Appl. Phys. Lett., Vol. 58, 222-224.

15. Ralph, S.E. and Grischkowsky, D. (1991) Trap-enhanced electric fields in semi-insulators; The role of electrical and optical carrier injection, Appl. Phys. Lett, Vol. 59, 1972-1974.

16. Ralph, S.E. and Grischkowsky, D. (1992) THz spectroscopy and source characterization by optoelectronic interferometry, Appl. Phys. Lett., Vol. 60, 1070-1072.

29

17. Johnson, C., Low, F.J. and Davidson, A.W. (1980) Germanium and germanium-diamond bolometers operated at 4.2K, 2.0K, 1.2K, 0.3K, and 0.1K, Optical Engr., Vol. 19, 255.

18. Grischkowsky, D. and Katzenellenbogen, N. (1991) Femtosecond pulses of terahertz radiation: Physics and applications, Proc. of the Psec. Elect. and Optoelect. Conf., Salt Lake City, Utah, March 13-15, 1991, T.C.L. Gerhard Sollner and Jagdeep Shah, Eds. (Opt. Soc. of Am., Washington D.C. 1991), Vol.9, pp. 9-14.

19. Lesurf, J.C.G. (1990) Millimetre-Wave Optics, Devices and Systems, Adam Hilger, Bristol, England.

20. Grischkowsky, D., Keiding, S., van Exter, M. and Fattinger, Ch. (1990) Far-infrared time-domain spectroscopy with terahertz beams of dielectrics and semiconductors, J.Opt.Soc.Am.B, Vol.7, 2006-2015.

21. Monteath, G.D. (1973) Application of the Electromagnetic Reciprocity Principle, Oxford:Pergamon Press.

22. van Exter, M. and Grischkowsky, D. (1990) Optical and electronic properties of doped silicon from 0.1 to 2 THz, Appl. Phys. Lett., Vol. 56, 1694-1696; (1990) Carrier dynamics of electrons and holes in moderately doped silicon, Phys. Rev. B15, Vol.41, 12,140-12,149.

23. Doany, F.E., Grischkowsky, D. and Chi, C.-C. (1987) Carrier lifetime versus ion-implantation dose in silicon on sapphire, Appl. Phys. Lett., Vol. 50, 460-462.

30

ANTENNA TRUE-TIME-DELAY BEAMSTEERING
UTILIZING FIBER OPTICS

I.L. Newberg, J.J. Lee, W. Ng
G.L. Tangonon, A.A. Walston, and H.W. Yen
Hughes Aircraft Company, Radar Systems Group, Advanced Systems Division
Bldg R10, MS 11070
P.O. Box 92426
Los Angeles, CA 90009
(310) 334-6834; FAX (310) 607-5699

ABSTRACT

This paper discusses true-time-delay (TTD) beamsteering concepts for active array radars using optoelectronic technology. Both radar and active arrays are described as well as beamsteering techniques, types of optoelectronic TTD beamsteerers, and manifolds utilizing optoelectronics.

1.0 Introduction

The application of optoelectronics (also termed fiber optics, photonics, and light-waves) in active array radars has been visualized for many years. The operation frequencies of those radars currently lie in the low frequency to 18 GHz range and are spreading into the millimeter-wave regime. Recently, the need to achieve large instantaneous bandwidths and large aperture antennas further prompted the exploration of new concepts for broad-band beamsteering. One such concept is true-time-delay (TTD) beamsteering; an optoelectronic time-delay system is extremely attractive for TTD beamsteering because it is lightweight, compact, nondispersive over multiple microwave bands, and immune to electromagnetic interference. Microwave transmission via fiber optics can be used in those radars

for remoting the radiating elements, controlling their relative phase, and strategically processing return signals in various electronic warfare (EW) endeavors.

TTD beamsteering can utilize optoelectronic components to achieve the wide instantaneous bandwidth needed in next-generation shared aperture active arrays for conventional and conformal array applications. TTD beamsteering uses optoelectronic technology as a part of the active array radio frequency (RF) signal manifold in a manner that moves optoelectronics out of the traditional interconnect or signal transport area. It also provides a needed capability for future active array technology where wide instantaneous bandwidth and/or large aperture arrays will be utilized in radar, EW, and communications for ground, ship, airborne, and space applications. The application of optoelectronic integrated circuits (OEICs) to beamsteering will allow future beamsteerers to be small, lightweight, flexible, reliable, and affordable and to fit into the framework that is used to package monolithic microwave integrated circuits (MMICs) currently being developed for active arrays.

A simplified radar block diagram is discussed in Section 2.0 to form the basis for the remaining sections of this paper. Section 3.0 briefly describes active array radars, because beamsteering of active arrays is the main subject of this paper. Section 4.0 discusses TTD beamsteering and important related parameters, and Section 5.0 talks about different types of optoelectronic TTD beamsteerers and their location in the RF manifold of the radar. The paper closes in Section 6.0 with comments and conclusions.

2.0 Radar

The primary function of a radar is to detect a very small target at a relatively long range, while differentiating the target from much larger interference, such as noise

and clutter. Typically, the radar determines the location of the target in range and angle (azimuth and elevation) and the speed of the target, proportional to the relative Doppler. A radar functional block diagram is shown in Figure 1.

An exciter unit generates a continuous wave (cw) RF carrier (F_c) signal [called transmitter oscillator (T.O.)] that is pulsed (gated) and amplified in a transmitter unit. The transmitter signal goes to the antenna through a duplexer unit and is radiated out the antenna in a direction established by the antenna pointing angle. The antenna is characterized by its mainlobe, where most of the signal energy is directed at the target, and by its unwanted sidelobes, which send out signal energy in many directions relative to the mainlobe. The mainlobe-radiated signal reflects off the target, and the mainlobe and sidelobes reflect off any other objects in their respective directions. The reflected signals that come back through the antenna
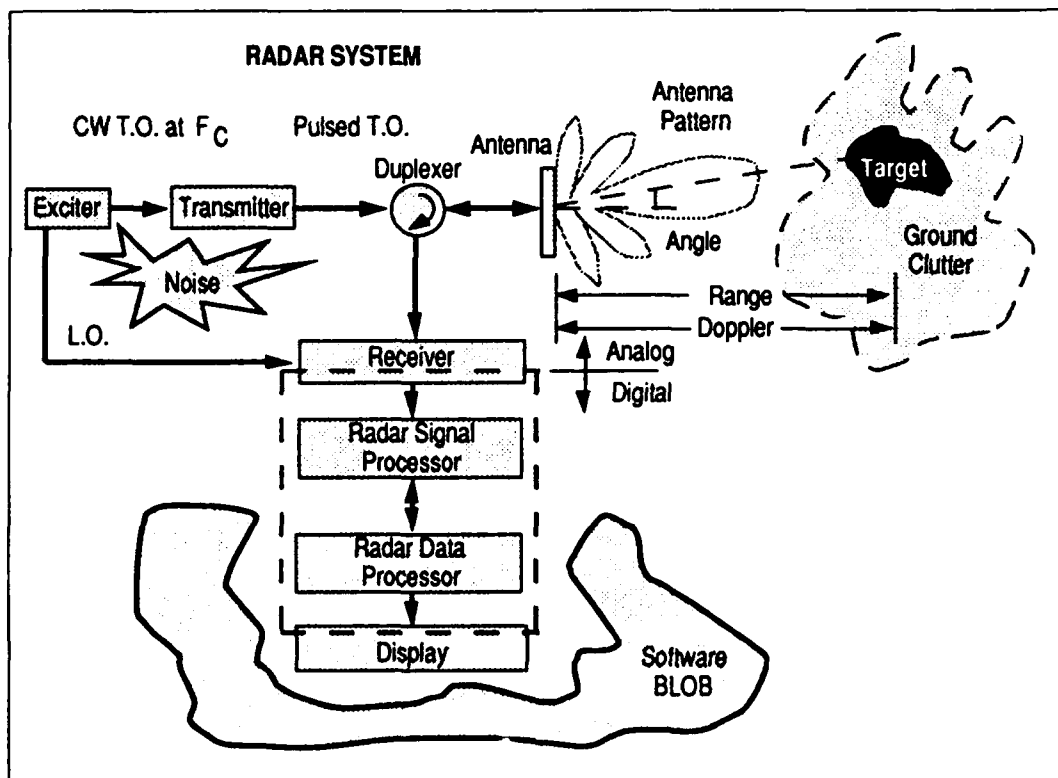
Figure 1. Simplified Block Diagram of Radar System

go through the duplexer and into the receiver unit. The purpose of the duplexer is to isolate the transmitter signal from the receiver signal, and vice versa. The receiver translates the received RF signals, by mixing them with the local oscillator (L.O.) signal(s), to baseband signals (modulation envelope on the carrier signals) and sends a digitized signal to the radar signal processor. The received radar signal is then processed to obtain the range, angle, and Doppler information and sent to the radar data processor unit for formatting. The radar data processor sends the received signal to the display and also generates the control signals for the radar.

Figure 2 shows the major units of a radar located in the nose of an aircraft. The software programs provide algorithms that direct the radar digital units and
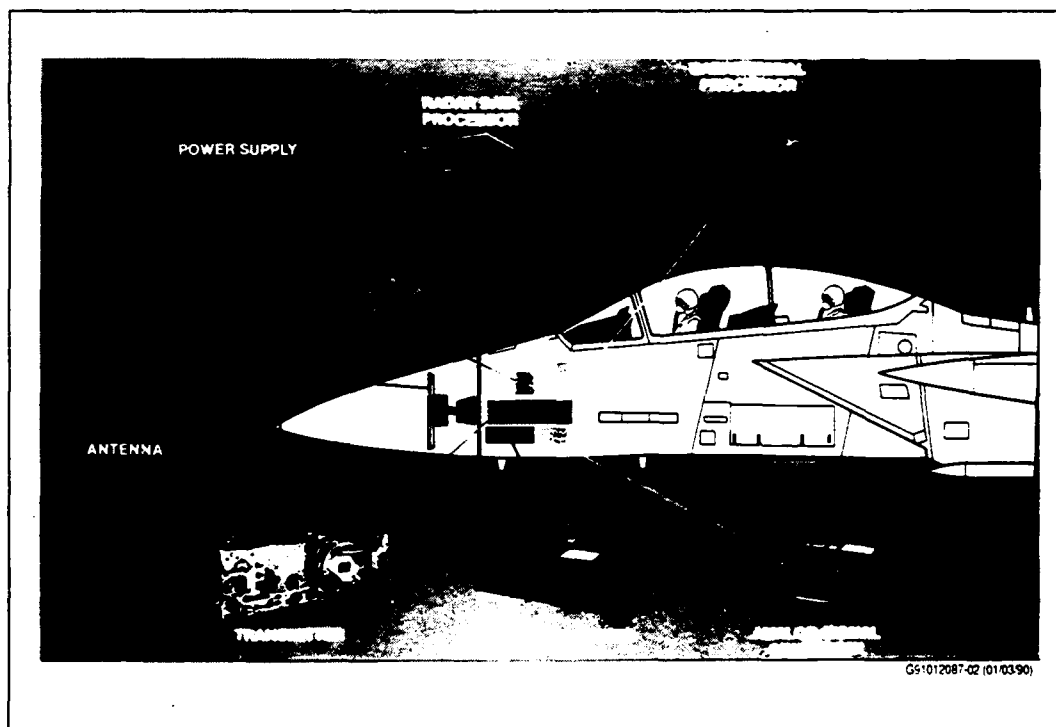
Figure 2. Radar Installation in Aircraft with Mechanically Scanned Antenna

control the other radar units. Many sources of noise are generated in the radar and affect radar performance.

The radar system can be viewed as a signal analyzer that processes signals in both the time and frequency domains. Figure 3 shows the target return in both the time and frequency domains along with the time delay and Doppler frequency equations. Each domain is useful to "view " the target and the various noise sources, and all information on the target is available in each, related mathematically via convolution or Fourier analyses.

Major parameters that affect radar performance and that are affected by beam-steerer performance are sidelobes, noise figure, stability, and dynamic range.

TIME DOMAIN
PULSED WAVEFORM DETECTOR

FREQUENCY DOMAIN
BASEBAND DOPPLER SPECTRUM ANALYZER

Time Delay Equation

$$T_D = \frac{2R}{C}$$

T_D = Time Delay
R = Range
C = Velocity of Light

Doppler Frequency Equation

$$F_D = \frac{2V_R}{\lambda}$$

F_D = Doppler Frequency
V_R = Relative Velocity
λ = Wavelength of Carrier Frequency

Figure 3. Two Views of Radar Signals

Those parameters show up as noise corruption that limits the radar's ability to perform its mission.

3.0 Active Arrays

One way to classify radars is by the method used to steer or point the antenna mainbeam. Most radars in current use are mechanically steered and have mechanically scanned antennas. More recent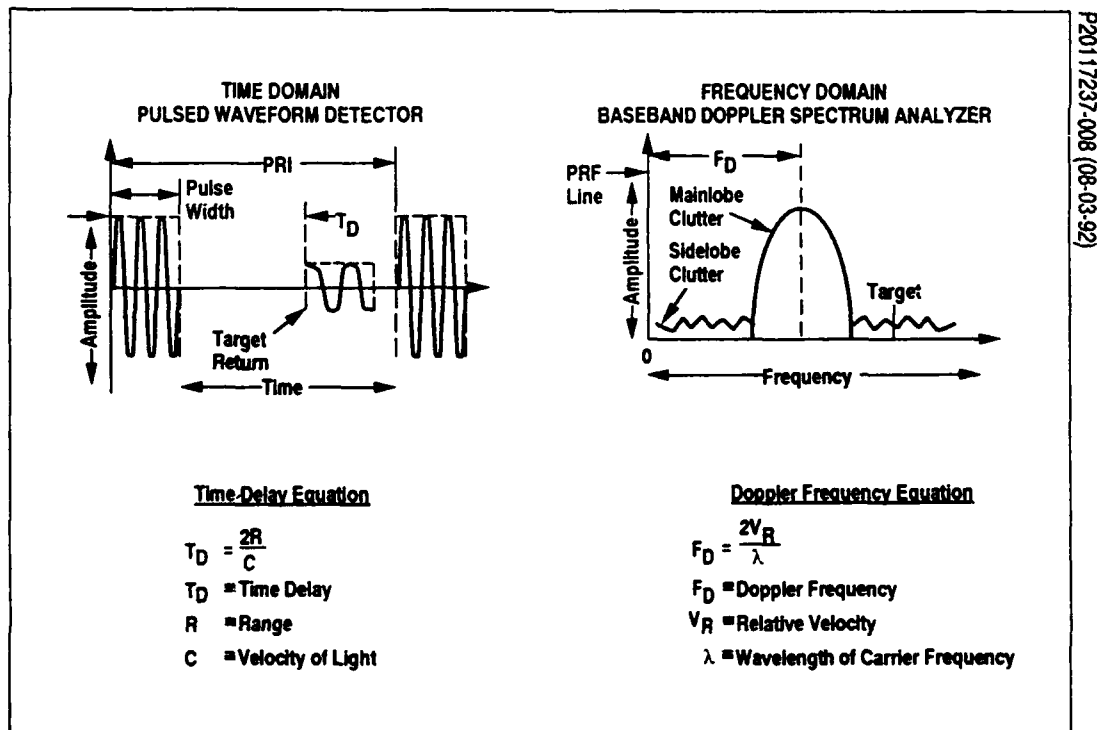ly designed radars are steered electronically and have electronically scanned antennas (ESAs). ESAs can be either passive or active. Passive ESAs have an RF manifold for RF signal distribution to the array of radiating elements (array or aperture) that contains only passive components and receives inputs from a central high-power transmitter and also sends outputs to a low-noise receiver. Active ESAs, called active arrays, have an RF manifold that contains active components assembled into small packages called transmit/receive (T/R) modules. Both passive ESAs and active arrays have RF manifolds that have components that quickly change the phase to each radiating element. ESAs use phase steering to point the mainbeam.

Figure 4 is an artist's conceptual drawing of an active array radar antenna. The major components of the antenna are aperture, T/R modules, manifold, and cooling. Both the design and the state of development of the active array make that array an excellent candidate for the insertion of optoelectronics.

Figure 5 gives both a picture and a corresponding block diagram of a T/R module. This particular X-band (10 GHz) T/R module illustrates the use of MMIC chips
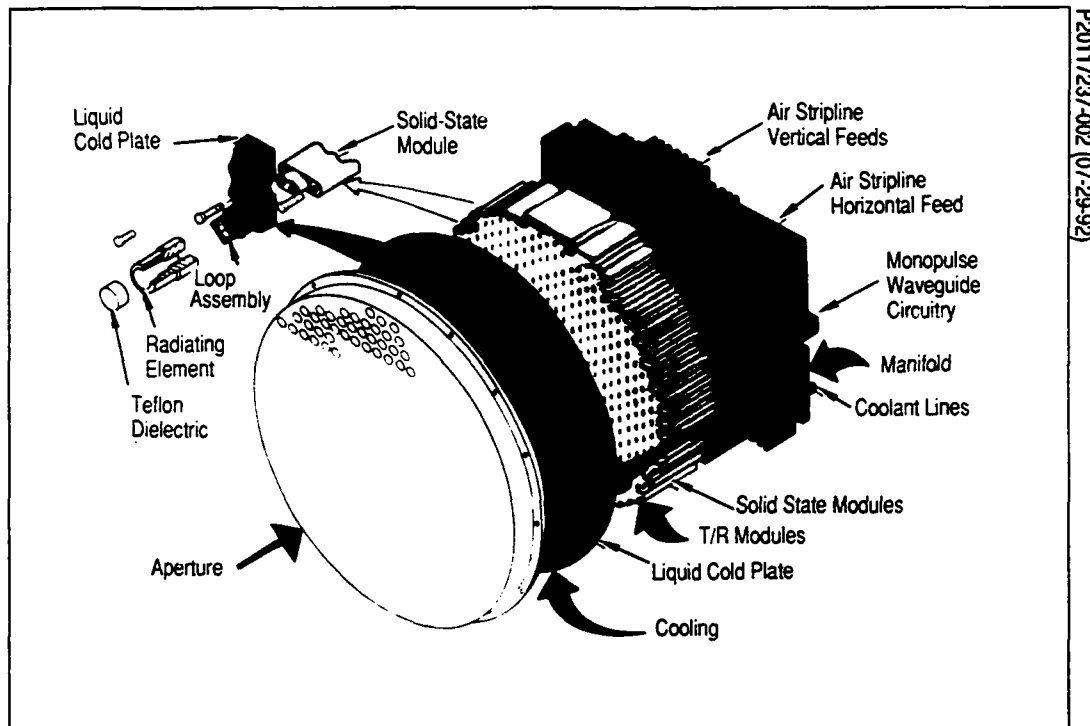
Figure 4. Typical Active Array Radar Antenna

and the compact packaging required for typical T/R modules. The T/R module is like a radar itself because it has a transmitter, receiver, control logic, and antenna (radiator). It also has a phase shifter that is used in combination with other T/R module phase shifters to steer the antenna array. The T/R module is a part of the RF manifold that transmits, receives, and steers the radar signals.

4.0 TTD Beamsteering

ESAs can be pointed by various forms of phase steering that establish the direction of the mainbeam energy by generating an RF wavefront that has the RF energy in phase along the perpendicular to a line that is in the direction of the desired pointing angle. The phase steering concept is shown in Figure 6, along

Receive RF Output

Switch 1 (SW 1)

Xmit RF Input

Phase Shifter (5 Bit)

SW 2

FET Amp

FET Amp

High Power Xmit FET Amp

Receive

FET LNA

SW 3

Radiator

Power and Control

Module Control Logic (MCL)

Block Diagram of T/R Module

Picture of Transmit/Receive (T/R) Module

Figure 5. Typical X-Band MMIC T/R Module

Phase Shifter or True Time Delay Unit

True-Time-Delay is $\dfrac{(m-n)\, d \sin \theta}{v}$

Element No.= n = 1 to r

m=7

Phase Setting is $\dfrac{(n-1)\, 2\pi\, d \sin \theta}{\lambda}$

d

θ Pointing Angle
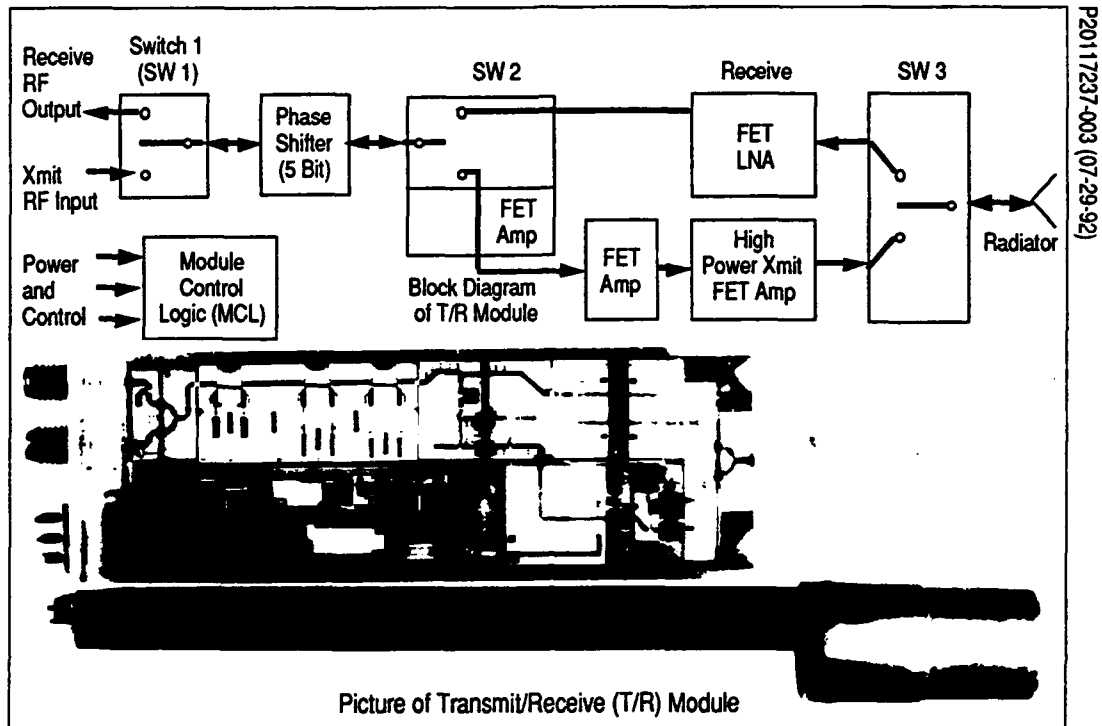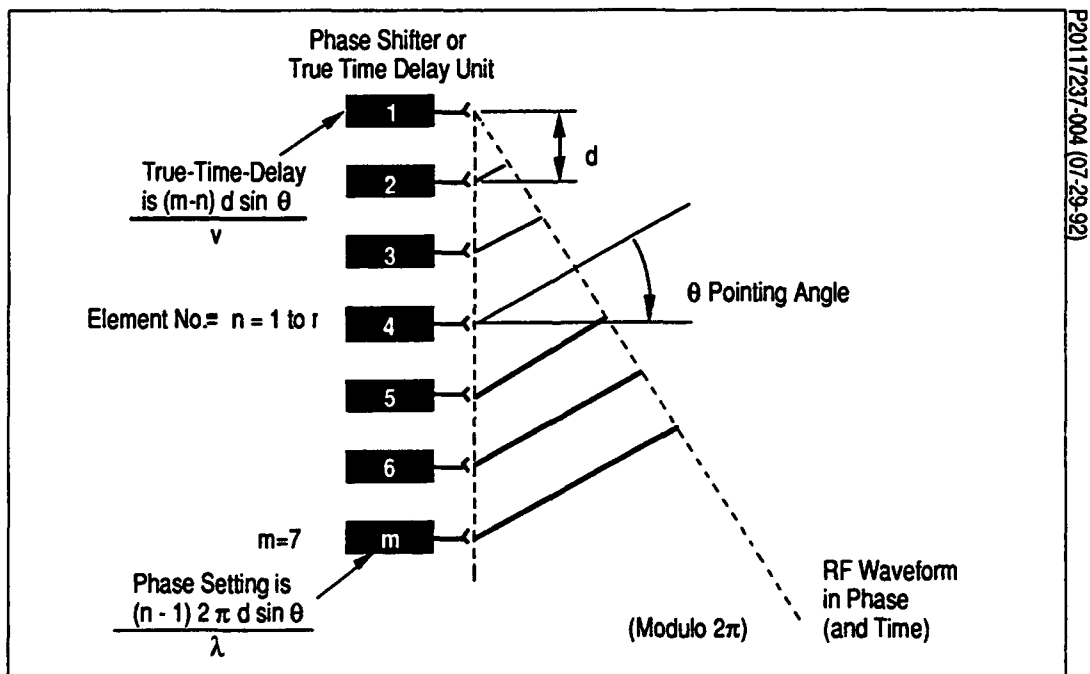
RF Waveform in Phase (and Time)

(Modulo 2π)

Figure 6. Phase and TTD Beamsteering Equations

with the equation used to calculate the antenna steering phase for each of the radiating elements in the array. The term "phase steering" is used here to distinguish it from TTD steering, which is also shown in Figure 6, along with its corresponding steering equation.

The major difference in the two types of steering is that TTD steering is not frequency dependent, as can be seen in its equation, which does not have a frequency dependent term. The equation for phase steering shows it is frequency dependent because it has the wavelength, λ, which is proportional to frequency. In addition, because a phase shifter is used to set the pointing phase in a phased steered antenna, the phase setting is called modulo 2π, meaning that the phase calculated in the equation is rounded off to the nearest 360 degrees (2π radians). Thus, the phased steered antenna is only pointed correctly for one specific frequency, the one used in the equation to calculate the phase steering angle.

Figure 7 shows pictorials of both TTD and phase steering. For TTD steering, the RF energy from each radiator arrives at the wavefront of the antenna pointing direction at the same time and with the same phase. The pictorial of phase steering shows that the RF energy arrives in phase, but does not arrive at the wavefront of the pointing direction at the same time. The level of signal degradation that this time arrival spread will cause depends on several factors. One factor is the instantaneous bandwidth of the RF signal. The particular waveform modulation envelope on the RF carrier signal can produce a large number of frequencies that will all occur simultaneously, producing large instantaneous bandwidth. In phase steering, where only one frequency is pointed exactly, all others are steered incorrectly. Other factors are the length of the antenna array and the pointing angle relative to broadside (the straight-ahead pointing direction); the
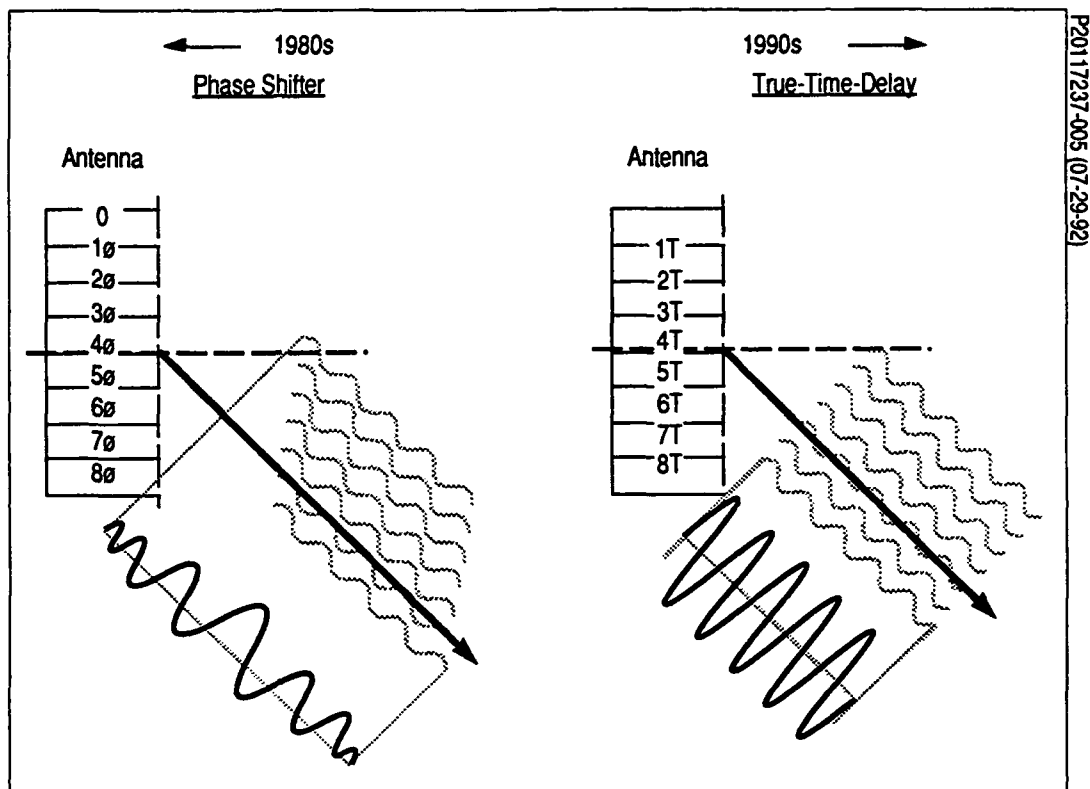
Figure 7. TTD Versus Phase-Shifter Steering of Phased Array Antennas

larger both of those factors are, the larger the signal degradation is. Those error effects can be viewed in both the time and frequency domains because they are related mathematically. Thus, the amount of degradation that can be accepted has to be calculated for each antenna design.

There are several important TTD beamsteerer parameters that affect radar performance. A brief discussion of those parameters is given below:

- Number of bits. This determines the resolution of the time delay for each beamsteerer and will affect pointing and the sidelobe level of the radar;

- Noise figure. This effect will determine the amount of added noise power, and its effect will be determined by the amount of noise introduced by other sources;

- Loss. The attenuation of the beamsteerer can add to its noise figure by attenuating the desired signal and also added gain stages to obtain the required output signal level may be required;

- Dynamic range. Limited dynamic range introduces unwanted, additional signals (intermodulation products) and may reduce the level of the desired signal;

- Isolation (crosstalk). This is defined as the fractional part of the signal from one beamsteerer delay section that corrupts the desired delay section. This corruption changes the amplitude and phase of the signal in the desired delay section;

- Errors. This occurs when the desired relative value of TTD is in error in time and/or phase, and when the loss (or gain) in the signal path varies from that of other beamsteerer signals;

- Stability. Signal stability refers to the amplitude and/or phase noise that is added to the signal because the beamsteerer is an active device. The effect appears on the desired signal as a reduced signal-to-noise level.

All of the above parameters should be determined to characterize the performance of any beamsteerer.

5.0 Optoelectronic TTD Beamsteering and Manifolding

Sections 2.0 through 4.0 have discussed beamsteering and radar in somewhat general terms. This section will introduce the use of photonic technology into active

array radar manifolds and beamsteering. Active arrays can benefit from the use of optoelectronics for "leap-ahead" technology applications in TTD beamsteering for wide instantaneous bandwidth and wide bandwidth; in RF and digital signal manifolding; and also for testing, calibration, and built-in test. The characteristic of photonics that make optoelectronics components so well suited for the above functions are wide bandwidth, small size, light weight, and the elimination of electromagnetic interference.

Figure 8 shows a block diagram of how an active array radar might be configured using the remoting capability of fiber optics so that most of the radar units can be conveniently located away from the antenna and how all electrical inputs and outputs (except dc power) of RF and control signals are carried over a fiber optic manifold. The beamsteerer is shown as a separate unit of the radar units only to indicate its location in the manifold.

Several ways that an optoelectronic TTD beamsteerer can be configured are with laser, photodiode, or optical switches. The use of each of those switches allow the selection of different links of fiber cable or other means of guiding lightwaves (as waveguides in materials) to obtain the desired delay time. Both the laser and the
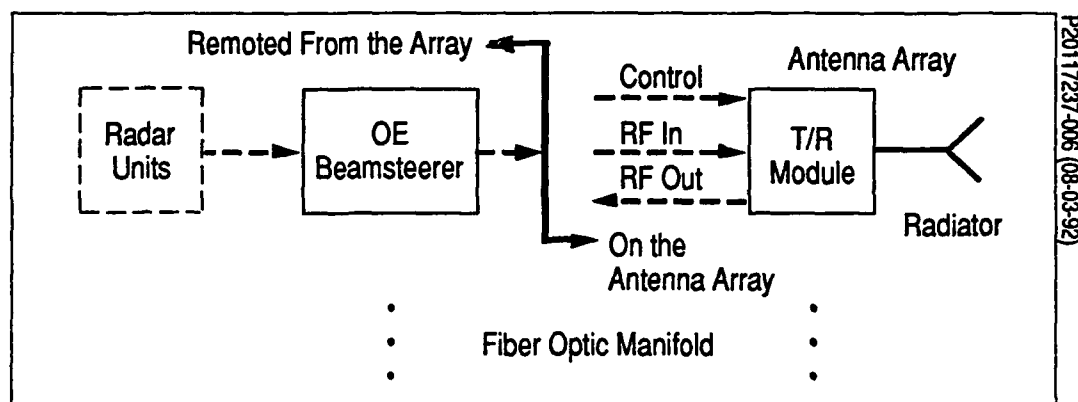

Figure 8. Active Array with Remoted Optoelectronic Beamsteerer and Fiber Optic Manifold

photodiode act as switches by respectively controlling their bias current or voltage and also perform their normal function of light generation and modulation or detection when they are biased on. All optical switches (light input and light output) can be fabricated using several electro-optical materials where the switch activation is done electronically. Hybrid switches can be made up of combinations of various types of switches to take advantage of the best capability of each switch type. Because the switching is a discrete process of selecting delays, the use of some means of optical or electronic analog trimmer in a beamsteerer to obtain variable delays that allow delay values between discrete steps and provide a means for correcting errors in the overall delay is desirable.

The description and radar demonstration of a laser switched beamsteerer is given in reference [1], which reports on work that was supported in part by a U.S. Air Force Rome Laboratory contract. A current DARPA/ Rome Laboratory radar program that will use optoelectronic beamsteerers was described in a presentation at the 1991 DARPA/Rome Laboratory Symposium [2]. Several other papers given at the same symposium describe photodiode, optical, and other types of switches for optoelectronic beamsteerers [3-8].

Because of the flexibility of fiber optic components for remoting, the beamsteerer can be located at any convenient place in the manifold, either within the antenna array, adjacent to or within the T/R module, or wherever the RF signals are provided. There are also several ways to configure the RF modulated light source for the beamsteerer even though it can be considered a part of the beamsteerer. The choice will depend on many system design factors and also on the state of optoelectronic technology. One way to configure the manifold that offers the capability to "grow" with both of the above factors is shown in Figure 9, a block diagram
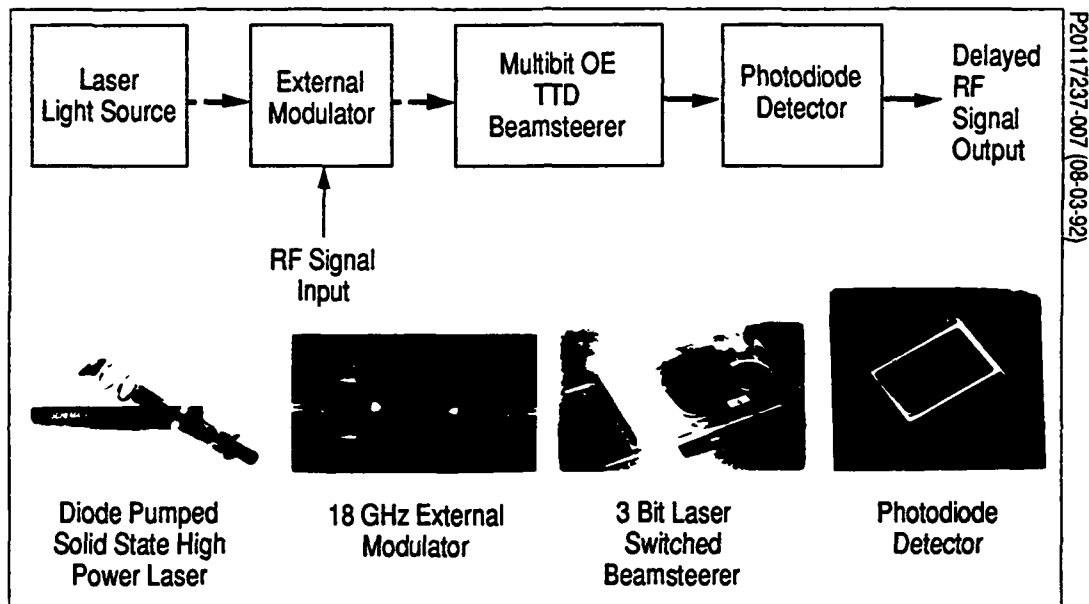
Figure 9. Optoelectronic Beamsteerer in Fiber Optic Manifold Link

with pictures of some components that can be used. This remoted beamsteerer is in a fiber optic manifold that consists of an external modulator [9-11], supplied by a remoted solid-state diode pumped high-power laser [12-13], and provides an RF modulated lightwave signal to a laser switched fiber optic beamsteerer and an output photodiode detector [14] that can be located in or adjacent to a T/R module of an antenna active array.

The description of manifolding thus far considered only the direct one-to-one connection between the beamsteerer and T/R module. It is also possible to use a single beamsteerer to control a group of T/R modules in what is called a subarray configuration. The use of an optoelectronic TTD beamsteerer or a phase shifter in each T/R module of the subarray should be traded off.

6.0 Comments and Conclusions

The manifold and beamsteerer used in future radar systems will be determined by many factors in the radar market. The desirable features of the optoelectronic TTD beamsteerer are that it has large potential use in systems; can be made to be cost effective; has minimum effect on the electronic part of the radar; can meet radar parameter requirements; and can be brought quickly to the market now that the technology is ready.

There is no question that TTD beamsteering is needed in future shared aperture active array radars to give them the capability to utilize wide instantaneous bandwidth. Optoelectronic TTD beamsteerers can fill that need. The best opportunity to get optoelectronics into active array radars in a signal processing usage is via TTD optoelectronic beamsteerers. Current and future DARPA and USAF Rome Laboratory programs give us the opportunity to achieve that goal. To achieve the goal it is important that we address the issues of affordability/design to cost; packaging; environmental; "illities" (i.e., reliability, etc.); and system design, performance, and interfacing.

Thus, the challenge is there, so let's go to it!

Acknowledgement

References

All references that are followed by an asterisk were published in the *Proceedings of the Second Annual DARPA/Rome Laboratory Symposium on Photonics Systems for Antenna Applications,* December 1991.

[1] Ng, W., A. Walston, G. Tangonan, J.J. Lee, I.L. Newberg, N. Bernstein. "The First Demonstration of an Optically Steered Microwave Phased Array Antenna Using True-Time-Delay." *Journal of Lightwave Technology,* September 1991.

[2] Lee, J.J., W.W. Ng, G.L. Tangonan, H.W. Yen, I.L. Newberg, N. Bernstein. "Opti · lly Controlled Phased Array Program Overview."*

[3] Ng, W., A. Narayanan, R. Haya, D. Yap, A. Walston. "High Efficiency Waveguide-Integrated MSM Detectors."*

[4] Sullivan, C.T., S.D. Mukherjee, A. Gopinth. "Switched Path Integrated Optic Delay Lines in GaAs."*

[5] Goutzoulis, A.P., D.K. Davies. "Hardware-Compressive Wavelength-Multiplexed Fiber-Optic Architectures for True Time Delay Steering of Phased Array Antennas."*

[6] Hemmi, C., C. Takle. "Optically Controlled Phased Array Beamforming Using Time Delay."*

[7] Hartman, N.F., L.E. Corey. "Wideband Phased Array Time Delay Networks Based on Integrated Optics Technology."*

[8] Gesell, H., T.M. Turpin. "True Time Delay Beam Forming Using Acousto-Optics."*

[9] Buckley, R.H. "Progress in Microwave Modulated Fiber Optics." *Proceedings of the International Society for Optical Engineering, Optical Technology for Microwave Applications*, Vol. 1102, 78-92, 1989.

[10] Bulmer, C.H., W.K. Burns, A.S. Greenblatt, G.K. Gopalakrishnan. "Broadband, Traveling Wave Phase and Amplitude Modulators for Photonics Applications."*

[11] Glomb, W.L., J.D. Farina, W.J. Green, N. Bernstein. "Deployable Analog Fiber-Optic Links for Antenna Remoting."*

[12] Olson, T.E., T.J. Kane, F. Adams. "Fiber Coupling and Phase-Locking of Low-Noise Diode-Laser-Pumped Nd:YAG NPRO Lasers."*

[13] Anthon, D.W., A.T. Eggleston, T.J. Pier. "Developments in Diode Pumped Solid State Lasers."*

[14] Eastman, L.F., K. Litvin, J. Burn, D.W. Woodard, W.J. Schaff. "High Frequency Optical Receivers."*

AN OPTICALLY CONTROLLED KA-BAND PHASED ARRAY ANTENNA

R. R. Kunath
R. Q. Lee
K. S. Martzaklis
K. A. Shalkhauser
A. N. Downey

NASA Lewis Research Center
Cleveland, Ohio

and

R. Simons

Sverdrup Technology, Incorporated
Middleburg Heights, Ohio

Abstract

Future communications satellites applications are considering phased array antennas as an integral part of the overall communications system. Monolithic Microwave Integrated Circuit (MMIC) based phased array antenna systems enable multi-functional system attributes such as electronic beam steering, multiple beams, system reconfigurability, and graceful system degradation. NASA Lewis Research Center's Space Electronics Division has been actively pursuing the development of MMIC-based phased array antennas for communication satellite applications in the Ka-band. However, due to the compact spacing of these arrays, methods of reducing the number of control signals to each element of the phased array are being investigated. NASA Lewis has

developed an OptoElectronic Interface Circuit (OEIC) which enables the distribution of control signals to each antenna element through a single fiber optic cable. With the application of this technology, the number of phased array interconnections has been minimized with a corresponding decrease in system weight.

This paper will discuss the design and development of a small, optically controlled phased array antenna suitable for communications satellites applications. A vertical integration architecture is used which minimizes the size of the array with its associated beamforming network (BFN). The antenna features a 4-element linear microstrip array that uses aperture coupling of the antenna elements to the BFN; a modified Wilkinson power divider BFN; and 32 Ghz, 4-bit MMIC phase shifters in customized quartz packages with corresponding OEICs for control signal reception.

I. Introduction

Phased-array antennas have long been investigated to support the agile, multibeam radiating apertures with rapid reconfigurability needs of radar and communications. With the development of the Monolithic Microwave Integrated Circuit (MMIC), phased array antennas having the stated characteristics

are becoming realizable. However, at K-band frequencies (20-40 GHz) and higher, the problem of controlling the MMICs using conventional techniques either severely limits the array size or becomes insurmountable due to the close spacing of the radiating elements necessary to achieve the desired antenna performance.

Investigations have been made that indicate using fiber optics as a transmission line for control information for the MMICs provides a potential solution[1]. By adding an optical interface circuit to pre-existing MMIC designs, it is possible to take advantage of the small size, lightweight, mechanical flexibility and RFI/EMI resistant characteristics of fiber optics to distribute MMIC control signals. Additionally, vertical integration, separating the antenna into discrete functional layers, further minimizes the space required to implement the antenna. This paper will describe the architecture, circuit development, testing and integration of an optically controlled K-band MMIC phased-array antenna.

II. Vertically Integrated Antenna Architecture

Figure 1 shows an optically controlled, vertically integrated 1X4 rectangular patch array architecture. The dimensions of the patch antennas, which are etched on a 10 mil PTFE substrate (e=2.2), are 0.239 cm by 0.417 cm. The patch antennas are aperture coupled to a microstrip line through a slot in the ground plane. The ground plane on the antenna layer is common between the

65

RF and antenna layers. The slot dimensions are 0.407 cm in length by 0.0254 cm in width, and are oriented along the H field line. It was experimentally determined that a 90% coupling efficiency is achieved with this method.

The MMIC phase shifters were developed by Honeywell through a contract with NASA Lewis. The four-bit design consists of three switched-line bits (180°,90°,45°) and one loaded-line (reactive) bit (22.5°). The MMICs were designed for a center frequency of 32 GHz and a bandwidth from 31-33 GHz. The targeted insertion loss was designed to be 2 dB/bit with an S11 and S22 of greater than 10 dB.[2] The device size is 6.41mm X 2.65 mm. Each switched-line bit is controlled by two pairs of FETs as shown in Figure 2. At any given time, the RF signal propagating through the bit is directed to either a delay path or a reference path by differentially biasing the pairs of FETs with zero and minus five volts. The loaded-line is controlled by applying a variable zero to minus five volt signal to it. While the loaded-line phase response is not linear, it does provide some trimming capability to accommodate the in-exact settings of the switched-line bits.

The OEICs were also developed by Honeywell through a contract with NASA Lewis. These devices are follow-ons to a successful proof-of-feasibility, hybrid OEIC development. The current OEIC features a fully monolithic receiver which includes an integrated photodectector, LNA, link status moni-tor, clock recovery circuit, and a 1:10 demultiplexer with a 4B/5B decoder.

Additional features include: operation from 10 to greater than 400 Mbps, burst and continuous mode operation, on-chip addressability and diagnostics, and a mil-spec, foundry compatible process. The die size is 0.215" by 0.109", and the device operates at wavelength between 780 and 820 nanometers (Figure 3). A specialized, two-layer carrier was fabricated on which to mount the devices. The two-layer design was designed to conform to the dimensions of the MMIC package lid, and to enable the bias connections to the OEIC to be limited to two.

Each phase shifter MMIC is packaged in an individual fused silica package fabricated by Hughes Aircraft Company to facilitate its RF characterization prior to use in the array. This approach not only adapts the MMIC for connection to the test fixturing, but also provides a stable mounting platform for the MMIC to help protect it from damage during handling. Fused silica was chosen because its electrical properties enable its use at high frequencies with the lowest known loss. Furthermore, because the OEIC requires no ground plane, the lid of the package provides a surface upon which it can be mounted. Figure 4 illustrates the package design, while Figure 5 details the "piggy-back" OEIC mounting.

A 1X4 power divider was designed to split the signal from the RF source into four equal amplitude and equal phase signals to present to the MMIC phase shifters. Three modified Wilkinson[3] equal-split (3 dB) power dividers are

formed on copper clad, 10 mil PTFE substrate material, with a copper/resistive metal composite layer from which shunt resistors were formed (Figure 6). The shunt resistors provide isolation between the legs of the power divider by absorbing signals reflected from the MMIC phase shifters that propagate back through the divider network.

The final layer of the antenna provides both structural support and bias signal distribution. Each of the MMIC phase shifters requires seven control signals, which are provided by the OEIC, but the bias of zero and minus five volts is routed on this layer. This layer is fabricated from 62.5 mil PTFE material. The bias/control layer must lay directly on top of the microstrip lines of the 1x4 power divider as shown in Figure 1. The low dielectric constant of this board minimizes its impact on the 1X4 microstrip power divider. Additionally, four "windows" are cut into this board to provide wire bonding access to the MMIC phase shifters.

III. MMIC and OEIC Characterization and Performance

The main objective of the MMIC testing was the determination of the relative insertion phase as a function of phase shifter state setting. The MMICs were characterized using a specially designed alumina carrier and an test fixture. A 50 ohm, 500 mil long through line on a 10 mil thick Alumina substrate

served as the thru standard. Multiple insertion of the thru standard demonstrated good test fixture repeatability (Figure 7). Calibration verification with regard to insertion phase was achieved via a 527.68 mil line resulting in a 527.72 mil measurement. The characterization of the MMICs in the package has not yet been accomplished.

A total of 24 packaged MMIC's were characterized. For each of the 16 phase states, measurements were conducted for insertion loss and relative insertion phase. The variable loaded line bit was also characterized. Typical insertion loss values ranged from 10 to 12 dB for the test assembly (carrier, MMIC & bondwires) over the 16 phase states (Figure 8). To measure relative insertion phase, the MMIC was set to its reference state (0 °) and this measurement was stored to memory. Since a division of two complex numbers in polar form is equivalent to the ratio of the magnitudes and the difference of the angles, the (S21/memory) display feature of the ANA was utilized to show the additional insertion phase as each state was switched in (Figure 9). The curves were generally linear at the frequencies of interest. Performance of the loaded line bit is shown in Figure 10. Eight of the 24 MMIC's were chosen for array integration.

The OEICs were tested by Honeywell in both bursted and continuous modes. Figure 11 shows the results of the OEIC being tested in bursted mode. The device was tested up to data rates in excess of 400 Mbps with no signs of

device was tested up to data rates in excess of 400 Mbps with no signs of degradation in performance. Testing instrumentation limitations prevented characterization beyond these data rates.

IV. Conclusions

An optically controlled 1X4, 32 GHz subarray antenna has been presented. The antenna features a vertically integrated architecture that uses MMIC phase shifters with "piggy-backed" OEIC control devices. Experimental results of the testing and characterization of the devices and components have been discussed. This type of architecture minimizes the space of the antenna, and the use of fiber optic control signal distribution minimizes the number of control signal lines to the devices, with an associated mitigation of weight.

V. References

1. Kunath, R.R. and Bhasin, K.B. (1988) Optically Controlled Phased-Array Antenna Technology for Space Communication Systems, Pro. SPIE, O/E LASE.

2. Mondal, J., Geddes, J., Contolatis, T., Bauhahn, P., and Sokolov, V. (1990) 30 GHz Monolithic Receive Module Final Report, NASA Contractor Report No. CR 187085.
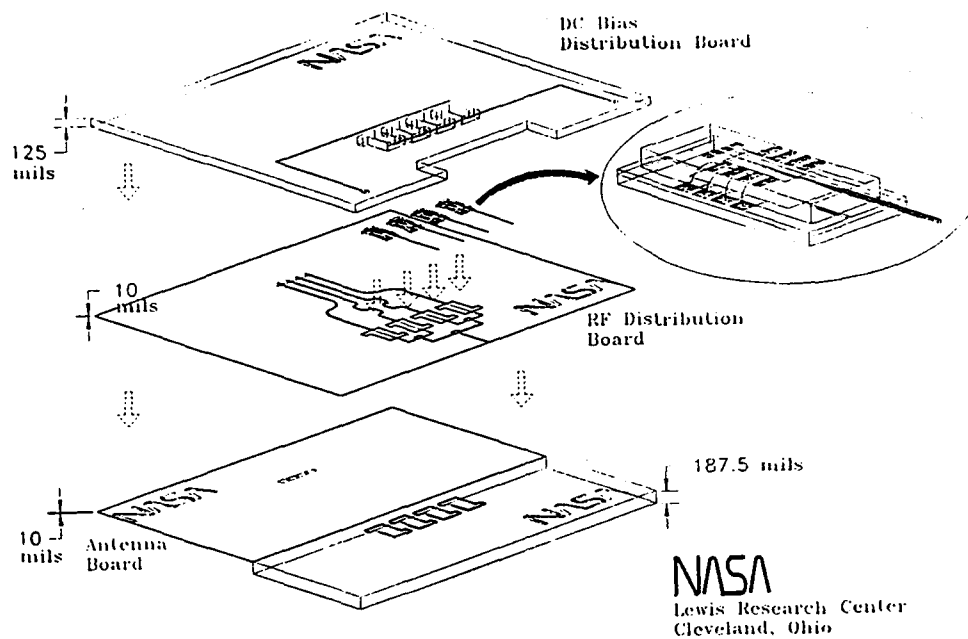
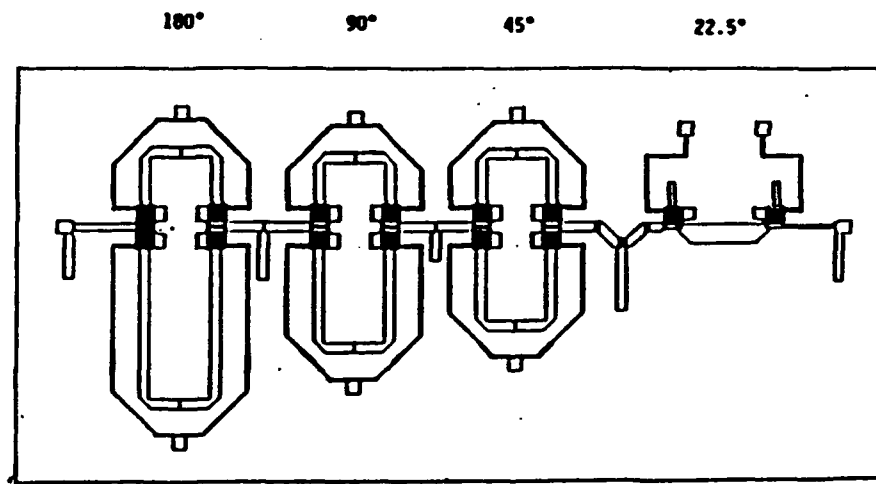**Figure 1. 1X4 Optically Controlled Ka-Band Phased Array**

**Figure 2. 32 GHz, 4-bit Honeywell Phase Shifter**

Objective
Develop an optoelectronic interface circuit (OEIC) capable of interfacing MMICs in a phased array antenna controller using a fiber optic distribution network

Current Focus
Fabricate OEICs for an experimental optically controlled phased array antenna demonstration

Honeywell OEIC with Fiber Optic Pigtail

Highly Integrated Monolithic Optical Receiver

Rationale
MMIC-based phased array antennas require multi-bit control signal distribution

OEICs enable fiber optic signal distribution to MMICs in antenna arrays

OEICs enable lightweight, low loss signal distribution networks that feature high EMI suppression and mechanical flexibility
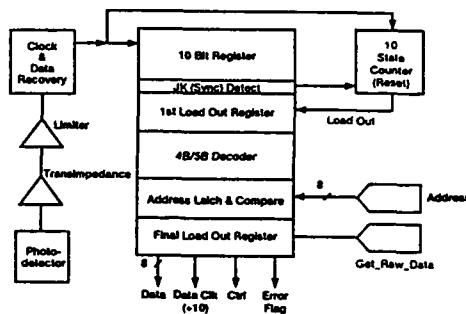
CD-91-58392

Figure 3. Honeywell OptoElectronic Interface Circuit
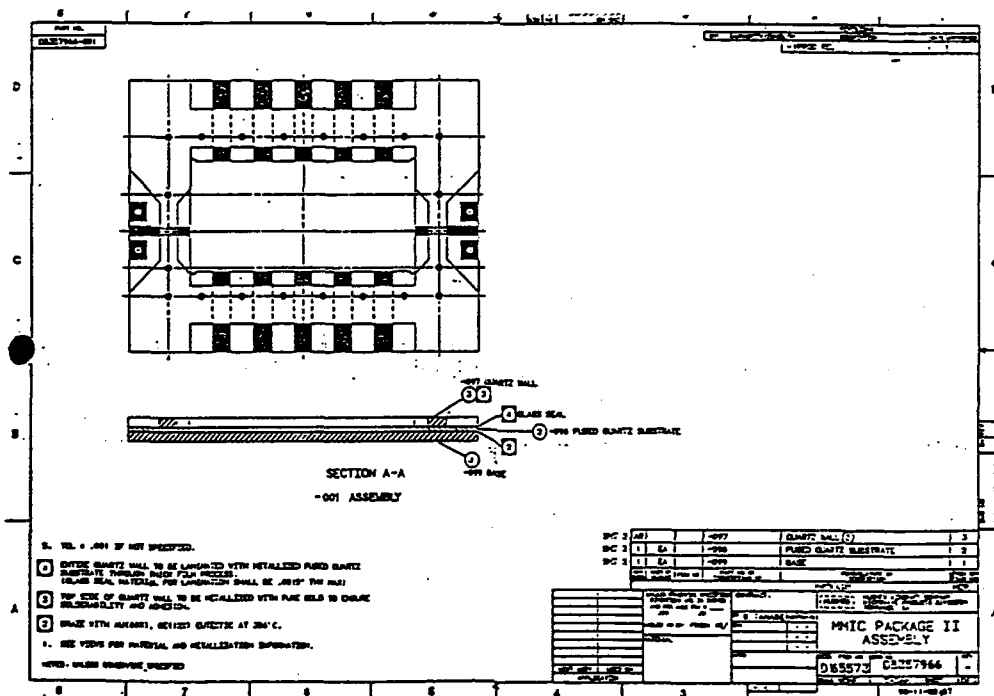
Figure 4. Hughes Fused Silica MMIC Package

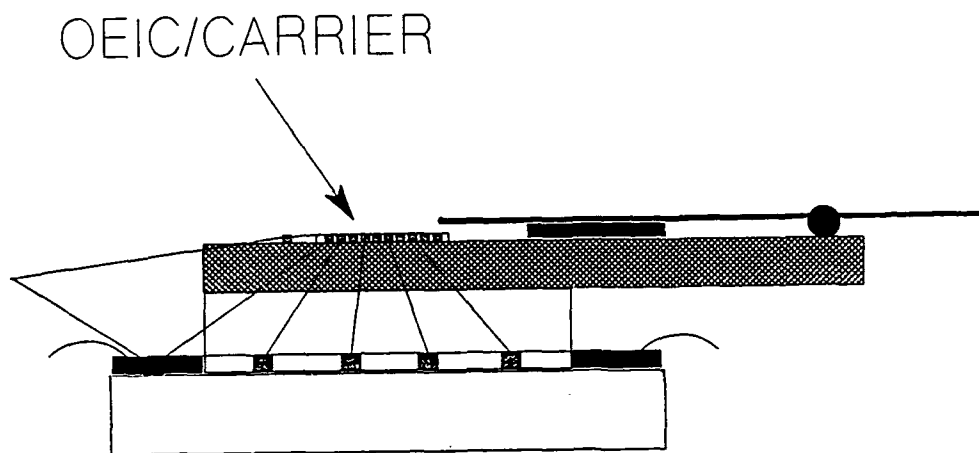**OEIC/CARRIER**

Figure 5. OEIC "Piggy-Back" Mounting

port 2

P/S

←resistor

P/S

port 3

port 1

←resistor

port 4

P/S

←resistor

P/S

port 5
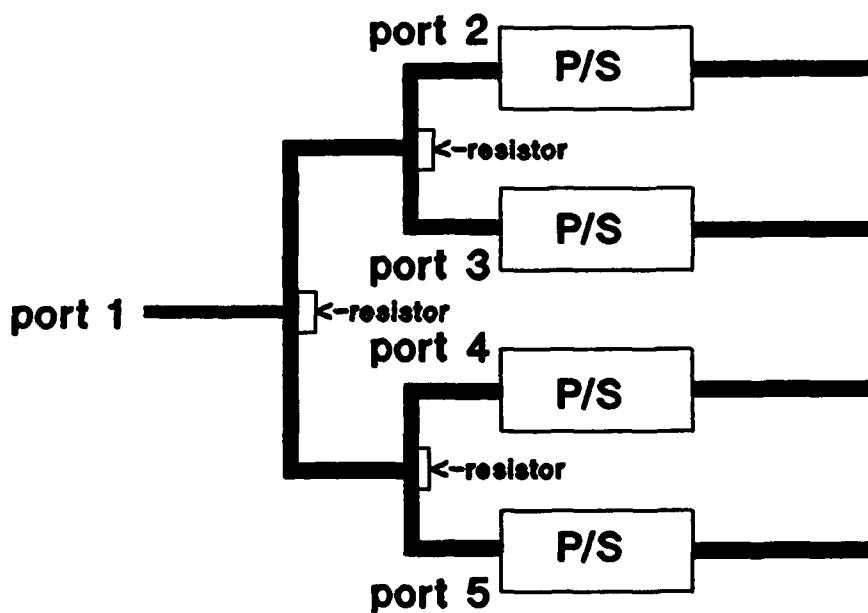
4-way modified Wilkinson divider/combiner

Figure 6. 1-to-4 Modified Wilkinson Power Divider

S21
REF 0.0 dB
2.0 dB/

hp

1

START   30.000000000 GHz
STOP   34.000000000 GHz
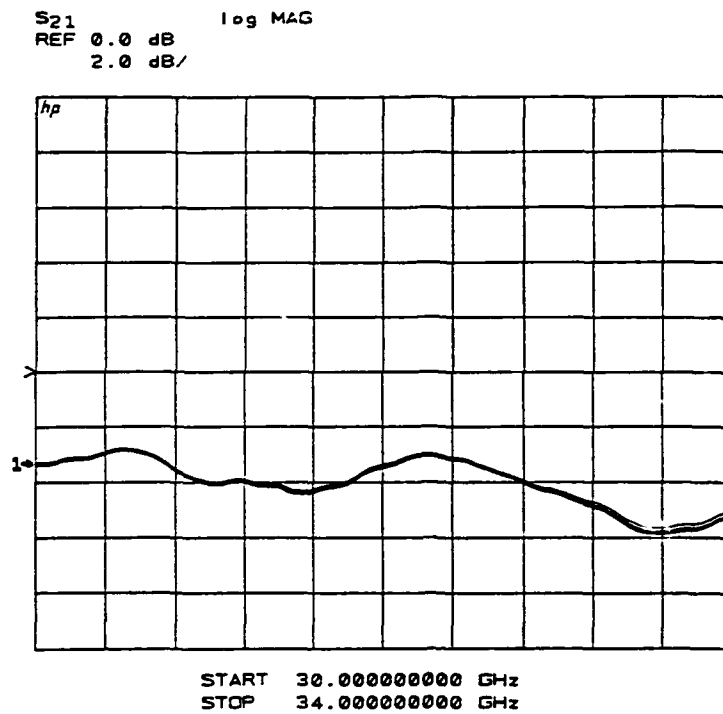
Figure 7. S21 of Test Fixture

S21
REF 0.0 dB
1   10.0 dB/
V   -13.32 dB

T. 2 TYPE 2 2/5189-8 #8A (3,2) 2/15/91 -5V
MEMORY RECALLED

C

M

START   30.000000000 GHz
STOP   34.000000000 GHz

Figure 8. Phase Shifter Insertion Loss

74
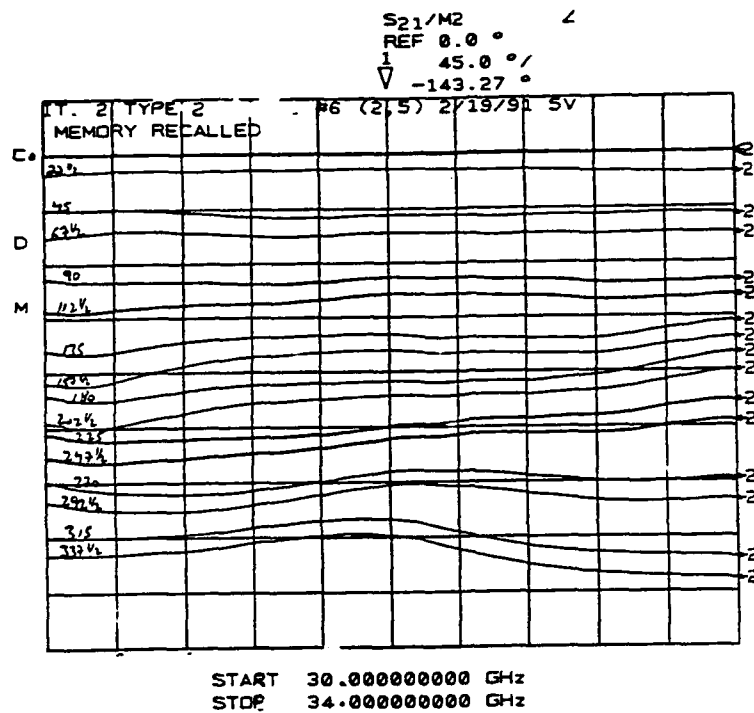
Figure 9. S21 of Phase Shifter in all 16 Phase States
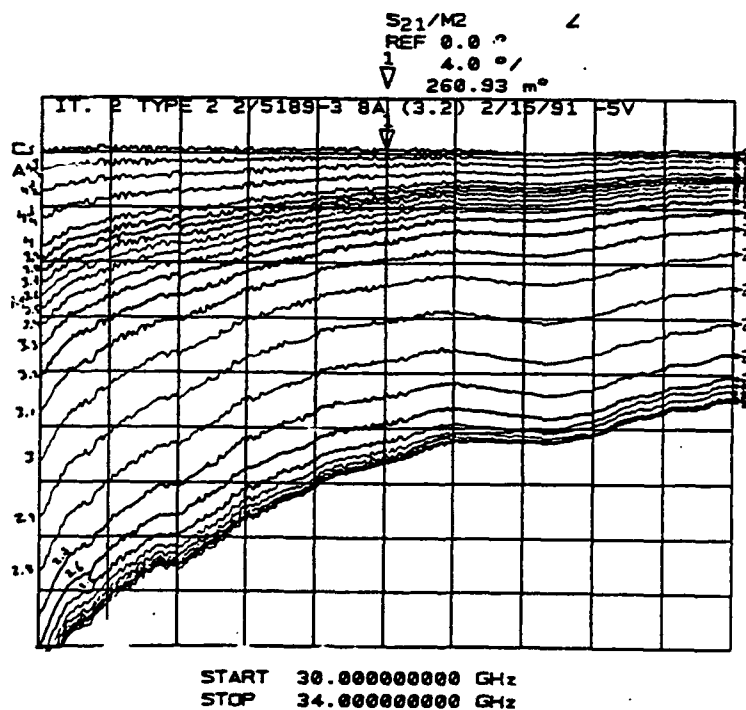
Figure 10. S21 of Phase Shifter Loaded Line

75

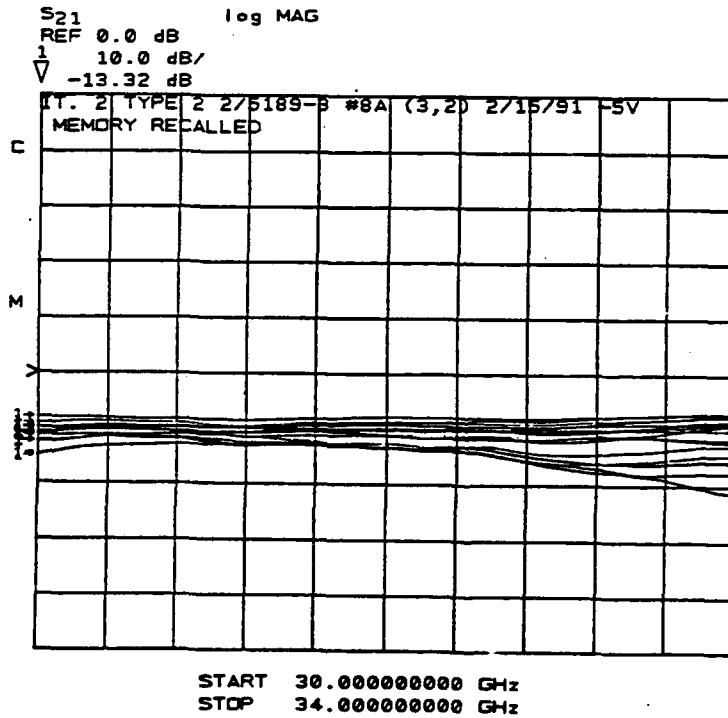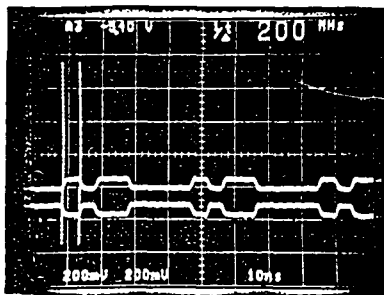Tested from 7-480 Mbps   Tested in Burst Mode to 130 Mbps
(Test System Limited)   (Test System Limited)
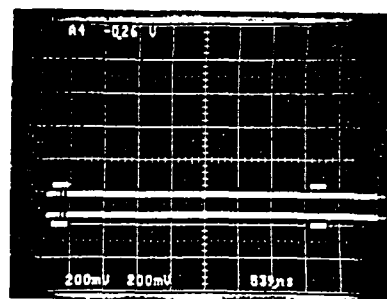
Contains the analog and digital circuits required to recover data and clock without the
need for external components or a phase-locked loop.

Additional Advantages: No preamble or set-up time required
                              Robust to jitter and amplitude variation
                              Broadband
                              Low cost

Figure 11. OEIC Bursted Test Demonstration

THz Electromagnetic Radiation from Planar Photoconducting Structures

X.-C. Zhang
Physics Department
Rensselaer Polytechnic Institute
Troy, NY 12180-3590
    and
J.T. Darrow, N.M. Froberg, D.H. Auston
Electrical Engineering Department
Columbia University
New York, NY 10027

Abstract

We present a novel optoelectronic technique to generate and detect THz electromagnetic waves by using large-aperture planar photoconducting structures. We describe the basic concepts and preliminary applications of steerable THz radiation from photoconductor antenna array structures. This technique provides an alternative method to produce optically steerable and electrically controllable ultrafast radiation pulses in free space.

1. Introduction

Recent advances in high speed photoconductors have led to devices which have subpicosecond response times. Various approaches have been used for generating and detecting ultrafast millimeter and submillimeter-waves [1]. These include elementary Hertzian dipoles, resonant dipoles, tapered antennas and transmission lines [2-5]. Large-aperture photoconducting antennas developed recently provide an alternative source to generate and detect directional submillimeter electromagnetic pulses with a terahertz bandwidth [6,7]. These devices have previously demonstrated novel and

potentially very useful properties that permit them to steer the THz radiation by an optical [8] or electrical approach [9,10].

In this paper, we discuss the basic properties of larger aperture photoconductive antennas and antenna arrays for generating and detecting the electromagnetic radiation with the frequency range from GHz to THz .
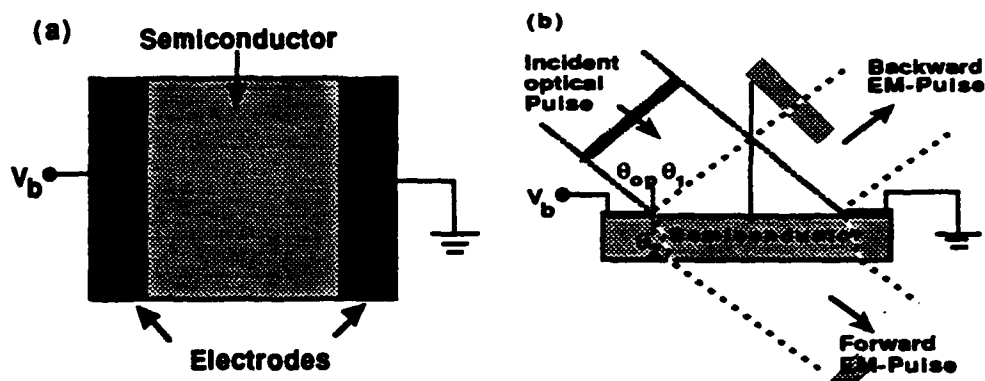
Figure 1: (a) Top view of a photoconductive antenna. The transverse dimension (the semiconductor gap between the electrodes) is large relative to the spatial duration of the radiation pulse. (b) The optical illumination, which consists of an ultrashort optical pulse, is absorbed in the photoconductor at an angle θ_{op}. The surface currents in the photoconductor radiate electromagnetic pulses in the direction of the specular direction, θ_1, and into the substrate at the refracted angle, θ_2.

The physical mechanism for the generation of subpicosecond electromagnetic pulses from large-aperture photoconducting antennas is the radiation from a fast time-varying photocurrent. By a large-aperture antenna (shown in figure 1(a)), we mean one whose transverse dimensions are large, relative to the spatial duration of the submillimeter-wave pulse. The technique is based on the following concept. When illuminat/ 1 by ultrashort optical pulses with the photon energy greater than the bandgap of the

semiconductor, as shown in Figure 1(b), a planar photoconductor absorbs the photons and produces free carriers. The photocarriers and external bias on the electrodes form a transient surface current. The photocurrent has a risetime on the order of optical pulse and a fall time comparable with the carrier decay time. The electromagnetic wave radiated by a time-varying current in the far field is proportional to the first time derivative of the current. The fast risetime of the current provides a high-frequency component of the radiation signal. The tilted wavefront of the optical beam determines the timing of the photocurrent distribution. If the dimension of the aperture is greater than the radiated median wavelength, according to elementary diffraction theory, the radiated signal is directional and diffraction-limited. The directions of the radiation can be steered by varying the angle of incidence of the optical beam. The submillimeter-wave radiates in both the backward and forward directions (θ_1 and θ_2). If the angle of incidence of the optical pulse is θ_{op}, the angles of the radiated electromagnetic pulses satisfy the generalized Fresnel's law equations:

$$n_1(\omega_{op})\sin\theta_{op} = n_1(\omega_{el})\sin\theta_1 = n_2(\omega_{el})\sin\theta_2 \qquad (1.1)$$

where $n_1(\omega_{op})$, $n_1(\omega_{el})$, are the indices of refraction of the optical and electromagnetic pulses outside the photoconductor, and $n_2(\omega_{el})$ is the index of refraction of the electrical pulse in the photoconductor. If $n_1(\omega_{op}) = n_1(\omega_{el})=1$, as is true for the case where air is medium 1, the angle of the backward radiated electromagnetic pulse is equal to the angle of the incident optical pulse. For an aperture size of the photoconductor on the order of cm, which is larger than the spatial pulse duration of the electromagnetic radiation, the electromagnetic wave is directional and diffraction-limited.

We can estimate the behavior of the electric field by the following arguments. Near the transmitter, we expect the field to be

approximated by a plane wave whose amplitude can be derived by simple boundary value conditions at the surface of the photoconductor. The following boundary conditions

$$\hat{n} \times (\vec{E}_2 - \vec{E}_1) = 0 \tag{1.2}$$

$$\hat{n} \times (\vec{H}_2 - \vec{H}_1) = \vec{J}_s \tag{1.3}$$

gives us the following approximate expression for the electric field close to the transmitter (TM polarization of the radiated pulse):

$$E = -E_b \frac{\sigma_s \eta_o}{\cos\theta_{op}} \left[\sigma_s \eta_o + \frac{1}{\cos\theta_{op}} + \frac{\sqrt{\varepsilon}}{\cos\theta_2} \right]^{-1} \tag{1.4}$$

where E_b is the bias field, η_o is the characteristic impedance of free space, ε is the dielectric constant of the photoconductor, and σ_s is the surface photoconductivity, given by the expression:

$$\sigma_s(t) = \frac{e\mu(1-R)\cos\theta_{op}}{\hbar\omega} \int_{-\infty}^{t} I_{op}(t') e^{-(t-t')/\tau_r} \, dt' \tag{1.5}$$

where μ is the carrier mobility of the photoconductor, R is the optical reflectivity, $\hbar\omega$ is the photon energy, I_{op} is the incident optical intensity and τ_r is photocarrier decay time. From expressions (1.2), we see that at low optical excitations, the electric field is proportional to the incident optical intensity. Note, however, that its sign is opposite to the applied bias field.

2. Generation and Detection

A number of semiconductor materials, including InP, GaAs, CdTe, polysilicon and radiation-damaged silicon-on-sapphire were evaluated, for use as large-aperture photoconductors to generate submillimeter-waves. They were chosen because all have strong absorption at the wavelength of our femtosecond laser (625 nm) and high dark resistivities. The later requirement was necessary to hold

off the high electric field used to bias them. Electrode spacings varying from 2 to 10 mm and voltages ranging from 100 to 3000 Volts were used.

The source of optical pulses in our experiments was a balanced colliding pulse, mode-locked rhodamine 6G dye laser, The pulse duration was 75 fs, and the wavelength was 625 nm. Approximately 10 mW of average optical power was used for the pump beam and 5 mW for the probe beam. The pump beam was used to illuminate the large area transmitting antenna with a defocused Gaussian beam which had a 1/e beam diameter comparable to the electrode spacing of the photoconductor.

The radiated field was detected with a photoconducting dipole antenna. It consisted of a 100 μm dipole having a radiation-damaged silicon-on-sapphire photoconductor at its feed point. A 3.2 mm sapphire ball lens was placed over the dipole to improve its collection efficiency. The small size and high speed of the detecting antenna permitted its use as a movable probe to measure both the temporal and spatial distribution of the radiation field of the large-aperture photoconductors. Due to its small size, the dipole antenna could also be scanned in space to measure the spatial distribution of the field.

The field strength as a function of time was obtained by recording the gated output current from the dipole detector while varying the relative time delay between the pump pulses which illuminated the large-aperture antenna and the probe pulse which gated the detector. The current signal from the detector was amplified, averaged and digitized by a current amplifier, phase lock-in amplifier and a computer.

As previously mentioned, the amplitude of the radiated electromagnetic waves at far field is proportional to the first time

derivative of the photocurrent in the photoconductor. If the fall time of the photocurrent is much longer than the rise-time, the risetime is found to be more important than the fall-time in determining the relative sensitivity of photoconducting materials [7]. Indium phosphide is found to be more sensitive than the other semiconductors used.
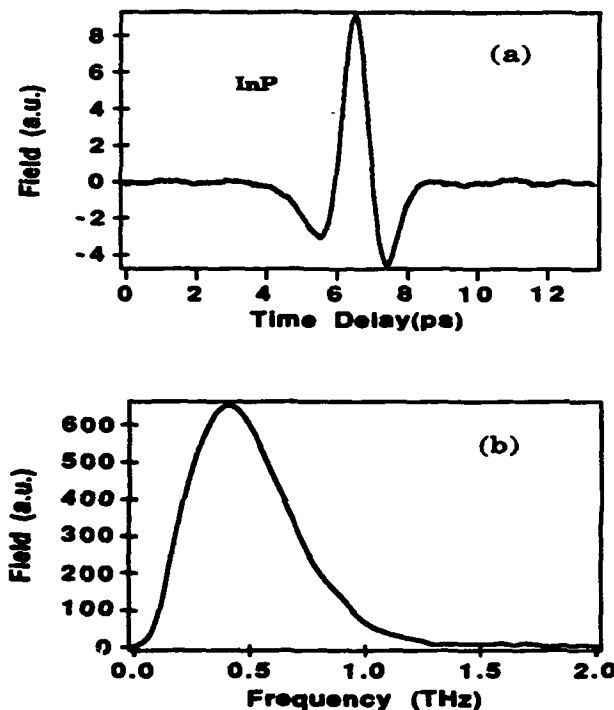

Figure 2: (a) The temporal waveform of the radiated pulse measured with a 100 mm dipole antenna at a distance of 7 mm from an InP large-aperture photoconducting antenna. (b) The Fourier transform (frequency spectrum) of the temporal waveform.

Figure 2(a) shows the detected electric field waveform from an InP planar photoconductor having an electrode spacing of 10 mm. Figure 2(b) is the numerical calculation of the Fourier transformation of the waveform. This waveform was measured in the far field using a 5 cm focal length fused silica lens to focus the electromagnetic pulse onto the dipole detector which was aligned in the specular direction

of the emitted radiation. The radiated electric field was found to be linearly proportional to the bias voltage and optical power (bias voltage up to 3000 V and optical energy up to 0.2 nJ). The observed waveform was strongly influenced by the response of the dipole detector and does not correspond to the true electric field waveform.

The electric field radiated by the each antenna was probed in the transverse direction to measure its directionality. This was achieved by scanning the dipole detector in the far field of the large-aperture photoconductor and recording the time domain waveform for each angle. An example of the angular variation of the radiated signal is plotted in Figure 3.
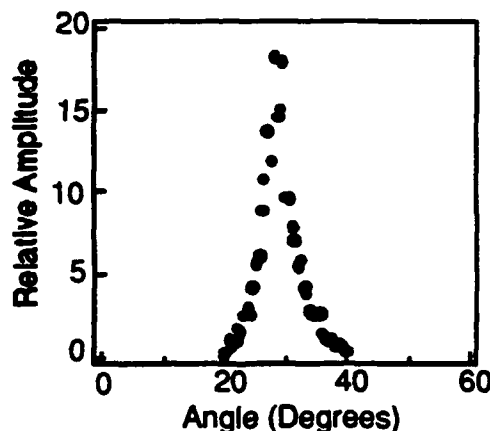

Figure 3: The measured angular distribution of the amplitude of the electric field of the electromagnetic pulse radiated from a 1 cm InP photoconducting antenna. The peak field is in the specular direction of the reflected optical beam and has a beam-width of approximately 6 °.

This shows the variation of the peak amplitude of the radiated signal from a 10 mm InP antenna. The data was taken at a distance of 16 cm between the transmitter and the detector. In this case, no lens was used. The radiated field had a beam-width that measured only 6° at the 3 db points. The maximum signal was observed at an angle corresponding to the specular reflection of the optical beam, which

was at 30° relative to the normal. The pulse width was observed to broaden off axis, and became more flat-topped as the angle increased, consistent with a theoretical model of the radiation field. In principle, an apertures of 5 x 5 cm photoconductor antenna is realistic in InP material (assuming a single wafer is used), which would result in a beamwidth of approximately 2°.

3. Power Scaling and Saturation

One of the potentially important features of large-aperture devices is the ability to scale the optical power up to very high levels to produce very large amplitude directional sub-millimeter-wave pulses. Unlike the small photoconducting dipole antennas, which are limited by the damage, the large-aperture antennas can be increased in size to accept high optical powers. The large-aperture photoconducting antennas show power scaling and saturation properties [8]. At high optical fluences, the radiated electric field (near field) approaches to a value comparable to the bias field.

At normal incidence (for simplicity), the radiation field (near field) from equation (1.4) can be rewritten as:

$$E = -E_b \frac{\sigma_s \eta_o}{\sigma_s \eta_o + (1 + \sqrt{\varepsilon})} \qquad (3.1)$$

With the increase of the optical power, the number of the photocarriers increases, causing an increase of the surface conductivity σ_s (equation (1.5)). When the surface photoconductivity σ_s becomes comparable to the radiation admittance of the antenna, the radiated near field E is expected to saturate at a value comparable to the applied bias field E_b. Therefore the maximum radiated field value can be derived from the equation

$$\lim_{\sigma_s \to \infty} E = -E_b \qquad (3.2)$$

From expression (3.1), we see that at low optical excitations, the electric field is proportional to the incident optical intensity. Note, however, that its sign is opposite to the applied bias field. Consequently, it subtracts from the total field at the surface of the photoconductor, and at high optical intensities, will saturate at a value comparable to the bias field. At normal incidence, this occurs when $\eta_0 \sigma_s \approx 1 + \sqrt{\epsilon}$. The saturation can not be observed by using an unamplified CPM laser, due to its very low optical flux (approximately 100 pJ per pulse). An amplified laser with the pulse energy up to μJ or mJ is necessary.

The saturation behavior is analogous to the "switching" behavior of a photoconductor in a transmission line. In that case, the maximum voltage that can be generated on the line is equal to one-half the applied bias voltage. In effect, our plane-wave model of the large-aperture photoconducting antenna is equivalent to a current source in a circuit in which the substrate and free space are treated as transmission lines having characteristic impedances of $\eta_0 \cos\theta_{op}$ and $\eta_0 \cos\theta_2 / \sqrt{\epsilon}$ (if the laser beam is not at normal incident), respectively.

When the surface photoconductivity becomes comparable to the free space characteristic impedance, the electric field saturates at a value comparable to the bias field. From equation (3.1), for normal incidence, this occurs when:

$$\sigma_s(t) = \frac{1}{\eta_0}\left(1 + \sqrt{\epsilon}\right) = \frac{e\mu(1-R)W_{op}}{A\hbar\omega} \tag{3.3}$$

from which the required optical pulse energy, W_{op} per unit area, is equal to:

$$\frac{W_{op}}{A} = \frac{\hbar\omega\left(1 + \sqrt{\epsilon}\right)}{e\mu\eta_0(1-R)} \tag{3.4}$$

For a radiation-damaged SOS samples which have a mobility, μ, of approximately 30 cm^2/Vs, we estimate this saturation property will occur at optical power levels of approximately 1 mJ/cm^2. For the more sensitive InP samples, however, which have effective mobilities that are approximately 450 cm^2/Vs, the required optical pulse energy would be only 6 x 10^{-5} J/cm^2. A 2 mJ optical pulse could thus saturate an aperture as large as 5 x 5 cm^2. The bias field is limited by the breakdown voltage. From previous experience, it can be as high as 30 kV/cm in air, and even higher if covered by a material with high dielectric strength.

Figure 4 schematically illustrates the Experimental setup for the study of the saturation behavior in the GaAs emitter. The source of the pulsed optical beam is a balanced colliding pulse, mode-locked ring dye laser amplified by a copper vapor laser pumped amplifier.

Vb   photocurrent

pump pulse   probe pulse

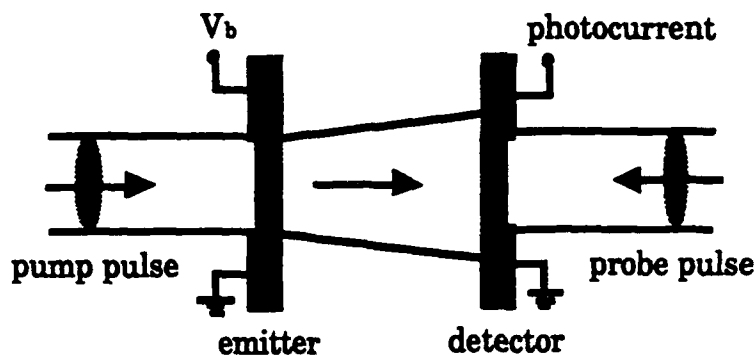emitter   detector

Figure 4: Experimental setup to study the saturation behavior in the GaAs emitter. Both emitter and detector are large-aperture antennas.

It provides a pulse energy of a few microjoule at a repetition rate of 8 kHz and a 70 fs pulse duration at a center wavelength of 625 nm. The GaAs emitter has a photoconducting gap of 1 mm. A large-aperture planar photoconducting antenna was also used as a detector of the terahertz pulses, as shown in Figure 4. Like the emitting antenna,

the detector consisted of a planar photoconductor with two parallel electrodes. The detector was illuminated by an ultrafast optical pulse focussed with a spot size just large enough to overlap the electrodes. A 0.5 mm gap radiation-damaged silicon-on-sapphire detector placed 10 mm from the emitter with a maximum optical excitation fluence 400 μJ/cm^2. The principal of operation of this detector is that it behaves as a coincidence detector by producing a photocurrent when the terahertz electrical pulse arrives at the same time as the optical pulse. This provides a gating action, since a photocurrent will be produced only if there is both a bias field (the terahertz pulse) and an optical pulse arriving at the detector at the same time. To provide a gating action, it is necessary that the detector be made of a material that has a very short photocurrent decay time. We used radiation-damaged silicon-on-sapphire (RD-SOS) which has a lifetime of 0.6 ps. Low temperature growth GaAs, which has a carrier lifetime comparable with RD-SOS but a higher mobility, is another candidate for the detector.

An important property of the large-aperture detector is that, like the large-aperture emitters, it has a directional property and, in principle can also be steered by varying the angle of incidence of the optical beam. It also has a flatter frequency response than the dipole antennas which have resonances at frequencies where the dipole length equals odd multiples of a half-wavelength.
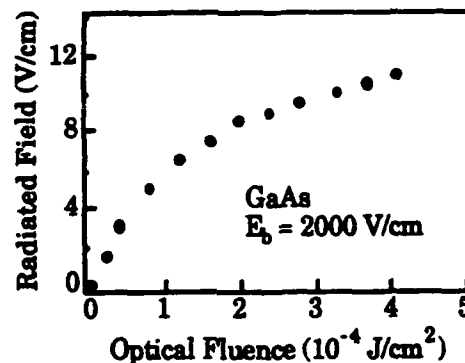

FIGURE 5

Figure 5: The radiated electric field from the GaAs emitter as a function of pump optical fluence at 2000 V/cm bias field.

Figure 5 shows the experimental data of the radiated electric field from the GaAs emitter as a function of pump optical fluence at a 2000 V/cm bias field. When the divergence and Fresnel losses are considered, the radiated field is estimated to be 1750 V/cm, close to the bias field of 2000 V/cm. We have also observed similar saturation properties from semiconductors, such as InP and CdTe.

The power scaling feature of large-aperture photoconducting antennas is a unique property which can be understood intuitively by the following argument. A large-aperture photoconductor can be pictured as an optically-activated switch which releases the stored electrical energy of the bias field into a radiated electrical pulse. The speed of the switching mechanism permits it to radiate efficiently. In fact it is entirely possible for the antenna to have net gain, i.e. the total energy in the radiated pulse can exceed the energy of the switching optical pulse. This does not violate conservation of energy, since the radiated signal derives its energy from the bias field and not from the optical pulse.
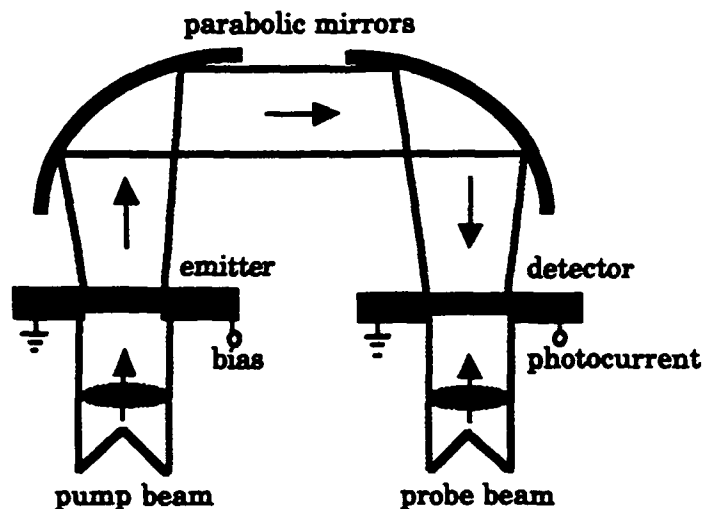
parabolic mirrors

FIGURE 6

Figure 6: Schematic illustration of the generation and detection of the ultrafast electromagnetic radiation by the large-aperture photoconducting antennas.

With appropriate power scaling, it should be possible to generate electromagnetic pulses with peak powers up 1 GW and local electric fields greater than 10 MV/cm. Figure 6 schematically illustrates the experimental set up for the generation of very high electromagnetic fields. Two off-axis parabolic mirrors are used to collect the radiation and to focus the radiation to the detector. If the emitter area is 100 cm^2 with a pulsed bias field of 100 KV/cm, the radiated power from the emitter is over 1 GW. Assuming the radiation is focused to 1 mm^2, the local electric field can be as high as 10 MV/cm. Such field strength can be used for the study of nonlinear properties of the dielectric materials at submillimeter wave regions.

The saturation property of the photoconductive antennas provides the power scaling of the radiation. This implies that at very high bias fields, the radiated pulse energy can in principle be greater than the optical pulse energy without violating the conservation of energy, because the far infrared pulse energy is derived from that stored in the static bias field.

4. Antenna Arrays

The concept of a single photoconducting antenna can be easily extended to an antenna array [9,10]. The direction of the emitted radiation from the array can be electrically controlled by varying the static bias applied to the individual antenna elements.
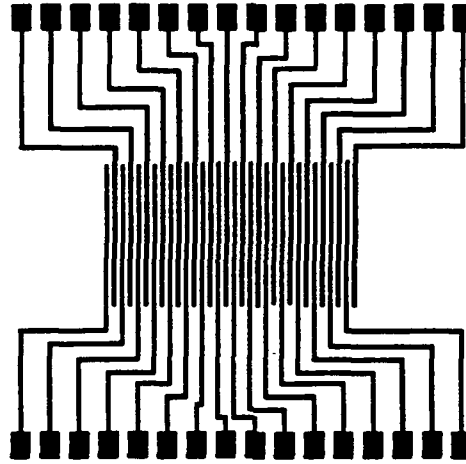
Figure 7: Top view of a photoconducting antenna array with 32 electrodes. The electrodes are 2 mm long and 25 μm wide, spaced 100 μm apart center to center.

The array of photoconducting antennas is created by a pattern of parallel electrodes, each independently biased, on a semi-insulating GaAs substrate as illustrated in Figure 7. By setting the bias voltage on the electrodes appropriately, the amplitude of the photocurrent between every two adjacent electrodes can be controlled. When an optical pump pulse illuminates the structure, each current element acts roughly like a short dipole antenna. The far-field pattern of the array can be calculated according to conventional antenna theory and is given by the approximate expression:

$$E(\theta) = \frac{A\cos\theta}{4\pi\varepsilon_0 c^2 r}\left[\frac{\mu e}{\hbar\omega}\right]\sum_{n=1}^{n=N}\left(\frac{V_n - V_{n-1}}{d}\right)\cdot I_n(\Omega)e^{-inKd\sin\theta} \qquad (4.1)$$

where A is the optically illuminated area of the array, θ is the angle defined from the array normal as in Figure 8, r is the radial distance, N is the number of electrodes under the illumination, V_n is the bias voltage on the nth electrode, d is the spacing between the photoconductor elements, $I_n(\Omega)$ is the optical intensity at the nth electrode, modulated at the microwave frequency Ω, and K is the

microwave free-space propagation constant. If the strengths of the static bias voltage on each antenna element are made to vary periodically with respect to one another, the array will act like an amplitude grating, steering the beam in a direction which can be controlled by varying the bias period. Specifically, if the static bias voltages vary sinusoidally in space, with period Λ_{bias}, as:

$$V_n = \frac{E_o}{\kappa}\cos(n\kappa d + \phi)$$
(4.2)

where E_0 is the maximum static field between adjacent electrodes, $\kappa = (2\pi/\Lambda_{bias})$, ϕ is the phase which can be set to zero. With the assumption of an uniform distribution of the optical intensity, the radiated signal in the far-field can be approximated by the expression:

$$E(\theta) \approx \cos\theta\left[\frac{A\mu e E_o I(\Omega)}{4\pi\varepsilon_o c^2 r\hbar\omega}\right]\frac{\sin\left(\frac{Nd(\kappa \pm K\sin\theta)}{2}\right)}{\sin\left(\frac{d(\kappa \pm K\sin\theta)}{2}\right)}$$
(4.3)

where K is the microwave free space propagation constant, which can be written as $K=(2\pi/\lambda)$ where λ is the center wavelength of the radiation. Four main lobes are expected, one pair inside and one pair outside the semiconductor. In free space, the maxima are at angles where $\sin\theta=\pm\kappa/K$. Clearly, by varying the periodicity of the voltage bias, the emission angle of these lobes can be steered continuously over a range from zero to nearly $\pm\pi/2$. The concept is illustrated in Figure 8.
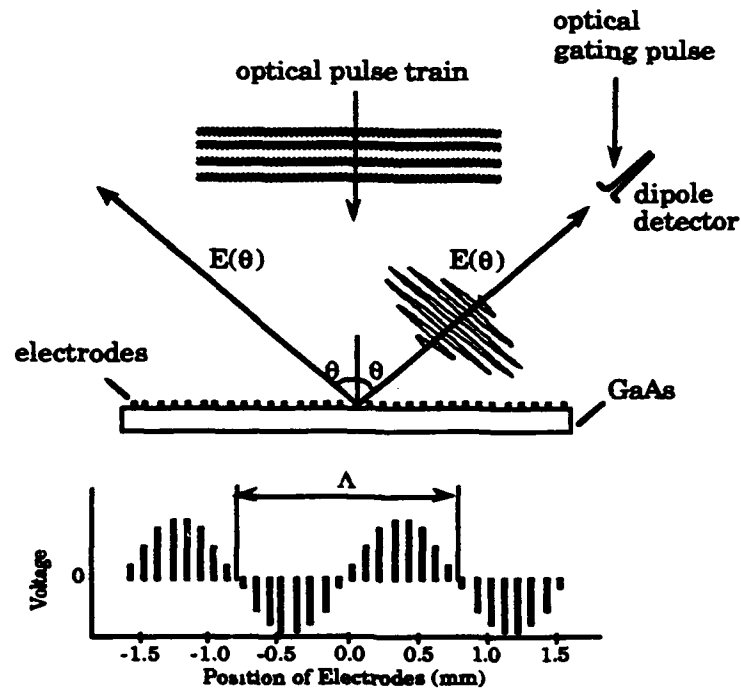
Figure 8: Periodically biased planar array radiates electrically-steerable submillimeter wave beam.

Ideally, the temporal modulation on the optical illumination should be sinusoidal at the frequency of the emitted radiation. To approximate this condition, we have used a train of ultrashort optical pulses spaced by 2 ps to produce a burst at 500 GHz. A dual-jet, hybrid mode-locked dye laser, synchronously pumped at 78 MHz by a frequency-doubled YLF laser (Coherent Antares-Satori system), generated optical pulses at 640 nm with a duration of approximately 150 femtoseconds. The unfocussed beam, having a Gaussian profile 3 mm wide and an average power of 130 mW, was used to illuminate the antenna array. A train of four optical pulses of equal intensity, each spaced 2 psec apart, was generated by passing a single optical pulse through two calcite crystals having birefringent delays of two and four picoseconds.

The antenna array used in our experiments (figure 7) consisted of 32 parallel electrodes, each 2 mm long and 25 microns wide, spaced 100 microns apart center to center. The electrodes, on a semi-insulating GaAs substrate, were made of gold germanium with a top layer of pure gold to facilitate wire bonding, giving a total thickness of about 2000 angstroms. The electrodes in the array were biased sinusoidally with respect to one another, as shown in figure 8, using slide potentiometers so that the bias period could be easily varied. The voltages were scaled so that the maximum E field between elements was kept constant at 1.25 kV/cm for all bias periods, ensuring that the amplitude of the emitted radiation was constant. Due to the relatively low transient mobility of this material, we expected the photocurrent to be proportional to the product of the applied field and the absorbed optical flux.
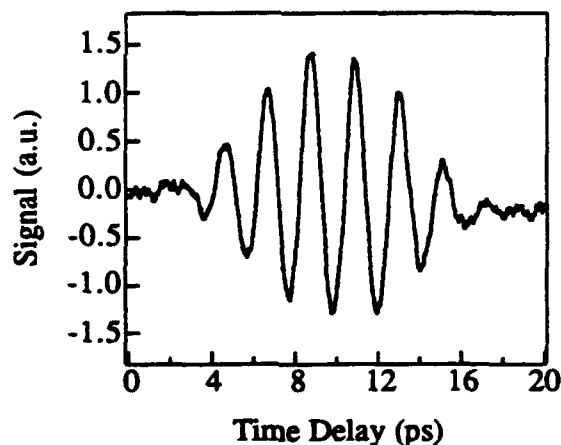

Figure 9: Waveform of radiated electrical beam at an angle of 45 degrees from the normal and a bias period of 0.9 mm.

To verify the tuning property of this array, the detected waveform at an angle of 45 degrees off normal and 3 cm from the array is shown in Figure 9. The periodicity of the voltage bias in this case was adjusted to be 0.9 mm to produce a maximum signal in the direction

of the detector (equation 4.3). The 500 GHz burst is clearly resolved. Because the radiation from different antenna elements experiences different delay times, the emitted pulse train is broadened in time with respect to the optical pulse train. Using multiple pulse trains to produce a 100% modulated optical signal is an expedient that served well to illustrate the basic properties of this device. A more effective approach might be to mix two quasi-continuous optical pulses with carrier frequencies separated by a microwave frequency as in optical heterodyning experiments.

To test the steerable property of the array, the detector was kept fixed at 45° and the periodicity of the voltage bias was varied to sweep the angle of the emitted beam across the detector. The bias voltage amplitude was changed with period to maintain a constant maximum electric field, as in equation (4.2). The time traces obtained for each bias period were Fourier transformed so that the signal amplitude at 500 GHz could be measured. The 500 GHz signal is plotted as a function of the bias period in Figure 10.
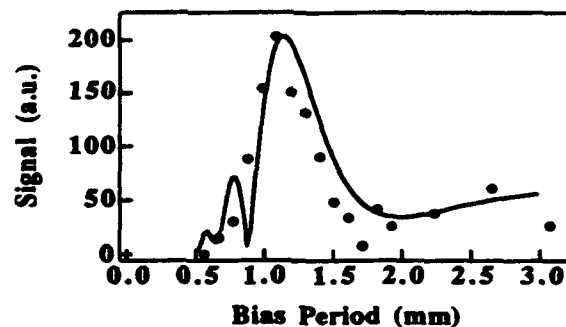

Figure 10: Signal amplitude of the 500 GHz component as a function of bias period. Solid dots are data; the solid line is the theoretical calculation.

The signal peaks for the bias period close to the expected value. A theoretical curve of the variation in the signal is also plotted in

Figure 10. It is based on the simple model of equation (4.1), assuming that the optical intensity profile is Gaussian. The width of the scanning beam at the 3 db points was approximately 10°. This width is determined by the overall length of the array (3.2 mm) and could be much narrower if a larger array was used.

Array structure has also been used for the experiment of the frequency tuning of the submillimeter-wave. A single optical pulse with a 150 fs pulse duration illuminated the array at a normal incident angle, as shown in Figure 11. The center electrode (No. 16) of the array was always biased at the highest voltage. The dipole detector was placed 30 mm away from the emitting array at a detection angle of θ.
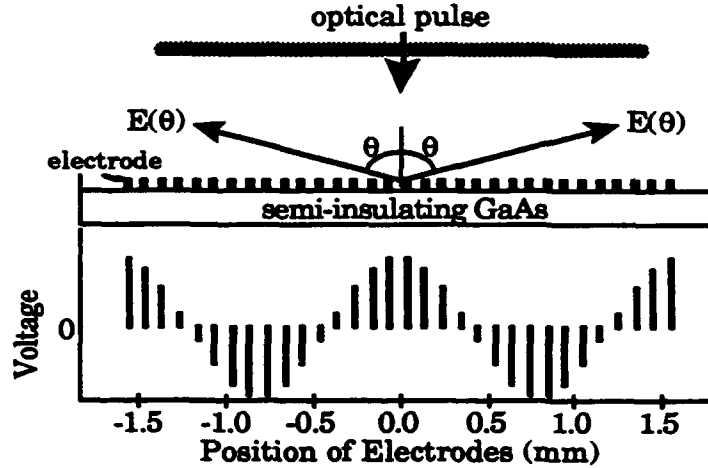

Figure 11: Schematic setup for the frequency tuning experiment. Two bias cycles (Λ_{bias}=1.6 mm) are shown. The frequency of the radiated field at a fixed direction varied when the bias period was tuned.

From equation (4.3), the maxima radiation is at the condition of $\kappa=\pm K\sin\theta$. This condition can be rewritten as $\lambda=\pm\Lambda_{bias}\sin\theta$. It is clear that for a fixed angle θ, the center wavelength λ is proportional to Λ_{bias}. Therefore, by varying the bias period Λ_{bias}, the radiation wavelength λ (or radiation frequency f) can be electrically tuned at a defined direction.
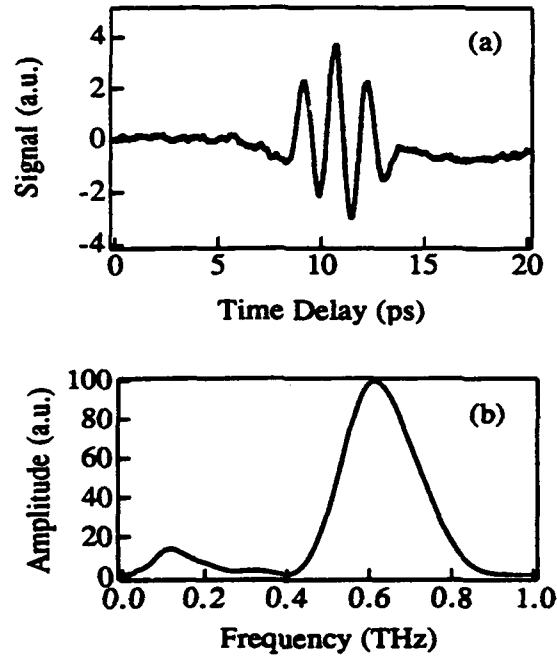
Figure 12: (a) Waveform of the radiated field at θ=37°. The detector was 30 mm away from the array. (b) Fourier transform of the waveform. The carrier frequency is approximately at 600 GHz and the width of the main peak depends on the envelope frequency of the pulse package.

Figure 12(a) shows a measured waveform of the radiated field. The dipole detector was placed at 37° from the normal. The duration of the pulse package is approximately 7 ps, corresponding to the array retardation time τ_a which is defined as $(Nd\sin\theta)/c$. At a fixed angle, the retardation time τ_a determines the duration of the pulse package, and it is independent of the bias period Λ_{bias}. Figure 12(b) is the Fourier transform of the waveform. The main peak at 620 GHz is the carrier frequency and the width corresponds to the envelope of the pulse package in Fig. 12(a).

To illustrate tuning properties of the photoconducting antenna array, we plot the temporal waveforms of the radiated fields versus the bias

period Λ_{bias} , as shown in Figure 13. The number of the pulses in a wave packet is proportional to the number of the bias cycles across the array. For a better vision, the curves have been offset. The bias period Λ_{bias} was varied from 0.4 mm to 3 mm while the No. 16 electrode was kept at the highest voltage. Since the center wavelength λ of the radiation is proportional to the bias period, increasing the bias period Λ_{bias} , causes the radiation wavelength to increase and the pulse width to broaden.
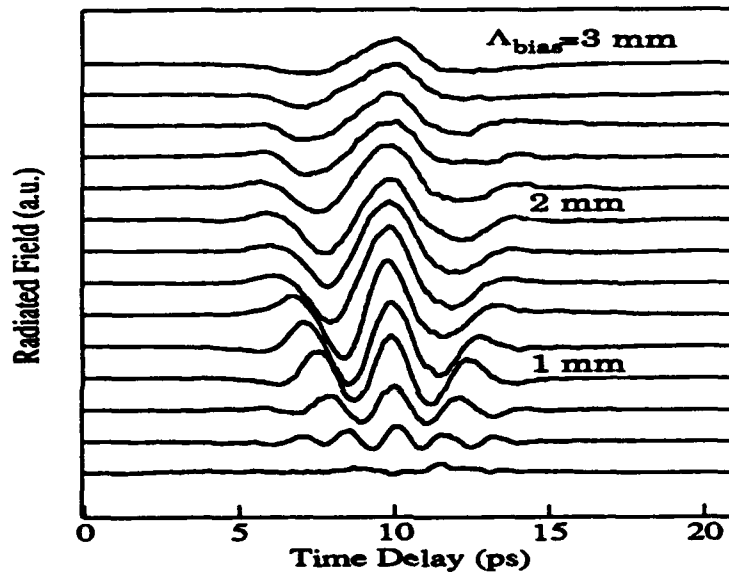

Figure 13: Waveforms of the radiated fields with different bias periods. The detector was set at 45° from the normal. The number of pulses within a wave package is proportional to the number of the bias cycles across the optically illuminated array.

The temporal waveforms have been transformed into a frequency spectrum. The center carrier frequency of each waveform has been plotted versus the bias period Λ_{bias} , as shown in Figure 14.
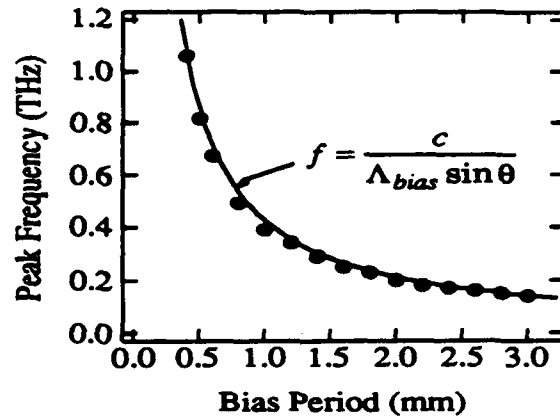
Figure 14: Plot of the center frequency f of the radiation versus the bias period. The theoretical calculation (curve) and the experimental results (dots) agree.

The solid dots are the measured values and the curve is the calculation from the equation $f = c(\Lambda_{bias} \sin\theta)^{-1}$. When the bias period increases from 0.4 mm to 3 mm, the main peak of the frequency decreases from 1.06 THz to 140 GHz. The experimental data and the theoretical calculation are in good agreement. When the frequency was tuned to over 1 THz, the measured amplitude of the radiation decreased, due to the frequency response of the dipole detector and the frequency response of the radiation from a single antenna. No radiated signal was measured when the bias had linear distribution ($V_n = nE_0$). In this case, the radiation direction satisfies Fresnel's law equation [1]. The tuning bandwidth and resolution is largely determined by the size of the array and the number of the antenna elements. For an array size of 10x10 cm^2 with 50 μm photoconducting gaps, we expected that the tuning range could cover from 3 GHz to over 1 THz. The upper limit of the tuning range is comparable with the bandwidth of radiation from a single antenna.

With an ultrafast optical pulse excitation (assuming the pulse width of the radiated field from a single antenna is much less than the array retardation time τ_a), the temporally spread radiation waveform reflects the spatial distribution of the bias across the array, because the radiation from different antenna elements experiences different delay times. For example, the voltage of the center electrode (No. 16) was kept at the highest value when the periodicity of the bias was changed. This made the waveforms in Figure 13 have a symmetry about their centers (approximately at 10 ps position). Also, when the bias phase ϕ in equation (4.2) varied, pulses within the wave package shifted in time. The amount of the shift was $(\phi \sin\theta)/(c\kappa)$. The direction of the shift depended on the sign of the phase ϕ, and the shift was confined within the duration of the array retardation time τ_a.

The key to steer a THz radiation in free space or to tune the center frequency of an electromagnetic wave for the spectroscopy measurement is to form and to control the spatial periodic distribution of the transient current. The spatial light modulator is an other candidate to produce a periodic distribution of the photocurrent on the semiconductor surfaces. In this case, the best geometrical method for the semiconductors as the emitter is the p-n or p-i-n structure, similar to the solar cell. Optically induced THz electromagnetic beams can be steered by controlling the pattern structure of the spatial light modulator with two degrees of freedom, providing a comprehensive method to steer submillimeter-waves in a line-of-sight arrangement. Meanwhile, the structure of an imaged antenna array can be easily varied to meet user's applications.
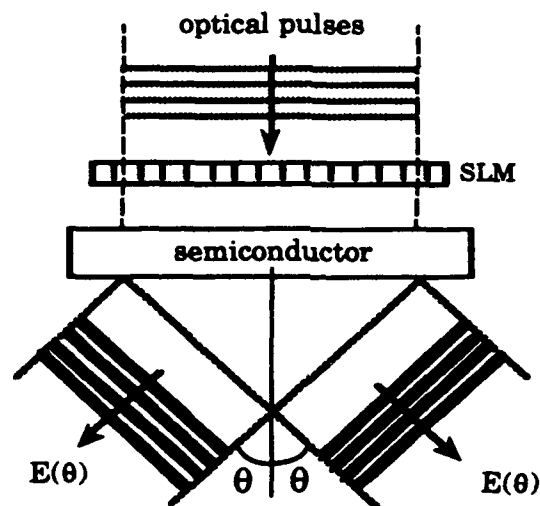
Figure 15: Submillimeter-wave beams generated by illuminating a femtosecond laser pulse train on a semiconductor surface and steered by varying the period of a spatial light modulator (SLM).

Figure 15 schematically illustrates the basic concept of the generation of steerable electromagnetic waves by a spatial light modulator. Briefly, a semiconductor wafer under optical irradiation by a femtosecond laser pulse train produces submillimeter-wave radiation [11]. The semiconductor absorbs incident photons and creates electron-hole pairs in the surface region. The surface bias (such as depletion field, Schottky field or piezoelectric field) drives the photocarriers to form a transient photocurrent, which flows normal to the surface. The current pulse has a rise time on the order of the laser pulse duration and a fall time comparable with the transient time of the free carriers across the depletion width (assuming the carrier transient is longer than the carrier life time). The photocurrent with ultrafast risetime radiates femtosecond electromagnetic pulses. In the far field, the amplitude of submillimeter-waves are proportional to the first time derivative of the photocurrent. If the total illuminated area is greater than the center wavelength of the electromagnetic pulse, the electromagnetic

radiation is directional and diffraction-limited. In contrast with the case of the planar electrodes on the semiconductor surface which has a current flow parallel to the surface, the flow direction of the photocurrent in the solar cell structure is perpendicular to the surface.

When a spatial light modulator (SLM) is introduced in the optical beam path, the optical pattern which has a spatially periodic structure on the semiconductor surface determines the spatial distribution of the surface photocurrent. If the repetition rate of the optical pulse train is comparable with the inverse of the spatial variation of the spatial light modulator (on the order of millimeter), the emission from each current source (antenna element) reconstructs coherent radiation in far field, resulting in directional radiations which can be steered by varying the period of the pattern. If the laser beam has a normal incident angle and the pattern has a periodic structure, the current array emits four first-order submillimeter-wave beams, two at each side of the semiconductor wafer, with equal angles from the normal. Clearly there is no radiation along the normal direction (zero-order), since there is no radiation along the dipole axis (direction of the transient current), which is perpendicular to the semiconductor surface. Figure 15 shows two forward electromagnetic beams (backward beams are not plotted). A perpendicular optical irradiation on the semiconductor surface is probably the best geometrical method for steering the submillimeter-waves. By using an oblique light incidence, zero-order radiations appear at specular and forward directions. Two of the four first-order radiations (one forward and one backward) can be suppressed; the other two do not gain in amplitude, and their scanning range is limited.

The far field radiation is the superposition of the contribution from all the current elements. Its general form can be expressed as:

$$\vec{E}(t, \theta) = \frac{1}{4\pi\varepsilon c^2} \sum_{n=1}^{N} \frac{\partial}{\partial t} \int_{s_n} \frac{\hat{r} \times (\hat{r} \times \vec{J}_n(t, r'))}{|\vec{r} - \vec{r}'|} \cos(n\phi) \, ds' \qquad (4.4)$$

where ε is the dielectric constant, c is the speed of the light, $\vec{r}$ and $\vec{r}'$ are the vectors to the observation point and the nth current element, respectively. J_n is the photoinduced current (proportional to the light intensity) at the nth light strip, ϕ is the phase from the nth current element to the observation point, and θ is the angle defined from the array normal. The summation is over the optically illuminated area. If the optical beam has a sinusodial spatial modulation, the equation (4.4) with a single frequency approximation can be rewritten as:

$$E(\theta) \propto \sum_{n=1}^{N} \sin\theta \, (1 + \cos(2\pi nd / \Lambda) \, \cos(2\pi \, d(\sin\theta - \sin\alpha)/\lambda) \qquad (4.5)$$

where d is the width between two adjacent lines in the spatial light modulator, α is the optical incident angle, Λ is the spatial modulation period and λ is the center wavelength of the submillimeter-wave. In equation (2), the first term comes from the product of the vectors from equation (1), the second term from light sinusodial modulation and third term from the phase.
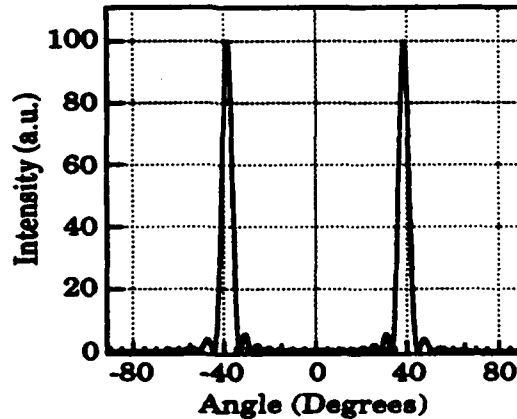

FIGURE 16

Figure 16 Calculated angular distribution of radiation intensity in far field from equation (4.5) with the parameters used in the text.

Figure 16 plots the radiation intensity (square of the field) versus emitting angle from this current array, with the parameters N=32, d=0.1 mm, Λ=0.8 mm, λ=0.5 mm and α=0 (we use these parameters for the comparing with the antenna array with the planar electrodes). With the decrease of the period Λ, the azimuth angle θ of the maximum radiation increases. The phase of the field is found to be opposite when the radiation angle θ changes from negative to positive. The radiation strength increases with the emitting angle θ and can be approximately described by the function of sinθ (For an antenna array with the planar electrodes, the maximum radiation strength is at normal direction, due to the cosθ term in the equation (4.1)).
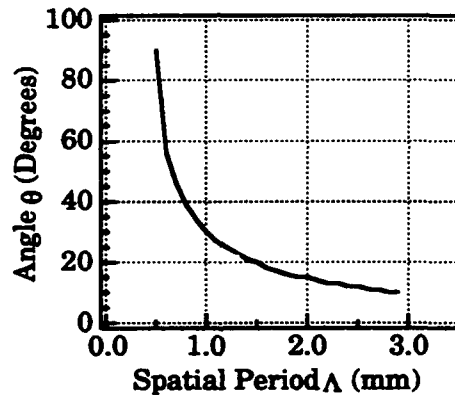

Figure 17: Calculated maximum radiation direction θ versus spatial period Λ of the SLM.

Figure 17 shows the steered direction θ of the submillimeter-wave versus the modulation period Λ with the same parameters used above. With the decrease of the period Λ, the radiations depart from the normal and approach to ±π/2 if the period Λ is comparable with the wavelength of submillimeter-wave λ. Further decrease of the period Λ beyond the center wavelength of the submillimeter-wave λ results in a production of many higher-order beams and reduces the directionality.

It should be mentioned that the use of surface depletion of the semiconductor for the emitter is not the only choice; many other possible candidates, such as the piezoelectric field in <111> oriented strain-layer layer superlattices [12], may be more suitable for their higher static fields.

5. Acknowledgement

References:

[1]   Kaiser, W. (1987) For example, see chapter 5 in "Ultrashort Laser Pulses and Applications", Ed. New York: Springer-Verlag.

[2]   Auston, D.H. Cheung, K.P and Smith P.R., (1984) "Picosecond Photoconducting Hertzian Dipoles," Appl. Phys. Lett. 45, 284

[3]   Smith, P.R. Auston, D.H. and Nuss, M.C. (1988) "Subpicosecond Photoconducting Dipole Antennas," IEEE J. Quantum Electron., 24, 255

[4]   DeFonzo, A. P. and Lutz, C. R. (1987) "Optoelectronic Transmission and Reception of Ultrashort Electrical Pulses," Appl. Phys. Lett., 51, 212

[5]   Fattinger Ch. and Grischkowsky, D. (1989) "Terahertz Beam," Appl. Phys. Lett. 54, 490

[6]   Hu, B.B. Darrow, J.T. Zhang, X.-C. Auston D.H. and Smith, P.R. (1990) "Optically-Steerable Photoconducting Antennas," Appl. Phys. Lett. 56, 886

[7]   Darrow, J.T. Hu, B.B Zhang, X.-C. and Auston, D.H. (1990) "Subpicosecond Electromagnetic Pulses from Large Aperture Photoconducting Antennas," Opt. Lett., 15, 323

[8] Darrow, J.T. Zhang, X.-C. and Auston, D.H. (1991) "Power Scaling of Large-Aperture Photoconducting Antennas," Appl. Phys. Lett. 58, 25

[9] Froberg, N. Mack, M. Hu, B.B. Zhang X.-C. and Auston, D.H. (1991) "500 GHz Electrically-Steerable Photoconducting Antenna Array," Appl. Phys. Lett. 58, 446

[10] Hu, B.B. Froberg, N. Mack, M. Zhang, X.-C. and Auston, D.H. (1991) "Electronically-controlled Frequency Scanning by Photoconducting Antenna Array," Appl. Phys. Lett. 58, 1369

[11] Zhang, X.-C. Hu,B.B. Darrow,J.T. and Auston, D.H. (1990) "Generation of Femtosecond Electromagnetic Pulses from Semiconductor Surfaces," Appl. Phys. Lett. 56, 1011

[12] Zhang, X.-C. Hu, B.B. Xin S.H. and Auston, D.H. (1990) "Optically Induced Femtosecond Electromagnetic Pulses from GaSb/AlSb Strained Layer Superlattices," Appl. Phys. Lett. 57, 753

Neural Beamforming for Phased Array Antennas

Terry O'Donnell*
ARCON Corporation
260 Bear Hill Road
Waltham, MA 02154

Major (Dr.) Jeffrey Simmers and Daniel J. Jacavanco
USAF Rome Laboratory
Electromagnetics and Reliability Directorate
Hanscom AFB, MA 01731

Abstract

Contemporary digital beamforming techniques require calibrated apertures with well-behaved, known characteristics. We present an alternate approach, neural beamforming, which can perform aspects of digital beamforming with uncalibrated or degraded antennas. We demonstrate an adaptive radial basis function neural network which is capable of resolving the direction of a single far-field source from measurements taken with an uncalibrated phased-array antenna aperture having unknown degradations. We discuss our experiment to train a neural beamformer network to perform single-source resolution with an eight-element uncalibrated X-band switched-element array. We compare the network's resolution accuracy to results obtained using the monopulse technique on antenna measurements from an operational, uncalibrated antenna and degraded, uncalibrated antenna. After training on twenty-five representative samples of far-field source measurements for each antenna case, we discovered that the network's performance was comparative to monopulse for the operational antenna and significantly better than monopulse when the antenna had unknown degradations.

1 Introduction

Classical phased-array antenna beamforming algorithms, such as monopulse, depend on antennas which have been calibrated to consist of nearly-identical elements. These algorithms typically do not adapt to uncalibrated antennas or antennas having system or element degradations or failures. As phased-array antennas become larger and more integrated within

---

physical structures, the cost to first produce and then maintain large quantities of identical elements becomes increasingly prohibitive to the use of these arrays for many applications.

The requirement for costly, nearly-identical elements results from a lack of beamforming algorithms which are capable of handling the complexities introduced by non-identical elements with unknown behaviors. Traditional techniques synthesize aperture behavior as a mathematical combination of well-behaved individual element and receiver channel behaviors. Neural beamforming, in contrast, attempts to learn aperture behavior from discrete observations of that behavior under varying circumstances. If antenna aperture behavior is indeed a continuous function, it is theoretically possible to model it with a neural network trained to approximate the function with discrete samples of points along the function. This model can then be used to predict antenna behavior at other points not trained upon.

Our neural beamformer does not try to learn or measure radiating characteristics of individual antenna elements themselves, but rather the behavior of the antenna system operating as a whole. We believe that an appropriate neural network model could learn to perform beamforming with both calibrated, well-behaved apertures comprised of identical elements and also uncalibrated antennas containing non-identical elements, degradations, or failures. Such an adaptive beamforming technique could reduce the cost of large antennas by reducing element manufacturing tolerances and extending mission lifetime by adapting to degradations or changes in the operating environment.

This paper presents a method to perform aspects of digital beamforming with an uncalibrated phased-array antenna aperture containing unknown element degradations. We describe an adaptive radial basis function neural network which was designed and developed in-house to learn to resolve the angular location of a single far-field source. The network was trained and tested with samples from an eight-element uncalibrated X-band sampled array which was initially operational. We subsequently degraded several antenna elements and retrained the network with additional data samples. We present a comparison of the network's ability to resolve single far-field sources, compared to the monopulse technique, for the different aperture conditions we experimented with under various signal-to-noise ratios.

2 The Adaptive Radial Basis Function Network

The selection of an appropriate neural network architecture for both the beamforming problem space and the intended end-application was the first major decision we encountered during our neural beamformer research. We initially wanted to solve the direction finding problem for a single far-field source; however we did not want to rule out the potential for multiple source resolution in the future. We chose the adaptive radial basis function network as a likely architecture to meet our problem and application requirements.

Techniques used in digital beamforming imply that there is a continuous function

$$\hat{f} : \hat{X} \to Y \tag{1}$$

where $\hat{X}$ is the space of all possible antenna element excitations, and Y is the space of all possible angular directions to the source. Because we intended to model a continuous
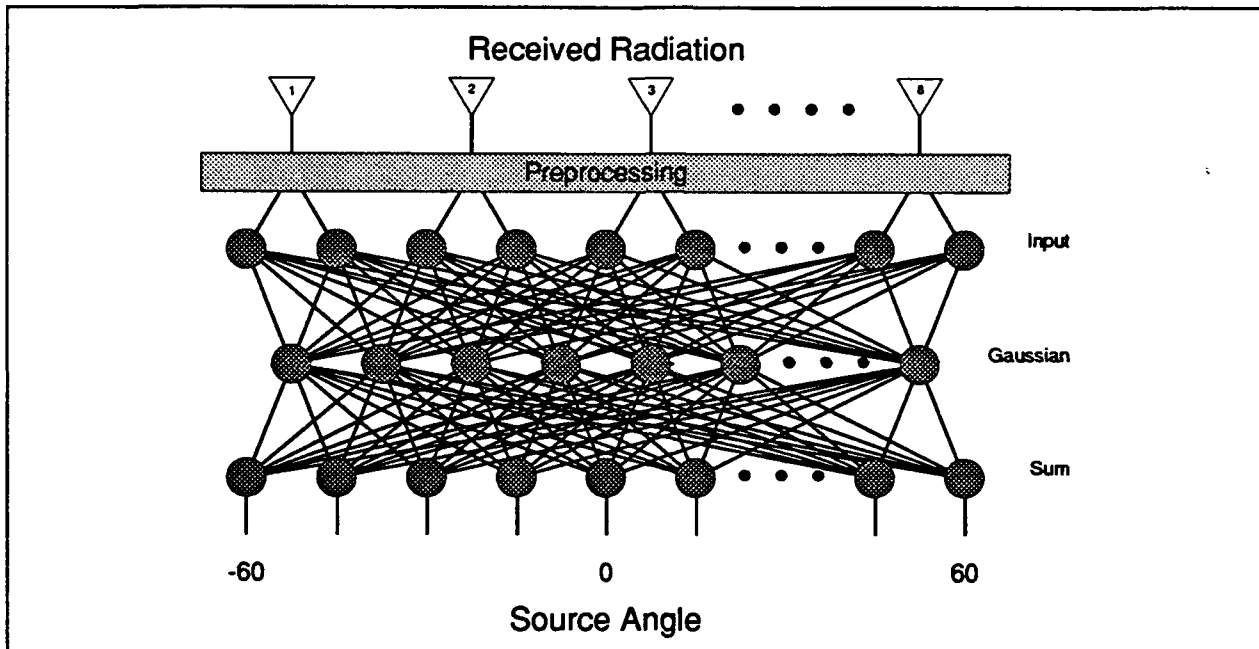
Figure 1: *Adaptive Radial Basis Neural Network architecture, as used in the Neural Beamformer.*

function, we considered the classic backpropagation and the radial basis function networks, which are two of the leading architectures for modeling continuous function mappings.

The neural beamformer project is part of a larger effort to achieve real-time processing of received antenna signals independent of antenna dimension. Other research sponsored by our organization indicates that this goal is supported by incorporating a parallel computer into phase-array antenna systems to process antenna element information in parallel. Each node of the parallel computer would receive signal information from one or more antenna elements, process this local data, and send the output to a global processing system.

The requirement for real-time processing independent of antenna dimension generated two specific guidelines for our neural beamformer network architecture. First, it is desirable that the network have a processing delay which can be kept constant regardless of the dimension of the inputs. Second, the network should have a minimum number of layers (layers defined by computations that must be performed sequentially). Thus as the number of inputs increases (as the dimensions of the antenna increase), the size of the network layers should grow no faster, and no additional layers should be required.

The radial basis function network architecture reportedly satisfies all of these constraints. The mathematical basis for these networks stems from the fitting (approximation) and regression capabilities of radial basis functions [5, 8], combined with a feedforward neural network architecture whose single "hidden" layer should not grow faster than the number of inputs [1, 4]. We initially chose a three layer network architecture, consisting of an input layer, a hidden layer of Gaussian radial basis functions, and an output layer whose nodes compute a weighted sum of the outputs of the hidden layer nodes. A diagram of this network architecture is shown in Figure 1.

The input nodes perform *data transformation*. As documented in [7], we found that using raw antenna measurements (consisting of either inphase and quadrature signal components or the amplitudes and phases of the signal) as inputs to the network yielded unacceptable network performance. We developed a preprocessing method that first determines the phase-difference between radiation received by consecutive array elements and then uses the sine and cosine of this phase difference as inputs to the network. The evolution of this input preprocessing technique is discussed in [7]. Since the raw antenna measurements lie within the $\hat{X}$ space of Equation 1, the input nodes perform the mapping $\hat{X} \rightarrow X$, where $X \subset [-1,1]^N$ and $N = 14$ for our eight element antenna. The N resulting values are fanned out to each of the hidden layer nodes in the second layer of the network.

The hidden layer performs a *projection* from the space X of the outputs of the input nodes into a space denoted by Ψ, such that $(\psi_1, \psi_2, ..., \psi_I) \in \Psi$, where I is the number of nodes in this hidden layer and typically $I \neq N$. Each hidden node performs a mapping $[-1,1]^N \rightarrow \mathbf{R}$ given by

$$\psi_i = e^{-\sum_{j=1}^{N} \frac{(x_j - m_{ij})^2}{2\sigma_{ij}^2}} \tag{2}$$

where $(x_1, x_2, .., x_N) \in X$ and ψ_i denotes the output of the ith hidden layer node. Based on the analogy that each ψ_i represents a Gaussian function, the σ_{ij}^2 can be considered as the entries of the covariance matrix that control the shape of each Gaussian "bump". Alternatively, a linear space analogy would be that these parameters represent the entries in a weight matrix used in computing a weighted norm. That is,

$$\psi_i = e^{-\|x - m_i\|_{w_i}^2 / 2} \tag{3}$$

where x and m_i denote the vectors whose components appear in Equation 2, and the w_i subscript indicates a weighted Euclidean (L_2) norm.

A radial function is one whose evaluation depends upon a radial distance from a given point called the *center* of the function. For each ψ_i, m_i is the vector denoting this center, with components are given by $(m_{i1}, m_{i2}, ..., m_{iN})$. Thus $\|x - m_i\|_{w_i}^2$ denotes the (weighted) radial distance from any vector x, where $x \in X$, to the center m_i.

Each output node computes a weighted summation of the values generated by the hidden layer nodes, that is

$$y_m = \sum_{i=1}^{I} w_{mi} \psi i \tag{4}$$

where the w_{mi} values are termed the *weights*. Thus the output layer maps $\Psi \rightarrow Y$, the space of possible angular directions to the source, where $(y_1, y_2, ..., y_M) \in Y$ for M output nodes. Hence the term *basis* in radial basis function network indicates that the output lies in the linear space spanned by the outputs of the hidden layer nodes. Note that the output of the network for a single-source resolution network could be a single number indicating the angular direction to the source. However, with our future goal of multiple-source detection and resolution, we designed our network so the output consists of a vector whose components represent angular "cells". The output values of these cells indicate the presence and strength of targets within those angular bins. The number of network output nodes therefore limits our potential angular resolution between different sources.
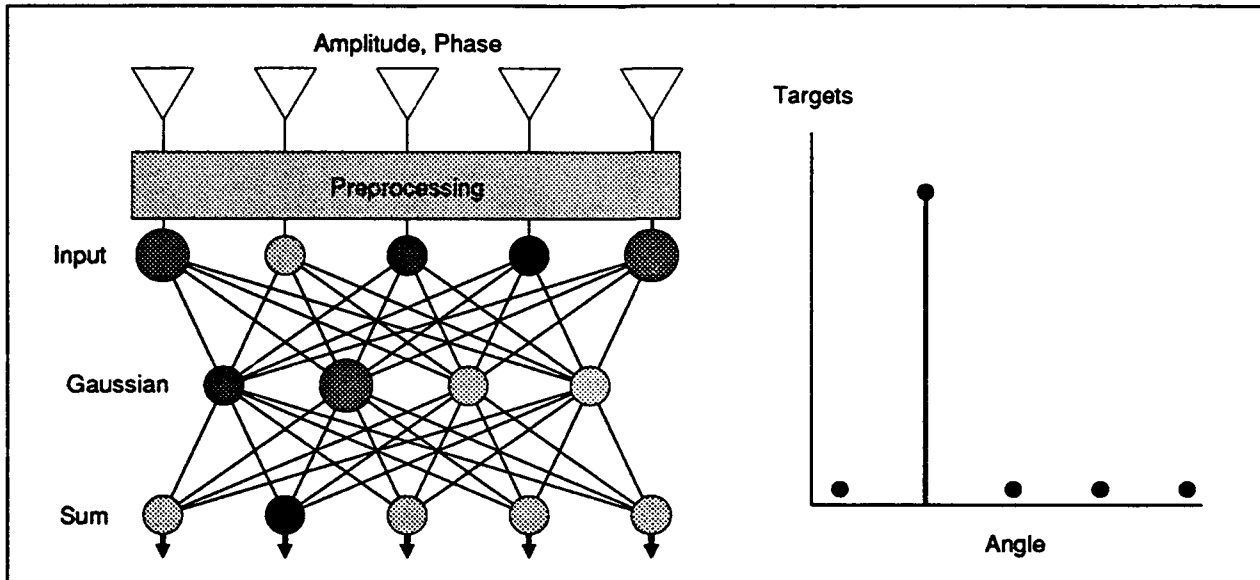
Figure 2: *The Neural Beamformer on the left is stimulated with the preprocessed received radiation from the elements of the array. The resulting network output indicates the existence of a target at a particular azimuth angle.*

Although an optimal set of weights for Equation 4 can be computed using linear algebra techniques [9], we decided to *train* the weights w_{mi}, along with the Gaussian centers m_{ij}, and the σ_{ij} values. This training is based on the gradient descent algorithm, with errors *back-propagated* through the network and used to modify network parameters. We implemented the radial basis function network to be *adaptive*, i.e. the network adds Gaussian nodes during the training phase whenever the network performance is unacceptable and there are no Gaussian nodes in the function space close to the current input. Whenever a hidden layer node is added, the center m_i is set equal to x, the vector value of the outputs of the input nodes for the input that yielded the unacceptable performance. The new weights w_{mi} for this node are set to values that force the network output to be within an acceptable interval about the desired output. Each new σ_{ij} in the new hidden node is set to an initial value dependent upon the "spacing" of the input vectors.

Thus our network training combine gradient descent iterative optimization of network parameters with the selective addition of new hidden layer nodes. Additional details regarding the network architecture and the adaptive training algorithm can be found in two articles by Lee [2, 3]. Although we followed the basic algorithms given in these articles closely, we also implemented variations based upon experimentation with our specific problem.

3   The Experiment

We decided to train our adaptive radial basis function network to approximate a digital beamforming single-source resolution function. We wanted to see if the network could learn the mapping between energy received by antenna aperture elements and the corresponding
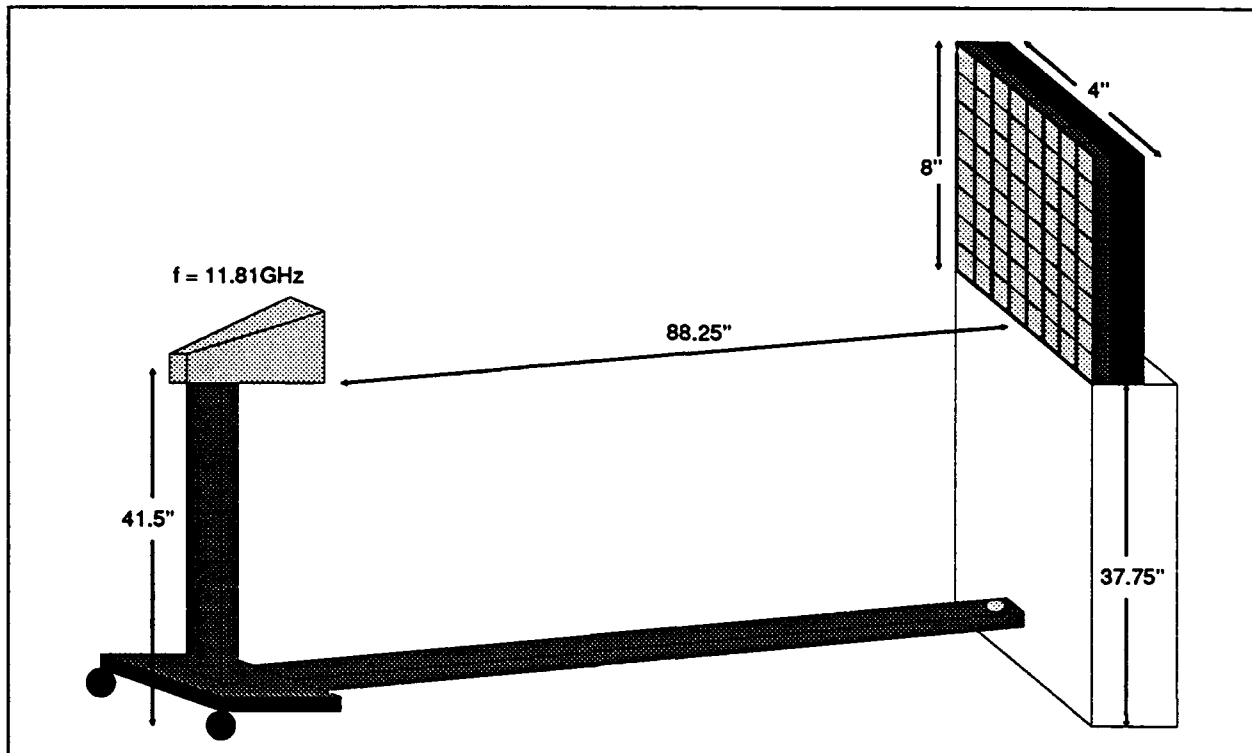
Figure 3: *Neural Beamformer Experimental Setup. Mobile source allowed far-field measurements of a source between* $\pm 60°$*, at* $1.0°$ *increments. Frequency used was* $11.81102GHz$.

angular location of a far-field radiating source, as shown in Figure 2. We believed that it was possible to train a neural network to approximate this function with a limited number of training samples, representing some subset of all possible source angle locations. Each training sample contained a potential input to the network and the desired output from the network for that input. As mentioned earlier, the inputs to the network consisted of preprocessed amplitude and phase measurements received by the switched array. The desired outputs from the network were non-zero values at the output nodes which represented the azimuth angles at which targets were present.

We constructed a software model of the adaptive radial basis neural network in Common Lisp, using the Common Lisp Object System (CLOS). This allowed us to model network arcs and nodes as software objects, capable of carrying out a common set of commands in many different ways. We were able to construct and test many different neural networks architectures simply by defining new types of arc and node objects and incorporating them into the network. This software was portable to all of our computer workstation resources, which included Sun SPARCstations and a Symbolics Lispmachine.

We developed an experimental test setup in the RL/ERTH anechoic chamber, consisting of a linear beamforming antenna and a mobile far-field source, shown in Figure 3. Our test antenna was an eight-element X-band linear aperture developed at Rome Laboratory by Dr. Robert Mailloux. Each array element consisted of a column of eight open-ended waveguide elements, uniformly combined with an eight-way stripline power divider. The columnar elements were connected to a eight-way switching matrix, which fed into a single receiver.

Our mobile far-field source consisted of an X-band horn mounted on a wooden cart. The cart was powered by a stepping motor which followed a semicircular track in front of the array. The circular track maintained a constant distance between the source and the array and allowed the source to be placed at known azimuth angles between ±60° off antenna broadside. The stepping motor, array switching matrix, and receiver were controlled by software written in HPBASIC running on an HP9836 computer.

Our experiment software directed the stepping motor to move the far-field source from −60° to +60° at 1.0° increments. After parking the mobile cart at a known azimuth angle, the software controlled the switching matrix to select each of the columnar antenna elements consecutively and polled the receiver to measure the amplitude and phase of the radiation being received by each element. Once all eight elements were measured, the source was then moved 1° to a new azimuth location and another aperture measurement taken.

As amplitude and phase measurements were received by the HP9836, they were transferred, along with the known location of the source, to an IBM-compatible personal computer which was networked to the HP9836 controller. This computer was also networked to our SPARCstation cluster and consequently wrote the measurement information to the disk of SPARCstation 330. Once the entire measurement set was recorded, it was then used to train and test our Common LISP neural network models on the SPARCstation.

Since we intended to train and test the neural beamformer on an uncalibrated, possibly degraded beamforming antenna, we made no attempt to calibrate the antenna measurements. We did, however, phase-center the aperture, such that the middle two antenna elements were centered over the rotating pivot of the arm which held the far-field source at a constant radius. During the course of our experimental measurements, we employed several non-destructive techniques to artificially degrade the antenna. These included placing foil over and into the slotted waveguides of entire element columns and locating different types of scatters, including a tower of coffee cans and a foil-covered model aircraft wing, directly in front of the aperture. We also had some help from Mother Nature, when our switching matrix periodically failed to switch.

4   Results

Our initial results depict how accurately and consistently the neural beamformer performed single-source target resolution at different signal-to-noise (SNR) ratios. We present results for two separate antenna conditions. For the first case, the antenna is uncalibrated, but otherwise operational. In the second case, the antenna is also uncalibrated and contains two degraded elements. For each case, we trained the neural network with samples from a single data set and then tested the network's ability to resolve source locations from data in other measurement sets, at the same or different SNR. In each instance, we compared the network's performance to source resolution results using the monopulse technique, as described in [6].

It is important to note that these are preliminary results. The neural network architecture used for the neural beamformer was not optimized for the eight-element X-band antenna
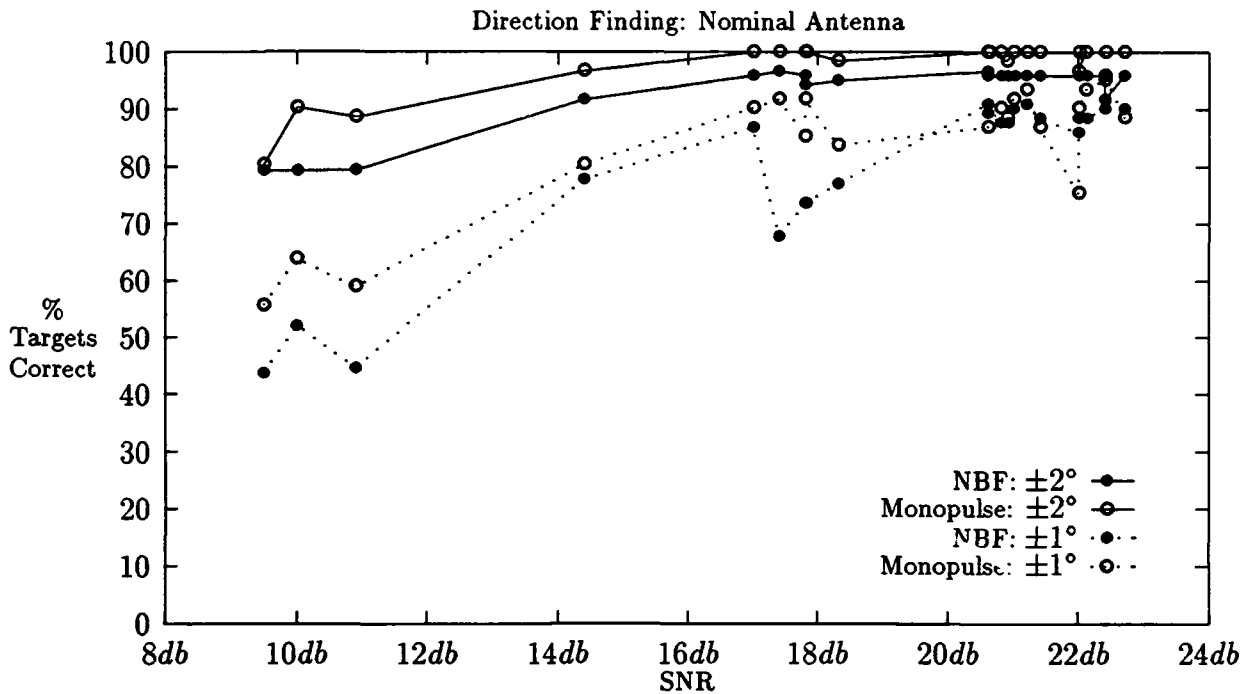
Figure 4: *Nominal Operational Antenna: Comparison of neural beamformer to monopulse at several signal-to-noise ratios. Both techniques were tested on the efficacy of correctly locating targets within ±2° and ±1° tolerances.*

or for either the optimal or degraded antenna conditions. It was, in fact, the same network architecture used previously to beamform the 32-element uncalibrated C-band digital beamforming aperture described in [7].

The plots shown in Figures 4 and 5 compare the effectiveness of the neural beamformer to the monopulse technique at performing single-source target resolution with experimental data measurements taken at different SNRs. Each plot compares the percentage of targets correctly resolved within ±2° (solid lines) and ±1° (dashed lines) by the neural beamformer and the monopulse technique. For each scenario, the neural beamformer was trained on twenty-five pairs of radiation measurements and corresponding source angles, for sources located from −60° to +60°, at 5° increments. The training data was chosen from a representative measurement set having an SNR around 22dB. The network was trained on three passes through the training set; this typically took under a minute on our SPARCstation 330. The data set that was used for training was excluded from those used for testing, as it would be an unfair positive bias to test the network on data it had already trained upon. The monopulse technique, which we compared the network against, computed the ratio of a -30dB Bayliss distribution to a -30dB Taylor weighting on the same measurement data.

Our results for the baseline case are shown in Figure 4. The case represents a nominal working antenna, having no degradations or external scattering. In this case, the network performed well, but not as well as the monopulse technique.

The results shown in Figure 5 are representative of the types of results we obtained
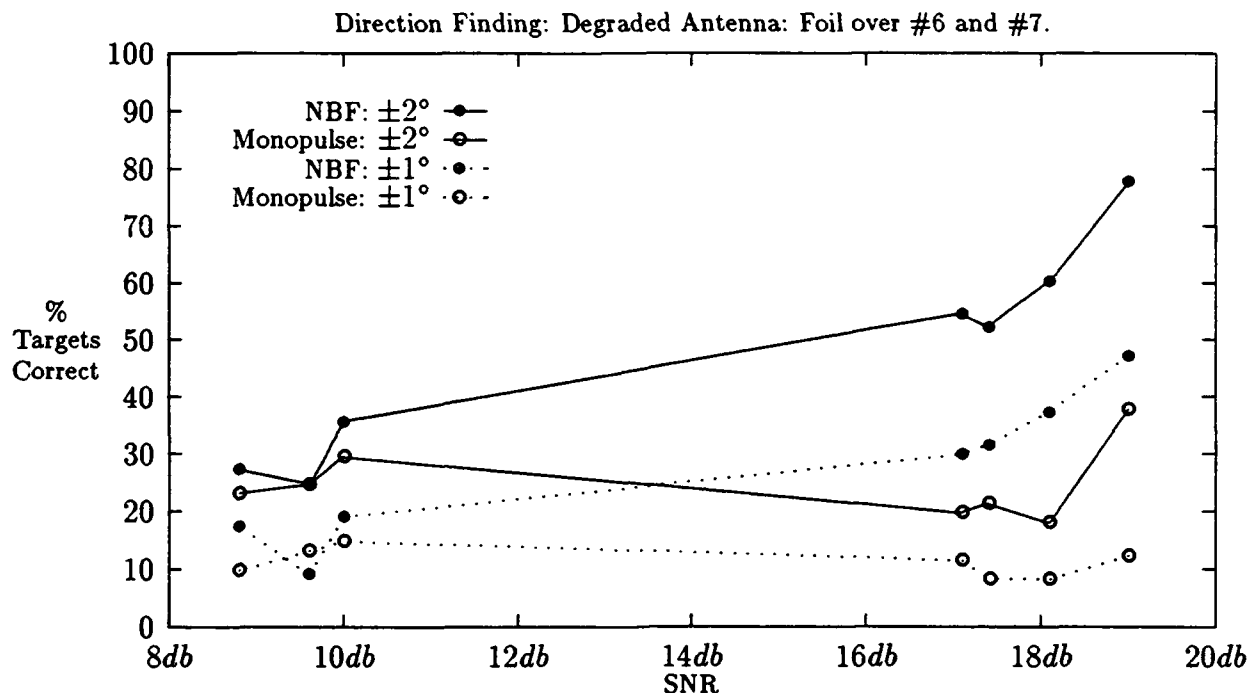
Figure 5: *Degraded Antenna. Elements 6 and 7 covered with foil to simulate dead. Comparison of neural beamformer to monopulse at several signal-to-noise ratios. Both techniques were tested on the efficacy of correctly locating targets within ±2° and ±1° tolerances.*

when the antenna was degraded. In this particular case, we simulated total element failure of two of the antenna columnar elements (columns 6 and 7) by stuffing and covering the sixteen open-ended waveguides making up the two elements with metal foil. In this scenario, the neural network adapted to the lack of meaningful information from the elements and performed significantly better than the monopulse technique for most of the measurement sets. At the low end SNRs, both techniques suffered about equally.

It is interesting to note that for some types of antenna degradations, the neural network performed as well with the degraded measurements as it did with the operational antenna measurements. This unfortunately made it difficult to notice when our experimental hardware was having problems. Such an incident occurred earlier on during our experiment, while we were still debugging our antenna configuration. Two of the switches in the switching matrix were operating incorrectly, one due to an incorrect software call, and the other from a hardware failure. The result of these system failures yielded redundant antenna measurements from non-consecutive elements. Without realizing this system failure existed, we successfully trained the neural beamformer and tested it on subsequent measurement sets, gaining results similar to those shown in Figure 4. However, when we implemented the monopulse technique as a comparison, we discovered that it performed poorly on the same measurement data. This led to a thorough study of the measurement data and the discovery of the hardware and software errors.

5   Conclusion

Neural beamforming shows promise as a technique for performing adaptive digital beamforming with non-ideal antenna apertures. Our experimentation showed that an adaptive radial basis function network could successfully approximate the mapping between received antenna radiation and the corresponding location of a single far-field source. More importantly, the network was able to approximate this function after training on only a small number of uniformly spaced antenna measurements at a single signal-to-noise ratio. The neural beamformer's performance was comparative to monopulse when the antenna was fully operational and better than monopulse when the antenna suffered element or system degradations.

References

[1] D. S. Broomhead and D. Lowe. Multivariable Function Interpolation and Adaptive Networks. *Complex Systems*, 2:321–355, 1988.

[2] S. Lee. Supervised Learning with Gaussian Potentials. In B. Kosko, editor, *Neural Networks for Signal Processing*, pages 189–227. Prentice Hall, Englewood Cliffs, NJ, 1992.

[3] S. Lee and R. M. Kil. Bidirectional Continuous Associator Based on Gaussian Potential Function Network. In *Proceedings of the 1989 IEEE IJCNN Volume I*, pages 45–53, San Diego, CA, 1989. IEEE.

[4] T. Poggio and F. Girosi. Networks for Approximation and Learning. *Proceedings of the IEEE*, 78(9):1481–1496, September 1990.

[5] M. J. D. Powell. Radial Basis Functions for Multivariable Interpolation: A Review. In J. C. Mason and M. G. Cox, editors, *Algorithms for Approximation*, pages 143–167. Clarendon Press, Oxford, 1987.

[6] S. M. Sherman. Monopulse Principles and Techniques. In E. Brookner, editor, *Aspects of Modern Radar*, pages 297–335. Artech House, Boston, 1988.

[7] J. Simmers and T. O'Donnell. Adaptive RBF Neural Beamforming. In *Proceedings of the 1992 IEEE Mohawk Valley Section Command, Control, Communications, and Intelligence (C^3I) Technology & Applications Conference*, pages 94–98, June 1992.

[8] D. F. Specht. A General Regression Neural Network. *IEEE Transactions on Neural Networks*, 2(6):568–576, November 1991.

[9] A. C. Tsoi. Multilayer Perceptron Trained Using Radial Basis Functions. *Electronics Letters*, 25(19):1296–1297, September 14 1989.

DIGITAL BEAMFORMING

Warren F. Brandow IV, 1Lt USAF
W. R. Humbert

ANTENNA APPLICATIONS
SYMPOSIUM
23 September 1992

Abstract

Beamforming theories have been developed and well understood for a long time. Digital Beamforming has "recently" gained recognition in papers discussing its advantages in such areas as: adaptive nulling, adaptive pattern shaping, and utilization of multiple beams over a single aperture. However, few if any of these papers discuss problems encountered in the actual implementation of these ideas.

The purpose of this paper is to provide details that may help others in their encounters with Digital Beamforming systems. It will discuss practical engineering considerations associated with the design and operation of the digital beamforming testbed at Rome Laboratory; starting with a general description of the system and later discussing problems encountered during operation. The paper will conclude by revealing important factors to be considered for those currently designing digital beamformers or those who will be.

System Description

Figure 1 is a block diagram of the digital beamforming system at Rome Laboratory. It consists of two separate systems with the antenna array common to both.

The array, designed for C-Band receive mode operation, consists of 360 microstrip dipole elements arranged in 36 columns of 10 elements. To reduce edge effects only 32 of the 36 columns and 8 of the 10 elements are active. The vertical elements are tied to one receiver giving a shaped elevation pattern.

Each element has its own receiver providing 500 Mhz of bandwidth. The receivers utilize triple conversion mixing schemes with separate analog to digital converters for the in-phase and quadrature phase components of the baseband signal. The 10 bit A/D conversion occurs at a rate of 500 Khz.
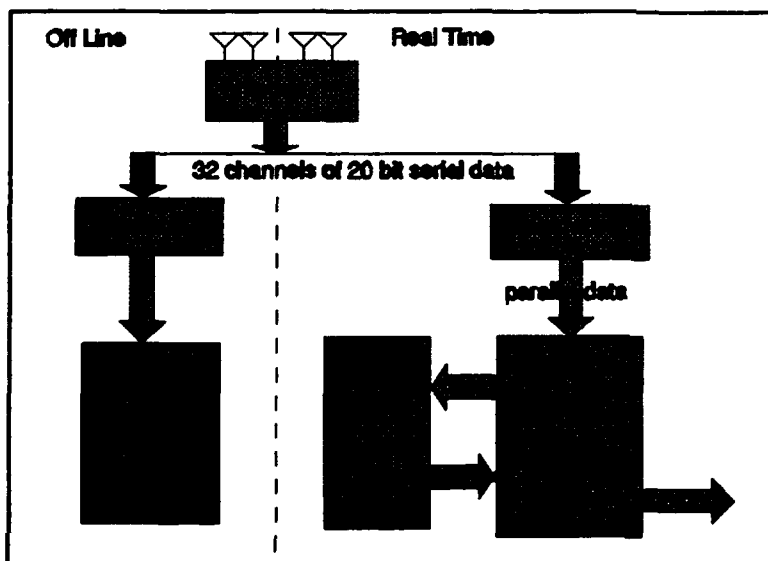
The "off-line" system consists of the Hewlett-Packard computer system and its interface. In this system, raw data (10 bit resolution) is taken in and stored for later use. This provides the flexibility of analyzing the data in various ways while preserving it at the same time.

The "real-time" system consists of the digital beamformer, its interface, and the Micro VAX III. In this part of the system raw data (9 bit resolution) is processed *in line* via complex multiplications and summations to form the beam.

Figure 1 System diagram.

All tasks are done by the digital beamformer.

The digital beamformer actually includes 4 beamformers that process data in parallel. The beamformers operate at 4 Mhz, 8 times the speed of the A/D operating frequency, and can thus form 8 beams in the same time the antenna sends one sample. Given 4 beamformers and 8 beams per beamformer, one can form 32 simultaneous and different beams.

The Micro VAX III serves as the beam controller. From here, depending on what task is to be completed, control commands are sent to the beamformer. Any steering vectors to be loaded are sent from the VAX, and individual channel data or final beam data to be retrieved are sent to the VAX. Therefore, the VAX also serves as the output device in the real time system. An obvious drawback to this setup is the slow communication between the VAX and the beamformer. To cut the VAX communication workload our next hardware acquisition will be a real time output device for the beamformer.

Definition - *"The Glitch"*

The purpose of this section is to define the term "glitch" as it will be used throughout this paper.

With the RF source off, examining individual channel data is the equivalent to looking at the DC offset for that channel. Here, the glitch could most easily be detected. Typical output is as follows:

	A/D Samples	
Sample #	I	Q
1	1	6
2	-1	5
3	0	6
4	-1	6
5	-128	5
6	0	5
7	1	6

The in-phase portion of this channel should have an average DC offset of 0 and the quadrature portion an average DC offset of about 5.5. However, at time sample #5 there is a "glitch" in the in-phase portion of the channel. Almost every problem we have had with our digital hardware has manifested itself in the form of a glitch of this or a similar type. The following sections are descriptions of the various systems in which these glitches appeared and how they were corrected.

Transmission Lines - *Crosstalk*

In this system data is converted from parallel TTL to serial ECL and then transmitted from the antenna to the interfaces via twisted pair where they are converted back to parallel TTL format. Originally, all data channel and clock twisted pair lines were shielded together in the same cable. Because all channels have a transition at the exact same time (between the I and Q data), the energy from this transition added coherently until it was strong enough to interfere with the 500 Khz clock (Figure 2). This produced a spike in the clock which added a clock transition and caused an extra data read. This extra data read produced the glitch. This problem did not show up in the off-line system because the clocks are filtered before they are used.
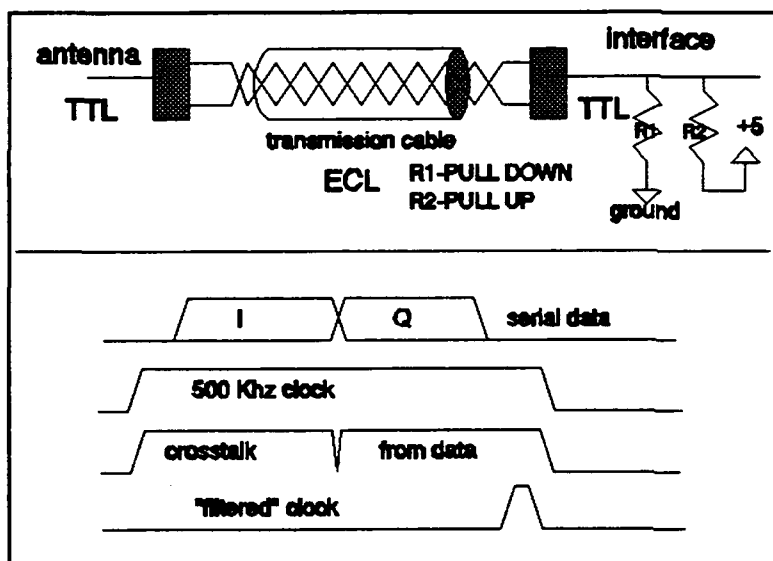
Figure 2   Data   transmission   and
crosstalk.

To resolve this problem the clock lines sent to the beamformer interface were isolated and transmitted via their own 50 ohm coaxial cables. This eliminated the crosstalk problem completely.

Terminations

At one point, glitches would appear in rapid succession in one channel only, then go away. After extensive searching it was discovered that the width of the data pulses in the transmission lines from the antenna to the beamformer interface were much larger than they should have been. Instead of 62.5 ns (16 Mhz) the pulse width was anywhere from 80 ns to 90 ns. This turned out to be an improper termination.

According to the data book and to theory we should have been, and *were* using 100 ohm resistors to terminate the ECL twisted pairs (Figure 3). Unfortunately, that did not work. Trying a second termination scheme made things worse. The second termination set up grounding loops between the antenna and the interface disrupting the PAL (Programmable Arithmetic Logic) integrated circuits in the system. Finally, the original termination scheme was restored, but with a 50 ohm resistor. While this is the correct value for terminating a 50 ohm coaxial cable it was determined that it worked well for the ECL twisted pair.

Noise - *Interface to Beamformer*

The beamformer interface circuitry appeared to be extremely noisy. The noise would frequently cause spikes to appear causing a glitch in the data lines. It was determined that the noise was caused by a combination of two things: the absence of a ground plane on the circuit board and pull-up/pull-down resistors on the TTL serial data lines (Figure 2). Energy was being transferred to ground through the pull down resistors and, because there is no ground plane to disperse the energy, would frequently add up and cause a glitch on one or more of the data channels (Figure 4).

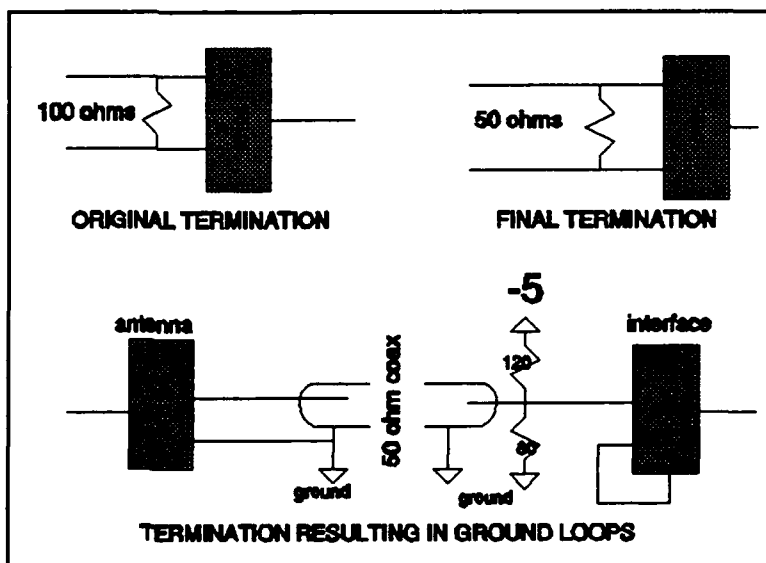It was quickly discovered that the pull-up/pull-down resistors are

Figure 3   Transmission line termination.

118

not necessary and were removed. That slowed the glitches down significantly but did not get rid of them. To help dispersion of the ground voltage the common ground for the 8 interface boards was split into two separate grounds with 4 boards connected to each. The noise thereafter did not create spikes large enough to cross TTL logic levels and cause glitches.

Figure 4 Interface ground.

Timing

In the digital scheme of things, bad timing can be a common source of error. Random intermittent glitches appearing on all channels indicated that our system was no exception. Close inspection by a qualified digital hardware engineer (Robert Jacobson at Atlantic Aerospace) revealed that the system timing was off. Apparently the original design engineer responsible for the timing was overly concerned with setup time; the amount of time the data must remain unchanged before the clock's rising edge. The specifications call for 20 ns as the minimum setup time for the 74LS595 (shift register for serial to parallel conversion). The initial design allowed for 56 ns which left only 6.5 ns (62.5 ns duty cycle) hold time; the time the data must remain stable after the clock's rising edge. The small hold time meant that the data was essentially being sampled at a data transition, and would sometimes read the bit *following* the correct bit.

To resolve this problem 24 ns of clock delays were taken out of the system. Figure 4 shows the resulting setup time of 32 ns and hold time of 30 ns.
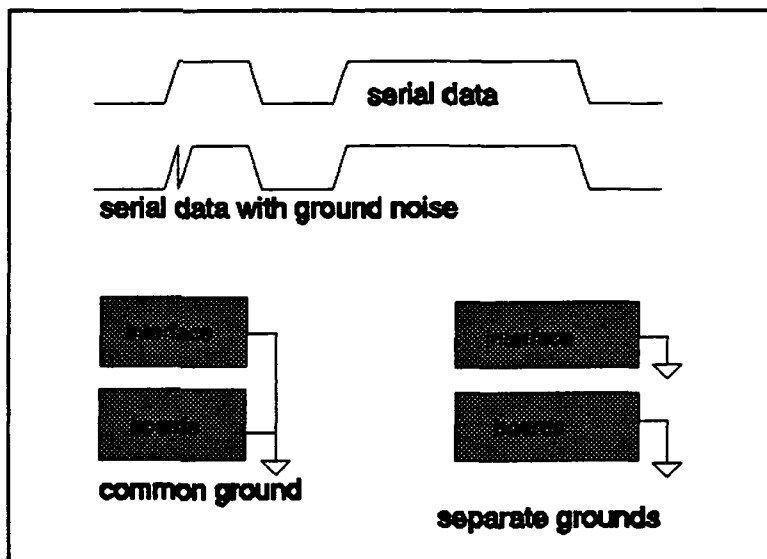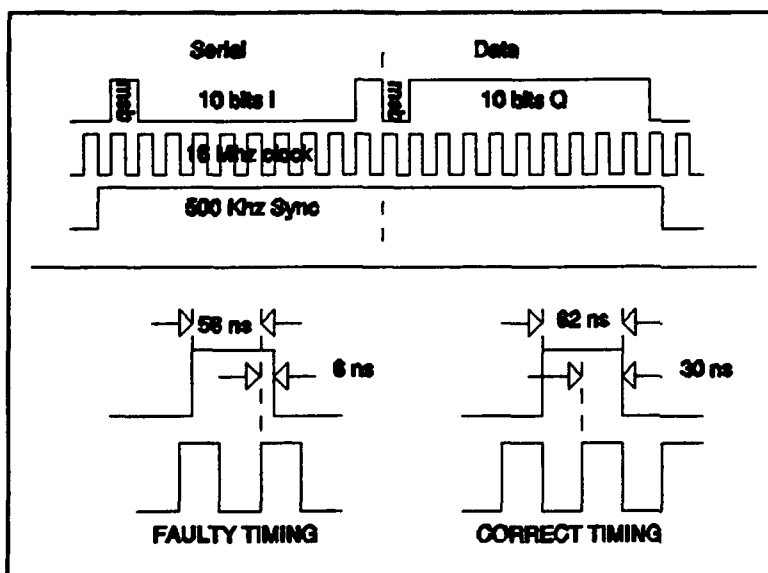

Figure 5 System timing.

Connectors

The digital beamformer, built by Texas Instruments, at times would not pass it's self test. The self test is used to isolate the board or boards causing the problems and from this test it has been determined that the boards were operating fine but the back plane connector is intermittently unreliable. This is a problem not with one board, but with at least three boards. The economic solution to this situation is to run a self test periodically and push on the right boards when it doesn't

pass. This is inconvenient, but it works.

Unresolved Problems

One of the advantages of digital beamforming is that calibrations which correct for gain and phase errors, I-Q imbalances and DC offset errors can be done digitally without any mechanical or physical changes to the system hardware. However, if the digital beamformer is not designed to make these corrections from the outset, this advantage is nullified. For instance, Pattern 1 shows a 30 dB Taylor amplitude taper with no DC offset corrections and Pattern 2 shows the same pattern with DC corrections. The pattern improvement is dramatic and shows that DC offset corrections are a significant factor. In order to make DC offset corrections, the measured DC offset is simply subtracted from the raw data before it is multiplied by the steering vector and then later summed. Unfortunately, the beamformer at Rome Laboratory does not have this capability in the real time system. Nor does it correct for any other errors in the system except element gain and phase errors. This short coming has limited us to 30 dB patterns. However, we are developing a method by which all of these errors and others are eliminated *in line* without the expenditure of massive hardware changes. That method will be discussed in further papers.

Results

The two areas of digital beamforming that we have given the most attention up to this point are calibration/error correction and low sidelobes. In the near future efforts will include adaptive nulling, and long range plans include pulse chasing and super resolution.

We have been able to isolate four types of errors in our data: gain and phase errors, DC offset errors, inphase and quadrature errors, and third order harmonic errors. Pattern 3 shows a 40 dB Taylor amplitude taper with only gain and phase corrections before all of the glitches in the system were found. Pattern 4 shows the same pattern with all of the glitches in the system corrected. Pattern 5 shows *all* errors corrected (this is done with a method not discussed in this paper). All of these patterns were corrected digitally and the antenna was mechanically rotated.

Conclusions

Basic phased array theories have been documented for a long time now. Gradually, more and more antenna applications are requiring much greater speed and accuracy than the analog systems can offer. The solution is to introduce digital hardware systems. In doing so, be it a digital beamformer or any other hybrid digital system, one should not overlook the subtleties involved with digital design. Encounters such as the ones described above can easily crop up in the system. The difficult task is tracking the errors because in a digital system the errors seem to always appear as these "glitches". Regardless, from the above discussion there are some basic principles to be considered.

Transmission lines should be very carefully considered, whether they are from one room to the next or one micron to the next. Avoid transmitting data and clock lines in the same shielded cable. A better method is to use individual cables. The best method might be to use fiber optics. Fiber optic transmission lines would decrease the number of cables needed because of the larger useful bandwidth. Fiber optic transmission would also eliminate the termination problems.
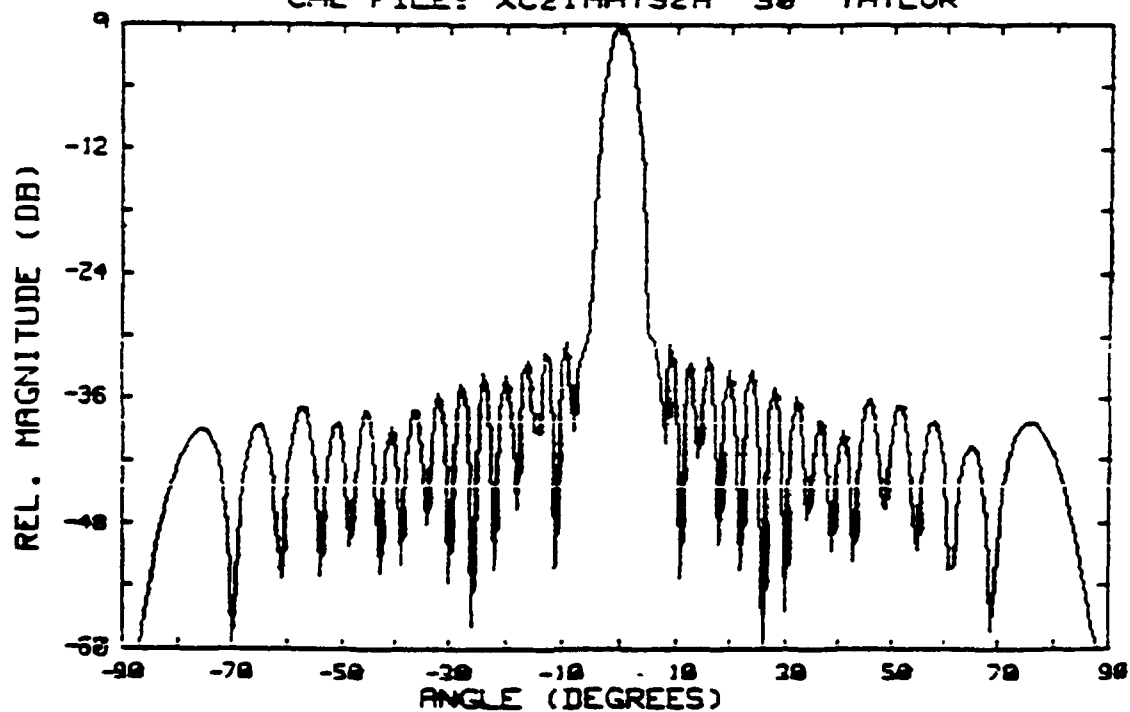
Circuit boards should be carefully designed. To avoid voltage buildups and voltage

SF:5.200000875 SP: -9 MAX: 109.5 AVG: 72.7
CAL FILE: XC21MAY92A 30 TAYLOR
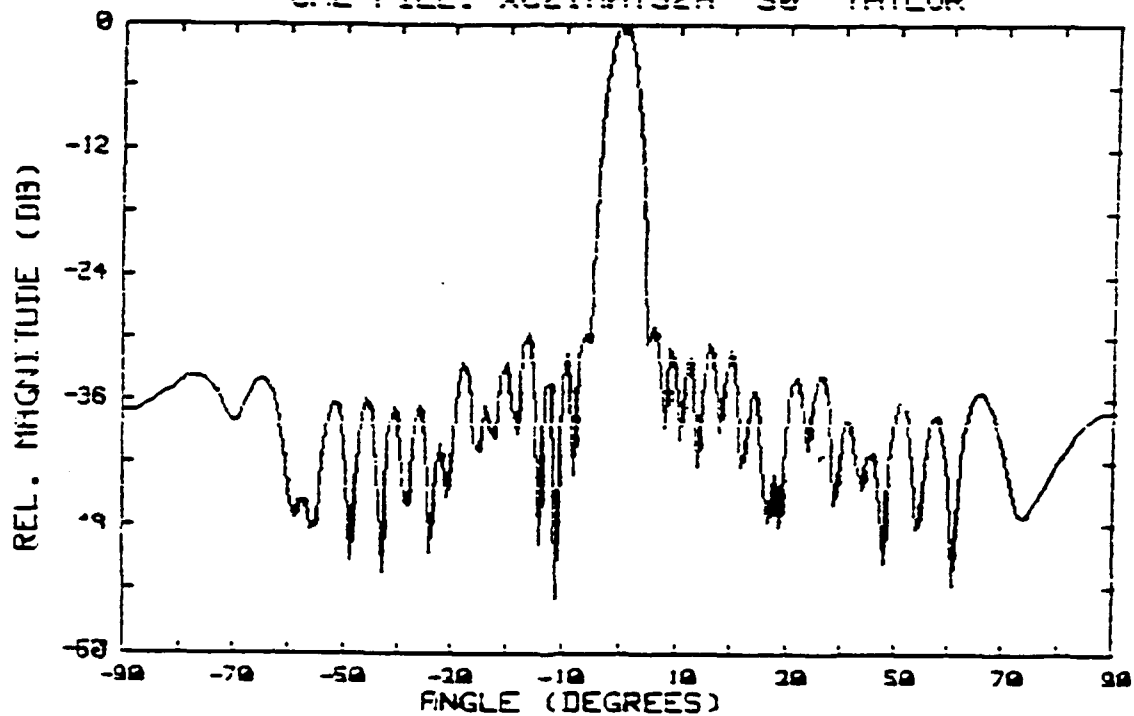
PATTERN 1

SF:5.200000875 SP: -9 MAX: 109.5 AVG: 70.6
CAL FILE: XC21MAY92A 30 TAYLOR

PATTERN 2

121

differences at ground a ground plane should definitely be incorporated in the design. The intermittent nature of ground problems make it very difficult to isolate these problems and distinguish them from other glitches in the system.

In general, be aware of proper termination schemes and alternate ones as well. It may be necessary to produce an alternate when interfacing two or more systems.

Connector problems are common to every digital system. Connectors wear out, corrode, and basically don't perform as well over long periods of time. Take this into consideration when designing digital systems. Be just as aware of the mechanical composition as the electrical make-up. Some of our interface board connectors have over 400 pins!

Finally, don't overlook the system as a whole when all of these things are considered. Transmission line terminations, and of course system timing are the heart of a digital system and yet the easiest to overlook. Producing separate systems and expecting them to work together as a whole without taking these subtle details into account will certainly cause many stressful days.
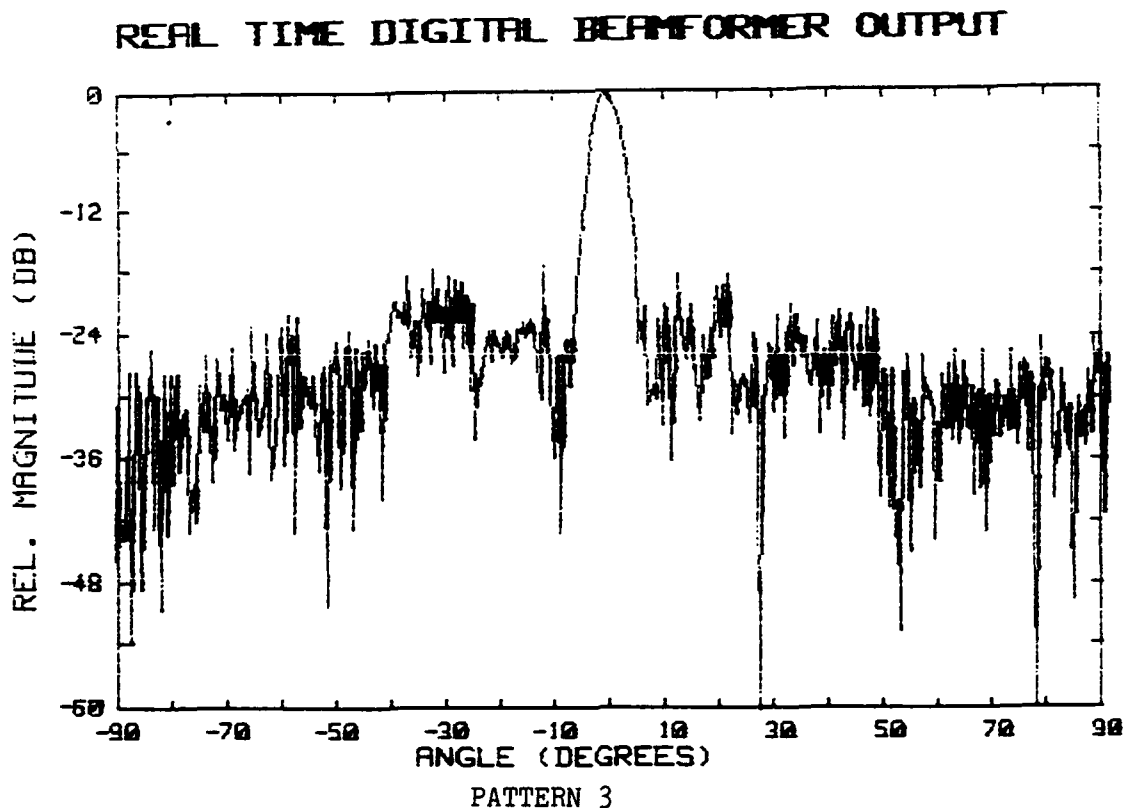
REAL TIME DIGITAL BEAMFORMER OUTPUT

PATTERN 3

122

REAL TIME DIGITAL BEAMFORMER OUTPUT

PATTERN 4

REAL TIME DIGITAL BEAMFORMER OUTPUT

PATTERN 5
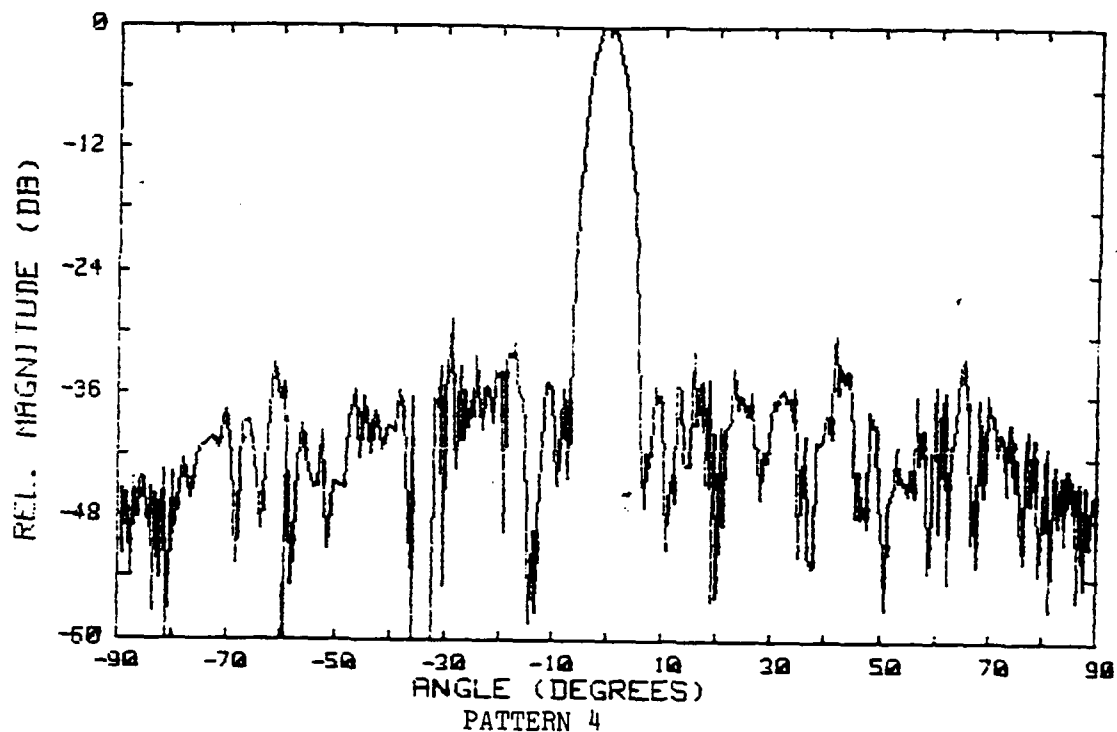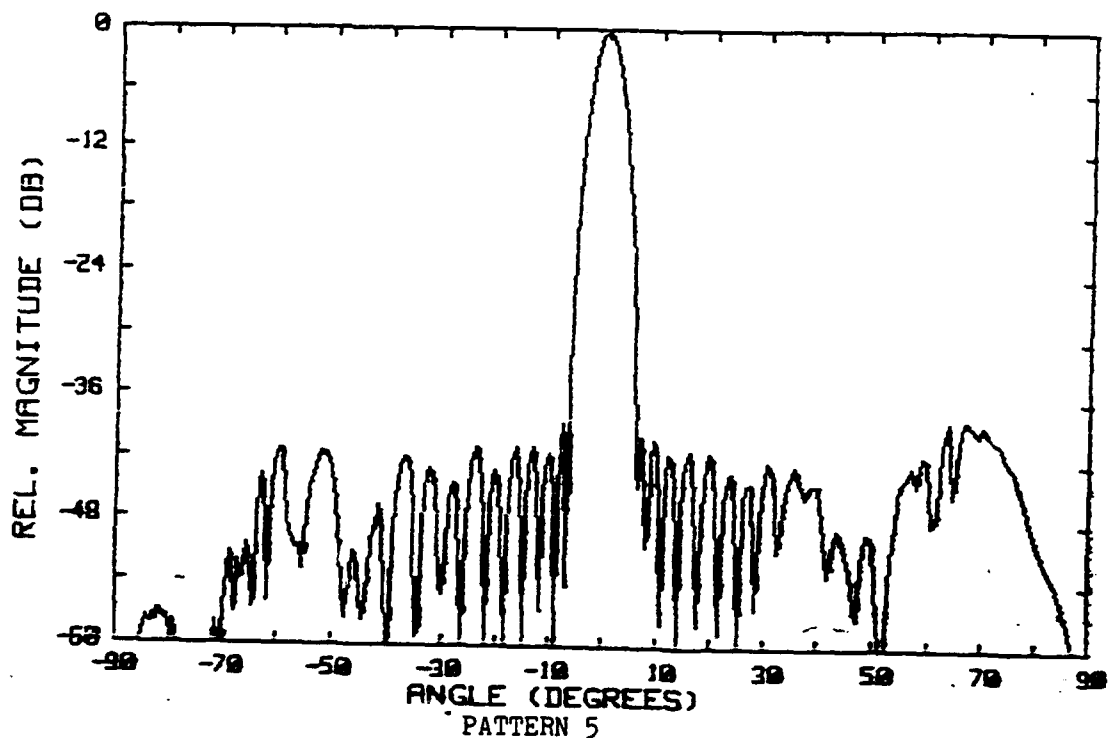
FAILURE MONITORING AND CORRECTION IN PHASED ARRAYS

Robert S. Worley, James B. Yon, Bruce L. Havlicsek, Peter D. Hrycak

Westinghouse Electric Corporation
Electronic Systems Group
Design and Producibility Engineering Division
Baltimore, Maryland   21203

ABSTRACT

Failure monitoring and correction of airborne phased arrays has become an area of much interest because of its ability to compensate for faults while in flight. Coupling Artificial Intelligence technology with antenna design can be applied to fault isolation and correction. This allows continuing the mission without the need for airborne replacement of failed components. This paper describes a state-of-the-art approach for fault detection, isolation, and correction in airborne phased arrays by combining antenna and artificial intelligence technologies. Modeled techniques demonstrate that an induced fault in an array can be detected and isolated using one or more monitoring methods as chosen by programed diagnostic decision rules. Also, mission requirements determine which parameters (gain, sidelobe level, etc.) should be optimized via various fault compensation techniques. The most appropriate compensation technique is implemented and the degree of improvement displayed via an antenna pattern plot. This paper shows that with the appropriate design forethought, airborne arrays can be developed that can be reconfigured to complete their missions even with the presence of antenna component failures.

1

1 INTRODUCTION

The objective of Failure Monitoring and Correction in Phased
Arrays was to explore novel approaches to health maintenance in
airborne phased arrays using Artificial Intelligence based
technologies. Emphasis of this program centered on failure
monitoring and correction of faults during airborne operation and
demonstration of the functional capacities of a candidate network in
a simulated environment. The program consisted of a Phase I study
and a Phase II demonstration which concentrated on integrating the
appropriate Artificial Intelligence (AI) techniques identified in the
Phase I effort with various failure monitoring, isolation, and
correction methods to investigate a functioning system. The
investigation of concepts, applicable AI techniques, and failure
monitoring and correction methods were done via computer simulation.
The simulation was used to answer the question whether an induced
fault in an array could be detected and isolated using one or more
monitoring methods as chosen by a diagnostic approach. Also, the
mission requirements determined which parameters (gain, sidelobe
level, etc.) would be optimized via various fault compensation
schemes. The chosen compensation technique would then be implemented
via the simulation and the degree of improvement would be displayed
on the screen via an antenna pattern plot. Thus, the method is an
automated one that offers the flexibility of accommodating real time
operator interaction, if desired.

2

2   INTEGRATION OF ARTIFICIAL INTELLIGENCE AND ANTENNA DESIGN

Artificial intelligence, or AI, is a generic term describing a variety of recent programming techniques. There are, however, general characteristics that distinguish AI programs from traditional programs. All AI programs are characterized by a decision making paradigm (pattern of use) and by the use of non-procedural programming. The first characteristic limits proper application of these programming techniques, and the second characteristic often provides solutions to previously intractable problems.

The failure monitoring and correction concept was demonstrated via a computer model of a phased array with failure monitoring on major components as shown in Figure 1. The software simulation block diagram shown in Figure 2 depicts the major elements of the simulated failure monitoring and correction system and the general sequence of the system. When faults are simulated (i.e., input through the keyboard), various high level fault detection monitors within the simulated system indicate that the system has determined that a fault exists but only provides limited information regarding the fault location. Subsequently, a rule based AI system determines what more intensive test(s) should be performed to fault isolate. Once a fault is isolated, another AI system prioritizes the correction techniques. The user may then select one of the recommended correction techniques for implementation and view the effect on the radiation patterns.

3

To demonstrate the failure monitoring and correction techniques, a simulated "test bed antenna" shown in Figure 3 was chosen to have an elliptical shape with a low sidelobe illumination taper. The array antenna is comprised of 408 elements forming an illumination taper that is a maximum at the center and tapers down to the edges. The pattern performance of such an array is shown in Figure 4. The purpose of selecting a low sidelobe performance antenna serves to demonstrate the effectiveness of the failure monitoring and correction techniques with state-of-the-art antenna technology. Various fault types were studied and simulated including element amplitude and phase errors that are constant or "static" that might be caused by a faulty cable or similar problem, element amplitude and phase errors that exist some of the time or are "dynamic" such as a problem with a particular phase shifter bit, and communication faults between an active component and its controller such as the line between a beam steering computer and and a phase shifter module. Faults were specified by array location, failure type and RF characteristic. In addition, amplitude and phase noise levels can be specified. Multiple faults can be specified and simulated, although the isolation and correction algorithms are not yet designed to handle arbitrary multiple fault sets. Pattern displays are provided to visually convey the operating performance of the array before and after implementing correction.

4

3 FAULT DETECTION, ISOLATION AND CORRECTION PROCESS

3.1 FAULT DETECTION

Studied fault detection schemes represent continuously operating monitors or tests that report faults when measured signals exceed a specified error level. Three fault detection monitors were studied: a module communications monitor, a subarray monitor, and a clutter monitor. Figure 5 shows the order in which the monitor detections are performed. If a fault is detected by any one test, monitoring stops and fault isolation begins. The common point of these tests is that their impact on the radar operation is minimal. Therefore, this class of tests may be performed on a regular schedule and thus can be used as a "trigger" to initiate more detailed, time intensive tests that impact the radar operation only when there is a strong indication that a fault exists.

Module Communications Monitor: The module communications monitor tests the external communications to each T/R module of the array. This fault detection scheme was simulated because it represents a built-in test actually implemented in existing phased arrays. As shown in Figure 6, the beam steering computer (BSC) sends digital commands to each T/R module in the array. The communications monitor provides a feedback link that sends the module command back to the BSC where it is compared to the original command. A communications fault is detected if the comparison fails.

5

Subarray Monitor: The technique of monitoring antenna subarrays involves illuminating the array with an externally mounted source. For an airborne phased array, it is proposed to mount a low power source on the aircraft wings such that the small source antenna illuminates the array with its broad beamwidth. Referring to Figure 7, the array's column beamformers would combine this test signal and subsequently groups of the column signals would be combined by couplers at the azimuth beamformer inputs. A switch would then be used to individually select each subarray's test line. The measured test level would then be compared to a known calibrated level to determine the error in each subarray. A fault is detected if any error exceeds its corresponding threshold level.

In this manner a relatively few number of groups of elements can be monitored and thus not require a significant amount of test time that might detract from radar operation. In choosing the subarray size, a tradeoff must be made that relates the subarray size, the test time, and the required measurement accuracy. Clearly a compromise is required that varies with target update rates, scan volumes and test hardware quality.

The variable thresholds relate non-equal subarray power such that errors which produce the same amount of sidelobe degradation are found in the different subarrays. Therefore, the fault detection sensitivity is placed on the far field domain and not the aperture domain.

6

Clutter Monitor: In principle, clutter spectral measurements could help indicate and, to some extent, isolate array faults. If continuous monitoring of clutter spectral density over scanned space is maintained, a sudden change in spectral levels would indicate a radar system malfunction. Since range/doppler cell detection threshold levels are often determined by averaging the levels in surrounding cells, detection thresholds are dependent on clutter levels. In this way, a sudden change in detection threshold level indicates that a fault probably exists in the array and that further testing is appropriate to confirm and isolate the failure. Since work centered on phased arrays rather than a complete radar system, pulse repetition frequency, ambiguous range, etc. were not modeled. Rather, the rms sidelobe level was checked. An array component failure will cause an increase in rms sidelobe level. The higher average sidelobe level will cause an increased clutter level. This is simply modeled in the simulation by checking the rms sidelobe level and performing further tests if the sidelobe level exceeds a specified level.

3.2 FAULT ISOLATION

Fault isolation begins only after a fault is detected. The isolation process has the goal of locating the source of failure to a level of detail that is sufficient to apply a correction scheme. Fault isolation is one of the areas in which AI techniques were applied. The isolation approach used is based on AI concepts

7

described in open literature[1] and, in fact, implemented in automatic test systems[2].

Empirical Knowledge Diagnostic System: The fault isolation approach implemented utilizes a domain specific, empirical knowledge model. Domain specific refers to the fact that the knowledge used is limited to diagnostics. Empirical knowledge refers to the nature of the knowledge, i.e., it is based on the judgment and experience of available diagnostic experts.

Using AI techniques, specific diagnostic knowledge is separated from general diagnostic knowledge. Specific diagnostic knowledge describes failure symptoms and tests for a specific circuit or system, e.g., a single array column can be faulty or there is a specific phase error limit. General diagnostic knowledge describes system independent fault isolation concepts, e.g., faults cause symptoms to appear, the presence of a symptom can be confirmed or not confirmed by tests, one symptom can lead to a more detailed symptom, etc.

Specific diagnostic knowledge was designed to be non-procedurally programmed as a symptom hierarchy. This permits new knowledge to be incrementally added without changes to the existing knowledge base. Figure 8 depicts the symptom hierarchy developed for this fault isolation system. Each block represents a symptom describing a fault in some level of detail. Under and connected to each block are more detailed description of the fault

8

131

symptom. The "TOP" symptom, for example, represents only the knowledge that some fault was detected and each successive level of blocks represents alternatives descriptions of that fault in more detail. The lowest level of symptoms represent a level of detail that is either sufficient for fault correction or is simply the most detailed description currently known. Clearly, this approach allows quick prototyping and incremental development of diagnostic knowledge.

The general knowledge of fault isolation has been programmed into a heuristic search algorithm. This algorithm searches the symptom hierarchy in a top-to-bottom, left-to-right manner.

There are actually two types of "tests" needed to perform fault isolation. In this program tests are referred to as "diagnostic tests" and "confirming tests".

Diagnostic tests describe actual or simulated procedures that make measurements or otherwise collect data about the system under diagnosis. Diagnostic tests consist of the communications monitor, the subarray monitor, the clutter monitor, the scan array test, the column calibration test and the element calibration test.

Confirming tests decide whether or not a symptom is present. Accordingly, a unique confirming test is associated with each symptom in the symptom hierarchy. Typically, confirming tests are purely logical in nature, applying error limits to the results of diagnostic tests to confirm or refute a symptom.

9

Scan Array Test: A common test that is frequently used by Westinghouse when calibrating and measuring phased array antennas provides a means of determining calibration data and/or the accuracy of the element (column) excitation by rotating an array antenna past a far field source. First, the antenna pattern is measured at the Woodward sample points with a probe in the approximate far field. Next, the element pattern is divided out to achieve the array factor. This data is then transformed back to the aperture and then compensated by a quadratic phase correction to account for measurement distortion due to the finite range. This provides empirical element (column) voltage data that can be compared to theoretical.

A more feasible in-operation approach was studied to serve the same diagnostic test purpose. This was done by moving the far field probe into the near field of the array and electrical scanning instead of rotating the array. This technique, called the Scan Array Test, is illustrated in Figure 9 for a probe located on the wing of an aircraft. The first step involves computing the necessary amplitude and phase compensation that is applied to each linear phase progression for scanning the beam in azimuth. This compensation focuses the forward radiation onto the near field probe, thus making the near field measurement representative of the far field probe broadside to the array. Furthermore, the element and probe patterns are already accounted for by the phase and

10

amplitude compensation. Therefore, the measured data through successive scan positions represents the array factor. This data is then transformed back to the aperture. This provides empirical element (or column) voltage data that can be compared to theoretical.

Since the Scan Array Test exercises all phase states of each phase shifter, it is possible to isolate faulty phase shifter bits using this technique. A computed electronically scanned pattern with a phase shifter bit fault is shown in the top graph of Figure 10. The scanned pattern measurement produces a dynamic error as a result of a stuck phase shifter bit. The error pattern is a near rectangular shape that is periodic in sine space. The period of the error is a function of the distance between the faulty element position and array phase center as well as the phase shifter bit state that is faulty. By transforming the error pattern back to the aperture domain, a series of spikes are formed with the largest spike occurring at the fault position. By the properties of the transformation, the spikes follow an envelope representative of a sin(N*x)/(N*sin(x)) function that folds over on itself.

Even though the previous discussion portrays the resulting fault data as very predictable, this is usually not the case when the random noise levels are fairly large compared to the fault error level and, worse yet, multiple faults of both types make the

11

fault identification task difficult. Initial investigations of a neural network approach was investigated to help decipher the data but further work is needed.

Column and Element Calibration Tests: Once faults have been isolated down to the subarray level, the individual columns in those subarrays can be tested via the Column Calibration Test. Using a near field probe, such as a probe on the wing of an aircraft, column measurements can be compared to previously stored non-faulty measurements to determine the health of the columns. If the difference between the column measurement and the calibration measurement exceeds the threshold, further testing at the element level is performed. Element calibration tests are performed in a similar manner.

3.3 CORRECTION DECISION

Corrective measures can be taken only when the faults have been isolated to a given location and it is known which antenna parameters have priority for compensation. The mission of the system sets the prioritization of antenna performance parameters.

It is possible to rank the many significant antenna performance parameters according to the primary mission of the radar system. Such a ranking is somewhat subjective and does not always uniquely rank each parameter. There are also many corrective actions, and since work continues is this area, it is safe to state that knowledge of potential fault corrections is incomplete.

12

Based on this view of the available knowledge, an expert system to recommend fault corrections for phased arrays is well suited to a forward chaining, rule based implementation. The basic inputs -- fault details and radar mission attributes -- are dissimilar but are limited and well defined. The knowledge for ranking and correction of antenna performance parameters is heuristic and varying. Alternative recommended corrective actions are expected and desirable.

The fault correction expert system is divided into two subsystems. The first subsystem ranks the antenna performance parameters based on mission attributes. The second subsystem ranks corrective actions based on faul~ data and the results of the first subsystem.

Antenna Parameter Ranking Subsystem: The various missions and their associated antenna pattern parameter rankings are selected from the list that Figure 11 describes. While these rankings may be subjective, this list serves as a baseline that the correction decision software uses. By selecting a mission or radar mode, a prioritization table is established that ranks the various antenna parameters; gain, RMS sidelobe level, azimuth and elevation peak sidelobe level, and azimuth and elevation beam pointing.

Corrective Action Recommendation Subsystem: The general concept behind the corrective action recommendation subsystem is that given a single fault and a single rank 1 antenna parameter, a

13

small number of ranked corrective actions will be recommended. The rules that produce these results represent the knowledge of radar experts who, given a fault case, know what corrective action will restore a particular radar parameter. Figure 12 represents the correction method ranking implemented in the fault correction expert system. The necessary information for performing the ranking is shown in the first two categories; Fault Type, and Antenna Parameter Ranking. The output from the fault correction expert system is shown in the last category; Correction Ranking. Based on this information the expert system recommends as many as four correction methods ranked from 1 to 4.

3.4 CORRECTION IMPLEMENTATION

Various correction techniques provide interim solutions that will allow the antenna to remain operational in the event of a failure. The failures consist of one or more elements where each fault may be a "dead" element, constant amplitude or phase error, or phase shifter bit or commanded error. The corrections provide improvement in one or more of the pattern parameters at the expense of others, such as improving principal plane sidelobes at the expense of degrading intercardinal sidelobes or improving beam point accuracy while disregarding sidelobe performance. Each correction has its own unique function but uses a common rule that the solution be generated rapidly. This is an important consideration since most optimum solutions are very time

14

intensive. During a mission, an optimal solution cannot be solely relied upon since the antenna must remain in good health without otherwise aborting the mission. Therefore, the following discussion of correction techniques may be implemented immediately to recover critical radar parameters while an optimal solution is being computed in the background.

Adjust Faulty Elements: The phase and amplitude controls can be used to fully compensate for failures in the element path that do not exceed the control capability. This can restore antenna operation back to its healthy state.

Adjust Row/Column: Based on the manifold design, elements are combined first by either an azimuth or elevation manifold. A fault in the combining manifold will produce a fault on the whole column (azimuth manifold) or row (elevation manifold). As long as the fault does not exceed amplitude and phase control capability, it can be fully corrected in the same manner as a single element case previously described.

Adjust Nearest Neighbors: Given an element with a fault that cannot be directly compensated, the nearest neighbors can be adjusted to restore one of the principal planes of the radiation pattern. If the objective is to maintain azimuth pattern performance, then vertical neighboring elements can be adjusted to restore the collapsed azimuth distribution, thus, restoring the azimuth principal plane. The same technique can be applied to the

15

horizontal neighboring elements to restore the elevation principal plane. Figure 13 illustrates this concept.

Eliminate Faulty Element: There are fault conditions that would warrant that element to be turned off. Such a case is a T/R switch stuck in receive mode, thus, liable to cause damage to receive circuitry during transmit if it hasn't done so already. Another case is when a fault can be isolated to a particular element but its magnitude cannot be determined.

Eliminate Faulty And Diametrically Opposite Element: In a planar array antenna, one can show that an element amplitude fault produces an error that is symmetric about the main beam. However, a fault which results in an element phase error produces a nonsymmetric error about the main beam, thus, causing a beam pointing error. If the beam pointing accuracy is the most important criteria then the phase error must be removed. One possibility is to compensate using the phase shifter. However, this will not work if the phase shifter is faulty. Since time intensive procedures would have to be implemented to further assess the fault, a much simpler correction technique can be employed. This involves eliminating the faulty element as well as the diametrically opposite. This technique will improve beam pointing accuracy.

Eliminate Row/Column: Even though eliminating a whole row or column seems a drastic measure because of reduced gain and

16

increased sidelobes, it proves beneficial for a temporary fix while a more time intensive algorithm optimizes for a better correction. This technique approximately restores intercardinal sidelobes and either azimuth principal plane sidelobes when eliminating a row or elevation principal plane sidelobes when eliminating a column.

Separable Distribution Correction: In some situations one or both principal plane sidelobe performances are critical to the mission. One such example is jammers that are received through the azimuth principal plane, therefore maintaining low azimuth sidelobe performance is critical. In the event of multiple failures, both principal planes can be restored using a time efficient algorithm that solves a set of separable distributions that generates an illumination taper with the same collapsed nominal distributions. This technique will successfully work provided a sufficient portion of each significant column and row are non-faulty. As such, this technique can potentially restore the principal plane given many distributed faults across the array.

Roll Phase Bits: In a phased array, a potential failure is a stuck phase shifter bit. This introduces a radiation pattern error when the beam is electrically scanned. A well known correction technique is to roll the phase of each element so that the faulty phase states may be avoided. This involves shifting the desired scanning phase slope such that none of the faulty phase states are commanded. It is possible that given multiple faulty phase states

17

a solution may not exist, however, it is a viable solution for some number of phase bit failures.

4   RESULTS

Running the simulated model essentially takes four steps. An example follows for a case with three elements having various amplitude errors.

The first step is to input the desired faults via the Fault Editor menu shown in Figure 14. The fault can be a static amplitude or phase error, or amplitude or phase shifter bit error on one or more elements/columns.

The second step is to define the mission parameter via the Mission Menu. The various missions and their associated antenna pattern parameter rankings are selected from the list that Figure 11 describes.

The third step is to run the fault detection, isolation and correction sequence. The faulted principal plane patterns are displayed before running fault detection and isolation. The principal plane azimuth pattern for this example is shown in Figure 15. After viewing the faulted patterns and upon completion of the fault detection and isolation, the faults are displayed as Figure 16 shows. This information is then used in conjunction with the ranked antenna parameters to generate a prioritization of the available correction techniques as shown in Figure 17.

18

The fourth step is to select a correction and view the new principal plane patterns. Figure 18 shows the corrected azimuth pattern when selecting the separable distribution correction. Note the 5 dB peak sidelobe improvement even in the presence of random noise. Only one correction can be selected at a time and after viewing its effect, another correction can be selected where only that correction will be implemented. This way alternate corrections can be quickly viewed to make comparisons.

5 CONCLUSIONS

This program successfully combined antenna and artificial intelligence technologies to demonstrate the utility of fusing these disciplines by developing a working model of a fault detection, isolation, and correction system for an airborne phased array. The system separated these functions and demonstrated various methods of each one.

Three detection methods were demonstrated. Monitoring communication lines to array modules, monitoring range/doppler cell threshold levels, and monitoring subarray signal levels each showed that they can detect the presence of some faults. Several monitoring methods are required to detect every fault type.

Fault isolation was achieved by using the information available from the fault detection tests. A programed fault hierarchy confirmed a fault with known information if sufficient and if not

19

it performed the appropriate additional confirming test. Also, one of the fault isolation tests was implemented through hardware at the antenna range. Strong confirmation was achieved that a novel fault isolation scheme that scans the antenna beam past a near field "wing-tip" source can work in a real environment.

Ten correction techniques were demonstrated with each one improving one or more antenna parameters at the expense of other parameters. The selected correction scheme was based on the system mission requirements which prioritized various antenna parameters. Graphical display of the corrected antenna patterns highlighted the need to know the relative importance of the various antenna patterns for the particular mission or radar mode in order to select the most appropriate correction technique.

Overall, the program's favorable results show that with the appropriate design forethought and dedication, airborne arrays can be developed that can be reconfigured to complete their missions even with the presence of antenna component failures. Additionally, this program demonstrated the utility of Artificial Intelligence technology for fault isolation and correction.

20

6 ACKNOWLEDGMENT

7 REFERENCES

1. Havlicsek, B. 1., Integrating Diagnostic Knowledge, AUTOTESTCON '88 Symposium Proceedings (Best Paper)

2. Buck, F. L. and Havlicsek, B. L., ILSD ASSET and Artificial Intelligence, AUTOTESTCON '90 Symposium Proceedings

21
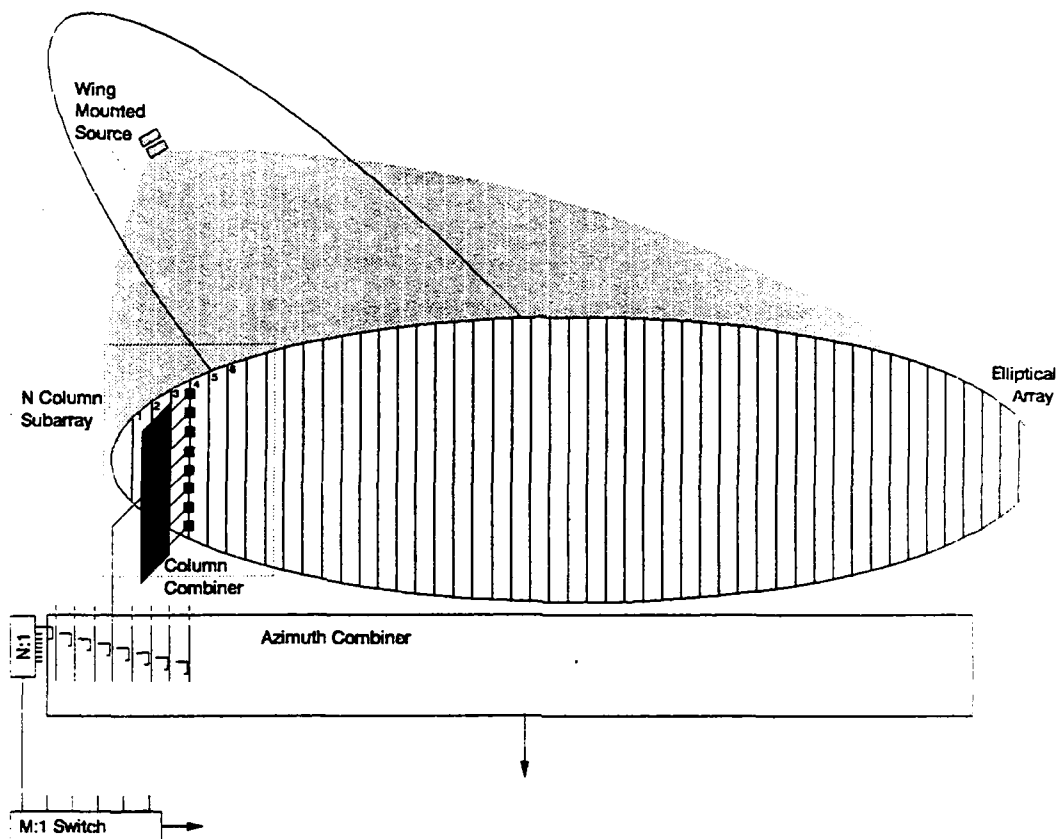
Figure 1   Simulated Array Block Diagram

Wing Mounted Source

Elliptical Array

N Column Subarray

Column Combiner

Azimuth Combiner

N:1

M:1 Switch

FAULT SELECTION

FAULTY PATTERN DISPLAY

FAULT DETECTION

no fault detected

fault detected

A.I. FAULT ISOLATION

A.I. CORRECTION TYPE DECISION

FAULT CORRECTION

CORRECTED PATTERN DISPLAY
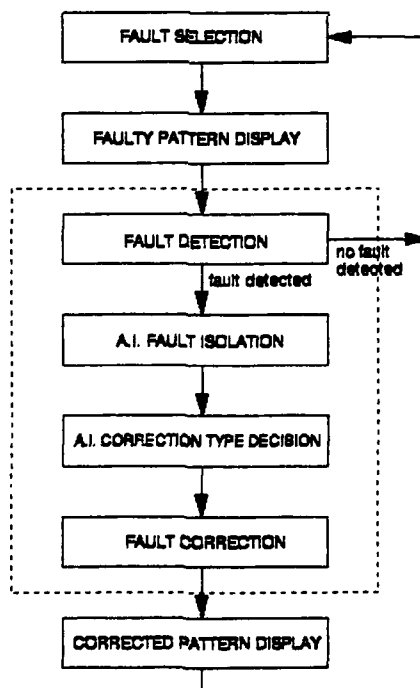
Figure 2   Software Simulation Block Diagram

22

COMPUTER TESTBED ARRAY OUTLINE
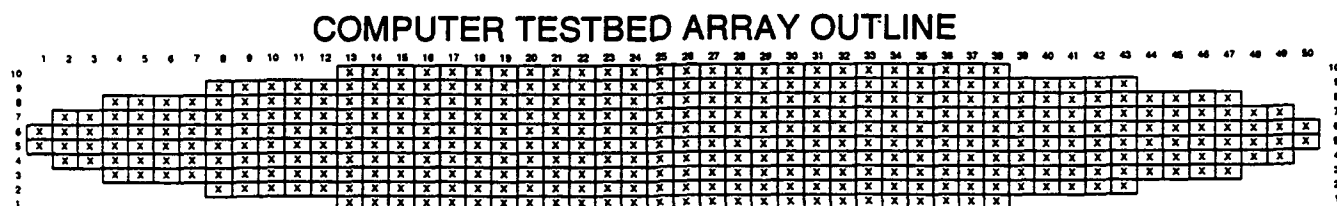
Figure 3   Computer "Testbed Array" Outline

RMS SIDELOBE = −46.83 dB

EFFICIENCY = −1.95 dB
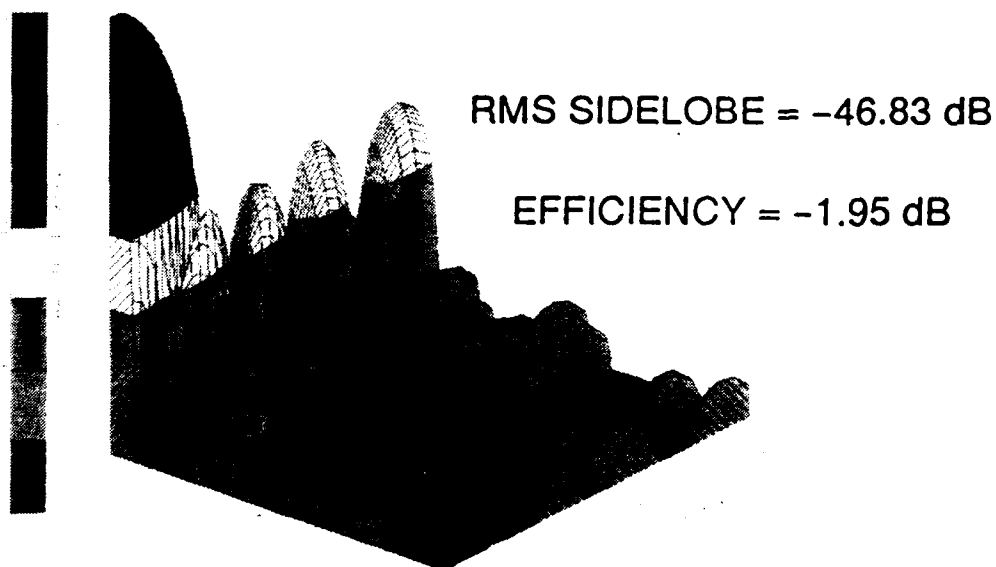
Figure 4   3-D Pattern of Testbed Array

23
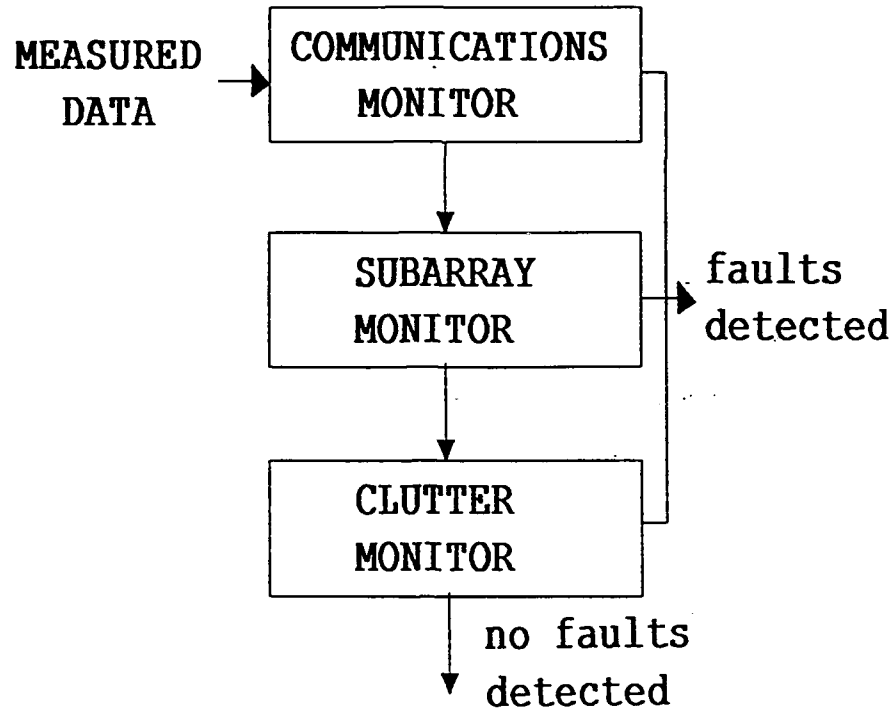
Figure 5 Fault Detection Tests
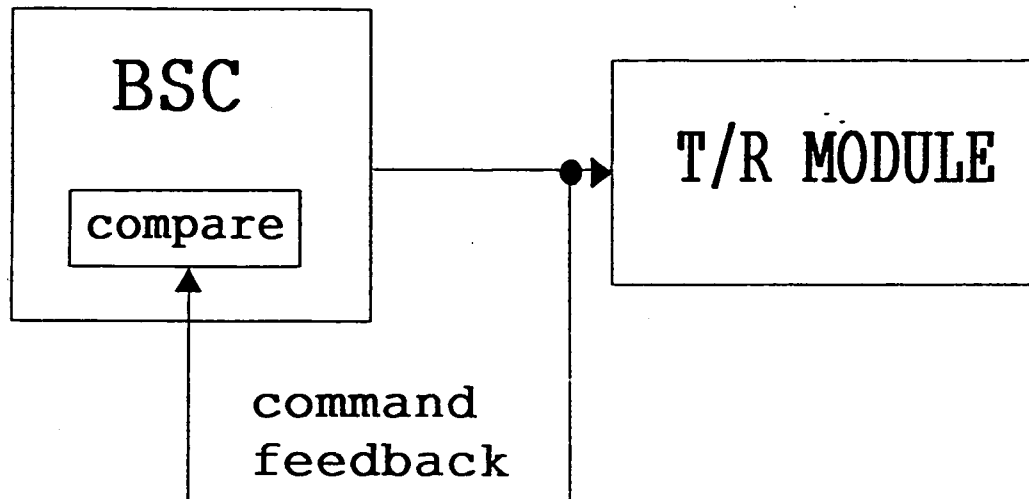
Figure 6 Communications Monitor

24
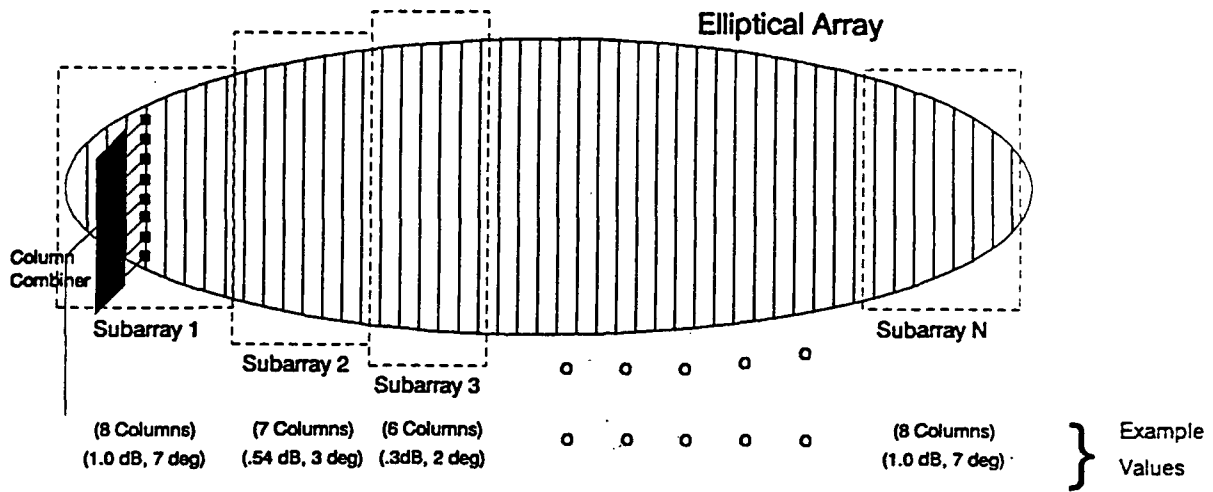
Setup Parameters Prior to running FMC:
- Specify Number of Subarrays
- Specify Number of Columns in each Subarray
- Specify Error Level that Defines Amp & Phase Thresholds for each Subarray

Figure 7 Subarray Monitor Scheme
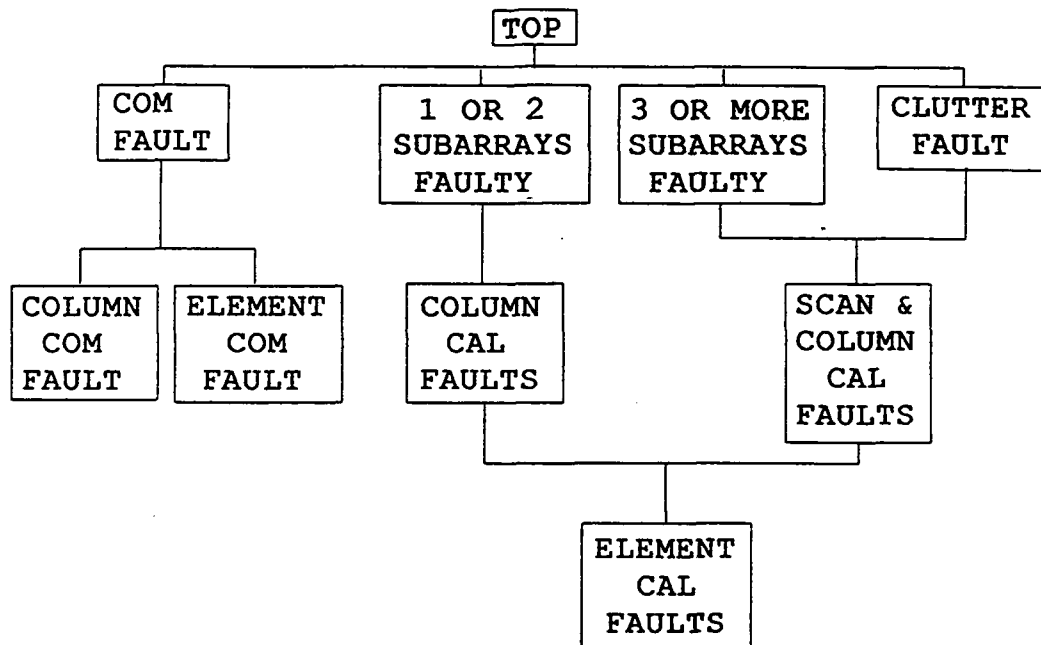
Figure 8 Symptom Hierarchy

25
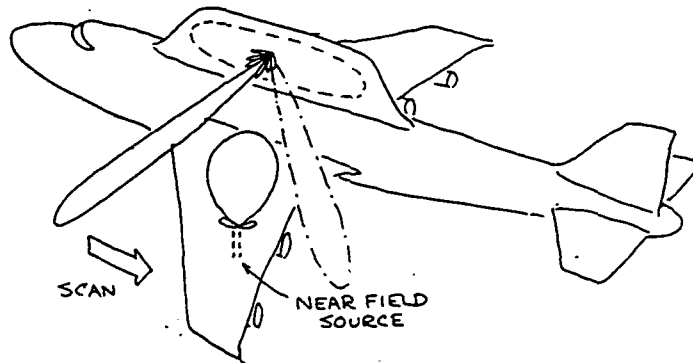
o   Focus forward RF on probe (amp + phase compensation)

o   Include linear phase progression to steer beam

o   Measure full azimuth pattern by changing phase progression

o   Transform array factor to the aperture

o   Compare resulting values to desired

Figure 9   Scan Array Test

SCAN ARRAY TEST

PHASE BIT FAULT
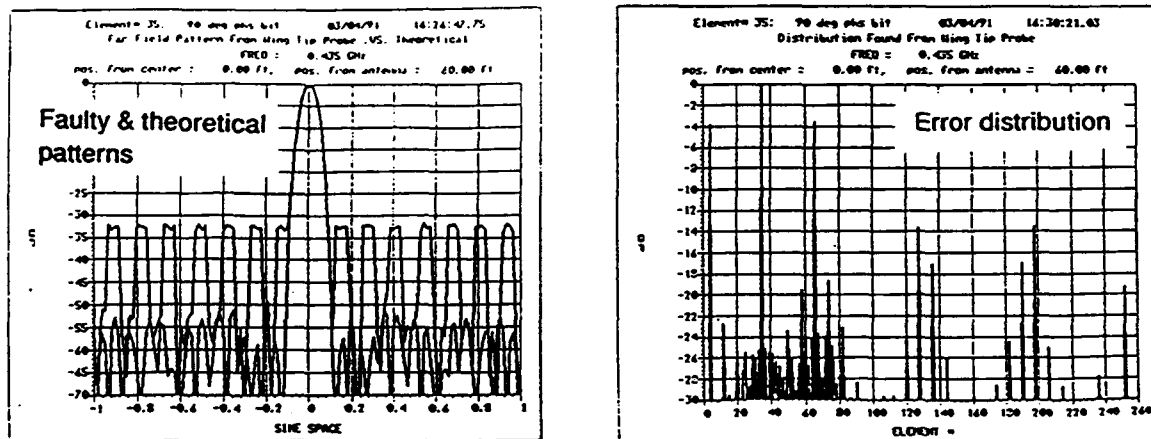
Figure 10   Dynamic Fault Data

26

149

CASE	FUNCTION	TARGETS	OBJECTIVE	ECM	CLUTTER	RELATIVE ANTENNA PATTERN PARAMETER IMPORTANCE	RATIONALE
Tactical	Air Surveillance	Fighter Bomber (Normal RCS)	Detect	Very Heavy (Line of SOJ's & Penetrating Escort Jammers)	Land	Az Peak Sidelobe El Peak Sidelobe RMS Sidelobe	
			Track	Very Heavy (Line of SOJ's & Penetrating Escort Jammers)	Land	Az Peak Sidelobe El Peak Sidelobe Az Beam Pointing El Beam Pointing	
			Identify	Very Heavy (Line of SOJ's & Penetrating Escort Jammers)	Land	Az Peak Sidelobe El Peak Sidelobe	
		Low RCS Aircraft at Low Alt	Detect	Heav			

Figure 11   Mission / Antenna Priorities

Faulty Item	Amp fault > 6 dB	More than 2	ANTENNA PARAMETER RANKING						CORRECTION METHODS			
			Gain	RMS SL	Az SL	El SL	Az beam	El beam	1st	2nd	3rd	4th
element	No	No	1	-	-	-	-	-	1	3	4	
element	No	No	-	1	-	-	-	-	1	3	4	
element	No	No	-	-	1	-	-	-	1	3	8	10
element	No	No	-	-	-	1	-	-	1	4	7	10
element	No	No	-	-	-	-	1	-	1	3	6	10
element	No	No	-	-	-	-	-	1	1	4	6	10
element	Yes	No	1	-	-	-	-	-	3	4		
column	No	No	-	-	-	-	-	-	2			
com. phs.	-	-	-	-	-	-	-	-	9			

CORRECTION METHODS
1 – Adjust fautly element
2 – Adjust faulty column
3 – Adjust nearest neighbors in same column
4 – Adjust nearest neighbors in same row
5 – Eliminate faulty element
6 – Eliminate faulty element and diametrically opposite
7 – Eliminate column
8 – Eliminate row
9 – Roll phse bits
10 – Resynthesize for separable distributions

(partial listing of table)

Figure 12   Correction Method Ranking

27

150
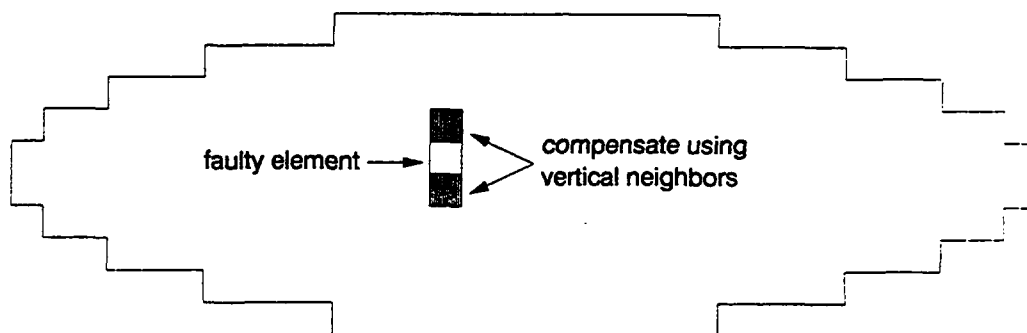
Corrects For The Azimuth Principal Plane

Figure 13   Nearest Neighbor Correction

```
┌──────────────────────[ ARRAY FAULT LIST ]──────────────────────┐
│                                                                 │
│   ELEMENT          AMPLITUDE              PHASE                  │
│   ROW COL      STATIC   COMMAND      STATIC   COMMAND    STATUS  │
│                                                                 │
│    4  22      -11.40dB     M          0.0°       M        ON     │
│    3  27       -8.50dB     M          0.0°       M        ON     │
│    6  32      -18.30dB     M          0.0°       M        ON     │
│    0   1        0.00dB     M          0.0°       M        OFF    │
│    0   1        0.00dB     M          0.0°       M        OFF    │
│                                                                 │
│   RANDOM NOISE (RMS): Amplitude  0.300dB   Phase  2.000°        │
│                                                                 │
│ — [F10]=Finished ——————— [F2]=Read File ——————— [Esc]=Abort — │
└─────────────────────────────────────────────────────────────────┘

   ┌─────────────────+ STATIC AMPLITUDE FAULT +───────────────────┐
   │ This entry represents a fixed amplitude error                │
   │ in the T/R module.                                           │
   │ Enter a value between -100.0 dB and +3.0 dB                  │
   └──────────────────────────────────────────────────────────────┘
```

Figure 14   Fault Editor Menu

28

151
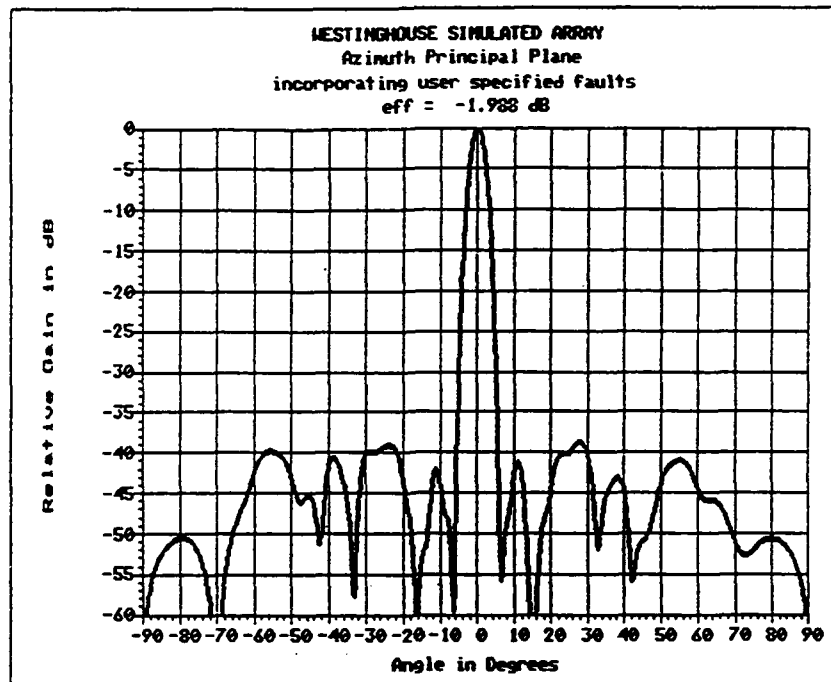
Figure 15   Azimuth Principal Plane with Faults

```
                        DIAGNOSIS

Faulty elements from element calibration
tests
DATA:
row: 4, col: 22
row: 3, col: 27
row: 6, col: 32

              Press a key...
```

Figure 16   Diagnosis

29

```
FAULT CORRECTION RECOMMENDATIONS
Correction 1: resyn_sep (row 4)(col 22)(amp-11.17)(phs  0.49)(bit  0.00)
Correction 1: resyn_sep (row 3)(col 27)(amp -8.10)(phs  1.37)(bit  0.00)
Correction 1: resyn_sep (row 6)(col 32)(amp-18.18)(phs  3.87)(bit  0.00)
```

```
┌──────────────────────────────────────────────┐
│ CORRECTIVE ACTION SELECTION MENU (ESC = EXIT)  │
│                                                │
│        1 ADJUST FAULTY ELEMENT                 │
│        2 ADJUST FAULTY COLUMN                  │
│        3 ADJUST VERTICAL NEIGHBORS             │
│        4 ADJUST HORIZONTAL NEIGHBORS           │
│        5 ELIMINATE FAULTY ELEMENT              │
│        6 ELIMINATE OPPOSITE ELEMENTS           │
│        7 ELIMINATE FAULTY COLUMN               │
│        8 ELIMINATE FAULTY ROW                  │
│        9 ROLL PHASE BITS                       │
│       10 RESYNTHESIZE DISTRIBUTION             │
└──────────────────────────────────────────────┘
```

Figure 17   Fault Correction Recommendations
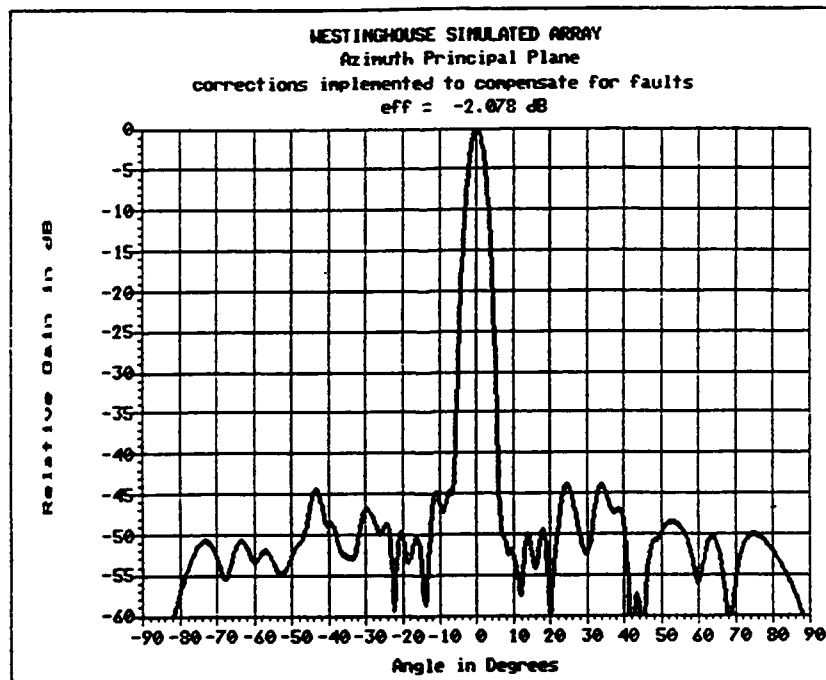
Figure 18   Azimuth Principal Plane with Corrections

30

WAVEGUIDE DISTRIBUTION NETWORKS FOR EHF PHASED ARRAY ANTENNAS

B. J. Lamberty, G. E. Miller, D. N. Rasmussen,
G. W. Fitzsimmons and E. J. Vertatschitsch

Boeing Defense and Space Group
Seattle, Washington

July, 1992

ABSTRACT

This paper describes use of slotted waveguide arrays as distribution networks for exciting EHF active phased array antennas. These networks consist of planar arrays of radiating slots distributed along a coplanar wall in each of an ensemble of parallel waveguides. The waveguide ensemble is excited by an orthogonal waveguide through a row of slots in a wall common to the parallel waveguide ensemble. A computer code was developed so that a predetermined amplitude distribution can be achieved across the phased array by adjusting the coupling parameters in all the slots. The array of radiating slots is used to feed identical, individual modules on a triangular lattice, that constitute a wide-scan-angle, active phased array antenna. These distribution networks are low profile, highly efficient and easy to detach from the active array. They form an efficient medium for conducting heat away from the modules and are easily fabricated.

As part of a Rome Laboratories contract, waveguide distribution networks were designed for uniform distribution, active phased arrays at 20 and 44 GHz, each containing over 1000 elements. We will show predicted results from these as well as measurements from proof-of-concept subarrays of nearly 100 elements each that were fabricated and tested to verify the computer code and construction techniques.

1.0 INTRODUCTION

In 1987 a research project was initiated in the RF Systems Laboratory of the Boeing Defense & Space Group to develop an active phased array antenna for airborne terminals of a satellite communications (SATCOM) system. Separate circular aperture transmit and receive arrays were to be provided, each of which could contain up to several thousand elements. Nominal operating frequencies of the SATCOM terminal are 20 GHz in the receive mode and 44 GHz in the transmit mode. Since the arrays will be mounted on the top of military aircraft, thin profile and low weight are essential. An overall array thickness of less than 6 inches, including heat exchanger, was a design objective. The overall bandwidth is 5%, but, since the SATCOM is a frequency hopping system, instantaneous bandwidth is only a small fraction of this. In both arrays a single, agile sum beam is to be provided; tracking of the satellite terminal is provided by electronically nutating the receiving antenna sum beam. Perhaps the most critical requirements were that the arrays must be available in the mid 1990's and "affordable", that is, delivered array cost should average less than $200 per element in production.

After evaluating several candidate approaches, it soon became apparent that availability of fully monolithic phased array antennas at 44 GHz in the mid 1990's was unlikely. Potential yield of MMIC circuits containing antenna elements, amplifiers, phase shifters, logic circuits plus multiple passive elements at these frequencies with quarter micron feature size requirements, were viewed as stretching credibility on both affordability and availability issues. Consequently, attention was focused on hybrid approaches, that is, approaches incorporating separate MMIC circuits for amplifiers, phase shifters, etc., that are wire-bonded together to form hybrid integrated circuit packages.

The principal hybrid candidates considered were subarrays (tiles), rows of elements (trays), and single module per element. For reasons outside the scope of this paper, the EHF phased array architecture we selected was the single module per element. Each module contains a separate MMIC amplifier, phase shifter and logic circuit as well as RF transitions to both the distribution network and to the radiating elements. This paper describes the distribution network designs used with this active phased array architecture.

2.0 OBJECTIVES

To be compatible with the SATCOM airborne terminal requirements and with our phased array architecture, the distribution network needed to meet the following objectives.
1)   Efficient at EHF.
2)   Uniform illumination.
3)   Thin profile.
4)   Low weight.
5)   Minimum quantization errors.

In addition, the following fabrication issues needed to be addressed.
1)   Cost to manufacture.
2)   Achievable manufacturing tolerances.

3)   Robust design.
4)   Ease of network integration with the array.
5)   Performance reliability.
6)   Reproducible in production quantities.

Finally, the role of the distribution network in thermal management of heat generated in the modules needed to be addressed.

3.0   CANDIDATE EVALUATION AND SELECTION

The potential distribution network candidates evaluated are shown in Figure 1: a corporate feed, a space feed, a radial line feed and a slotted waveguide array. Principal advantages and disadvantages of each candidate are summarized below.

a) Corporate Feed

b) Space Feed

c) Radial Line Feed

d) Slotted Waveguide Array
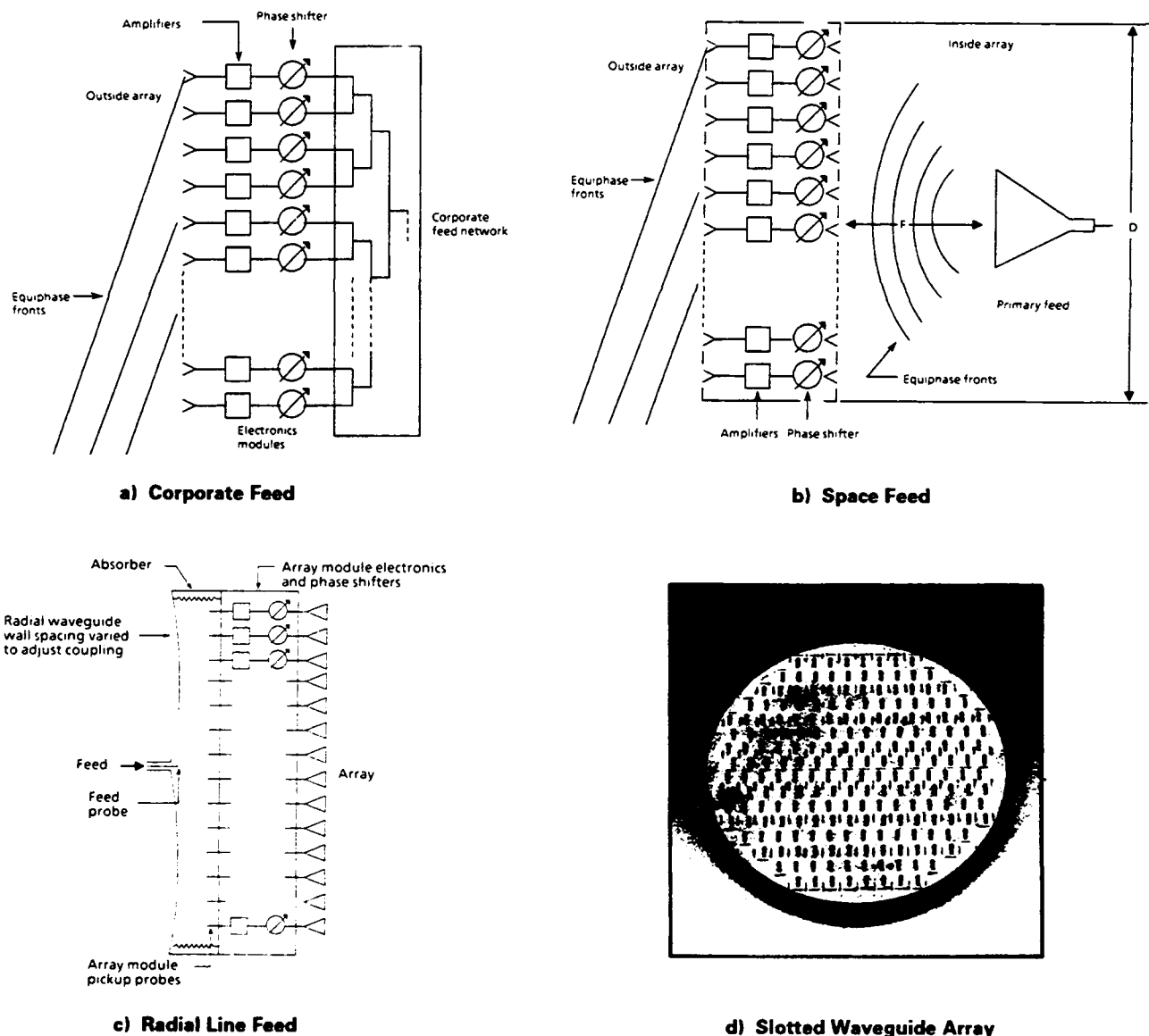
Figure 1. Candidates

Corporate feeds, which may be designed in stripline or waveguide, consist of trees of two-way power dividers. Their strongest feature is that distribution of equal, in-phase power to each of the elements is readily achieved. Disadvantages include: loss in efficiency in circular arrays, since such arrays are not amenable to binary power division (see Figure 2); either large transmission line losses in EHF stripline designs or a thick profile in waveguide designs; and inherent quantization errors that contribute to high sidelobes [1]. The latter disadvantage may not be significant in uniformly illuminated apertures for which high sidelobes are inherent. (See Appendix A for a discussion of quantization errors).
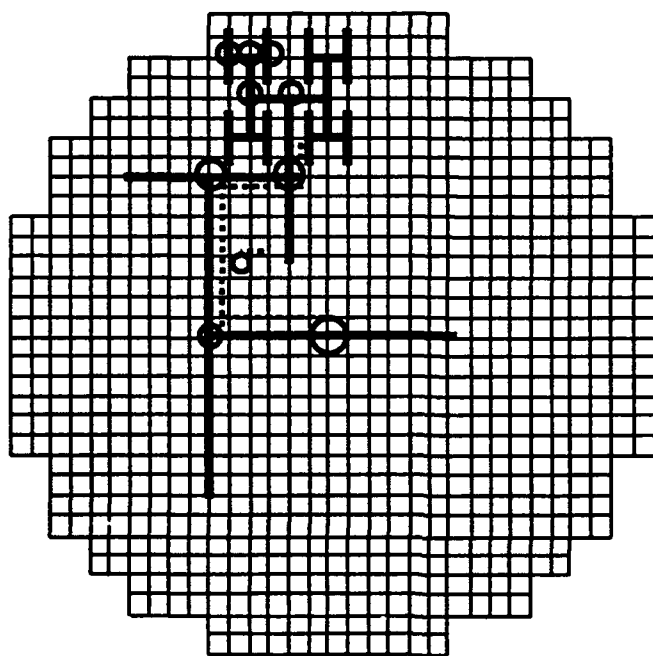
Figure 2. Distribution Network for 32 x 32 Element, Truncated Array

In space feeding, energy is distributed to or collected from all the elements of the array via the radiation pattern of a single antenna, for example, a feed horn. Each element has an antenna on the inside face of the array to interface with the space feed. The best feature of this candidate is its simplicity and therefore low cost. Its principal disadvantage is the space required between the feed and the array elements, nominally equal to at least half the array diameter. This limits its potential for low profile. Other disadvantages include the difficulty of conducting heat away from array elements, and variation in amplitude and phase with frequency across the array caused by variations in the feed horn pattern. Related to the latter is the difficulty in maintaining uniform amplitude illumination in applications with that requirement.

In radial line distribution networks, energy is coupled into the array elements off one wall of a radial transmission line [2]. Its design can be low profile and low weight. However, to maintain frequency independent amplitude distribution across the array, very critical mechanical tolerances are required, including wall spacing in the radial transmission line and in design of the coupling probes or slots. As with the space feed, thermal transfer from the array elements to an external heat exchanger is a problem. A slotted waveguide array as a distribution network takes

advantage of a mature technology in a new application [3]. In this approach, each slot in the array is coupled directly into an element of the active phased-array antenna. This candidate provides high efficiency, thin profile, low weight, a proven production record at EHF, and can act as an efficient thermal transfer medium for the antenna. An additional feature is that it can be designed for tapered amplitude distributions and/or sum and difference excitations for amplitude monopulse. Its principal disadvantage is the variation in coupling phase with frequency. However, this characteristic is easily overcome in a frequency hopping communications system by adjusting the element phase shifters with each hop (dehopping).

As a consequence of the trade study the slotted waveguide array was selected as the distribution network for our SATCOM arrays. Because of their extensive experience and reputation with large quantity, high quality production runs of EHF slotted waveguide arrays, mdm, Inc., of Chatsworth, Ca. was contracted by Boeing to help develop this distribution network.

4.0   DESCRIPTION OF APPROACH

A sketch of the selected distribution network is shown in Figure 3. It consists of a planar array of radiating slots distributed along a coplanar wall in each of an ensemble of parallel waveguides (branchlines). The waveguide ensemble is excited by an orthogonal waveguide (mainline) through a row of slots in a wall common to the parallel waveguide ensemble. Slot parameters are adjusted to provide a predetermined amplitude distribution across the array (uniform distribution for our antennas). Each waveguide is terminated in a load to inhibit the effects of reflected waves on slot performance. These reflected waves should be very low in magnitude if the network is designed properly.
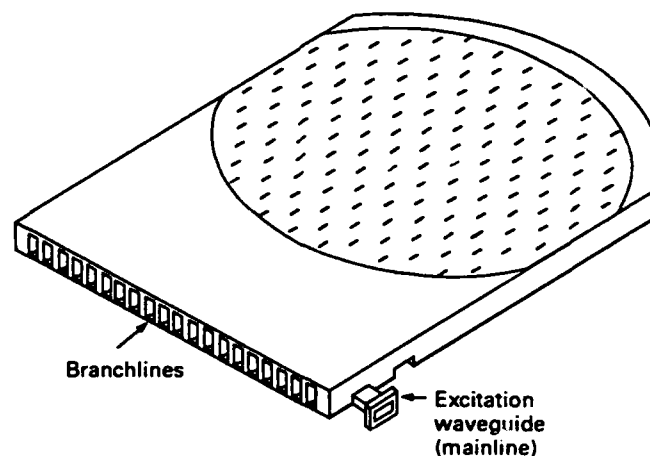
Figure 3. Slotted Waveguide Array Distribution Network

Each slot in the array is used to excite an individual module in the phased array (see Figure 4). All the modules are identical and contain a MMIC amplifier, MMIC phase shifter and CMOS logic chip plus RF transitions into and out of the module. The slots and the modules are arranged in a triangular lattice to minimize the number of elements in the array. Element spacing is $1/\sqrt{3}$ to preclude occurrence of grating lobes in visible space, even for wide angles of beam scan.
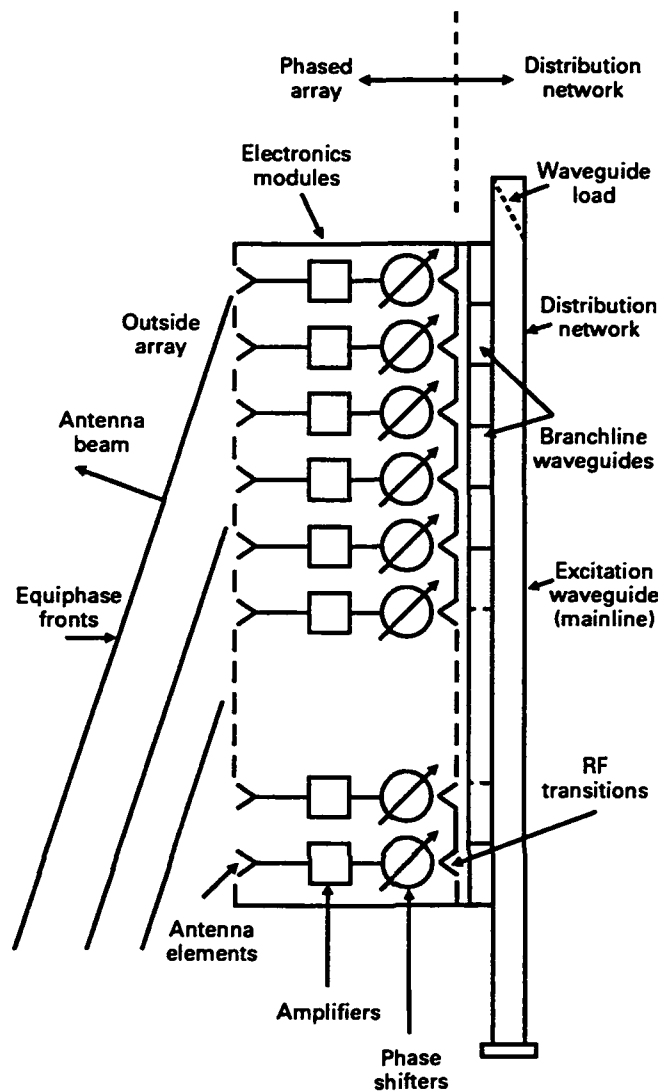
Figure 4. Active Phased Array with Slotted Waveguide Distribution Network

5.0 ANALYSIS

mdm, Inc. had computer programs available to model dispersive waveguide feed networks for 2-D electronically steerable arrays. A functional block diagram of the distribution network is shown in Figure 5, where each slot is represented as a three port junction. It was necessary to obtain accurate S-parameter data for a wide range of slot parameters for our particular configuration as inputs to the computer codes. A theoretical model using method of moments and including effects of wall thickness was developed. Several experimental models with various slot parameters were fabricated and measured to verify the theoretical model. Figure 6 shows a set of typical results. There was excellent agreement between theory and measurements.
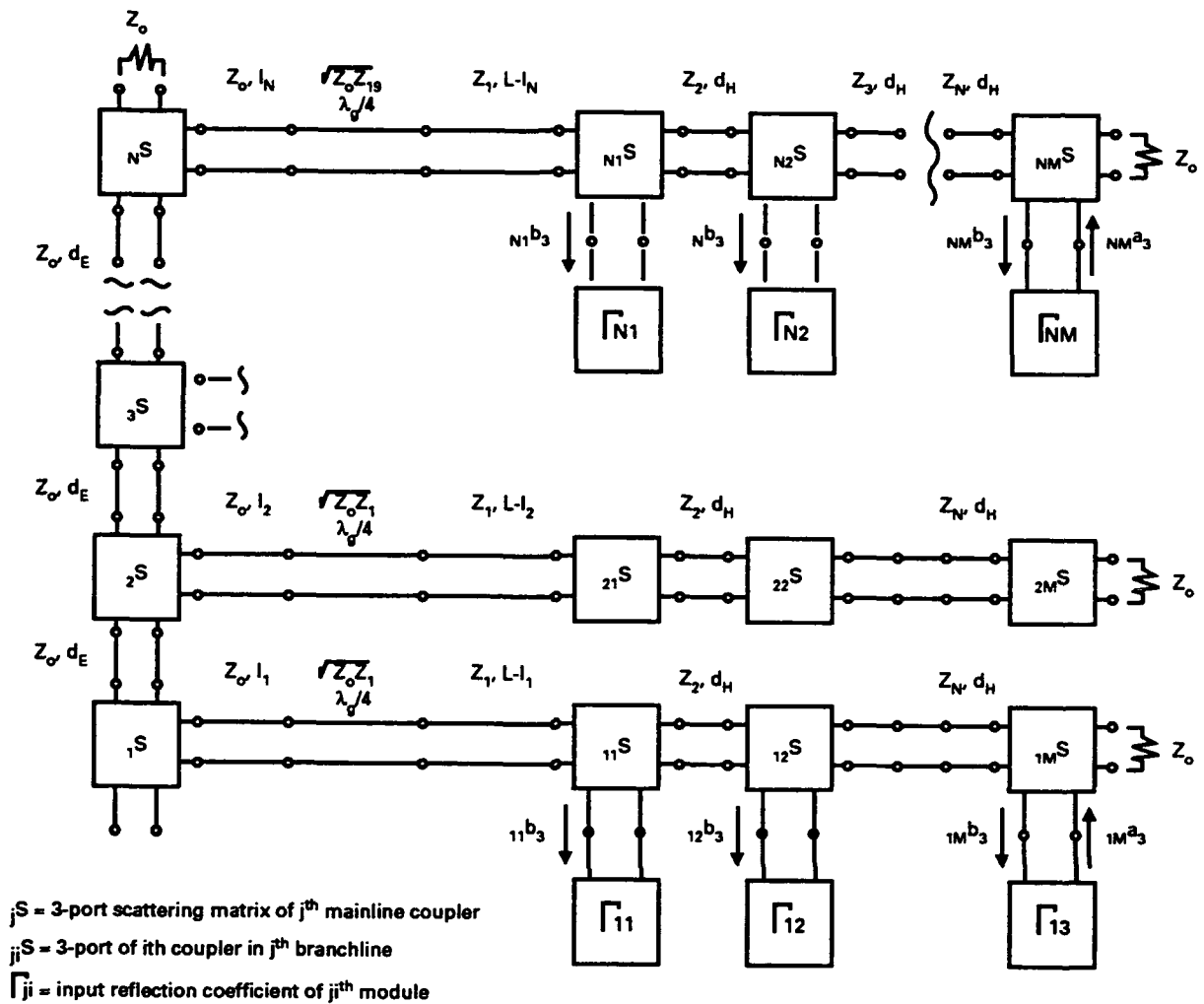
Figure 5. Functional Diagram of Waveguide Network

Branchline Coupler

Slot width = 0.100 in
Slot offset = 0.050 in
Frequency = 9.635 GHz

$a_1 = 0.900$ in
$b_1 = 0.400$ in

Slot length 0.500	Wall thickness: 0.050 inches	
	Measured	Theory
S_{11}	-18.90 dB ∠-116.8 deg.	-18.78 dB ∠-113.2 deg.
S_{21}	-0.38 dB ∠-9.3 deg	-0.34 dB ∠-7.0 deg.
S_{31}	-11.99 dB ∠-25.5 deg.	-12.08 dB ∠-24.3 deg.

Mainline Coupler

$a_2 = 0.900$ in
$b_2 = 0.400$ in

Slot width = 0.100 in
Frequency = 9.635 GHz
Wall thickness = 0.50 in

$a_1 = 0.900$ in
$b_1 = 0.400$ in

Slot length 0.500 in	Measured	Theory
S_{11}	-15.22 dB ∠68.0 deg	-15.907 dB ∠66.93 deg
S_{21}	-0.465 dB ∠-4.57 deg	-0.457 dB ∠-8.94 deg
S_{31}	-10.994 dB ∠157.16 deg	-11.295 dB ∠153.5 deg

Figure 6. Analysis Conducted by mdm, Inc.

160

6.0   CODE VERIFICATION

The code was used to design a distribution network for a 93 element subarray at 44 GHz with uniform amplitude distribution. A model was constructed, based on that design. A rectangular waveguide honeycomb structure was bonded on the distribution network, where each slot coupled into a rectangular waveguide. These waveguides, dielectrically loaded to prevent cutoff, were used to measure amplitude and phase of the signal coupled out of each slot. (Coupling from the branchline slots to isolated rectangular or circular waveguide output ports is part of the analysis code). Figure 7 shows that distribution network. In Figure 7b the test fixture for measuring relative amplitude and phase is shown mounted on the array. All honeycomb waveguides except the one under test are resistively loaded for these measurements.

Typical test results are shown in Figure 8. Note that the amplitude values of the even numbered rows (9 elements per row) are bunched together, as are the values for the odd numbered rows (8 elements per row). However, the two sets of data are about 5 dB apart. Two sources of error were discovered. First, the measured dielectric constant of the material filling the waveguides was different from assumed (catalog) values. Second, the analysis assumed square corners in the slot. The corners were actually round as manufactured. When compensations were made for these discrepancies, the analysis closely predicted measured results.

44-GHz Feed Network Validation Model
Model Ready for Test

Measured RF Parameters for Each
Element Led to Improve Array
Computer Prediciton Model
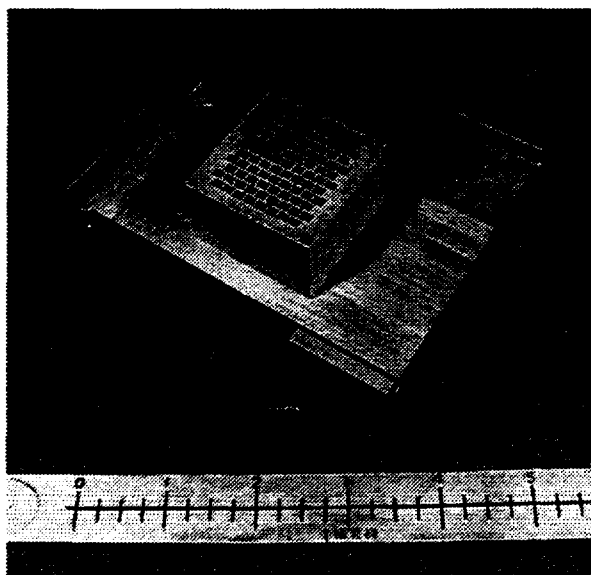
**a) 93-Element Honeycomb Attached
to the Waveguide Distribution Network**
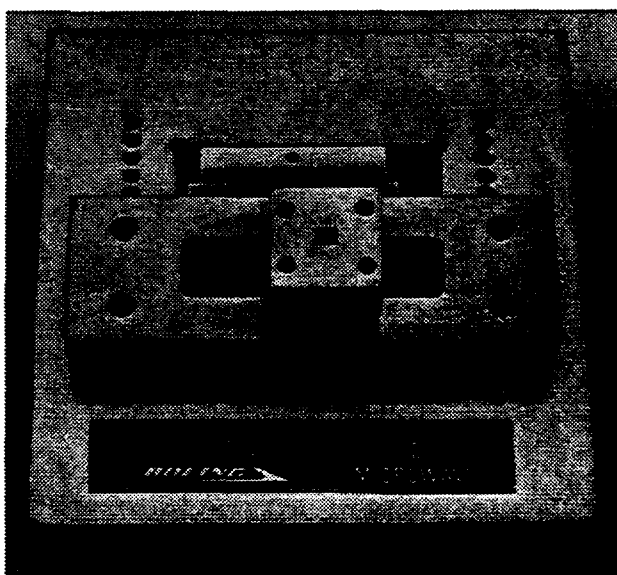
**b) Traveling Transition to Measure RF Level and
Phase Delivered by the Feed Network to Each
of the 93 Honeycomb Waveguides**

Figure 7. 44-GHz Waveguide Feed Network

161
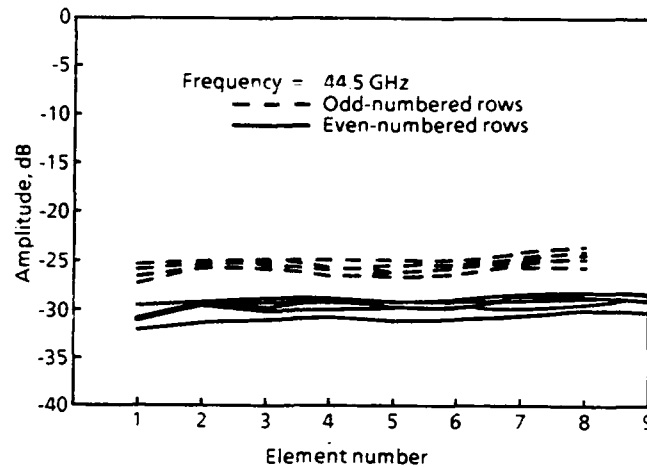
Figure 8. Measured Amplitude of All Honeycomb Apertures in 93-Element Subarray Referenced to WDN Input

7.0 DISTRIBUTION NETWORKS FOR LARGE ARRAYS

After the analysis code was verified, distribution networks were designed for full size SATCOM terminal arrays. A 4014 element distribution network was designed for the 44 GHz array and a 1500 element network for the 20 GHz array. (This work was performed under contract for Rome Laboratories [4]. mdm, Inc. continued to support Boeing on this contract.)

An objective in these designs was to achieve 80% efficiency in the distribution networks. In earlier work it was determined that efficiency suffered in networks where the branchlines contained too few elements. Insufficient power would be coupled through the slots and excessive power was transmitted to the loads. This problem was particularly acute in the end rows in a circular aperture because of the small number of elements they contain. Consequently, in the 4014 element array, the end 3 rows were sinuously connected using E-plane bends at the end of the rows. The fourth and fifth rows from the end were similarly connected. A drawing of the 44 GHz distribution network design is shown in Figure 9.

The analysis code was used to predict performance of that network. To make the prediction as realistic as possible, effects of waveguide losses, random manufacturing errors ($\pm$.001 inch rms, 3 sigma) and impedance mismatches to the electronics modules (VSWR = 1.5:1, random phase) were included. Four cases were evaluated: 1) No manufacturing error, no mismatch; 2) Manufacturing error, no mismatch; 3) No manufacturing error, VSWR mismatch; and 4) Both manufacturing errors and VSWR mismatch. Waveguide losses were included in all four cases. Predicted efficiencies from the four cases are shown in Table 1, where this efficiency is defined as the ratio of radiated power to input power. From these results it is expected that efficiencies close to 80% can be achieved in a full size network at 44 GHz. Additional array gain loss caused by element amplitude variations over the operating band for the four cases described above are shown in Table 2. These do not significantly affect overall performance of the network.
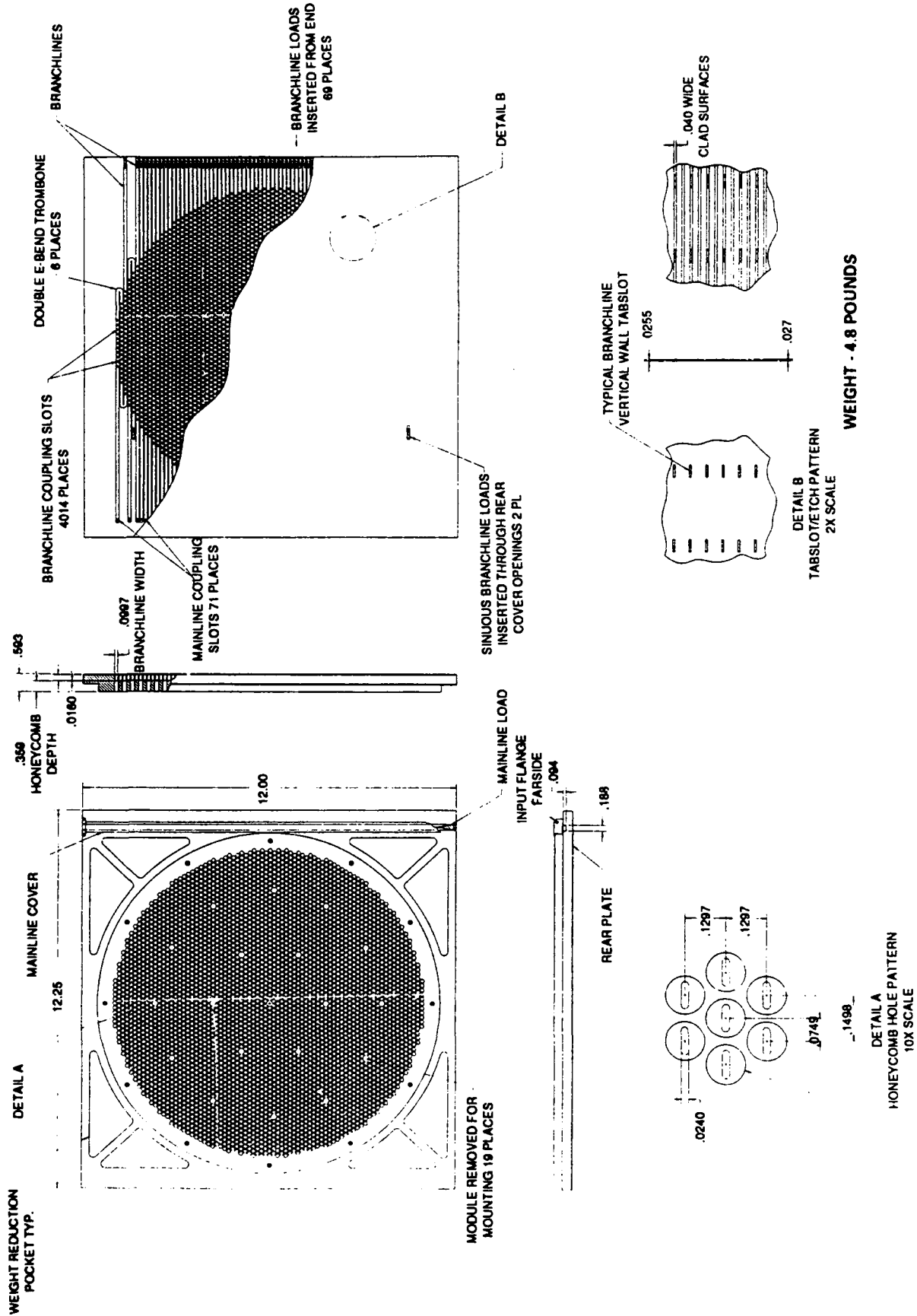
Figure 9. Full-Scale, 44-GHz Waveguide Distribution Network

163

Table 1. 44-GHz Full-Scale-Array Waveguide Distribution Network Efficiency (%)

	WDN Error Sources	
	Random Errors*	Module Impedance Mismatches**
Case 1	No	No
Case 2	Yes	No
Case 3	No	Yes
Case 4	Yes	Yes

*Gaussian random errors with a 3σ of (±.001 in)
** VSWR of 1.5:1, random phase

Frequency (GHz)	Efficiency (%)			
	Case 1	Case 2	Case 3	Case 4
43.5000	76.06	75.88	76.43	76.27
43.7500	76.45	76.58	76.36	76.47
44.0000	79.18	79.15	78.96	78.94
44.2500	78.78	78.73	78.66	78.61
44.5000	79.71	79.70	79.65	79.61
44.7500	82.06	81.95	81.92	81.81
44.0000	83.02	82.99	82.75	82.73
45.2500	83.71	83.75	83.40	83.44
45.5000	84.56	84.69	84.51	84.64

Table 2. 44-GHz Distribution Network Amplitude Fluctuation Gain Loss

Frequency (GHz)	Case 1	Case 2	Case 3	Case 4
43.5000	0.12	0.13	0.15	0.16
43.7500	0.07	0.08	0.21	0.22
44.0000	0.07	0.07	0.15	0.15
44.2500	0.08	0.09	0.19	0.21
44.5000	0.00	0.01	0.14	0.16
44.7500	0.03	0.03	0.12	0.13
44.0000	0.05	0.05	0.16	0.16
45.2500	0.06	0.06	0.13	0.14
45.5000	0.06	0.07	0.16	0.17

To approach the desired efficiency of 80% in the 1500 element 20 GHz network, more extensive use of sinuous branchlines was required. This raised the problem of efficient coupling from the mainline to the branchlines. Consequently, a hybrid distribution network was designed. In this design, the branchlines are connected to form 8 sets of sinuous waveguides. Each of these is connected to one port of an 8-way corporate waveguide feed. This configuration is shown conceptually in Figure 10. A drawing of the full size network design is shown in Figure 11. As in the 44 GHz design, four analysis cases were run to include the effects of random manufacturing error and module mismatch. Results are shown in Table 3. In all cases 80% efficiency is exceeded. The calculated gain reduction caused by element amplitude variations over the operating band for the four cases is shown in Table 4. The worse case is only 1/3 dB, which is not significant.
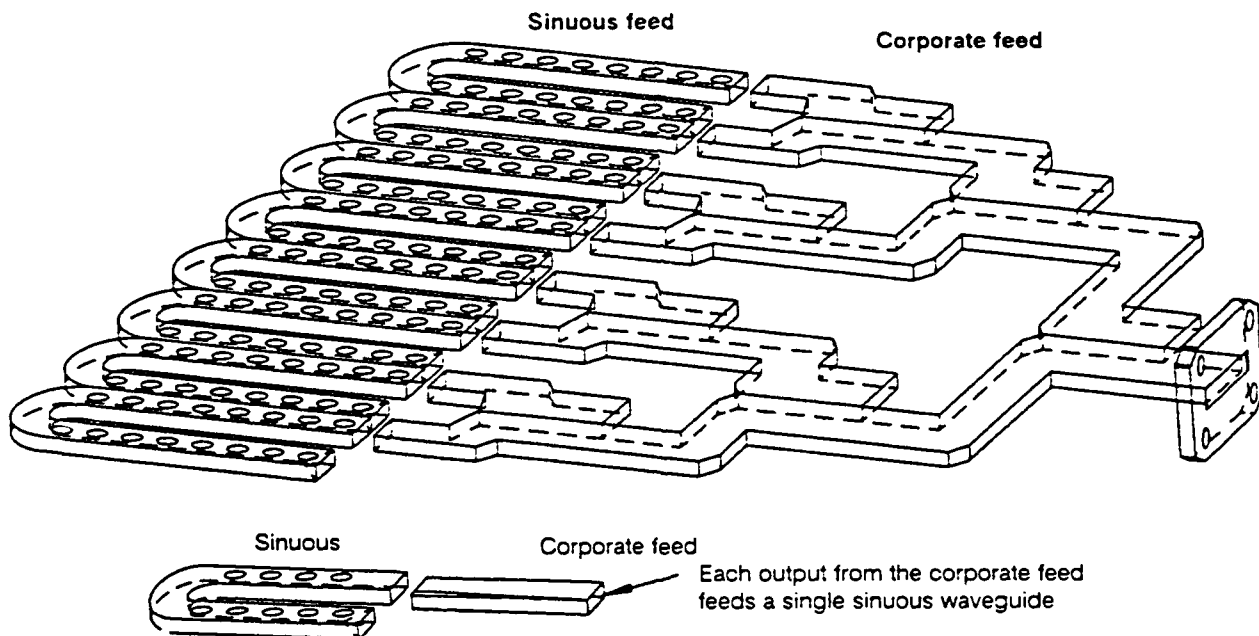
Figure 10. Corporate/Sinuously Fed Waveguide Distribution Network

Figure 11. Full-Scale, 20-GHz Waveguide Distribution Network

166

Table 3. 20-GHz Full-Scale-Array Waveguide Distribution Network Efficiency (%)

	WDN Error Sources	
	Random Errors*	Module Impedance Mismatches**
Case 1	No	No
Case 2	Yes	No
Case 3	No	Yes
Case 4	Yes	Yes

*Gaussian random errors with a 3σ of (±.001 in)
** VSWR of 1.5:1, random phase

Frequency (GHz)	Efficiency (%)			
	Case 1	Case 2	Case 3	Case 4
20.2000	82.93	82.82	82.95	82.85
20.3250	83.24	83.00	83.23	82.98
20.4500	83.25	83.41	83.27	83.41
20.5750	82.24	82.14	82.27	82.16
20.7000	83.84	83.90	83.87	83.91
20.8250	84.92	84.98	84.93	85.00
20.9500	85.22	85.29	85.24	85.32
21.0750	85.38	85.40	85.39	85.42
21.2000	85.27	85.20	85.30	85.22

Table 4. 20-GHz Distribution Network Amplitude Fluctuation Gain Loss

Frequency (GHz)	Case 1	Case 2	Case 3	Case 4
43.5000	0.12	0.13	0.15	0.16
43.7500	0.07	0.08	0.21	0.22
44.0000	0.07	0.07	0.15	0.15
44.2500	0.08	0.09	0.19	0.21
44.5000	0.00	0.01	0.14	0.16
44.7500	0.03	0.03	0.12	0.13
44.0000	0.05	0.05	0.16	0.16
45.2500	0.06	0.06	0.13	0.14
45.5000	0.06	0.07	0.16	0.17

8.0   FABRICATION OF DISTRIBUTION NETWORKS FOR SUBARRAYS

As part of our contract with Rome Laboratories, we are to deliver fully operational 91 element subarrays, one at 20 GHz and one at 44 GHz. The paragraphs below describe the distribution networks that will be delivered with those subarrays. The two networks are identical in design except for operating frequency.

To achieve the design goal of 80% efficiency in a network with only 91 slots, the hybrid corporate/sinuous feed approach was embodied. The networks consist of a single input port, an unequal 2-way split using a sidewall coupler, and two sinuous branchlines, one containing 6 rows with a total of 51 slots and one containing 5 rows with a total of 40 slots. Photographs of these networks are shown in Figure 12.

Testing of the 20 GHz network is completed. Figure 13 shows the measured efficiency as a function of frequency which varies from about 71% at the low end of the band to about 88% at the high end. Computed efficiencies varied between 76.1% and 87.1% over the frequency band. Measured amplitude variations will further reduce subarray gain by less than 0.13 dB.

Fabrication of the 44 GHz network is completed and testing has just begun. When testing is complete, measured results from both networks will be compared to predictions in detail.
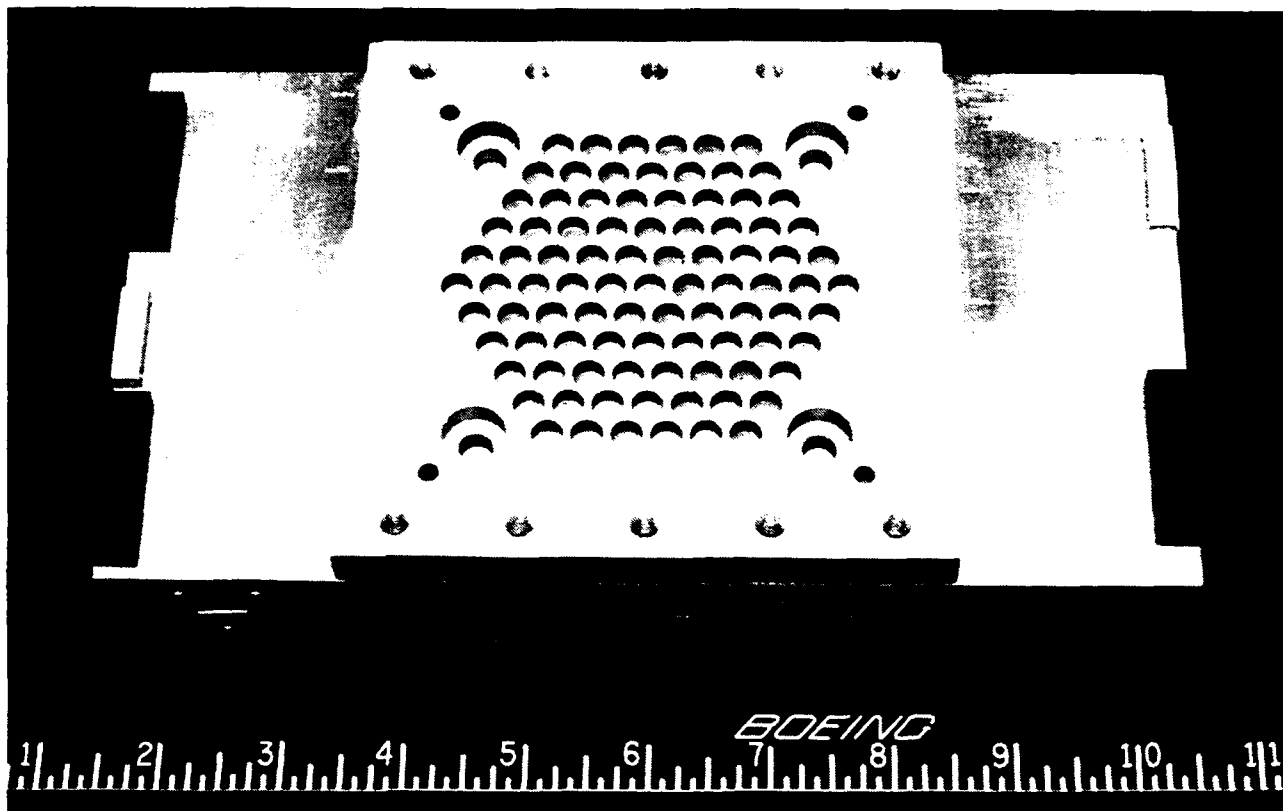
a) 20 GHz Network
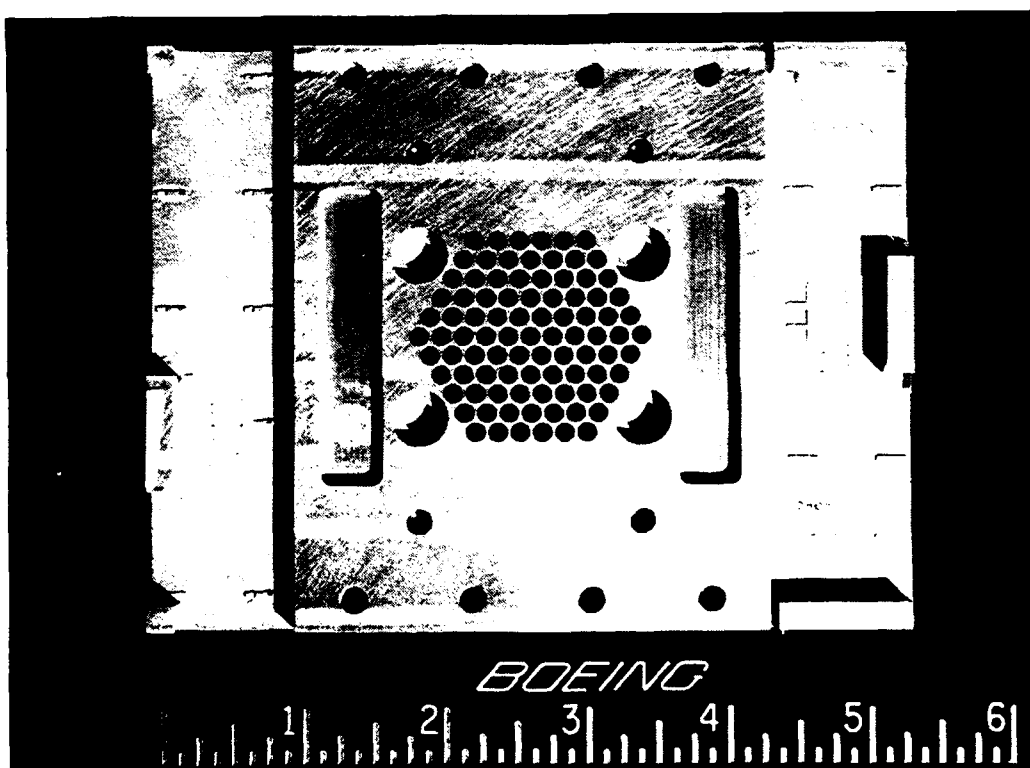
b) 44 GHz Network

Figure 12. Sinuous Line Proof-of-Concept Models

169
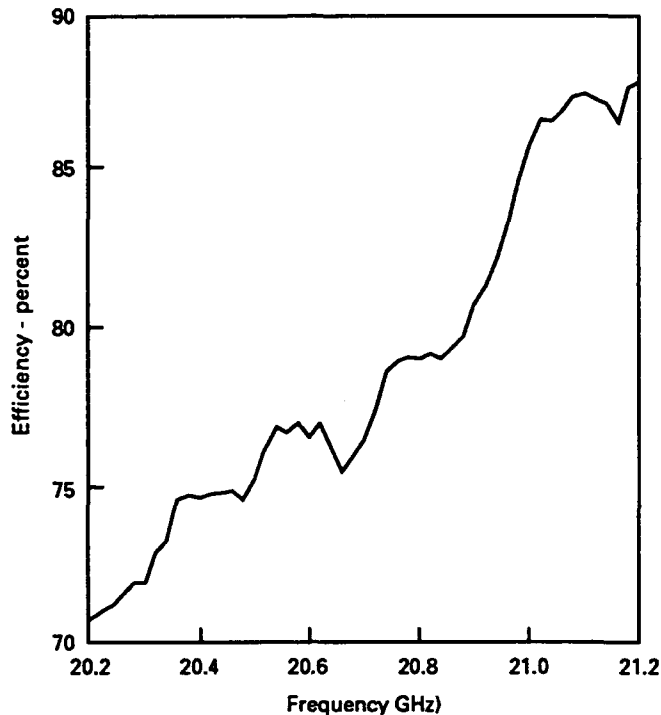
Figure 13. 20 GHz Subarray WDN Measured Efficiency

9.0   CONCLUSIONS

We have successfully demonstrated that slotted waveguides are the best choice for distribution networks for our EHF active phased array antennas. Near 80% efficiency appears achievable, instantaneous bandwidth is satisfactory for frequency hopping and other narrow band applications, and the design can be used for virtually any degree of tapered amplitude distribution as well as for monopulse applications.

Mechanically, these networks have a thin profile and can be fabricated with light weight. Proven, cost effective manufacturing methods are used to produce in quantity, a product that is robust and reliable. These networks readily integrate with the active phased array portion of the antenna and they provide an efficient thermal path from the heat generating modules to an external heat exchanger.

ACKNOWLEDGEMENTS

170

REFERENCES

1. C. J. Miller, "Minimizing the Effects of Phase Quantization Errors in an Electronically Scanned Array", Proc. 1964 Sympos. Electronically Scanned Array Techniques and Applications, RADC-TDR-64-225, vol. 1, pp. 17-38.

2. Alfred J. Appelbaum, et. al., "A Flat-Feed Technique for Phased Arrays", IEEE Trans. on Antennas and Propagation, Vol. AP-20, No. 5, September 1972, pp. 582-588.

3. Bernard J. Lamberty, et. al., "Distribution Network for Phased Array Antennas", U. S. Patent No. 4,939,527, Jul. 3, 1990.

4. "EHF Integrated Circuit Active Phased Arrays," Contract No. F19628-90-C-0168, Boeing Defense & Space Group, Seattle, WA

APPENDIX A
Phase Quantization Sidelobes

Ideally, the phase across an array aperture is adjusted to compensate for phase tilt of a wave incident on or transmitted to the desired beam direction. This is illustrated in Figure A-1 where an increasing amount of phase delay is required across the array from the –m to the +m ends of the aperture. There are two factors that prevent achieving that ideal. First, phase shift is applied incrementally both in level (because digital phase shifters are normally used in a phased array) and in position (element location). This quantized periodicity can result in excessively high sidelobes. Secondly, total variation in the phase shifter is 360 degrees whereas true time delay requirements could be several times that. So, true time delay is simulated by removing all increments of 2π from the phase shift. This approximation causes beam skew as a function of frequency, which increases with scan angle. Figure A-2 shows the desired phase shift (true time delay), its simulation using digital phase shifters, and the periodic error that results when modulo 2π is removed from the simulation.
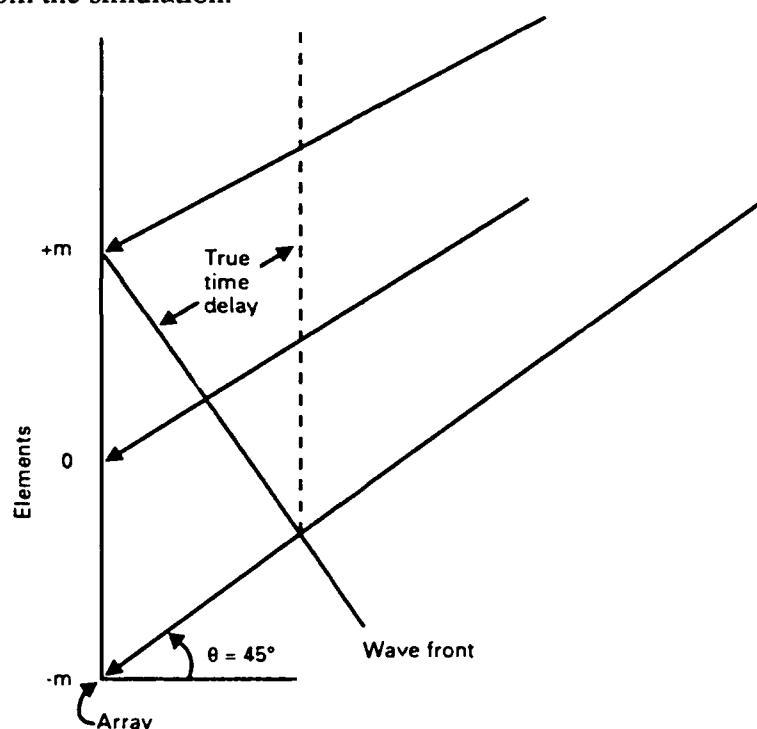
Figure A-1. Time Delay in Conventional Array

The effects of phase quantization periodicity is shown in Figures A-3 and A-4. Note that the rms quantization sidelobe level is inversely related to both number of bits and to number of elements in the array. As an example, a 1000 element array with 4 bits of phase quantization has an rms sidelobe level that is about -47 dB. However, because of the periodicity of these errors, the peak sidelobe level can be much higher (Figure A-4). The highest sidelobes occur at those scan angles where the required phase at each element is midway between the least significant bits, resulting in a quarter bit error of alternating sign in adjacent elements. For that case a 4-bit quantization error can result in a peak sidelobe level less than 20 dB below the main beam.
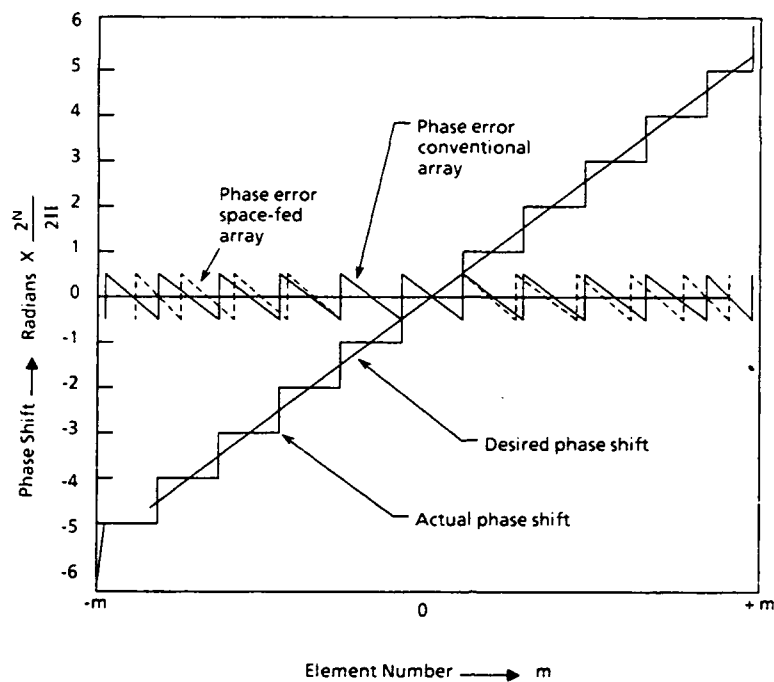
Figure A-2. Time Delay and Quantization Phase Er᠁
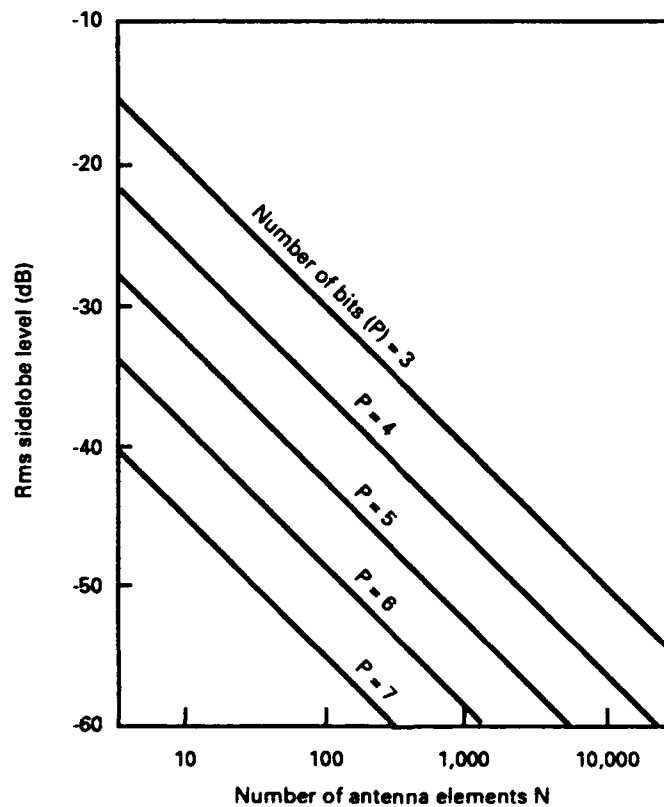
Figure A-3. Rms Sidelobes Due to Phase Quantization

173
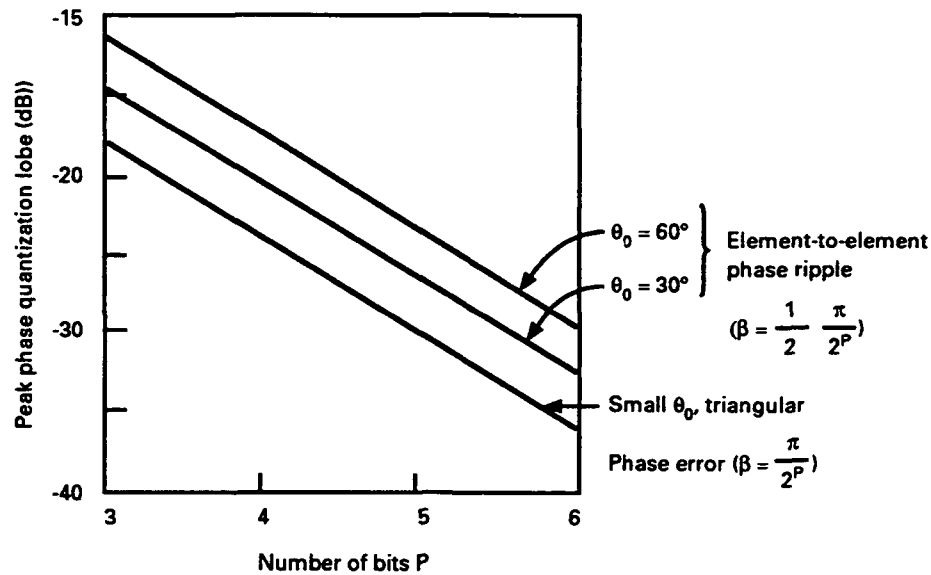
Figure A-4. Peak Sidelobes Due to Phase Quantization

In a space fed array, phase correction across the array is not linear. To focus the incident wave on the feed horn, phase in the elements near the center of the array must be delayed from that of the end elements. When this quadratic phase correction is combined with the linear correction required to compensate for wave front phase tilt, the periodicity of phase quantization is destroyed. (See dashed curve in Figure A-2). This is true for scanned beams as well as for the broadside case. Figure A-5 shows the required true time delay of a space fed array compared to a conventional corporate feed for a beam scanned at 60 degrees. As a consequence, the quantized phase errors approach a random distribution which reduces peak sidelobe levels significantly. Measurements verifying this phenomena have been reported in the literature.

There is some relief from periodic error, even in corporate fed arrays because of random errors in the modules themselves. Radial line distribution networks are a limiting case of space feeding and so are not subject to periodic phase errors. Because the slotted waveguide array distribution networks are fed unsymmetrically, they also do not suffer from periodic phase errors.

174
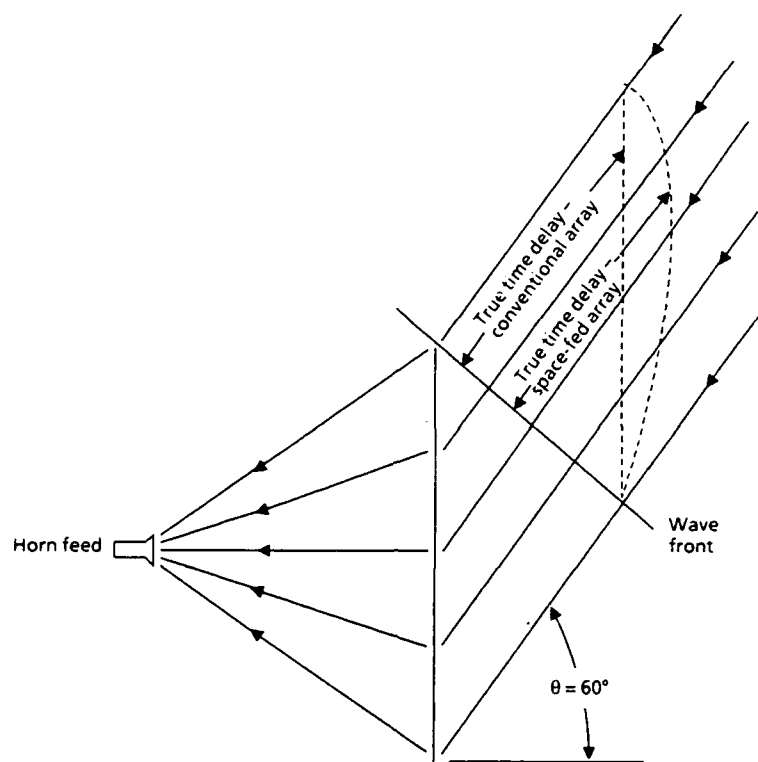
Figure A-5. Comparison of True Time Delay – (60 Degree Scan Angle)

175

WIDE ANGLE IMPEDANCE MATCHING SURFACES FOR CIRCULAR WAVEGUIDE PHASED ARRAY ANTENNAS WITH 70 DEGREE SCAN CAPABILITY

B. J. Lamberty, W. P. Geren, S. H. Goodman,
G. E. Miller and K. A. Dallabetta

Boeing Defense and Space Group
Seattle, Washington

July, 1992

ABSTRACT

It is well known that active element impedance varies widely with scan angle in phased array antennas. This can result in degraded beam performance at certain scan angles, even scan blindness under some circumstances. Wide angle impedance matching (WAIM) surfaces have been described in the literature to compensate for these impedance variations. In most cases these WAIMs consist of a single dielectric sheet across the array aperture with sheet thickness, dielectric constant and spacing from the aperture as parameter variables.

At Boeing we have written and verified experimentally a series of programs for WAIMs that apply to large arrays of either circular or rectangular waveguide elements in rectangular or triangular lattices. These programs are unique in that several dielectric layers may be specified in the waveguides and in front of the array. Also, an optimization routine is included to minimize reflection loss over a specified scan angle. This paper describes the design configuration, predicted performance and test results of practical WAIMs designed for airborne arrays at both 20 GHz and 44 GHz using this code. Less than 0.5 dB of reflection loss is produced over a scan angle of nearly 70 degrees.

1.0   INTRODUCTION

In 1987 a research project was initiated in the RF Systems Laboratory of the Boeing Defense & Space Group to develop active phased array antenn:s for airborne terminals of a satellite communications (SATCOM) system. Separate circu.ar-aperture transmit and receive arrays were to be provided, each of which could contain up to several thousand circularly polarized elements. Nominal operating frequencies of the SATCOM terminals are 20 GHz in the receive mode and 44 GHz in the transmit mode, each with an overall bandwidth of 5%. For cost considerations, each aircraft is limited to a single set of apertures. To provide maximum satellite coverage, the arrays must be mounted on top of the aircraft. 70 degrees of angular scan coverage, to within 20 degrees of the horizon, was a system objective, as illustrated in Figure 1.
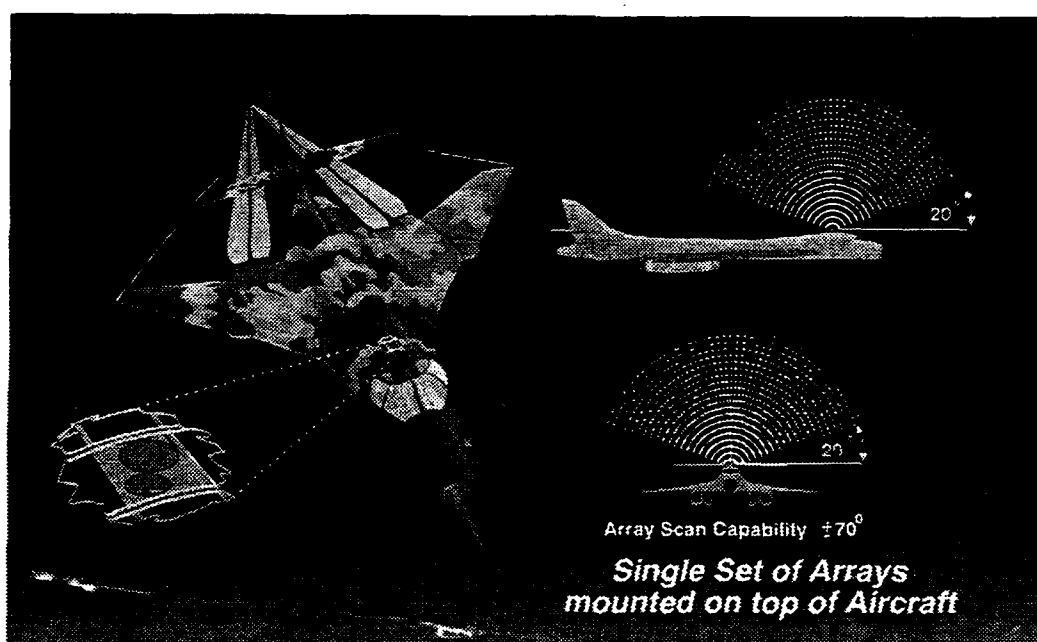
Figure 1. Mounting Location and Scan Capability

It is well known that, in order to provide such wide angle coverage, array elements must be closely spaced to prevent the onset of grating lobes in visible space. Close element spacing results in strong mutual coupling between elements, which varies as a function of relative position, scan angle and frequency. This mutual coupling can significantly affect the radiation patterns and reflection characteristics of the elements and therefore of the array [1].

To illustrate the problem, the theoretical embedded element pattern in a very large array is [2]:

$$G(\theta,\phi) = \frac{4\pi\ A\cos\theta}{N\lambda^2}\left(1 - |\Gamma(\theta,\phi)|^2\right)$$

where:

> A is area of the array
> N is number of elements
> $|\Gamma|$ is magnitude of the reflection coefficient

In dense arrays, $|\Gamma|$ can approach a value of 1, so G can approach zero. Therefore, there is a high risk of scan "blindness" in the array over some angles of scan. This problem has long been recognized and is addressed in the literature. A common solution is use of a wide angle impedance matching (WAIM) sheet of dielectric across the face of the array, usually spaced slightly off the aperture. Chen augmented that solution by including impedance matching dielectric plugs in waveguide elements and irises at the element apertures [3, 4].

Despite extensive coverage of the topic in the literature, there are no generic "design curves" for WAIMs available. Each author developed his own code and verified it by showing examples using a limited range of parameter values. We could find no source that addressed a 70 degree scan angle. Also, WAIM configurations described in the literature were single layer designs and so not particularly suited as array covers for conformal arrays in high performance aircraft. Consequently, we developed our own WAIM design capability, using sources in the literature for guidance. This paper describes the configurations and predicted performance of the WAIMs we designed for these SATCOM terminals.

2.0 APPROACH

Our WAIM design approach was to develop an analysis capability, using literature sources as a starting point; verify the analysis using simple experimental models; and then design the WAIMs for the 20 GHz and 44 GHz SATCOM terminals.

The array configurations for the airborne SATCOM terminals are as follows:
- The elements are in a triangular lattice to minimize their number in a wide angle scanning array.
- Element spacing is $1/\sqrt{3}$ to prevent onset of grating lobes in visible space.
- The elements are dielectrically loaded circular waveguides — the dielectric loading is required to operate the waveguides above cutoff.
- A circular polarizer is contained within each waveguide element.
- The array is covered with a low insertion loss WAIM to prevent scan "blindness" and to protect the array from the environment.

The following WAIM features were included in the code:
- Dielectric plug in the aperture.
- Iris at the aperture.
- Multilayer dielectric cover to provide for:
  * Ultraviolet protective paint.
  * Adhesive between layers.
  * Antistatic, rain erosion layers.
  * Structural layers, (e.g. foam or honeycomb).

3.0 ANALYSIS

Two approaches are used in analyzing large planar scanned arrays with periodic spacing, element-by-element (EBE) and infinite periodic structure (IPS). The EBE approach uses network coupling parameters to cast the solution for element excitation (e.g. currents) in the form

of linear network equations. The order of equations to be solved is equal to the number of array elements. Approximate solutions for large periodically spaced arrays may be obtained by analyzing an infinite periodic structure, the advantage of which is that periodic boundary conditions reduce the computational effort to that of a single unit cell of the array. Although Boeing developed codes for both approaches, the EBE code cannot handle finite WAIM sheets. Therefore, the IPS code was used for WAIM design.

The IPS code calculates the active admittance of an infinite array of waveguides arranged in either a triangular or rectangular lattice. The code is based on the modal approach described by Borgiotti [5]. Active admittance is obtained by expanding the external fields in Floquet modes and the internal fields in waveguide modes. Boundary conditions at the waveguide aperture are used to express intermodal coupling in terms of a grating lobe series. This results in a network model for active admittance, in which the ports are the pertinent waveguide modes for a single array element and the mode-to-mode coupling is provided by the grating lobe series. In its most general application the program treats dielectric-loaded waveguides covered with one or more dielectric sheets. Also the waveguide apertures may contain a metal iris.

The code was exhaustively compared against published data. An example is shown in Figure 2 [4]. Both analytical and measured results by Chen are seen to compare closely to our computed results. The code was also compared to measured pattern data of Tsandoulas & Knittel [6], and Amitay, Galindo & Wu [7], and to predictions of reflection coefficient and active admittance in Diamond [8], and Farrel & Kuhn [9] with equally impressive results.
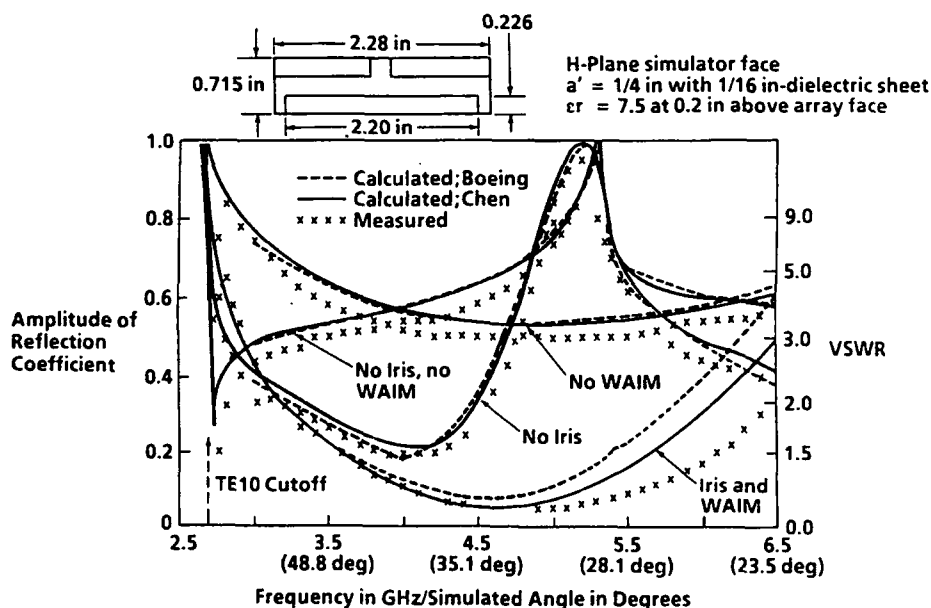
Figure 2. Verification of Boeing Code ITRIWG Against Published Data

Based on the success of these comparisons, we designed a simple WAIM for an array corresponding to the SATCOM configuration. A dielectric constant of 6.0 was used in the design because such material is readily available commercially. Embedded element impedance was computed both with and without the WAIM. The WAIM design was iterated for optimum thickness and spacing off the array.

179

Results are shown in Figure 3. From these it is apparent that, without the WAIM, a serious mismatch occurs in the H-plane direction. This results in a narrow H-plane element pattern and so arrays scanned to wide angles in that plane would be seriously degraded in gain. With the WAIM, spaced 0.066 inches away from the aperture, VSWR of the embedded element is under 2.0:1 in all planes of scan in all but the high end of the frequency band. There, the E-plane VSWR exceeds 3.0:1, but overall a significant performance improvement is predicted. We concluded that a 70 degree scan capability with low reflection loss should be achievable by using a wider range of dielectric constants and multiple layers in the design.

a) No WAIM, 20.7 GHz

b) WAIM, 20.7 GHz

WAIM Parameters

E_r = 6.0
t = 0.015 in
s = 0.066 in

a) No WAIM, 20.7 GHz

b) WAIM, 20.7 GHz
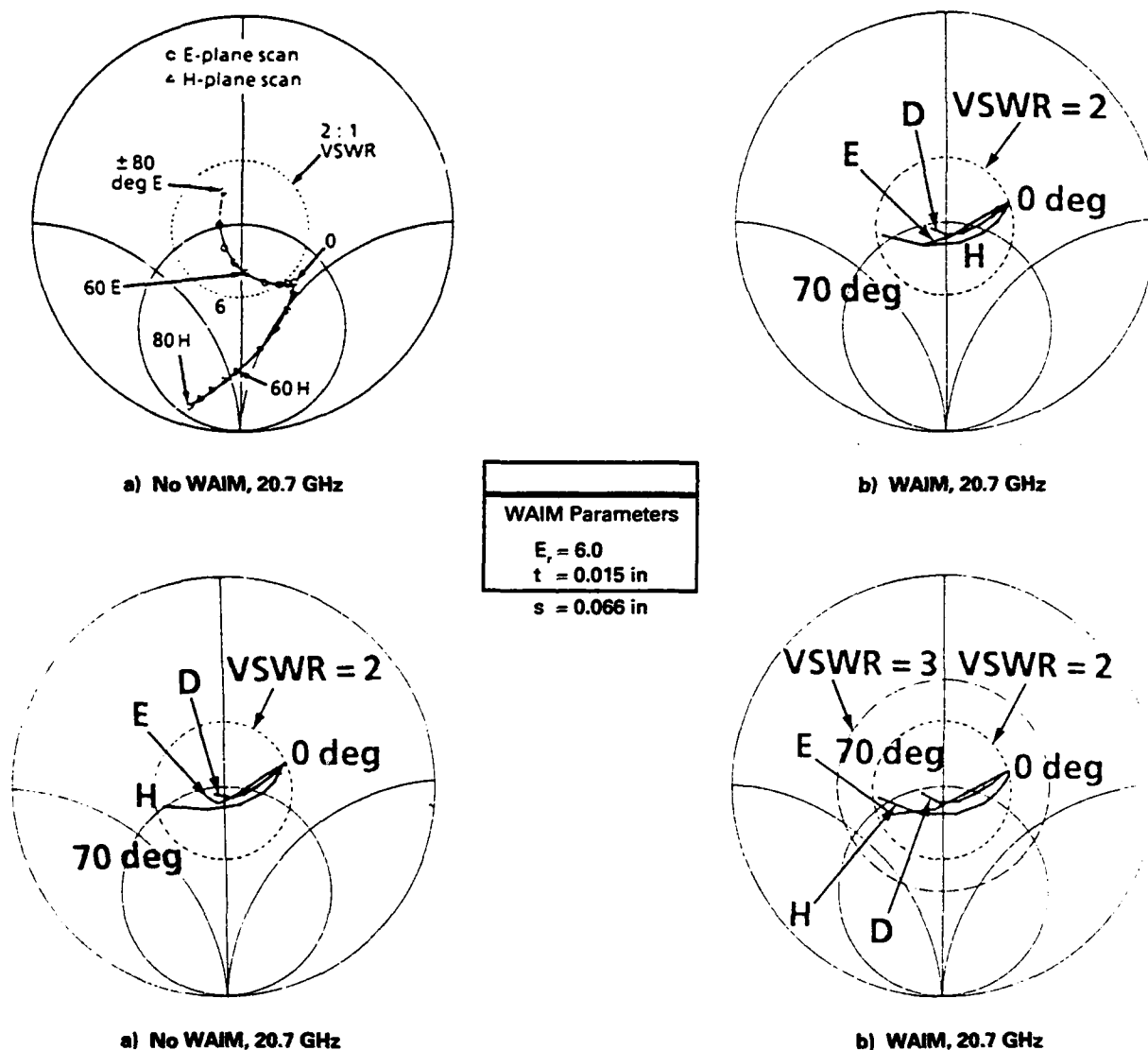
Figure 3. Effects fo Single Sheet WAIM on Element Impedance (Infinite Array)

During the course of this analysis study we determined that neither a dielectric plug nor an iris is needed to match these closely spaced elements. Also, radome designers at Boeing informed us that antistatic and rain erosion layers are unnecessary for top-of-aircraft mounted arrays as long as the normal to their surface exceeds about 70 degrees from the flight path.

4.0 EXPERIMENTAL VERIFICATION

Boeing uses its phased array test bed, a space fed array shown in Figure 4, to evaluate modules, polarizers, WAIMs, beam steering controllers and other components. The test bed geometry is shown in Figure 5. Note that the center 19 elements are actively fed. The outer 3 rings of elements may be used to simulate performance in a large array environment. The 91 element subarray size was selected as a result of comparisons made between active element admittance computed on various sized arrays by the EBE code, and on infinite arrays using the IPS code.
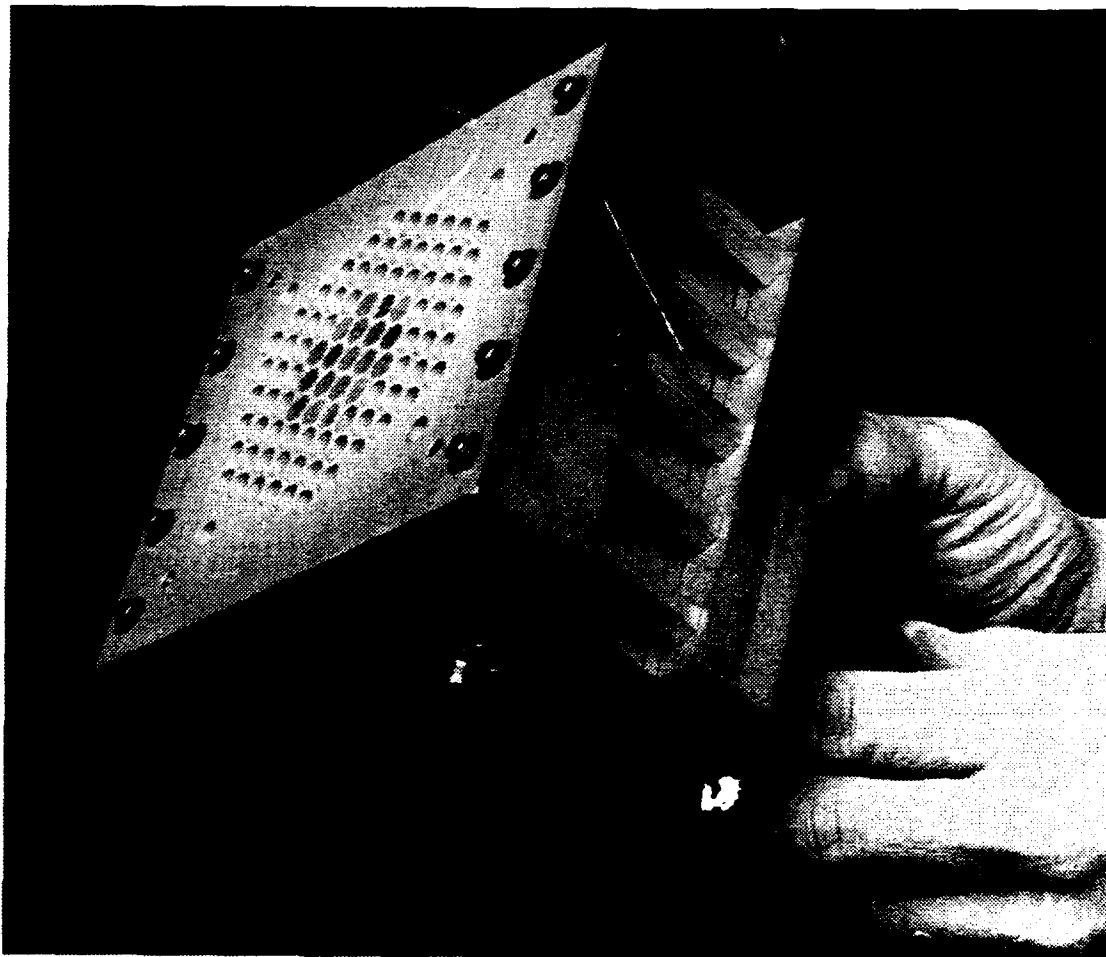
Figure 4. 91-Element Spacefed Subarray Assembled

The following measurements were made to verify the single layer WAIM design: 1) embedded element patterns in both a 19 element and a 91 element configuration, and 2) scanned array patterns using active receiving modules in the center 19 elements. The array was vertically polarized as viewed in Figure 5.
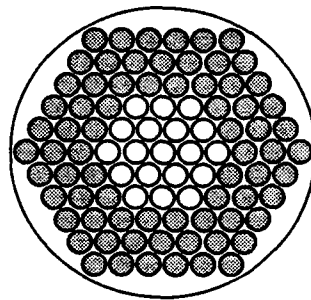
- 91 elements (19 active)
- 11 rows, 11 columns
- Subarray dia.: 3.54 in.
- Waveguide dia.: 0.262 in.
- Spacing
  - Vertical: = 0.2784 in.
  - Horizontal: = 0.3214 in.

⊛ Terminated with matched load
  or covered with ground plane

◯ Active receive or transmit element

Figure 5. 20 GHz Subarray (Testbed) Aperture Geometry

For the embedded element patterns, all the elements except the center one were terminated in a matched load. In the 19 element configuration the outer three rings of elements were covered by a thin ground plane. Measurements were made both with and without the WAIM sheet covering the array. Results are shown in Figures 6 and 7. Note that in each case, significant improvement in wide angle gain in the H-plane pattern was observed with the WAIM in place, thereby verifying predicted WAIM effects. Also, as predicted, there is a slight degradation in E-plane performance with the WAIM in place. This effect increases slightly at higher frequencies.
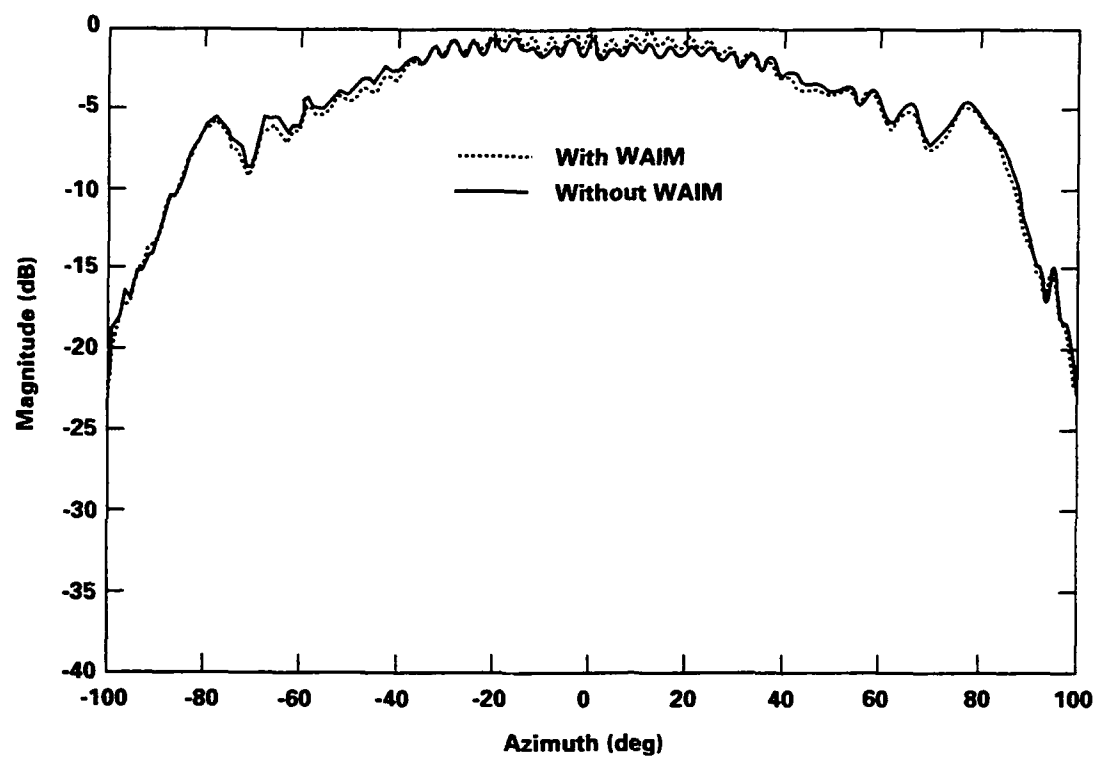
a) E-Plane
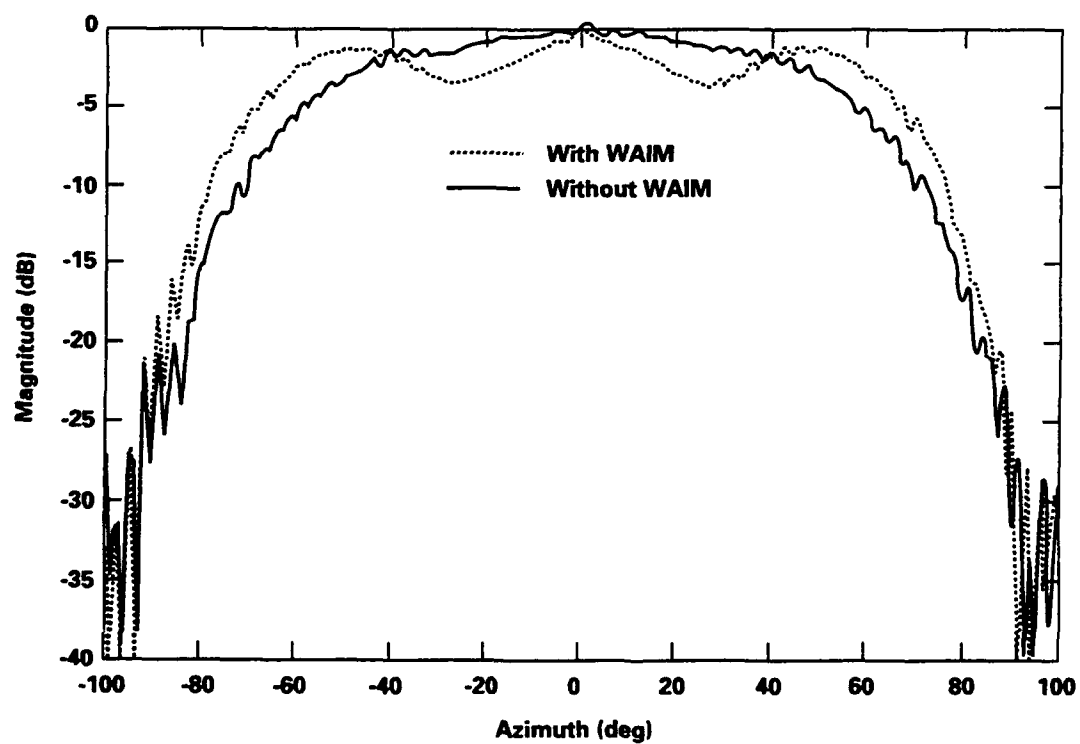
b) H-Plane

Figure 6. Embedded Element Pattern, 19-Element Subarray – 20.7 GHz
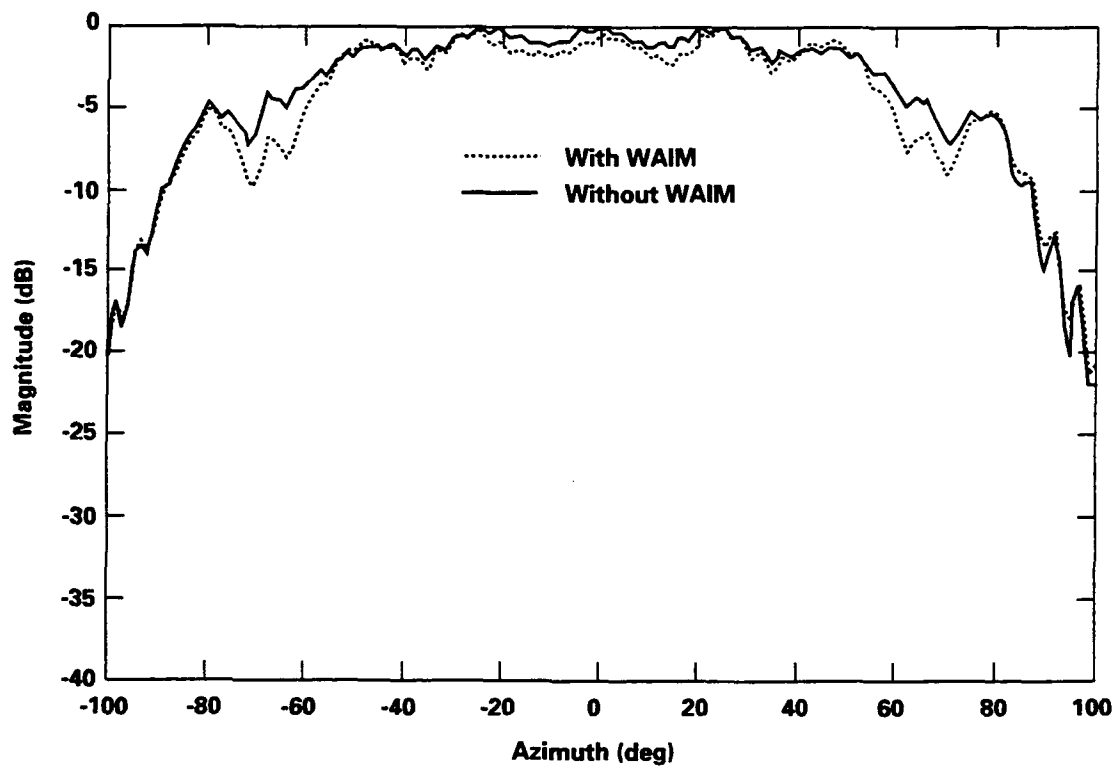
a) E-Plane
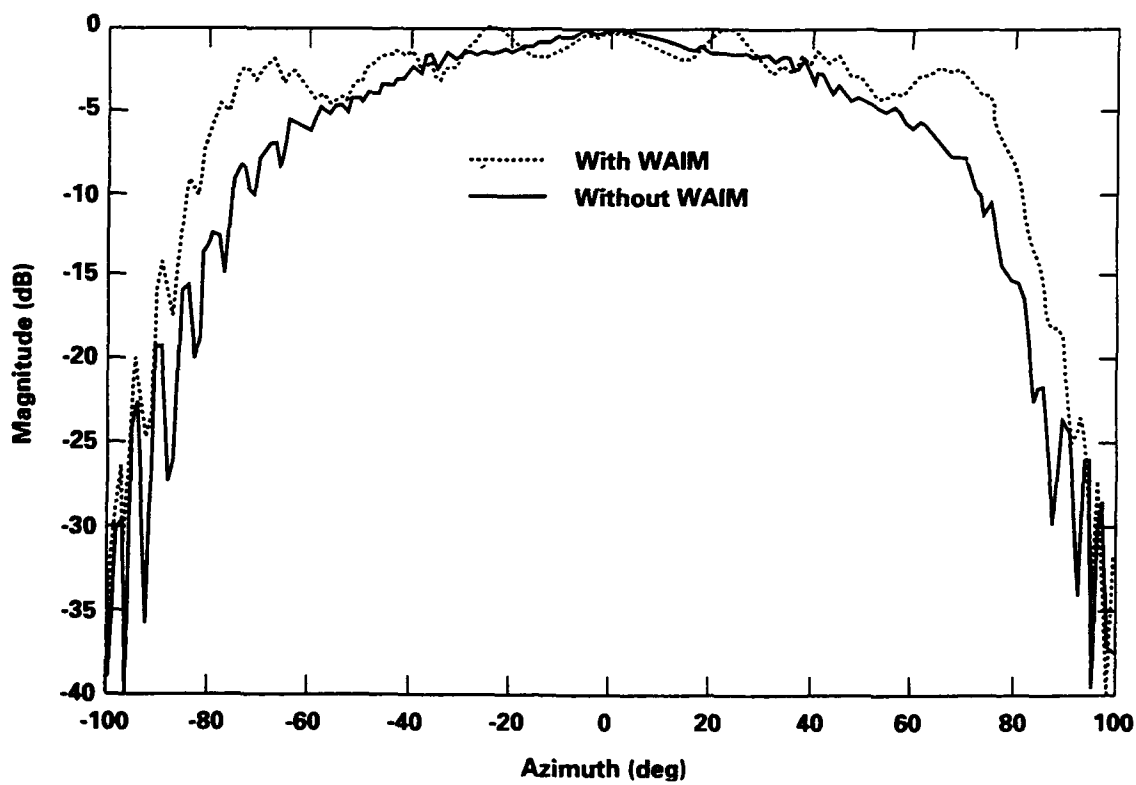
b) H-Plane

Figure 7. Embedded Element Patterns, 91-Element Subarray – 20.7 GHz

H-plane scanned beam performance of the 19 element active array is shown in Figures 8 and 9, Figure 8 without the WAIM and Figure 9 with the WAIM. The improvement in wide angle performance is dramatically evident.
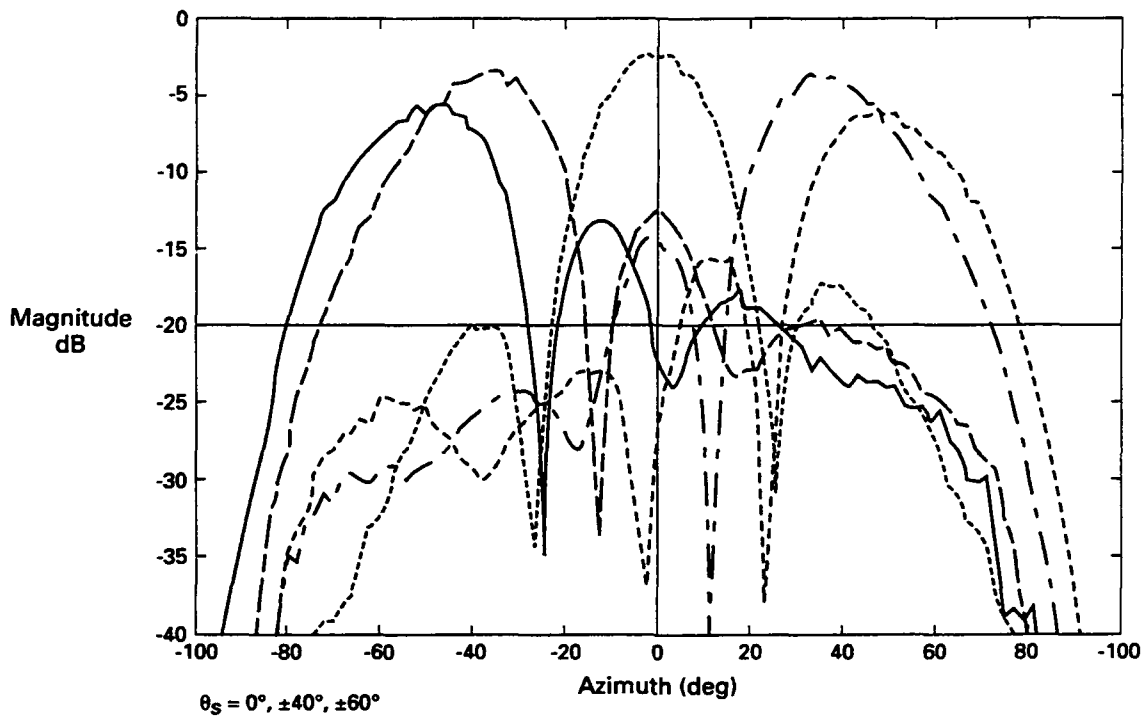
Figure 8. Measured Patterns for Phased-Array Testbed Antenna H-Plane Cut Without WAIM
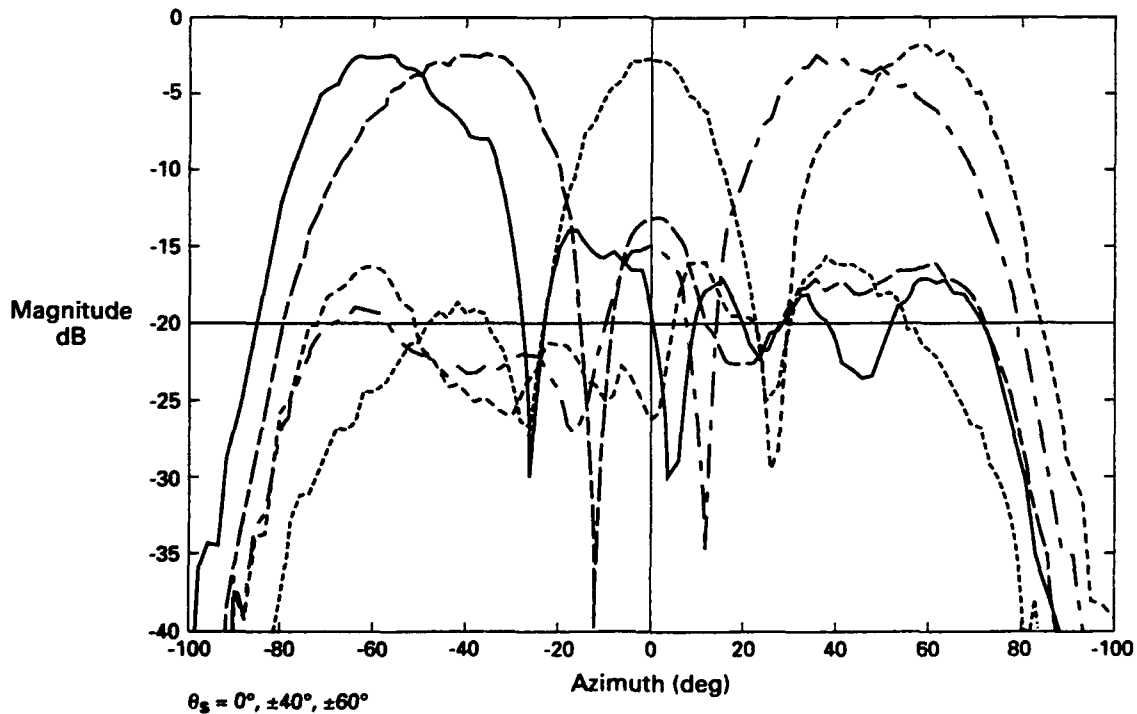
Figure 9. Measured Patterns for Phased-Array Testbed Antenna H-Plane Cut With WAIM

5.0 DESIGN OF SATCOM TERMINAL WAIMs

Equipped with the analysis tools described above, design of the WAIMs for the SATCOM terminals was undertaken under a Rome Laboratories contract [10]. The following features were included in this design activity:

- WAIM dielectric material needed to be structurally and environmentally acceptable for aircraft installations.
- Multiple dielectric layers were acceptable.
- An optimization routine was incorporated in the code to more efficiently converge to a design solution.

The code inputs are:

- array geometry
- polarization (circular)
- scan angle (0 to 70 degrees θ, 360 degrees ϕ)
- maximum VSWR (2.0:1)
- operating frequency
- dielectric constants of the layers.

The code outputs are:

- dielectric thicknesses
- reflection loss versus angle (θ, ϕ, as shown in Figure 10).
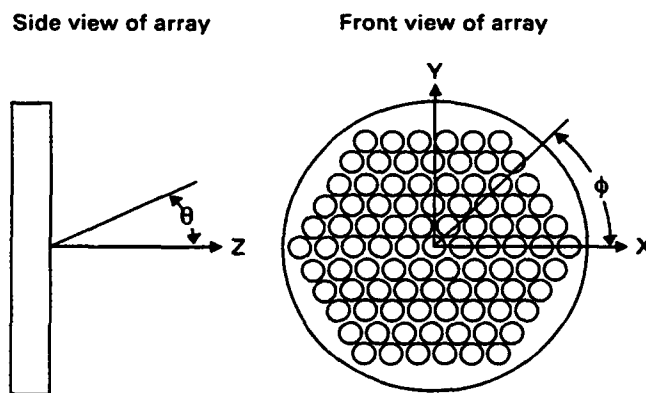
Figure 10. Coordinate System for Array Scan Angles

Figures 11, 12 and 13 show reflection loss of the 20 GHz array over the 5% frequency band with no WAIM present. Losses exceeding 1 dB are predicted at all scan angles greater than about 45 degrees off broadside. The same plots apply to the 44 GHz array since it is simply scaled from the 20 GHz array.

186
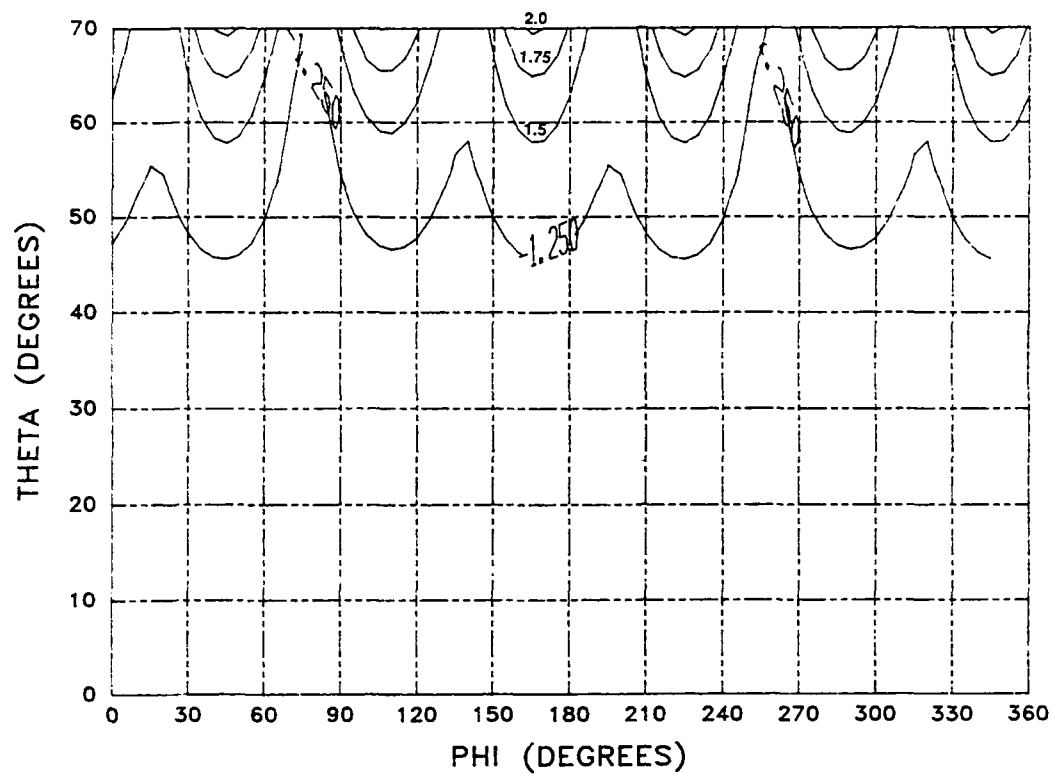
Figure 11. Reflection Loss dB, No WAIM at 20.2 GHz RHCP
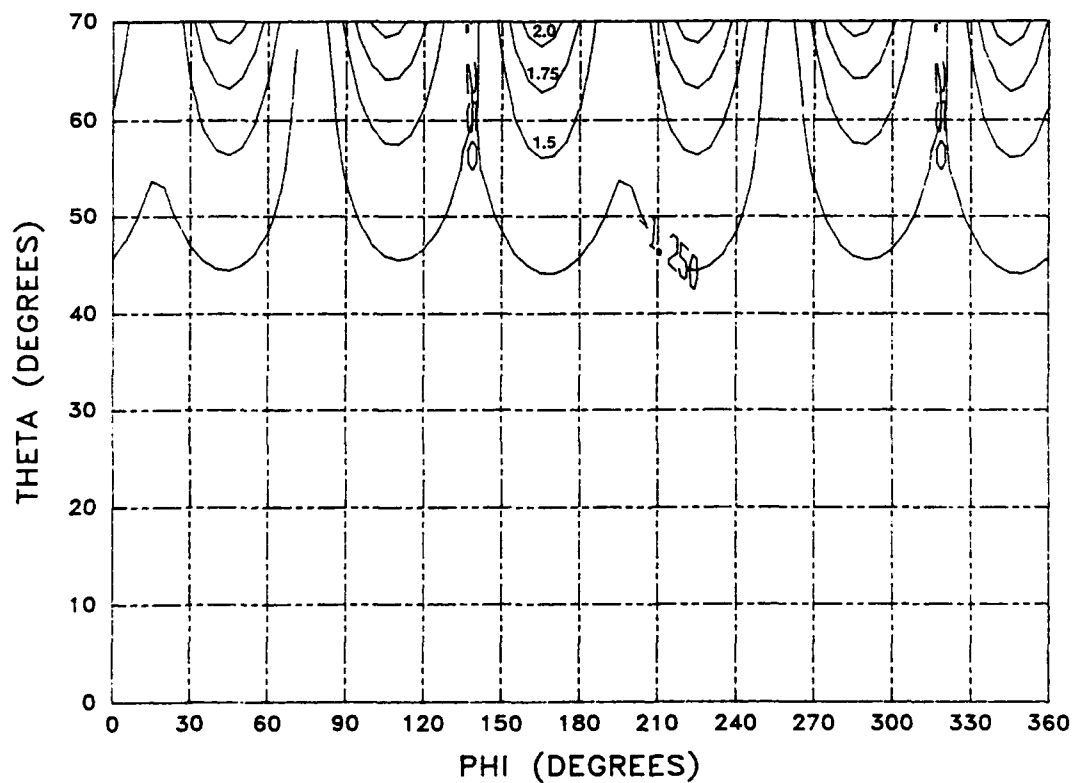
Figure 12. Reflection Loss dB, No WAIM at 20.7 GHz RHCP

187
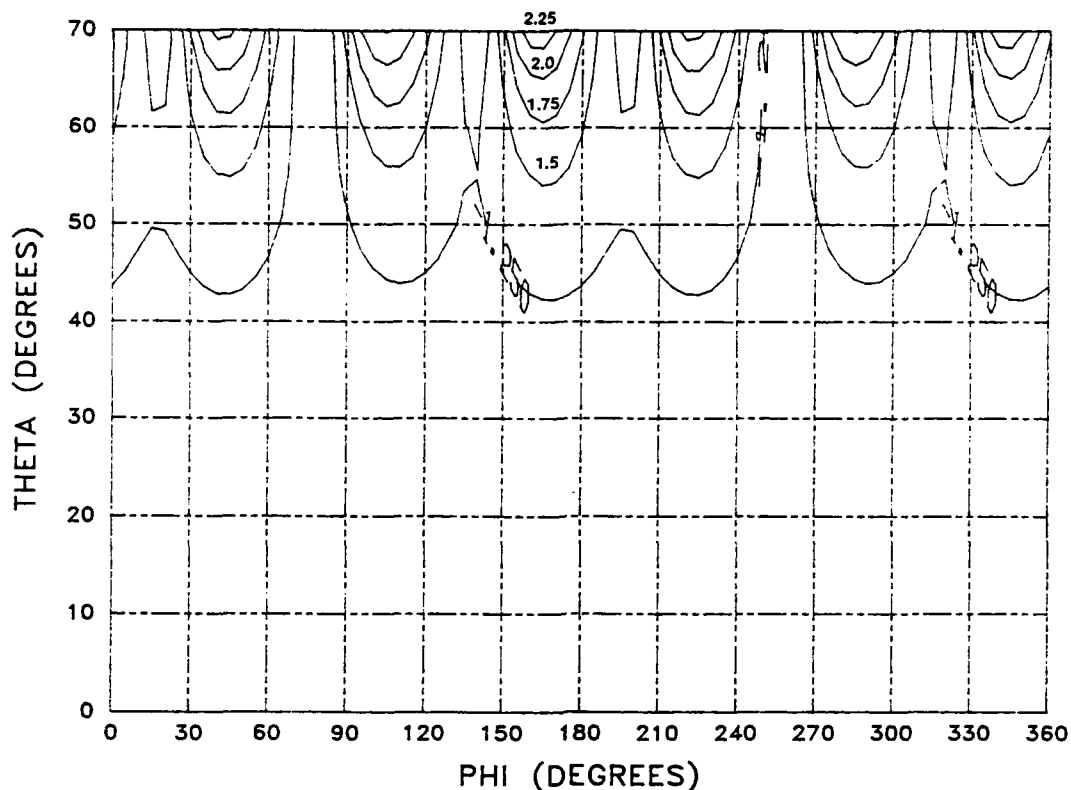
Figure 13. Reflection Loss dB, No WAIM at 21.2 GHz RHCP

WAIM designs derived from the code for the two SATCOM arrays are shown in Figure 14, a different configuration for each band. If the 20 GHz WAIM were simply scaled to 44 GHz, the outer skin would be too thin to provide practical environmental protection. If the 44 GHz WAIM were scaled to 20 GHz, its overall thickness would be excessive.
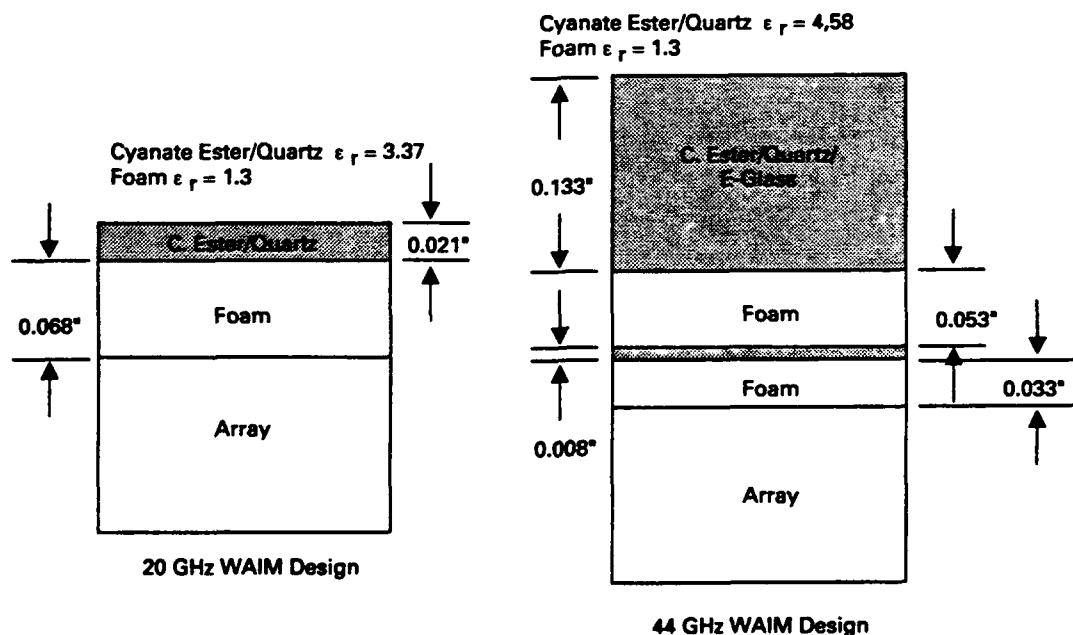
Figure 14. WAIM Configuration Selected by Analysis Program

188

Predicted performance of the 20 GHz array with the 2-layer WAIM specified in Figure 14 is shown in Figures 15, 16 and 17. Note that less than 0.5 dB of reflection loss is predicted to beyond 60 degrees of scan. The reflection loss is less than 1 dB out to 70 degrees of scan except for a small range of angles at the high end of the frequency band.
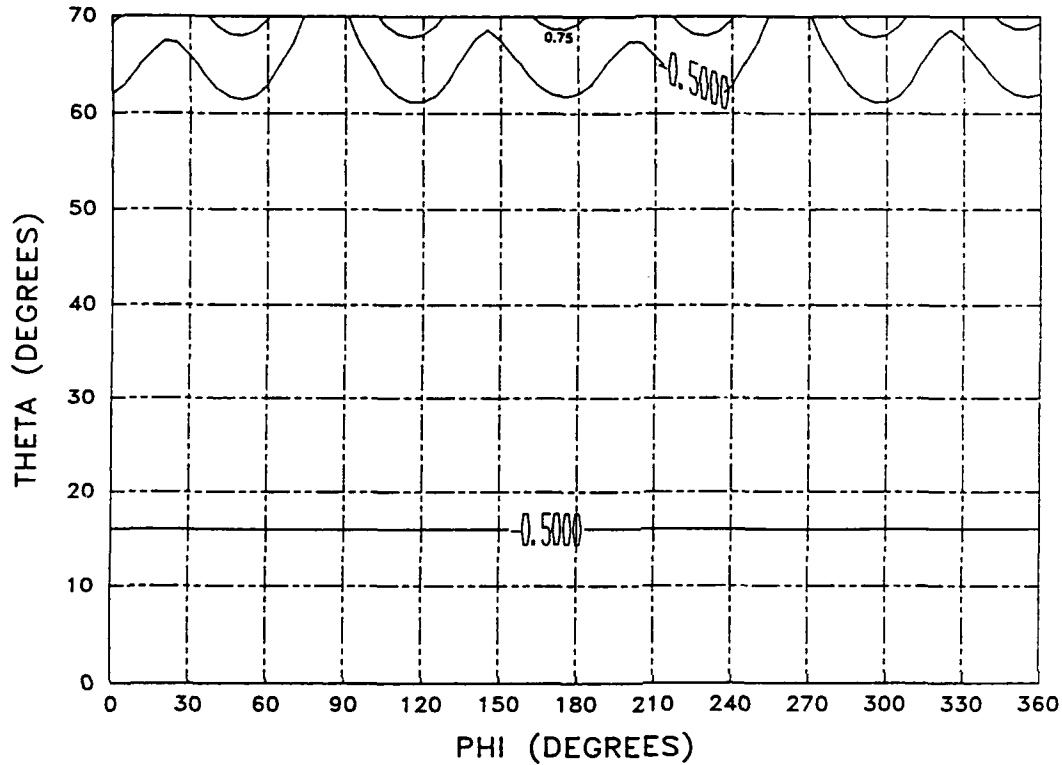
Figure 15. Reflection Loss dB, 2 Layer WAIM, er= 3.37 at 20.2 GHz RHCP
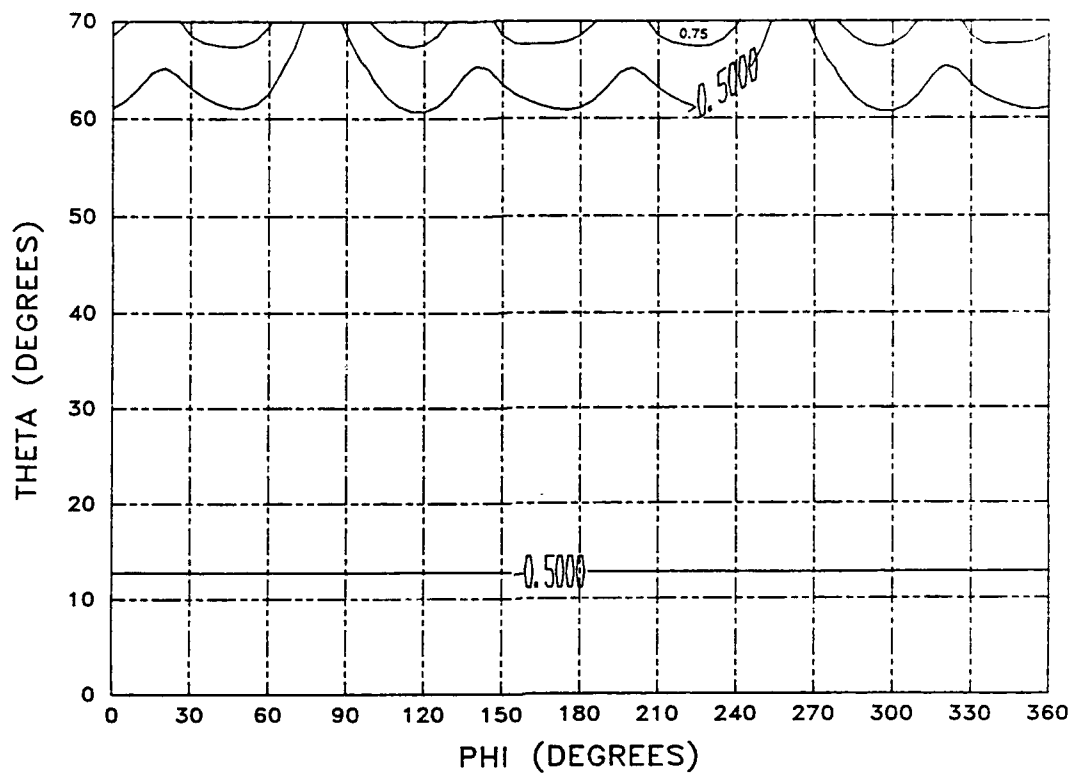
Figure 16. Reflection Loss dB, 2 Layer WAIM, $e_r = 3.37$ at 20.7 GHz RHCP
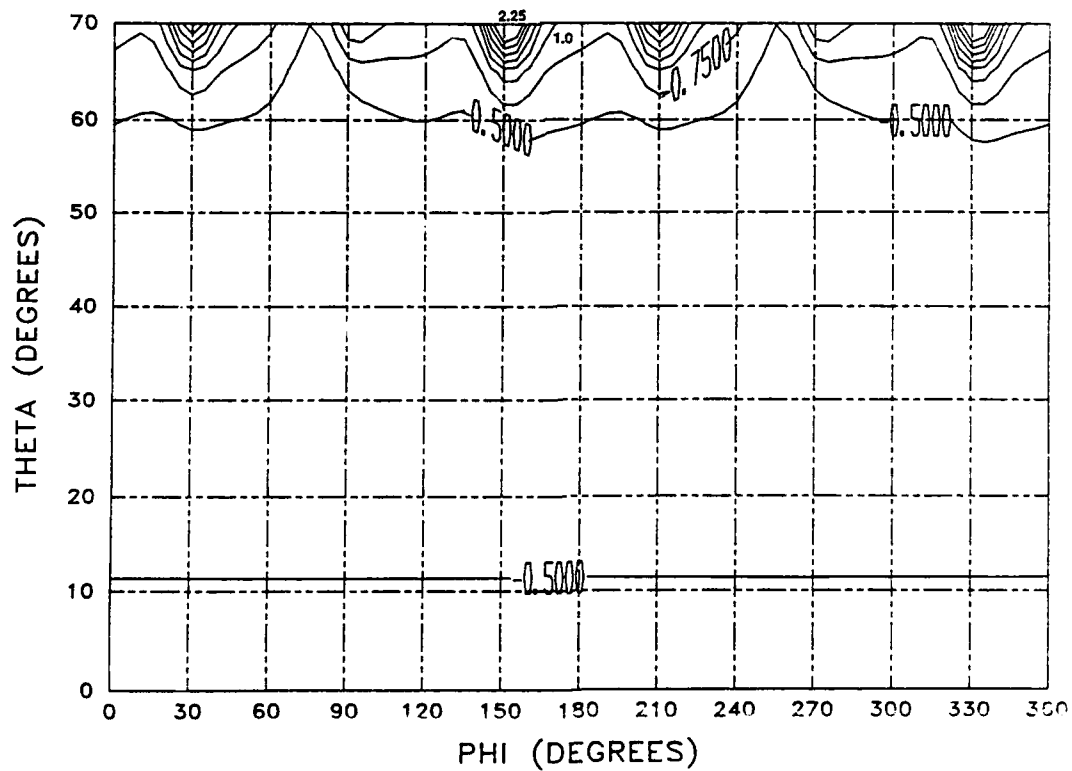
Figure 17. Reflection Loss dB, 2 Layer WAIM, $e_r = 3.37$ at 21.2 GHz RHCP

Predicted performance of the 44 GHz array with the 4-layer WAIM specified in Figure 14 is shown in Figures 18, 19 and 20. Again, less than 0.5 dB of reflection loss is predicted to beyond 60 degrees of scan, and the loss is less than 1 dB out to 70 degrees of scan except for a small range of angles at the high end of the frequency band.
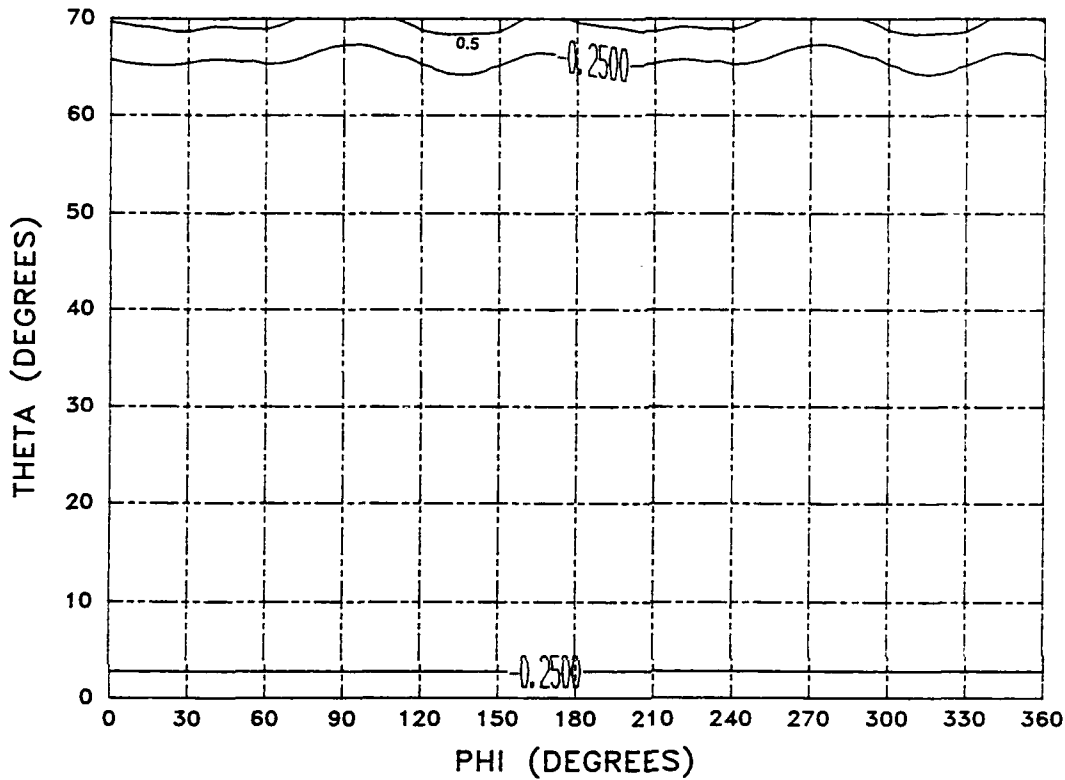
Figure 18. Reflection Loss dB, 4 Layer WAIM, e_r = 4.58 at 43.5 GHz RHCP
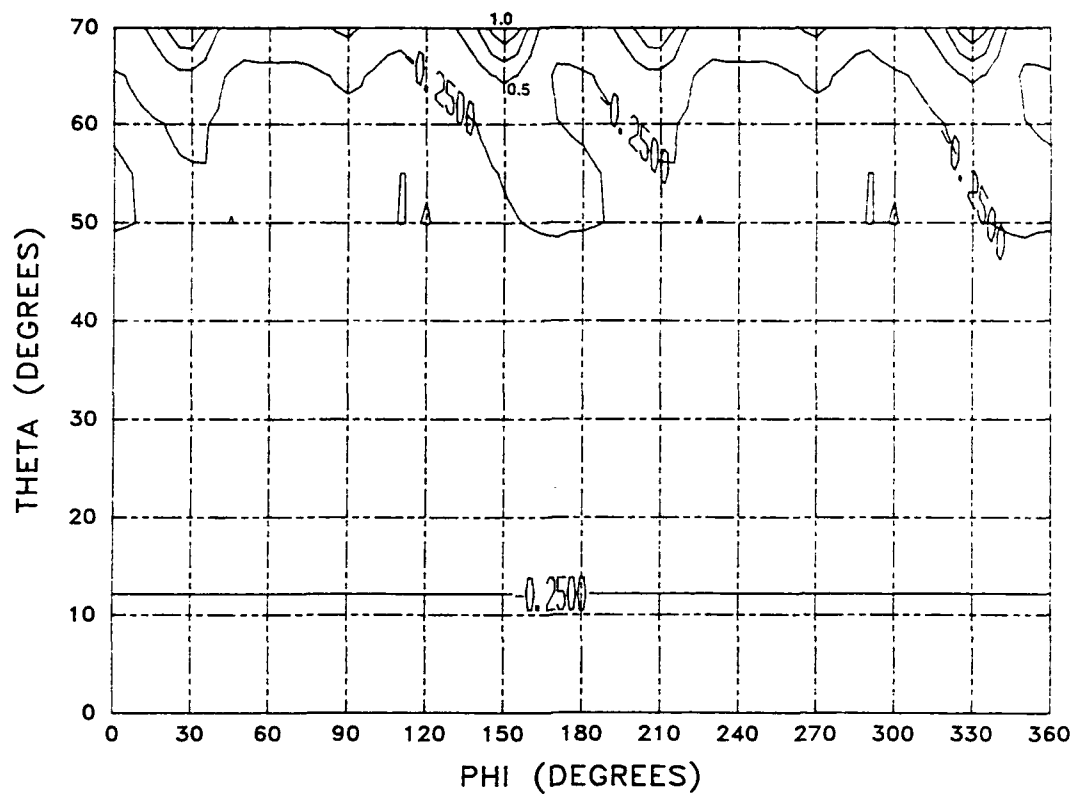
Figure 19. Reflection Loss dB, 4 Layer WAIM, e$_r$ = 4.58 at 44.5 GHz RHCP
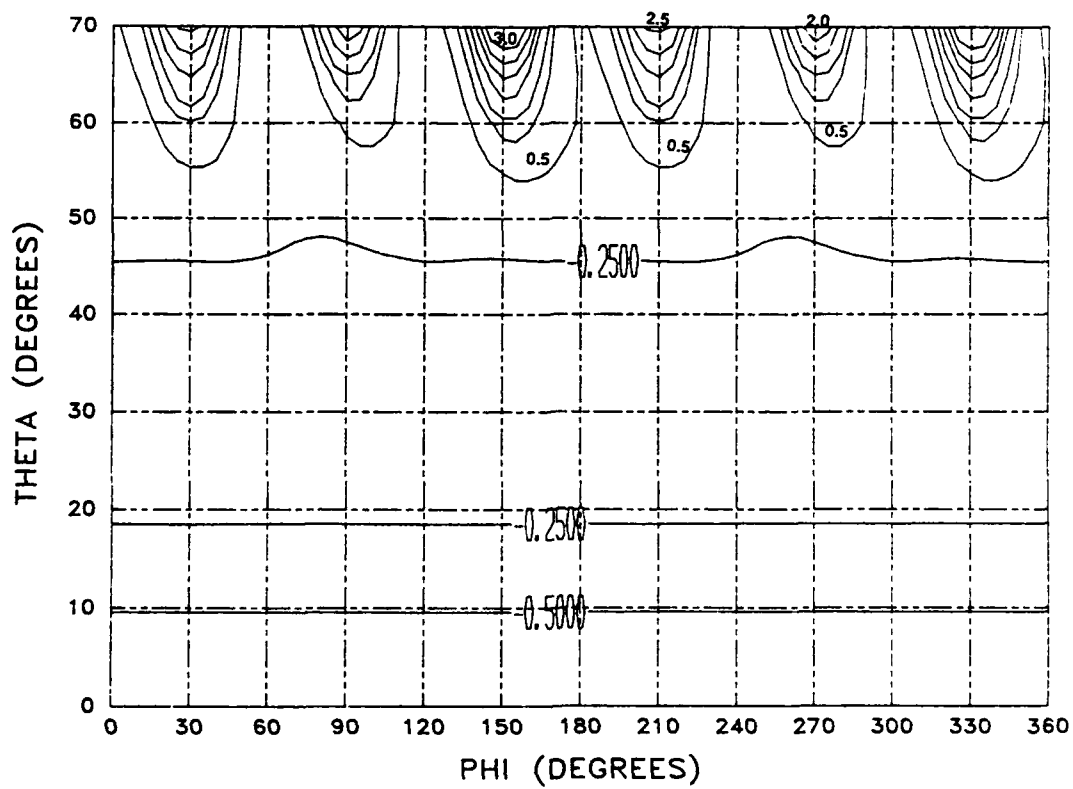
Figure 20. Reflection Loss dB, 4 Layer WAIM, e$_r$ = 4.58 at 45.5 GHz RHCP

A set of WAIMs manufactured to the designs of Figure 14 are shown in the photographs of Figure 21. Physical measurements were made of their as-manufactured dimensions. Then transmission phase was measured to verify dielectric constant values. From these as-manufactured WAIMs, reflection performance was again computed. Results for the mid and upper frequencies are shown in Figures 22 and 23 for the 2-layer, 20 GHz WAIM, and in Figures 24 and 25 for the 4-layer, 44 GHz WAIM. In all cases, as-manufactured WAIM performance compares favorably with that of the theoretical WAIM designs.
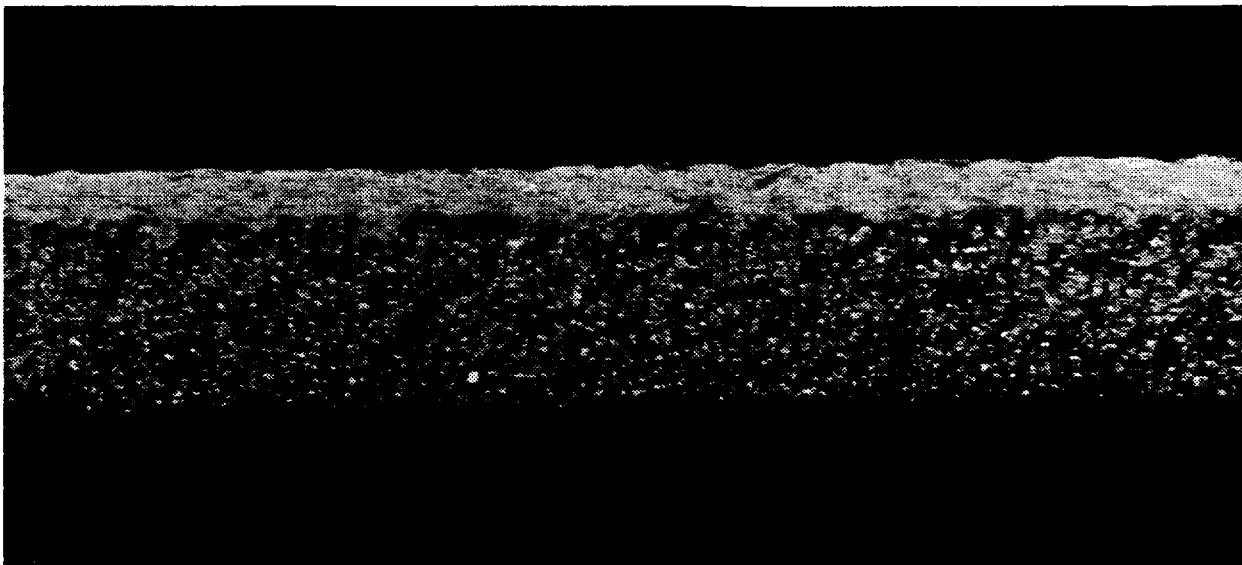
a) 20 GHz – 2 Layer WAIM
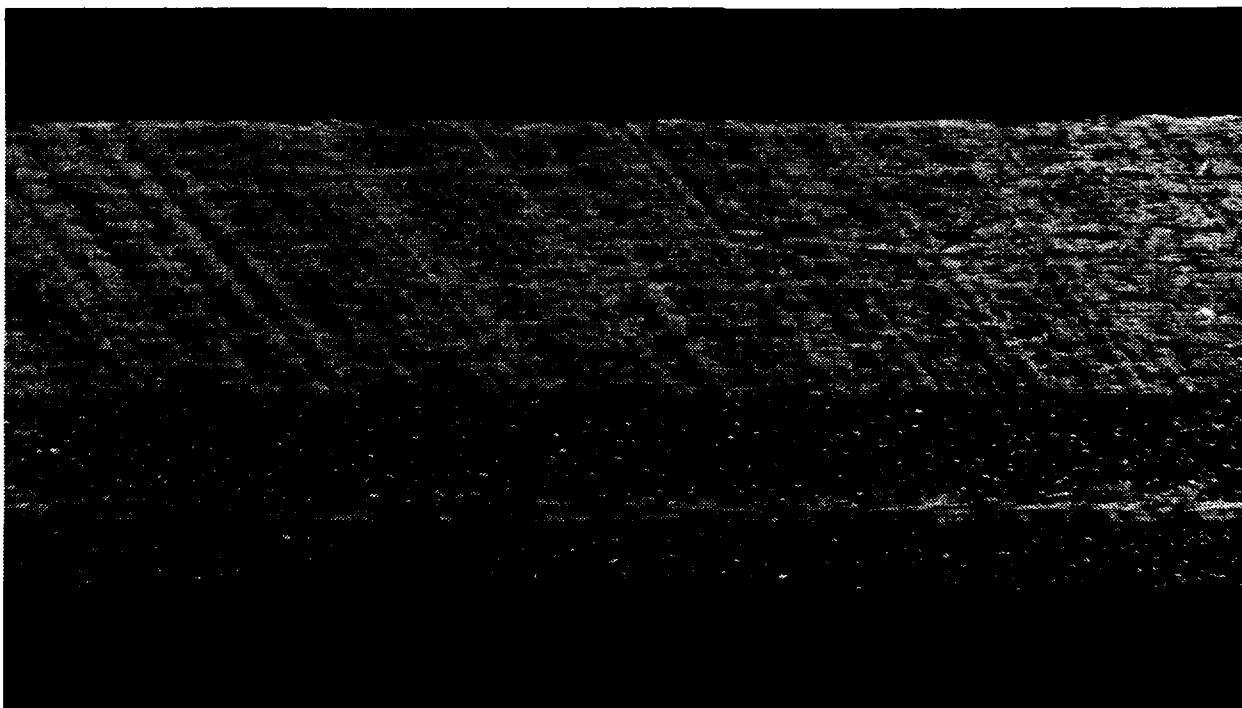
b) 44 GHz – 2 Layer WAIM

Figure 21. WAIMs Sheets Fabricated for SATCOM Terminals
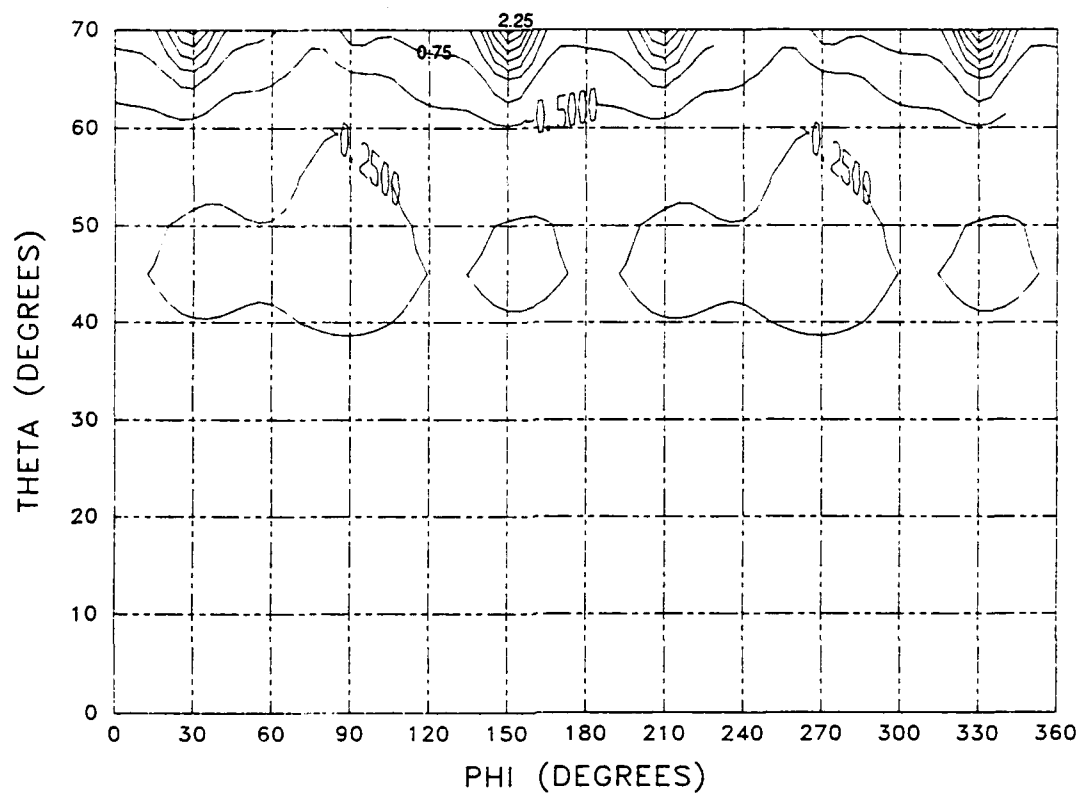
Figure 22. Reflection Loss dB, WAIM as Manufactured at 20.7 GHz RHCP
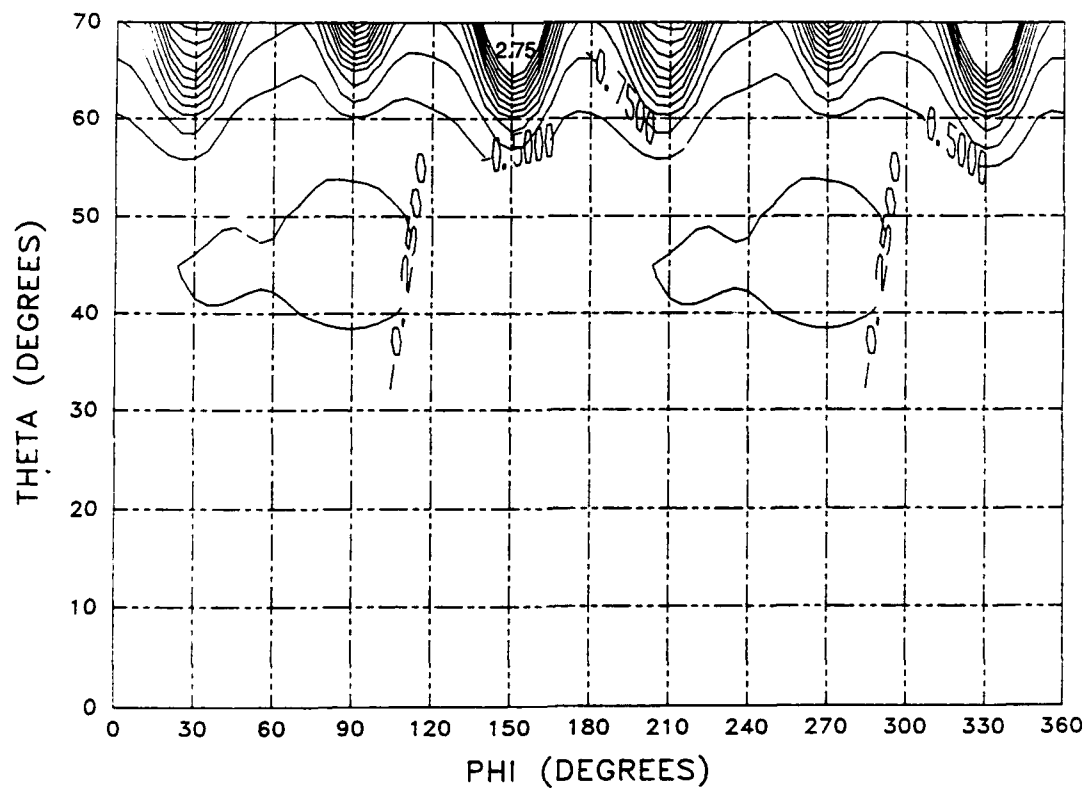
Figure 23. Reflection Loss dB, WAIM as Manufactured at 21.2 GHz RHCP

194
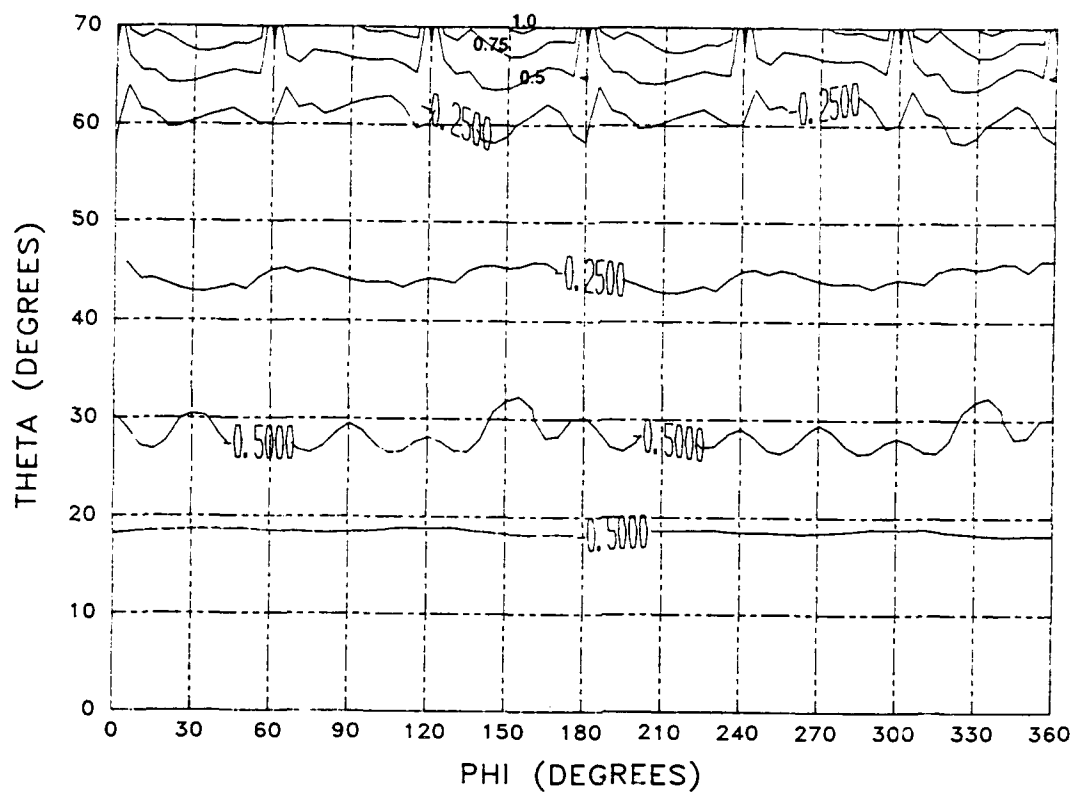
Figure 24. Reflection Loss dB, WAIM as Manufactured at 44.5 GHz
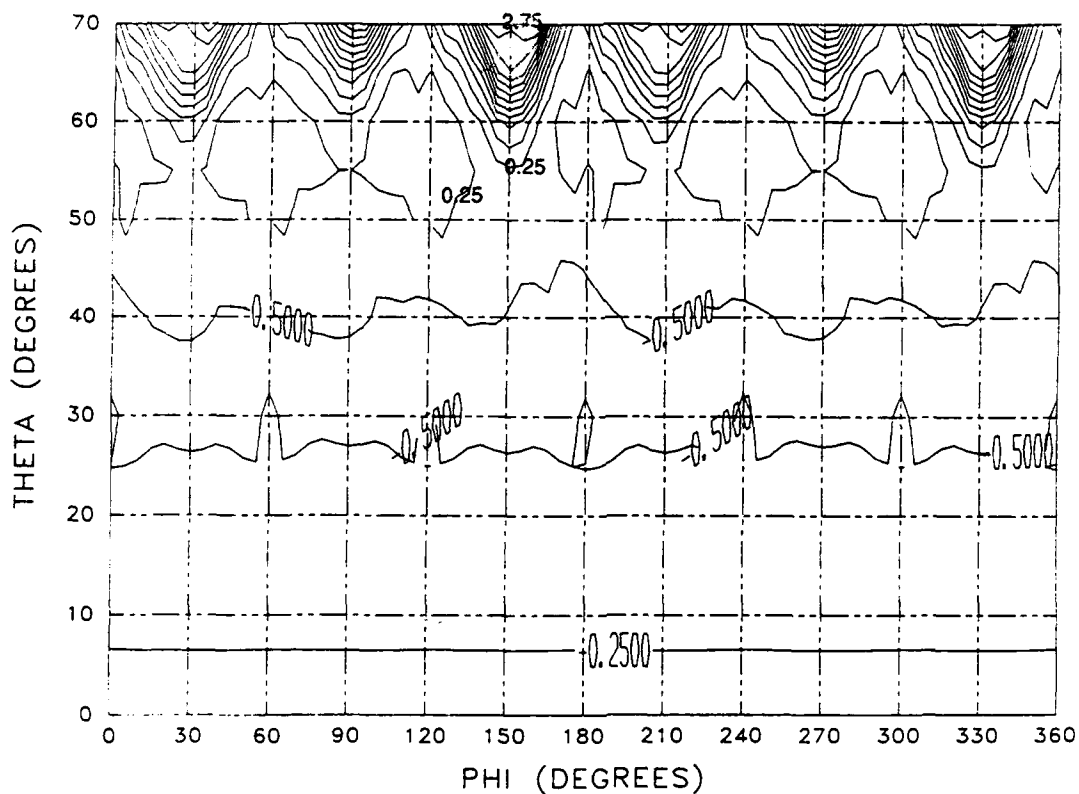
Figure 25. Reflection Loss dB, WAIM as Manufactured at 45.5 GHz

6.0 CONCLUSIONS

The following may be concluded from the work reported on in this paper.
- An analysis tool is available for multilayer WAIM design for EHF phased array antennas.
- Predicted performance shows that wide angle scanning, even out to 70 degrees is achievable.
- Manufacture of WAIMs for EHF phased arrays is practical.
- Theoretical performance will be verified by mutual coupling and pattern measurements on our subarray test bed.

ACKNOWLEDGMENTS

REFERENCES

1. R. C. Hanson, Ed., "Microwave Scanning Antennas", Vol. II, esp. Ch. 3. Peninsula Publishing, 1985.

2. Merrill I. Skolnik, "Radar Handbook", McGraw-Hill, Inc. 1970. p 11-24.

3. Chao-Chun Chen, "Wideband Wide-Angle Impedance Matching and Polarization Characteristics of Circular Waveguide Phased Arrays", IEEE Trans. on Antennas and Propagation, Vol. AP-22, No. 3, May 1974, pp. 414-418.

4. Chao-Chun Chen, "Broad-Band Impedance Matching of Rectangular Waveguide Phased Arrays", IEEE Trans. on Antennas and Propagation, Vol. AP-21, No. 3, May 1973, 298-302.

5. Georgio V. Borgiotti, "Modal Analysis of Periodic Planar Phased Array of Apertures", Proc. IEEE, vol. 56, No. 11, Nov. 1968, pp 1881-1892.

6. G. N. Tsandoulas and G. H. Knittel, "The Analysis and Design of Dual-Poiarization Square-Waveguide Phased Arrays", IEEE Trans. on Antennas and Propagation, Vol. AP-21, No. 11, Nov. 1973, pp. 796-808.

7. N. Amitay, V. Galindo, and C. P. Wu, "Theory and Analysis of Phased Array Antennas", Wiley-Interscience, John Wiley and Sons, New York, 1972, p 208.

8. B. L. Diamond, "A Generalized Approach to the Analysis of Infinite Planar Array Antennas", Proc. IEEE, vol. 56, No. 11, Nov. 1968, pp 1837-1851.

9. G. F. Farrell and D. H. Kuhn, "Mutual Coupling in Infinite Planar Arrays of Rectangular

Waveguide Horns", IEEE Trans. on Antennas and Propagation, Vol. AP-16, No. 7, July 1968, pp. 405-414.

10. "EHF Integrated Circuit Active Phased Arrays," Contract No. F19628-90-C-0168, Boeing Defense & Space Group, Seattle, WA, pp 298-302

Broadband Array Antenna of Dual Flared Notch Elements

W. R. Pickles and J. B. L. Rao

Radar Analysis Branch

Radar Division

Naval Research Laboratory

Washington D.C. 20375-5000

Abstract - An array of dual flared notch elements which has an input VSWR less than 1.6:1 and sidelobes less than -20 dB over a 3/1 bandwidth is described. The dual flared notch element consists of two flared notches paired together in the E-plane. Each flared notch is $\lambda/4$ high at the lowest operating frequency, so the total elevation plane aperture is $\lambda/2$ at the lowest operating frequency. The radiating notches have stripline feeds, and the transition from stripline to notchline is implemented by co-locating a short circuit (current maximum) in the stripline with a high impedance (voltage maximum) in the notch line. Details of the construction of the elements, the array, and the power distribution network are presented. Radiation patterns and impedance plots are presented. Simple design guidelines, and suggestions for extending the bandwidth are given.

1

1. INTRODUCTION:

Recently we were presented with the need to locate several radiating systems spanning a 3/1 bandwidth on a single platform. Size and weight constraints presented significant limitations - using separate antennas for each system was not an attractive alternative. On the other hand, there was enough commonality and flexibility in the specifications for the different systems that we decided a single broadband array was the best choice. Having decided on a broadband array, we ruled out a log periodic element design because of doubts about interelement coupling and power handling capability. Rather, we decided to investigate a flared notch design.

Flared notch antennas have been discussed in the literature for about a decade now. Flared notch technology, however, is not as mature as log periodic technology. The guidelines for designing flared notch antennas are not as specific as the rules for designing log periodic antennas. It was necessary to experimentally investigate flared notch designs, and in this paper we report our findings.

2. SINGLE FLARED NOTCH DESIGNS:

The first flared notch radiator we studied is shown in fig. 1. It had a single air dielectric stripline notch $0.6\lambda_o$ high and a flare length of $0.4\lambda_o$ (λ_o denotes the longest wavelength of the band of operation and f_o the corresponding frequency). The ratio of the length to height roughly matches what Frantz and Mayes[1] recommended for a VSWR of 2:1. The transition from stripline to notchline consisted of crossed stubs with the stripline stub slightly longer than the notch line stub. The width of the notch was determined by assuming the region between the ground planes was

2

199
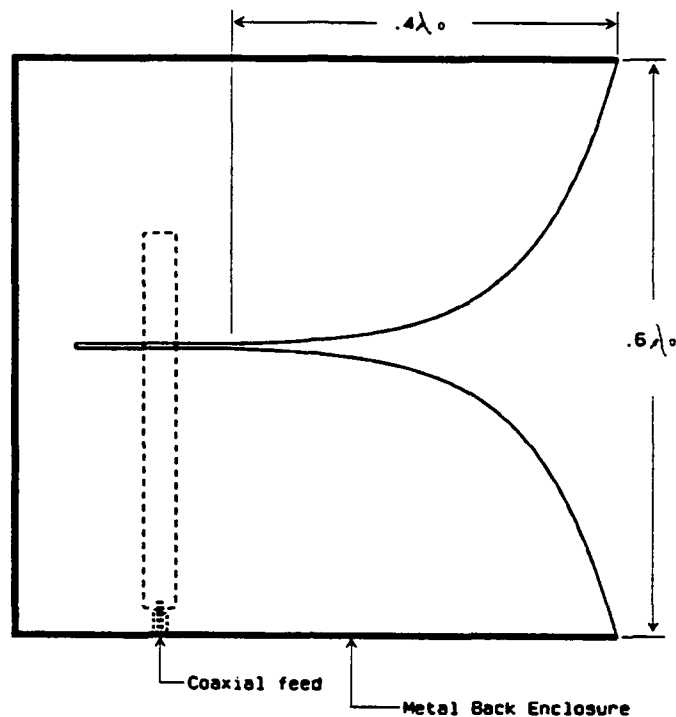
Figure 1 - Profile of first single flared notch element.

solid, then using the method of Hoefer and Burton[2] to determine the gap between

waveguide ridges with the same dimensions. This gave a ridge gap to ridge thickness

ratio of about 0.2. We made our notch width to ground plane spacing ratio the same.

We built an array of nine elements with a center to center spacing of $0.25\lambda_o$ and a

space between elements of $0.225\lambda_o$ (the elements were $0.025\lambda_o$ thick). The array had

a metal enclosure around the top, back and bottom which is shown as a heavy line in

fig. 1. In the experimental set-up, the center 4 elements were driven while the 5

outside elements terminated in 50Ω loads. The measured VSWR was lowest, about

1.1:1, when the stubs were 0.25λ long and degraded at higher and lower frequencies.

We were not able to get the VSWR below 2:1 at both ends of the band simultaneously

3

and the antenna displayed an anomalous decrease in gain and increase in E-plane beamwidth at a frequency of about $2.5f_o$.

The profile of a flared notch resembles the ridges in a ridged waveguide horn. This was the inspiration for a later design which was modeled after Kerr's[3,4] short
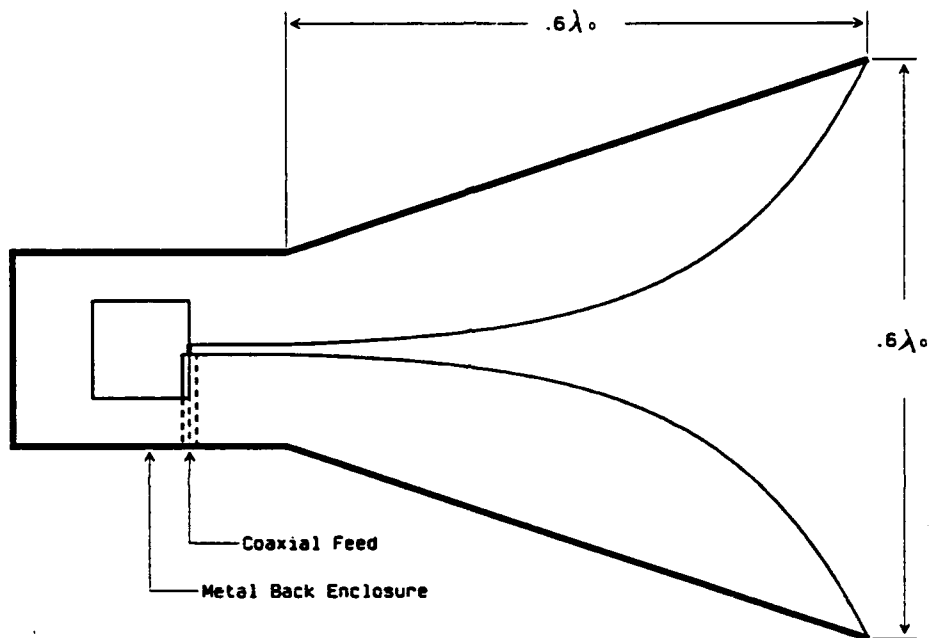
Figure 2 - Profile of Wageguide Ridge Element.

axial length [ridged waveguide] broadband horn. The basic element, shown in fig. 2, had an E-plane aperture the same height as the first antenna, $0.6\lambda_o$. The other dimensions were roughly scaled from Kerr's design. We tested the waveguide ridge design in two different arrays of 12 elements with the center 4 driven, the others terminated with 50Ω loads and metal enclosures around the outside contour of the ridges. The first array had a center to center element spacing of $0.25\lambda_o$ and a corresponding space between elements of $0.2\lambda_o$. It also displayed anomalous behavior

4

at a frequency a little above $2.5f_o$. However, it was more pronounced than with the first flared notch design. Then we built a second array with a center to center element spacing of $0.2\lambda_o$, and a corresponding space between elements of $0.15\lambda_o$. The anomalous behavior moved to a frequency just above the band of interest. The sidelobes were below 15 dB and the VSWR was under 2:1 across the desired 3/1 bandwidth (in fact the VSWR was below 2:1 across a 6/1 bandwidth because the waveguide ridge antenna was well matched at frequencies down to $f_o/2$). The waveguide ridge antenna was too large for the space requirement we were trying to meet, but it gave us some clues which were the turning point in our study: (1) The input transition of the waveguide ridges produced a good match over a broader frequency band than crossed stubs, and (2) some sort of resonance occurs when the space between elements is on the order of a half wavelength.

3.   DUAL FLARED NOTCH DESIGNS:

Povinelli[5] described a flared notch array in which the individual radiators were smaller than $0.5\lambda_o$. This was a motivation for our dual flared notch design which consisted of two flared notches arrayed together in the E-plane. The profile of the first dual flared notch antenna we built is shown in fig. 3. Each flare was $.3\lambda_o$ high and $.2\lambda_o$ long which retained the length to height ratio of our first single flared notch design. The flared notches are fed by a common 50Ω input strip line which splits into two 100Ω strip lines. We determined the 100Ω notch width the same way as discussed above and calculated that it should be about 80 percent of the ground

5
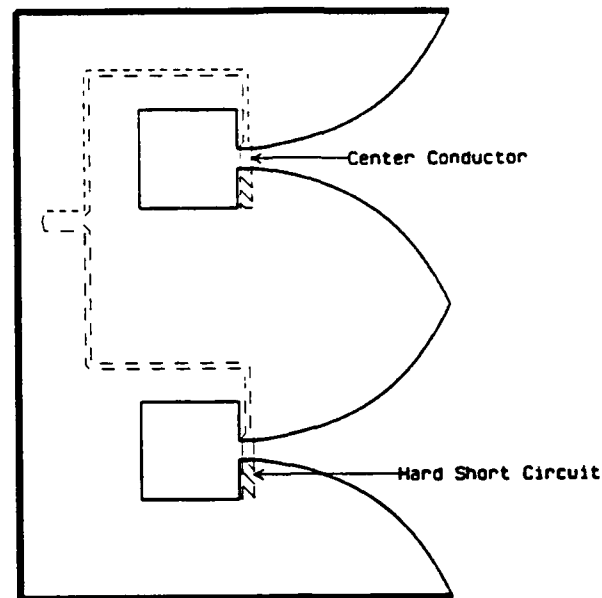
Figure 3 - Profile of first dual flared notch element.

plane spacing.

The stripline to notchline transition is modeled after the coaxial line to ridge transition presented above. The 100Ω striplines are terminated in short circuits immediately after crossing the notchline and the notchline is terminated in a high impedance loop immediately behind the stripline crossing point. This configuration co-locates a magnetic field maximum on the stripline with an electric field maximum on the notchline. This should provide broader band coupling than the crossed stubs because the position of the current maximum on the stripline does not change with frequency. The same may not be exactly true with the position of the voltage maximum on the notchline, but we still obtained better results than with the crossed stubs combination.

6

As with previous designs, this antenna was tested in a 12 element array with the 4 center elements driven and the others terminated in 50Ω loads. The VSWR of this antenna was under 2.3:1 and the E-plane sidelobes were below -13.5 dB across the 3/1 frequency band. Even though the waveguide ridge design performed better, the depth of the dual flared notch design was considerably less than any previous design. This was the motivation for further study of this design. The bandwidth requirement was reduced from 3/1 to 2.67/1 for the continued study.
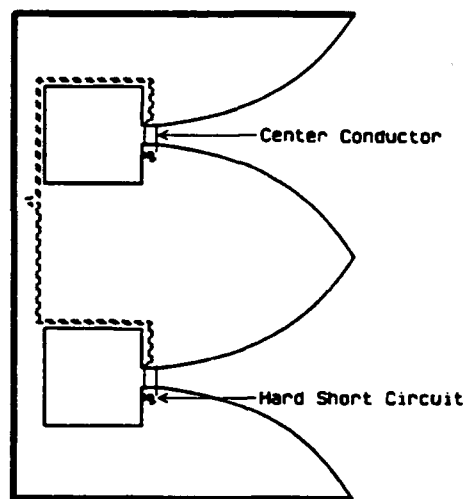
Figure 4 - Profile of Dual Flared Notch Element with reduced height and depth.

The next dual flared notch design, shown in fig. 4 had both a reduced height and depth. The height of each flare was reduced to $0.25\lambda_o$ while the length was kept at $0.2\lambda_o$. The space behind the high impedance notch lines was reduced to the absolute minimum into which we could fit the stripline power splitter. The VSWR of

7

this design was 4:1 at f_o. Obviously the length of the region behind the high impedance loop was important.
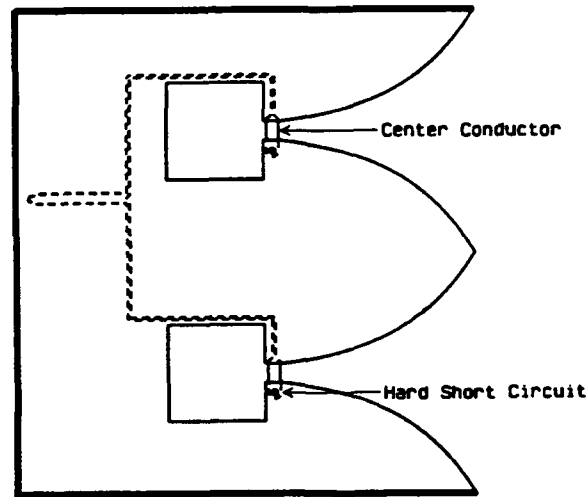
Figure 5 - Profile of Dual Flared Notch Element with reduced height and elongated depth. Our final design.

We increased the space between the notch line high impedance loops and the back wall of the antenna until we arrived at the design shown in fig 5. Increasing the length further did not improve the VSWR at f_o. The dual flared notch element with an elongated back section was tested in a 28 element array with a center to center spacing of $0.2\lambda_o$ and a space between elements of $0.175\lambda_o$. As with previous designs, the elements were enclosed in a metal box which followed the outside contour of the elements and was open at the radiating aperture. The VSWR of the dual flared notch with an elongated back section, measured in an array environment, is shown in fig. 6. and the E-plane radiation patterns are shown in fig. 7. The sharp rise in VSWR at

8

205
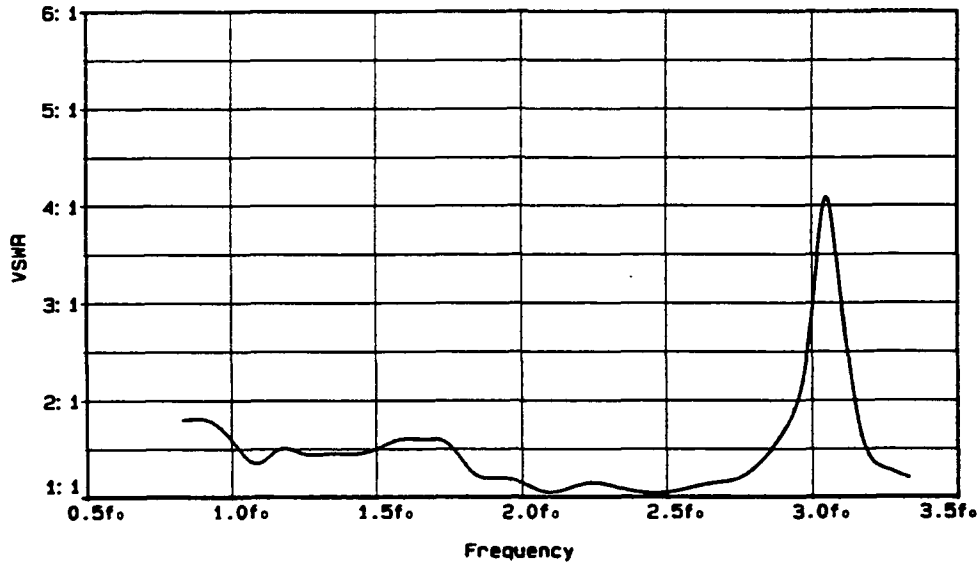
Figure 6 - VSWR of an array of Dual Flared Notch Elements.

$3.1f_o$ corresponds to the same anomalous behavior observed in earlier models. In

fig. 8 the measured gain of the 28 element array is compared with the calculated gain

for a Taylor 25 dB, $\bar{n}=3$ amplitude distribution in the H-plane and a uniform

distribution in the E-plane. Figure 9 shows a comparison of the measured E- plane

beamwidth with the beamwidth of a uniform E-plane distribution. The gain and

beamwidth calculations were made with reference to the complete pattern expression[6]

$$F(\theta) = \left[\frac{\sin[(\pi L/\lambda)\cos\theta]}{(\pi L/\lambda)\cos\theta} \right] \sin\theta \tag{1}$$

$(\theta = 90° \; represents \; broadside)$

which accounts for the E-plane pattern factor of a differential current element. The

9
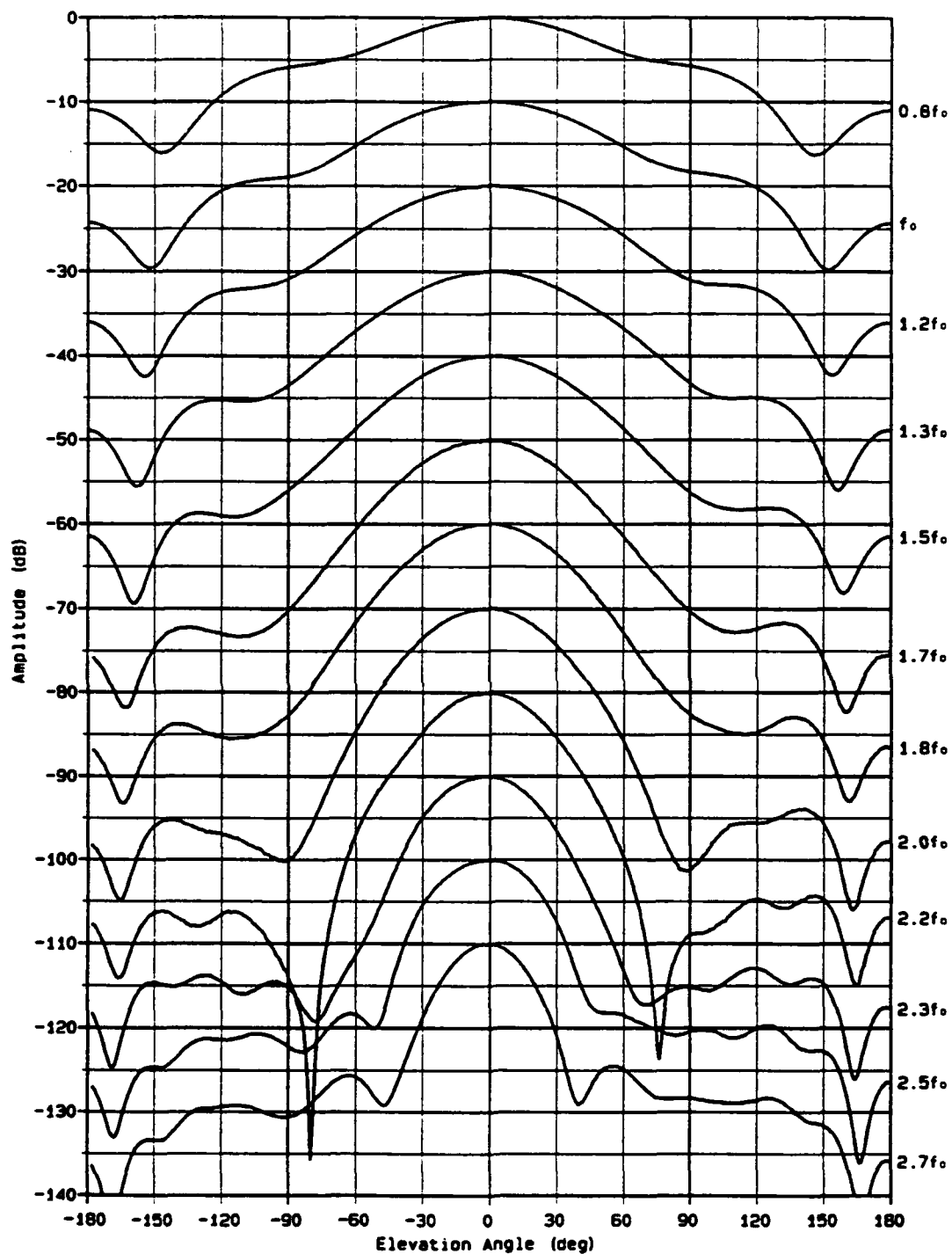
Figure 7 - E-plane radiation patterns of an array of Dual Flared Notch Elements with reduce height and extended depth.

10
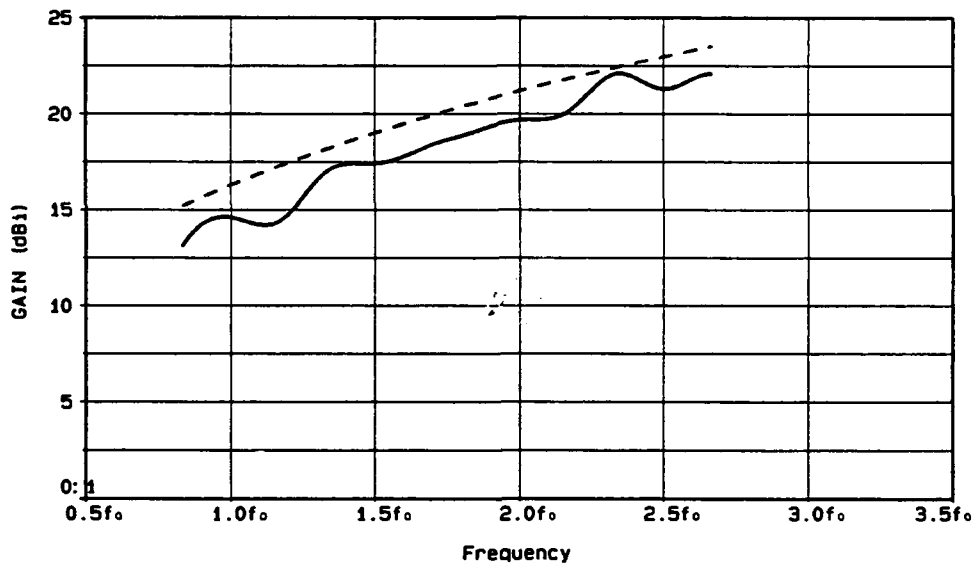
Figure 8 - Measured gain (solid line) of a 28 element array of Dual Flared Notches with reduced height and extended depth compared with the calculated gain (dashed line).

differential element pattern factor can be ignored for E-plane aperture distributions longer than 2λ but if it is not taken into account here the calculated gains and E-plane radiation patterns are too low and too wide respectively.

The measured gain compares favorably with the calculated gain. It is typically about 2 dB below the calculated gain. When the losses of the power divider are factored in, the measured gain is within a dB of theoretical predictions.

The H-plane radiation patterns are shown in fig. 10. With the exception of a measurement anomaly at f_o, the side lobe level is well below 20 dB across the band. This is largely a function of the power distribution network which is discussed below.

11
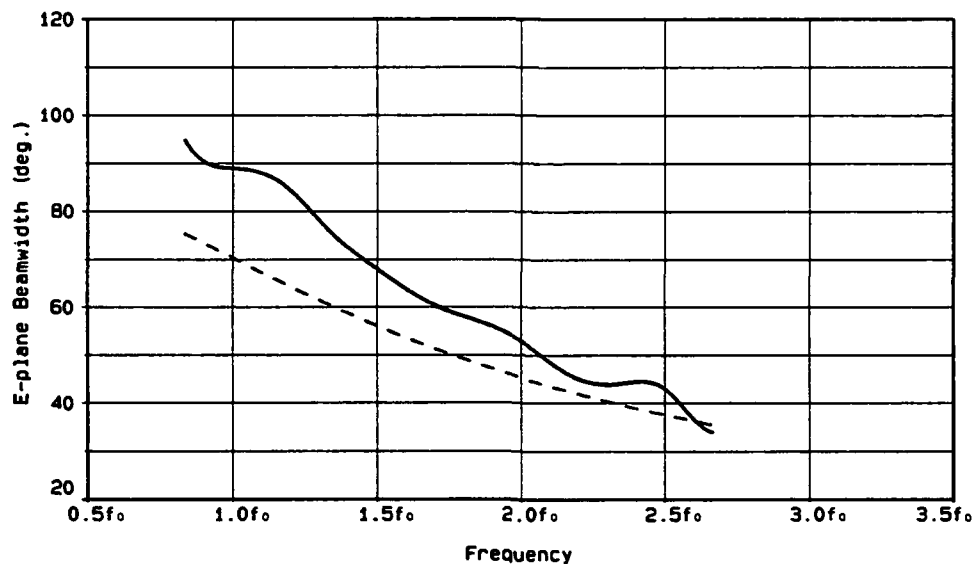
Figure 9 - Measured E-plane beamwidth (solid) of Dual Flared Notch elements with reduced height compared with calculated beamwidth (dashed) for same size aperture.

4.   POWER DISTRIBUTION NETWORK:

The power distribution network we built for the prototype antenna

implemented a 25 dB Taylor, $\bar{n}=3$ amplitude taper[7]. We built the power distribution

network using stripline with styrofoam dielectric. Use of styrofoam dielectric was a

key factor in the light weight and low electrical losses which were achieved.

Polystyrene foam has a loss tangent about an order of magnitude less than teflon[8] and

it weighs next to nothing. The power distribution network was produced in two

mirror image halves, each feeding 14 elements. A schematic of one half of the

power distribution network is shown in Figure 11. The schematic is broken up into

three regions which correspond to the three layers of the power divider; the input
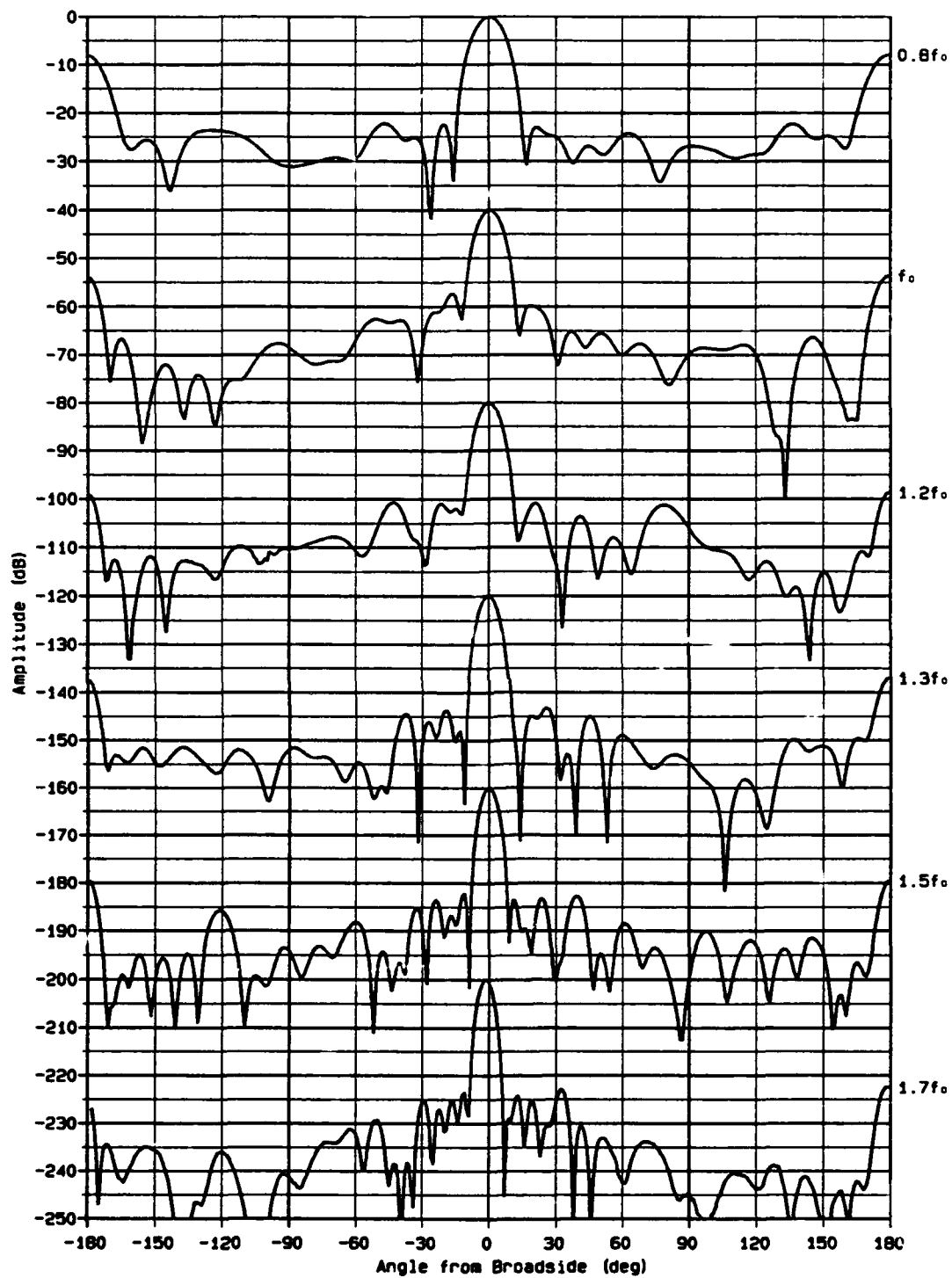
12

Figure 10 - H-plane radiation patterns of 28 element array of Dual Flared Notches with reduced height and extended depth.

13

Figure 10 - H-plane radiation patterns of 28 element array of Dual Flared Notches with reduced height and extended depth.

14

211
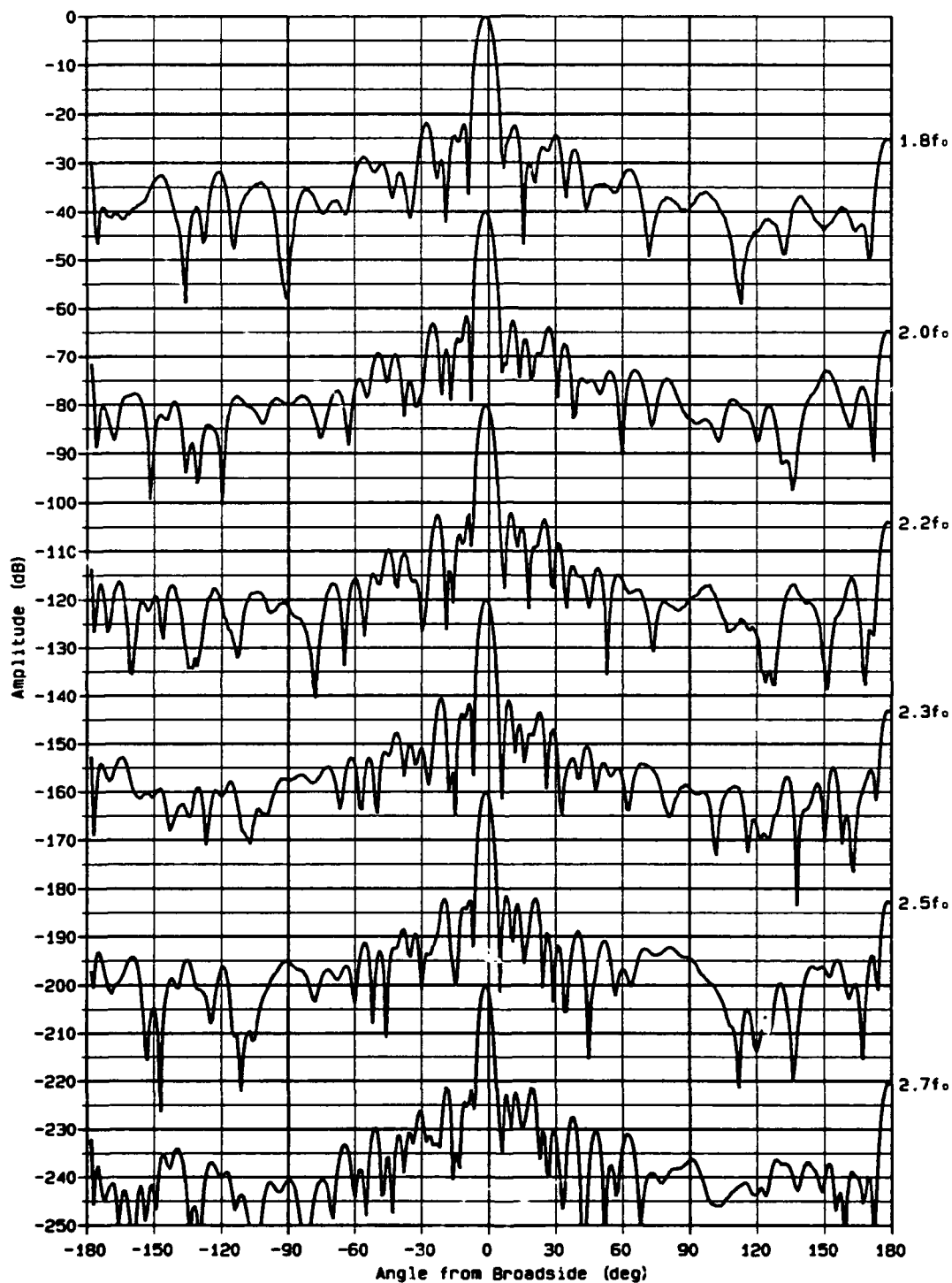
layer, the output layer, and the phase equalization layer. Also shown on the schematic are the calculated power levels relative to the input at each node. The nodes between the phase equalization section and the output layer also show measured power levels at mid band. These nodes are at points about 90% of the path length through the power divider so the losses for the entire power divider are about 1.3 dB.

The power divider was constructed in three layers shown in fig. 12. Figure 12 shows the 3 layers in the same order they are located in the antenna. The phase equalization layer is located in the outside layer, the input layer is located in the center layer, and the output layer is located closest to the radiating elements. Electrically, the phase equalization layer is between the input and output layers. The reason for this arrangement is that it was desirable to have the phase equalization layer on the outside so that a minimum of disassembly was required to adjust the phase equalization sections.

15

Figure 11 - Schematic diagram of one half of 28 element power distribution network which produces a Taylor 25 dB, ñ=3 amplitude taper.

213
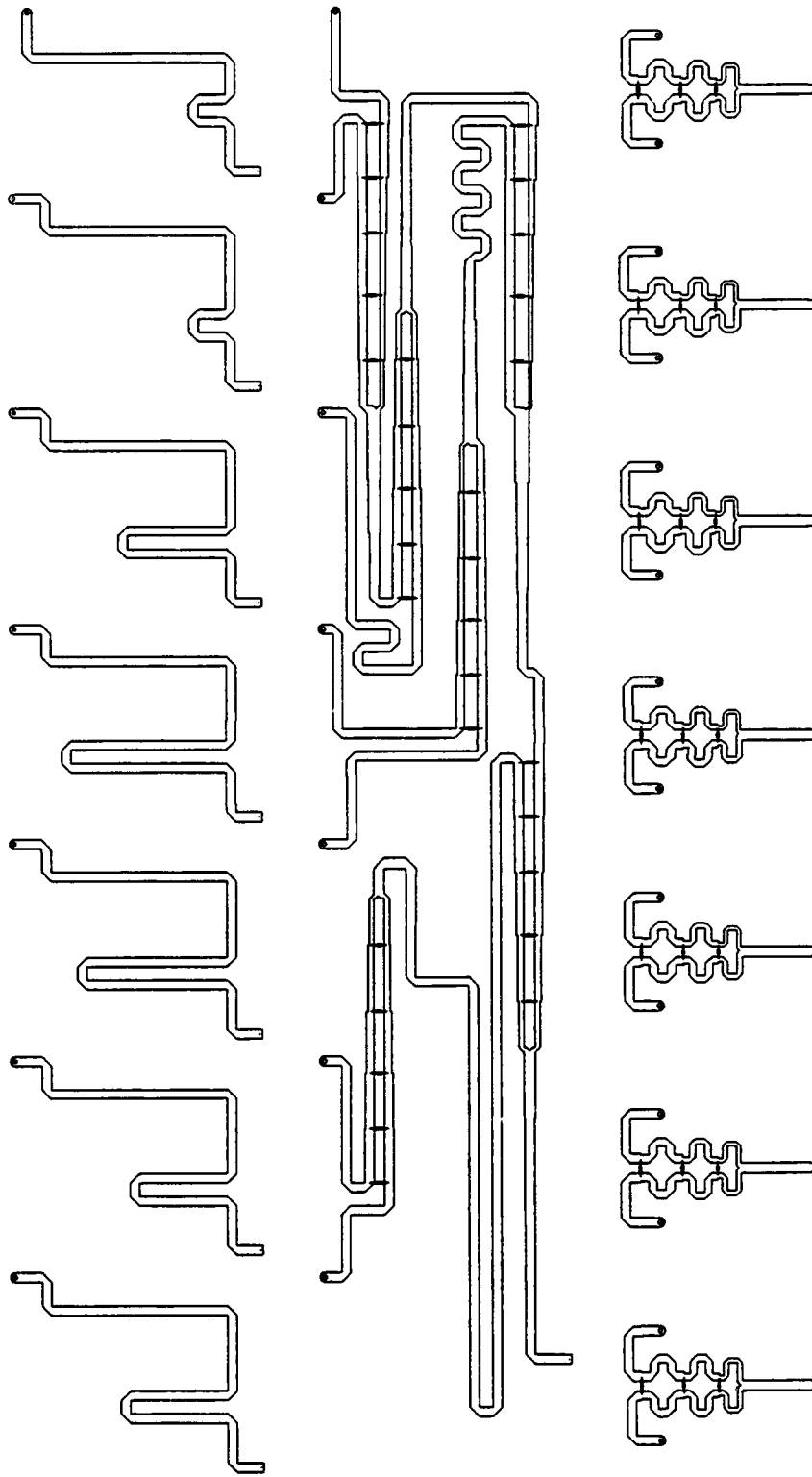
Figure 12 - Circuit trace for one half of 28 element power distribution network which produces a Taylor 25 dB, ñ=3 amplitude taper. Three layers are shown: the phase equalization layer, the signal input layer, and the output layer.

5.   BANDWIDTH CONSIDERATION:

We encountered several factors which influenced the bandwidth of the dual flared notch design. (1) An input transition consisting of crossed stripline and notchline has a wider bandwidth if the stripline is terminated in a hard short and the notch line is terminated in a high impedance loop. (2) The region between adjacent elements the top, bottom and rear metal enclosures and behind the stripline to notchline transitions forms a short circuited waveguide stub. The impedance of a short circuited waveguide is found by using a load of 0Ω in the transmission line transformer equation, giving

$$Z_{in} = Z_g \tanh(j\beta_g l + \alpha_g l) \tag{2}$$

where Z_g is the characteristic impedance of the guide, β_g is the propagation constant in the guide, α_g is the attenuation constant in the guide, and l is the length of the guide. Throughout most of the band of operation, the guide is cutoff so $\beta_g = 0$ and Z_g is imaginary. IF $\alpha_g l$ is small, then Z_{in} is small, which short circuits the electric fields in the antenna. However, if l is made sufficiently large then Z_{in} is made large enough that it does not adversely effect the antenna. (3) Throughout this report, reference was made to the space between elements (element center to center spacing minus element thickness). That is because all the antennas tested exhibited a loss of gain, increase in beamwidth, or increase in VSWR, or all three when this distance became slightly greater than a half wavelength. This appears to be another manifestation of the waveguide like structure between elements. We have done

18

215

calculations which show that the input impedance of the short circuited waveguide stub described above is very large at frequencies just above cutoff. At somewhat higher frequencies, however, the input impedance becomes small, and these frequencies correspond well with the frequencies at which the VSWR is observed to become very large.

6. CONCLUSIONS:

We studied the dual flared notch element and found it to be a good choice for a broadband array design. A 28 element array of dual flared notches was built which exhibited very good behavior over nearly a 3/1 bandwidth. The antenna exhibited high gain, low VSWR, and low sidelobes over the entire bandwidth. We believe moderate increases in bandwidth can be achieved without difficulty.

REFERENCES:

1. Frantz, K.M., and Mayes, P.E. (1987) Broadband Feeds for Vivaldi Antennas. 1987 Antennas Applications Symposium, Allerton Park, University of Illinois.

2. Hoefer, W.J.R. and Burton, M.N. (1982) Closed-Form Expressions for the Parameters of Finned and Ridged Waveguides, IEEE Trans. Microwave Theory Tech. MTT-30(12) 2190 - 2194

19

3. Kerr, J. L. (1970) <u>Short Axial Length Broadband Horns,</u> U.S. Army Electronics Command Technical Report ECOM-3344.

4. Kerr J.L. (1973) "Short Axial Length Broad-band Horns", <u>IEEE Trans. Antennas Propagat.,</u> AP-21(9), 710-715

5. Povinelli, M.J. (1988) Experimental Design and Performance of Endfire and Conformal Flared Slot (Notch) Antennas and Application to Phase Arrays: An Overview of Development. <u>1988 Antennas Applications Symposium,</u> Allterton Park, University of Illinois.

6. Stutzman, W.L. and Thiele, G.A. (1981) <u>Antenna Theory and Design,</u> John Wiley and Sons, New York, pp. 174-177.

7. Villeneuve A.T., "Taylor Patterns for Discrete Arrays," <u>IEEE Trans. Antennas Propag.,</u> PS-32(10), 1089-1093 (1984).

8. Collin R.E. (1966) <u>Foundations of Microwave Engineering</u> McGraw-Hill, New York, pg 580.

20

A MULTIBAND PHASED ARRAY ANTENNA

B.J. Edward, A.L. Pfannenstiel, B.L. Cleaveland, M.J. Devine

Electronics Laboratory

GE Aerospace

Syracuse, New York

ABSTRACT

The design and characterization of a multiband aperture comprised of two interleaved phased array antennas is presented. The aperture functions as independent L- and X-band arrays both providing wide angular coverage. It is populated with flush style L-band multislot elements and X-band stacked patch radiators which enable the antenna to conform to curved surfaces. The design accommodates active T/R modules at each of the radiating elements with the attendant RF feed, DC and control signal distribution, and thermal management systems. Details of the full array design, including development of the radiating elements, are presented. A 20 element L-band/ 80 element X-band test aperture is also described. Measured element in-place radiation patterns, element-to-element mutual coupling, and active impedance data are reported. A companion experiment, to be performed on a GE Electronics Laboratory/Rome Laboratory Photonics Center Cooperative Research Agreement, mates the L-band elements with a unique optical domain time-delay beamforming system.

1

1.0 INTRODUCTION

Because of their superior beam agility, electronically steerable phased arrays are the antenna of preference for high-performance radar. However, limiting future phased array radar systems to a single operating frequency band severely compromises the performance of target detection, tracking, and classification functions. For maximum utility, these systems must operate on two or more frequency bands. Separate array sub-systems can be configured to provide multiple frequency bands but the cost, size and weight of the total system is prohibitive. The best approach is a single aperture that supports operation on multiple bands.

Optimum performance is achieved when the frequency of operation is tailored to the specific function and target/environment characteristics. Six frequency bands are examined resulting in a choice of L-band for search and X-band for track and classification. Once the frequency bands are selected, the primary considerations in developing a viable multiband aperture concept are to interleave the radiating elements, T/R modules, thermal management system, and signal distribution systems into a common volume and to establish the RF interfaces to elements and beamformers – without compromising array performance on either frequency band.

The design of a multiband aperture is outlined with emphasis given to dual band active array requirements, radiating element design, and test array development and evaluation. Low and high frequency arrays share a common volume as opposed to merely juxtaposing separate apertures. The test aperture is comprised of 20 L-band multislot elements and 80 X-band stacked patch elements, with both designs amenable to interleaving in a dual band active aperture. The test aperture accommodates T/R modules, signal distribution systems, and thermal management systems and allows the evaluation of radiating element mutual coupling/active impedance data and in-place element radiation patterns.

2

2.0 MULTIBAND APERTURE CONCEPT DEVELOPMENT

2.1 Frequency Selection

The frequency selection effort focused on six bands from VHF through X-band. Each band was examined for its ability to perform search, measurement, and track functions for two different targets — one with a radar cross section (RCS) that varied as $1/f^2$ and one with an RCS invariant with frequency. System noise figure and propagation loss estimates were included for each band. In addition near term and future cost models for the active arrays were generated. A set of surveillance radar parameters served as the baseline with power and aperture values adjusted for each band to maintain the same performance for the three radar functions with both RCS models. Required array sizes and corresponding costs were then compared.

Performance analysis and cost modeling of the search frequency band indicates that choosing VHF would result in the most cost effective and lightest weight array when considering the $1/f^2$ RCS target model, and both the near term and future cost models. L-band is slightly less expensive than either UHF or VHF when considering the search function with a constant RCS target and the future cost model. Since UHF and VHF radar are not allocated for European operation, L-band is chosen for the search function.

C- and X-band are both candidates to perform target identification measurements and raid count functions. Both of these functions require high angle and range resolution as well as high Doppler sensitivity. X-band requires a larger aperture to overcome atmospheric and system losses, but provides nearly twice the Doppler sensitivity of C-band, which is a critical parameter in making jet-engine modulation measurements as well as SAR images. Thus, X-band is selected as the second operating band.

2.2 Design Constraints

Once the frequencies of operation are selected, the ground rules for the design of the multiband aperture are addressed. Table 1 lists these design requirements. In addition to interleaving the radiating elements, the multiband aperture must also co-locate the thermal management and signal distribution systems plus the T/R modules and still maintain a minimum overall thickness. Array repairability is also a principle design objective. Flush style radiating element candidates are examined in anticipation of their use in a dual band aperture where the

3

elements for both of the interleaved arrays occupy the same effective area, yet must remain sufficiently isolated from one another to avoid degradation of radiation and impedance properties.

Table 1. Requirements of the Multiband Aperture.

o Frequency coverage of the two distinct bands each of 10% bandwidth.

o Wide angular coverage of $\pm$ 60° azimuth, $\pm$ 40° elevation.

o Low profile aperture with flush mounted radiating elements and minimum overall depth.

o Readily repaired with front or rear plug-in replaceable T/R modules.

o Integrated thermal management system compatible with $1.74kW/m^2$ average radiated power at each frequency band.

o Accommodate RF signal, control signal, and DC power distribution systems for each band.

2.3 Full Size Array Design

A multiband array concept has been developed which fulfills all of the design constraint objectives. The enabling technology is the interleaved radiating element approach shown in Figure 1. Each L-band element consists of four reduced height slot radiators that extend rearward to a common cavity and interface to the T/R module at a single input port. Sufficient aperture area exists between the L-band slots to place X-band patch style radiating elements. Sixty-four patches are configured in an 8 X 8 arrangement and interleaved with each L-band element. The relative quantity is dictated by the frequency ratio between the two bands. Coupling between bands is minimized by orthogonally polarizing the patches to the slots. Elements for both bands are located on rectangular grids with element spacings compatible with the array beam scan requirements. Directly behind each patch lie the X-band T/R channels, which fit between the L-band reduced height waveguide sections. Therefore, the X-band T/R modules are accessible from the front of the aperture, while the L-band units are plug-in replaceable from the rear.

4
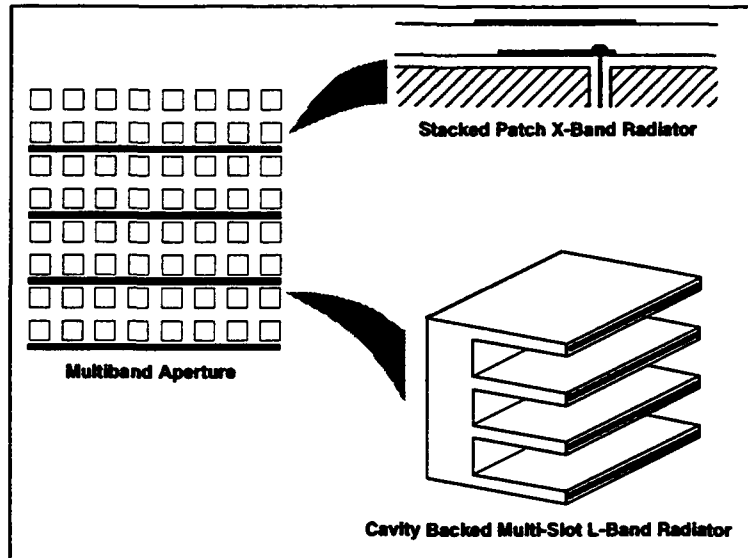
Figure 1. Interleaved L- and X- Band Radiating Elements. X-band T/R modules are replaceable from the front of the aperture and L-band units from the rear.

The interleaved array concept is illustrated in Figure 2. Eight adjacent X-band T/R channels are packaged together to form a module. The front plate is integral to the module and contains a row of 8 patches. Two of these modules are placed between each pair of L-band reduced height guides as also depicted in Figure 1. Located in between these two X-band modules are the horizontal coolant channels of the thermal management system. This arrangement places the high temperature surface of the modules in direct contact with the heat exchanger, resulting in a low resistance thermal path that removes heat efficiently. The RF signal, control signal, and DC power distribution systems are located immediately behind the X-band modules and in front of the L-band element cavities. These systems run horizontally across the aperture and therefore X-band beamforming is performed on a row-followed-by-column basis. Since eight T/R channels are packaged together, the number of interconnects required by each module is reduced. Each X-band module is mechanically retained with wedgelock fasteners at the front element plate. When these fasteners are engaged, downward pressure forces intimate contact between the module and the coolant channel.

5
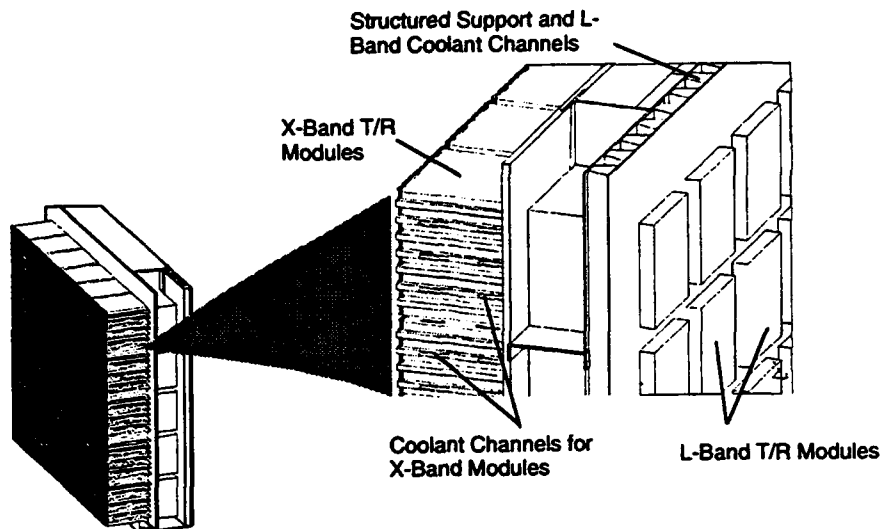
Figure 2. Full Size Multiband Active Array. Volume is available for T/R modules, cooling systems, and signal and power distribution networks for both frequency bands.

Again referring to Figure 2, the L-band T/R modules are located at the rear of the structure, with one channel packaged for each element. Coolant channels are placed directly beneath the modules for effective heat removal. RF signal, control signal, and DC power distribution systems are routed either vertically between columns of modules or horizontally between rows. The module packages are retained with mechanical fasteners.

Design of the thermal management system addressed the selection of coolant medium, coolant channel size, and coolant flow rates to ensure acceptable active device junction temperatures. The X-band T/R modules generate a higher heat density than the L-band units and therefore drive coolant medium selection. Analysis of the X-band configuration reveals that liquid cooling is preferable to air and to take advantage of commonality, the L-band modules share the same liquid cooling system. While use of air is feasible, it is neither efficient nor cost effective. Substantial volumes of air would be required resulting in the need for large blowers that would consume a high level of prime power and generate significant additional heat. Further analysis indicates that water, at moderate flow rates, provides acceptable performance with respect to maximum junction temperatures, device temperature uniformity from module to module, and thermally induced stress and distortion across the aperture.

6

3.0 RADIATING ELEMENT DEVELOPMENT

3.1 X-Band Stacked Patch Element

The X-band radiating element must be conformal (no protrusions from the array face), with active T/R circuitry accessible from the array front. Therefore, thin (minimum depth) elements amenable to a direct connection between their feed and the T/R circuitry are preferable. These elements will operate over a bandwidth on the order of 10% with linearly polarized angular coverage of up to 60° from array broadside. After considering feasible radiating element designs, a two layer, stacked microstrip patch element is selected as the best suited to fulfill these requirements.
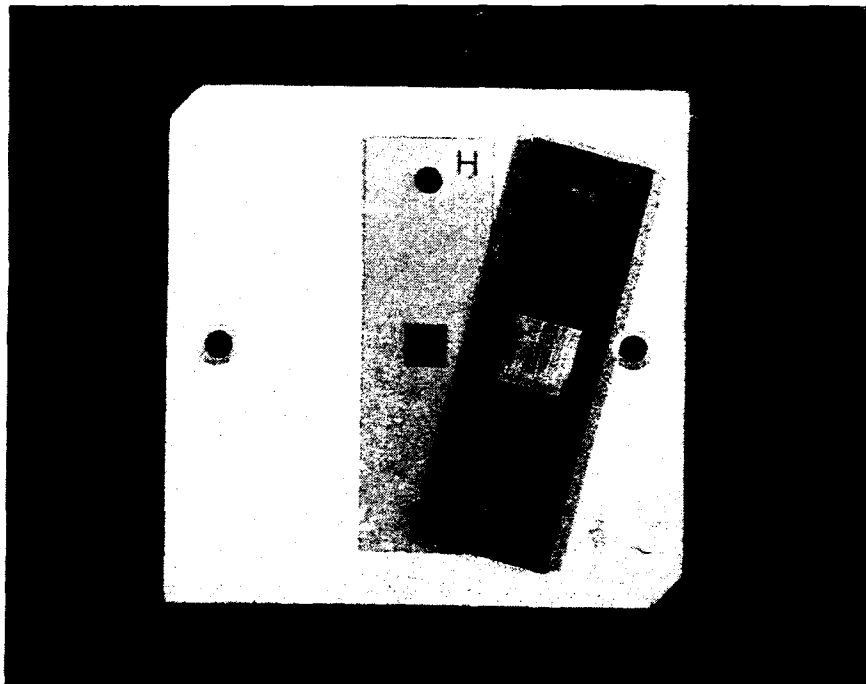
Figure 3. Stacked Patch X-band Radiating Element.
Element is fabricated using photolithographic and lamination processes.

The stacked patch element is displayed in Figure 3. It consists of two substrate layers with rectangular metalization patterns printed on each. The lower patch is fed by the center conductor of a coaxial line which connects directly to the T/R module, while the upper level patch is excited electromagnetically. The element's parameters, including the thickness and dielectric constants of the two substrates, dimensions of the patch metalizations, and position of the feed point, are selected to achieve the best impedance match when in the array environment. The most

7

appropriate combination of parameters is determined using Sonnet Software's em [1]. Initially developed for the modeling of multilayer microstrip circuits, em performs a method-of-moments analysis of planar type circuits. Any combination of dielectric materials may be taken into account as well as vertical vias for interconnecting various layers. Circuitry must be modeled within a box, but a lossy lid option enables the user to model patch radiating elements within a waveguide simulator for determination of impedance in the infinite array environment [2]. The box dimensions are chosen to simulate the array environment when elements are phased for beam scan of 30 degrees from broadside in the H-plane. The via option is used to model the coaxial feed. As shown in the exploded view of Figure 4, the final design consists of a thin (10 mils thick) lower layer of high dielectric constant ($\varepsilon_r = 10.5$) material laminated with a thicker (62 mils thick) upper layer of low dielectric ($\varepsilon_r = 2.2$) material. The dimensions of the two rectangular metalization patterns have longer lengths than widths as required to raise the impedance for matching the $50\,\Omega$ active circuitry. This aspect ratio is also favorable for reducing cross-polarization radiation levels [3]. For the best impedance match the feed point is located very near the edge of the lower patch.
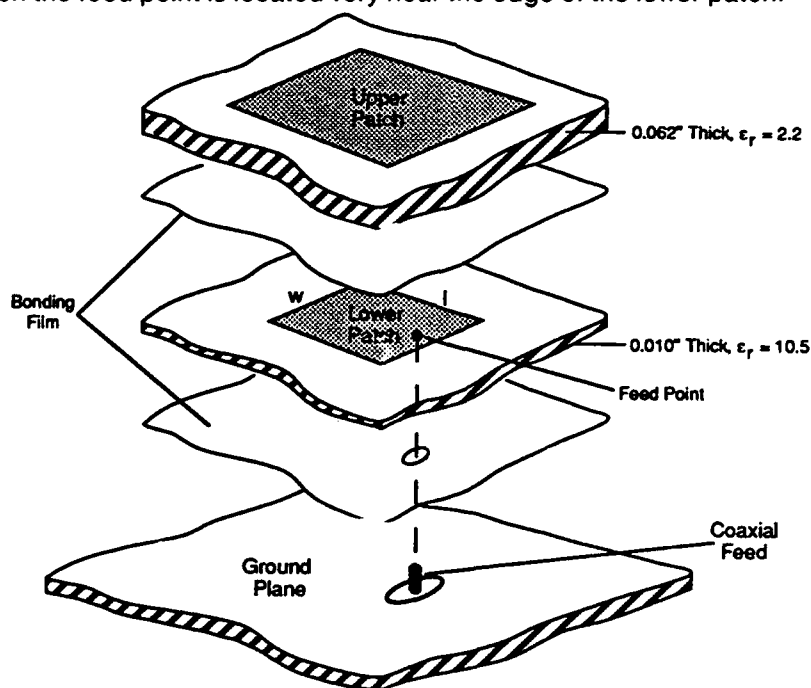
Figure 4. Exploded View of the X-Band Stacked Patch

The measured impedance of the stacked patch within a 30° scan H-plane simulator and the impedance as calculated with em are reported in Figure 5. The stacked patch design exhibits a

8

very good impedance match over the band of interest, 9.5 to 10.5 GHz. Agreement between measured and calculated performance is also very good. Measured radiation patterns for a single stacked patch are presented in Figure 6. Broad angular coverage is achieved, fulfilling the array's angular scan requirements. Measured cross-polarization levels for the isolated element are low, not exceeding -26 dB.
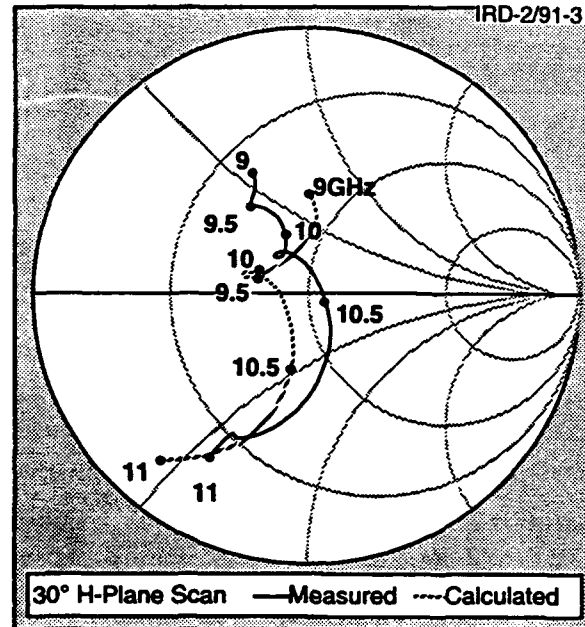

Figure 5. Measured and Calculated Feed Point Impedance of the Stacked Patch Radiating Element. Element exhibits a 12%, 2.3:1 VSWR bandwidth.
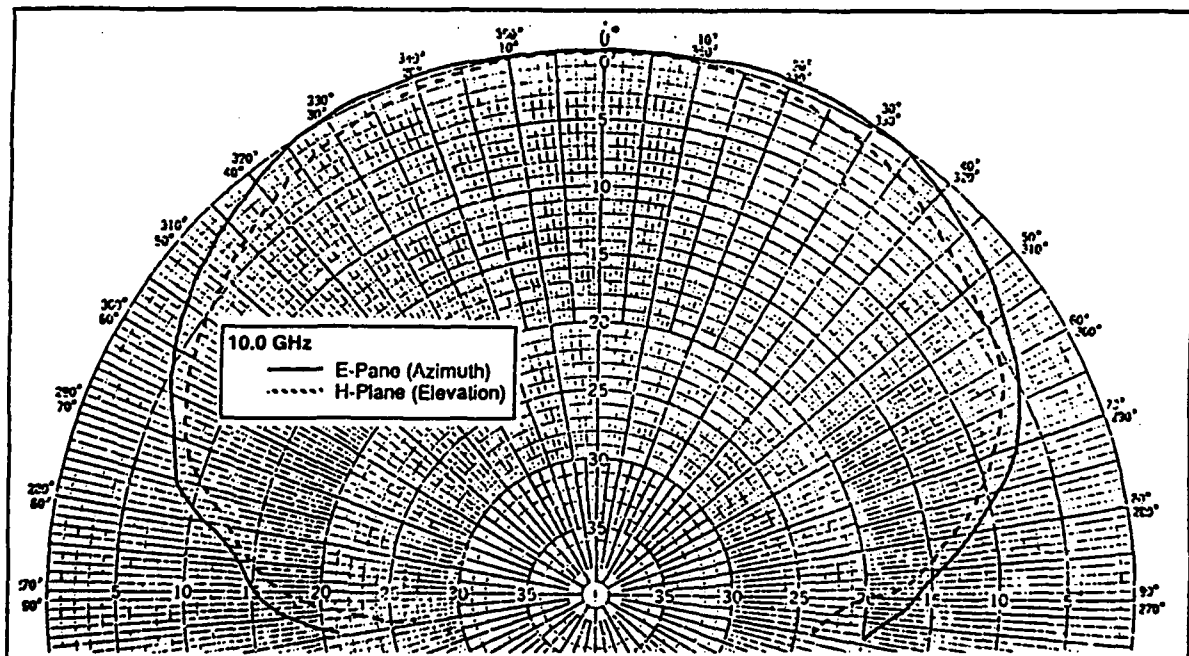
Figure 6. Measured Radiation Patterns of the Stacked Patch at 10GHz. Beamwidths are well matched to the array's angular coverage requirements.

9

3.2 L-Band Cavity Backed Slot Element

The L-band radiating element must satisfy the same conformal and angular coverage requirements as the X-band elements. In addition it must accommodate the X-band T/R modules and their attendant cooling system and signal distribution networks. Referring to Figure 1, a height of 0.150 inches exists between alternate rows of X-band patches for the L-band radiators. Adhering to the original grid requirements, four of these spaces are available for each multislot L-band element. This available height extends rearwards along the depth of the X-band T/R modules for approximately 4 inches.

Slot style radiators fed by reduced height waveguide satisfy the aforementioned requirements and are selected for the L-band elements. Four of these slots are excited by a common cavity, which is located behind the X-band modules. Use of four slots for each element results in a wider impedance bandwidth than is achievable with just a single slot. Dielectric loading is employed to reduce the waveguide to a width compatible with the element grid.

The open-ended waveguide (slot) impedance of an element within an infinite array is calculated using a mode matching analysis program. Both waveguide-to-waveguide and waveguide-to-virtual waveguide cascaded junctions are modeled, including the effects of evanescent modes scattered from steps in waveguide height and/or width. The element design is determined using these techniques with only the cavity feed probe dimensions (a printed dipole) optimized experimentally.

10
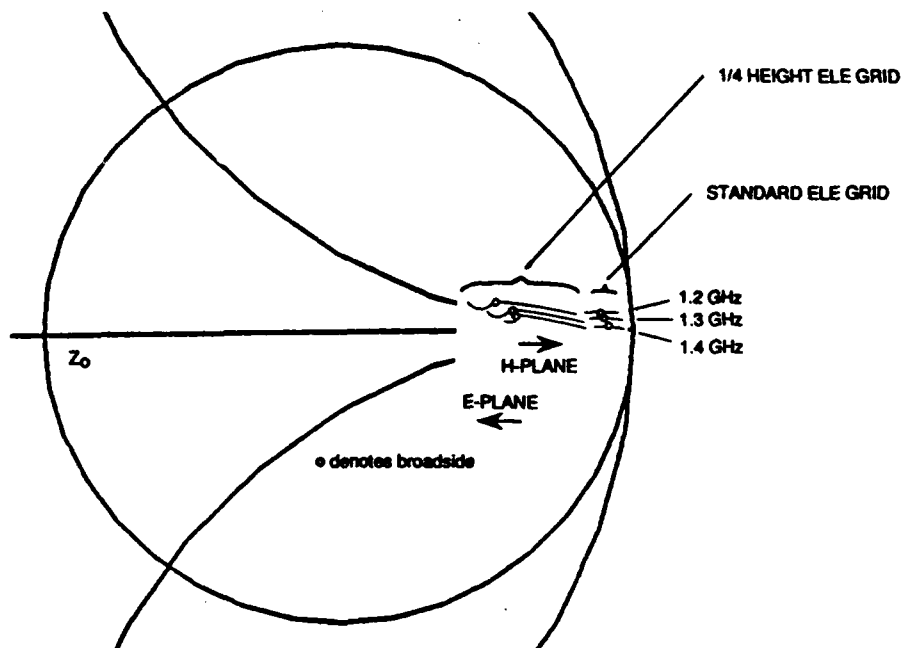
Figure 7. Reflection Coefficients of a Single Open-Ended Guide as a Function of Frequency and Beam Scan Angle. Calculated for a single slot on the standard element grid and for a slot on a 1/4 vertical height grid.

The calculated reflection coefficients for a single open-ended guide element with a height of 0.150 inches and filled with Rexolite (ε_r = 2.54) are shown in Figure 7. If the vertical element grid dimension is reduced by a factor of four so equivalently four of these slots are now within the element grid, then the reflection coefficient for one slot is reduced as reported in the figure. This result was compared to a single element of four times the height on the original grid. The taller element has about the same reflection coefficient magnitude as the low height element, but it exhibits more impedance variation with frequency.

The broadside beam radiation impedance of each of the four slots is approximately $120 + j25 \Omega$ with very little frequency variation. The characteristic impedance of the 0.150 inch height guide is about 12 ohms. To impedance match this combination to the cavity, a further reduced height waveguide section is inserted in series, approximately midway between the cavity and the slot. The calculated impedance behavior of the final design referenced at the cavity is given in Figure 8.

11
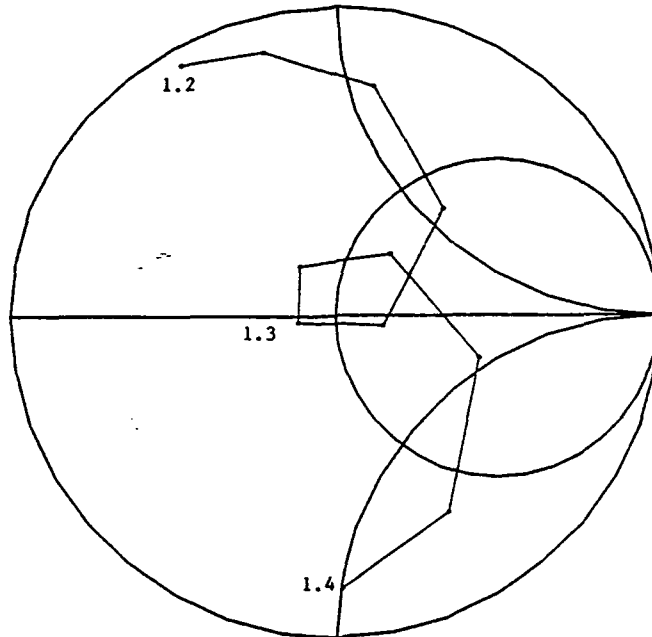
Figure 8. Reflection Coefficient of a Single Slot with Matching Section.
Reference plane at the feed cavity, broadside beam conditions.

An experimental multislot element is shown in Figure 9. The reduced height waveguide, including the matching section, are fabricated from Rexolite and tin plated on top, bottom and side walls. The cavity, bolted on the back, is made of two blocks of Rexolite with the excitation probe, printed on Duroid 5880, sandwiched between.
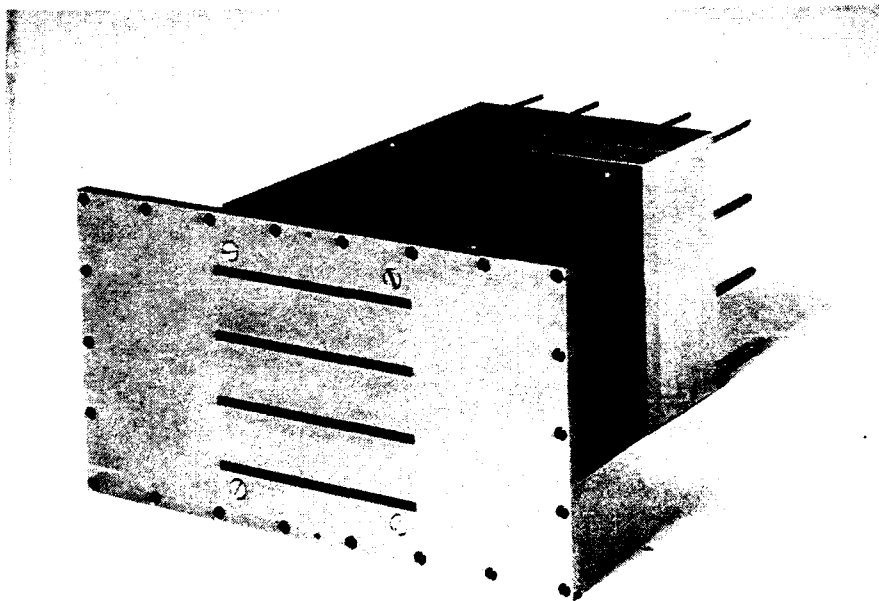

Figure 9. Multislot Element for Impedance Characterization in the Waveguide Simulator.

12

Impedance behavior of the sample element is examined in the simplest waveguide simulator, which mimics H-plane beam scan at 30 degrees. The first excitation probe was a simple open-ended line protruding from the bottom wall of the cavity, its length and width tailored to yield the best impedance match. However, the E-plane radiation pattern of an element using this probe design proved to be asymmetric. The four slots were not excited equally due to the evanescent modes excited by the probe. Thus a very symmetrical embedded dipole probe with a balun fed from the rear wall of the cavity, as shown in Figure 10, is employed to provide proper excitation of the four waveguides. Figure 11 presents the measured impedance of the final design element in the simulator. The E- and H-plane radiation patterns for this element are given in Figure 12. Broad, symmetrical patterns are achieved in both planes.
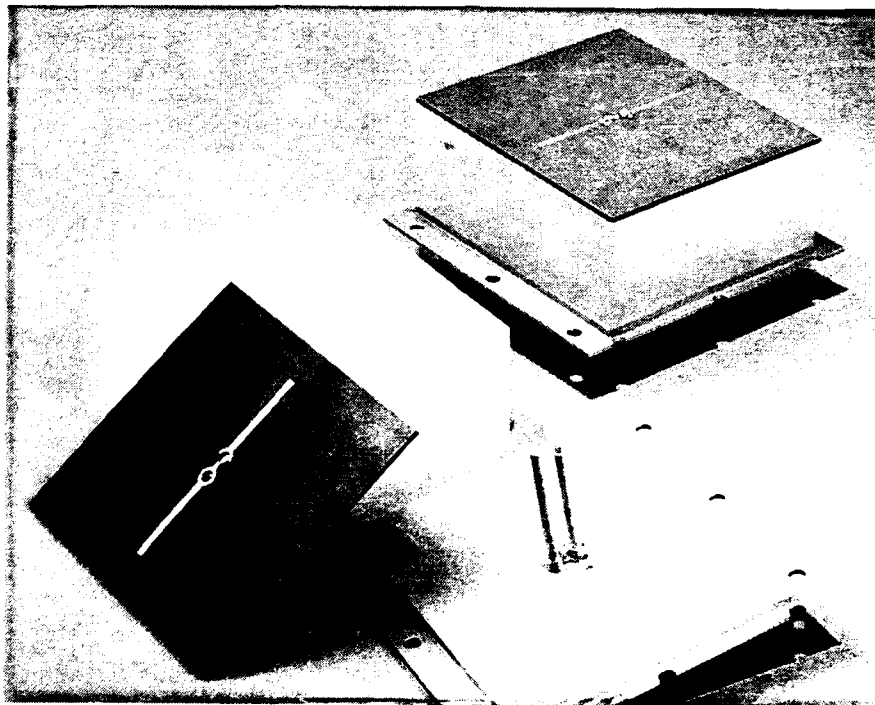
Figure 10. Components of the Cavity Feed and Excitation Probe. Dipole probe is printed on a Duroid substrate and the balun lines are fabricated in semi-rigid coax.

13
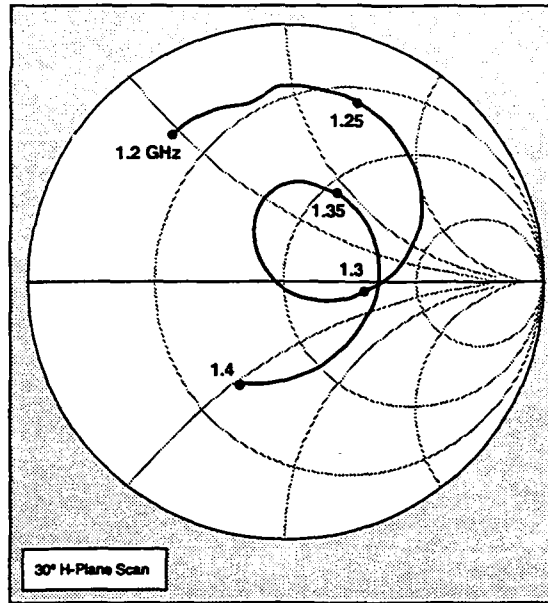
Figure 11. Reflection Coefficient vs. Frequency of the Multislot Element in a 30° H-Plane Beam Scan Simulator.
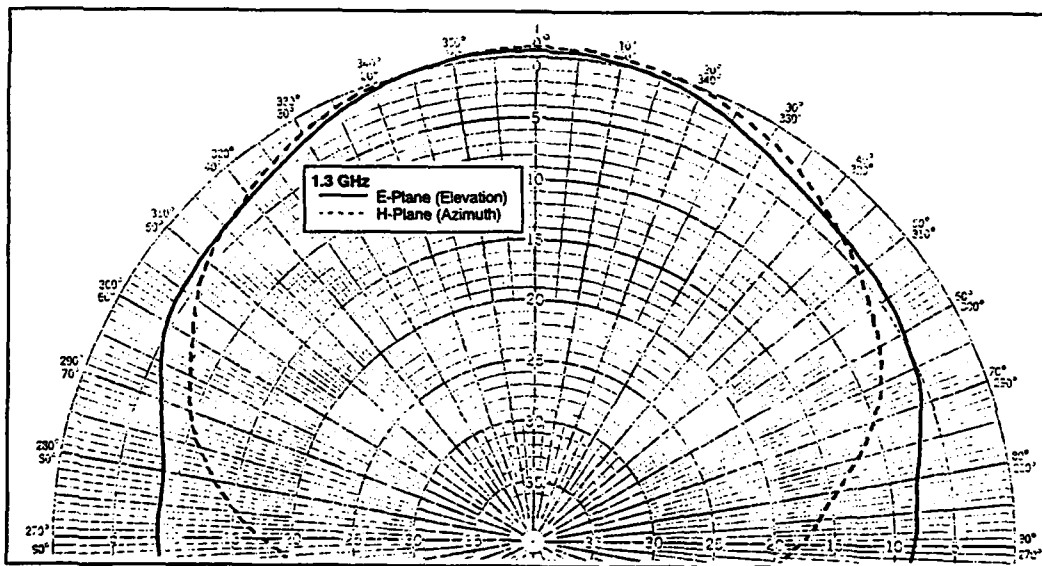
Figure 12. Measured Radiation Patterns of an Isolated Multislot element.

14

4.0 MULTIBAND TEST APERTURE

The salient features of the full size array concept are demonstrated in a multiband test aperture. The test aperture enables the evaluation of the L- and X-band radiating elements within the array environment. In-place radiation patterns and element to element mutual coupling data are measured, and active element impedances parametric in frequency and array beam scan angle are derived [4]. The in-place patterns are indicative of the beam scan capabilities of the array while the active impedance corresponds to the transmit mode load and receive mode source impedances seen by the T/R module circuitry. The test structure faithfully follows the design of the full array, accommodating and integrating T/R module volume, thermal management systems, and signal distribution systems.
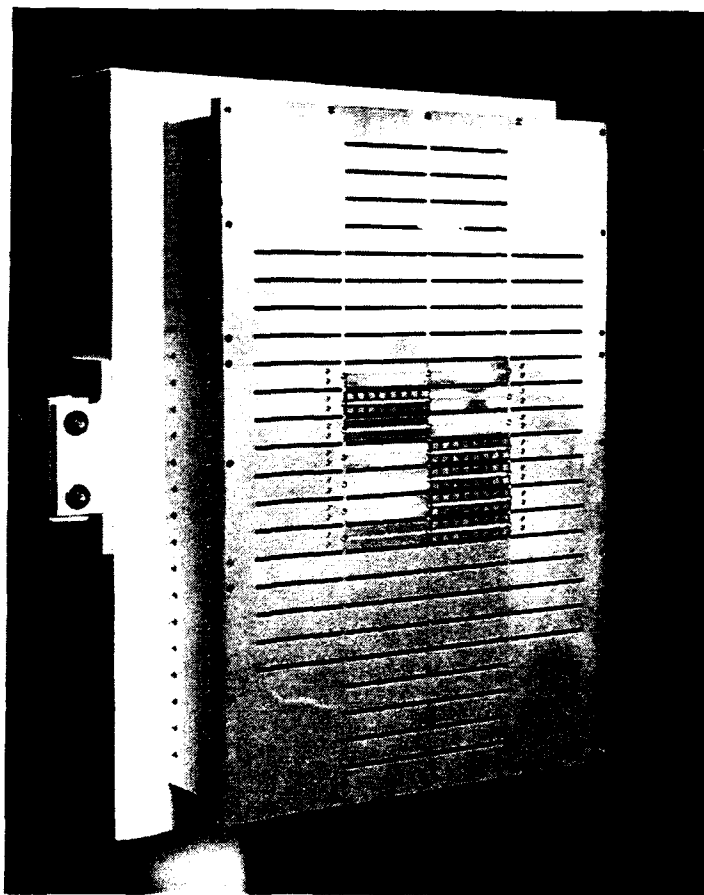
Figure 13. Multiband Test Aperture (front view).

Figure 13 shows the completed aperture mounted within our anechoic chamber. It is comprised of 20 L-band multislot elements and 80 X-band stacked patch elements. The L-band

15

radiators are configured in a 4 by 6 arrangement with elements absent at the corners. For economy, the entire L-band array is not interleaved with X-band elements; instead the X-band radiators are confined to the test aperture center region, but they may be reconfigured within this area to form an array that is wider either in its E- or H-plane scan.
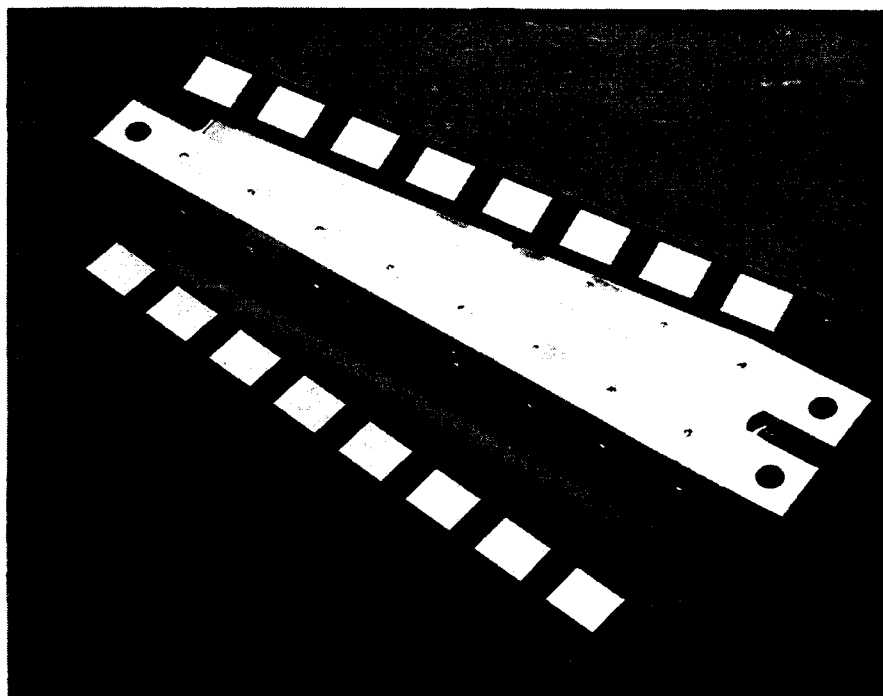

Figure 14. X-Band Patch Assembly. A dummy L-band slot between the two rows of patches results in a symmetric patch environment.

Figure 14 depicts a 16 element X-band assembly, prior to lamination of the stacked patches, which is positioned between the L-band slots. A coaxial connector at each element facilitates data collection. In order to achieve consistent in-place radiation patterns for low array sidelobes, the X-band patches require a symmetric environment. A dummy slot, included between patch rows, satisfies this need for symmetry by placing a slot immediately above and below each patch. The dummy slot has the same height, width, and dielectric loading as the active slots, but since it appears cut-off to the orthogonally polarized X-band signals it need only be of a shallow depth.

A rear view of the test aperture is displayed in Figure 15. The coaxial connector ports for the L-band elements are evident.
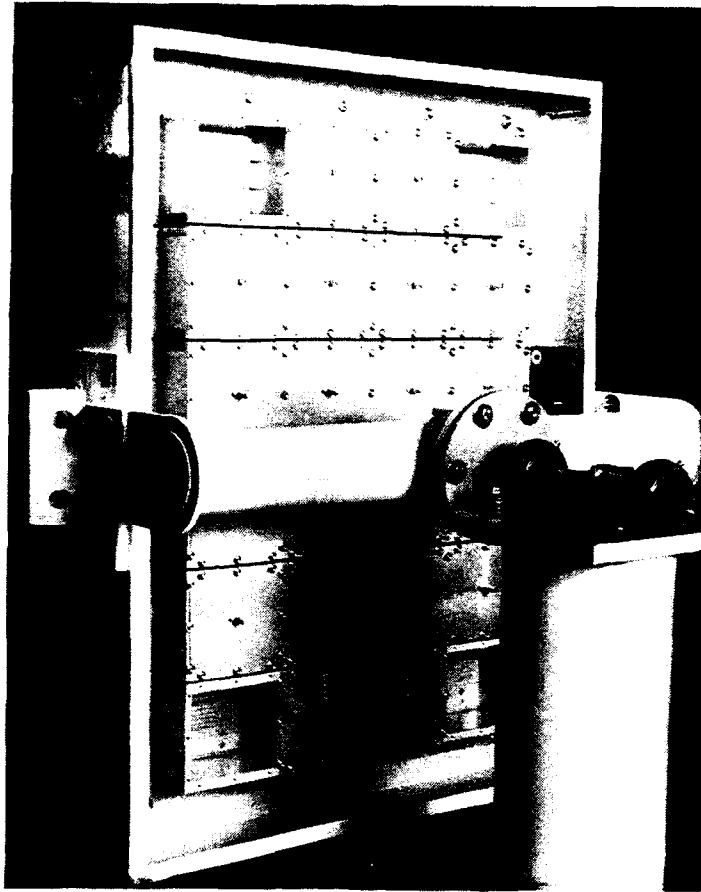
16

Figure 15. Multiband Test Aperture (rear view).

In-place element radiation pattern data was collected at both bands by measuring each element with all of its neighbors terminated in loads. The L-band in-place element radiation patterns, shown in Figure 16, are broad as required for wide angle beam scan. They are consistent with the isolated element patterns; however, some ripple appears due to the small size of the test array. The cross polarization patterns, also included in the plots, are relatively low. In-place patterns for an X-band patch are presented in Figure 17. Again patterns are very broad in both principal planes with some ripple introduced.

17

Gain A   Vs. Azimuth   Gain A   Vs. Azimuth
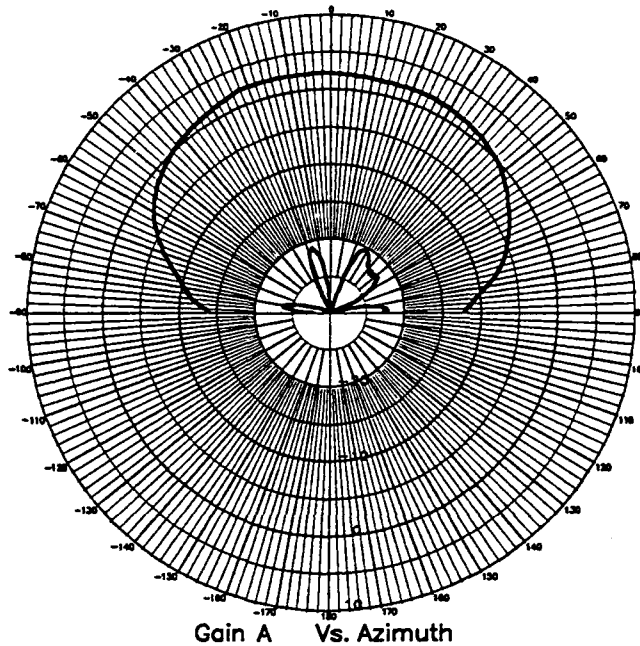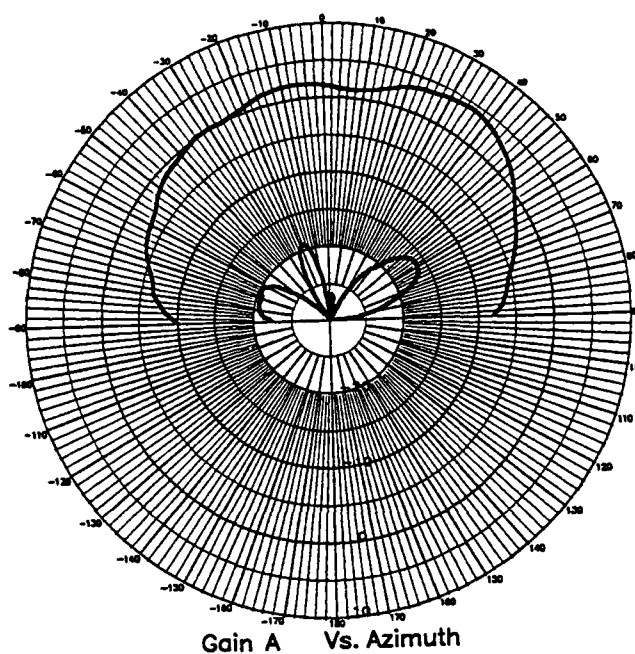
E-plane   H-plane

Figure 16. L-Band Multislot Element In-Place Radiation Patterns.

Gain A   Vs. Azimuth   Gain A   Vs. Azimuth
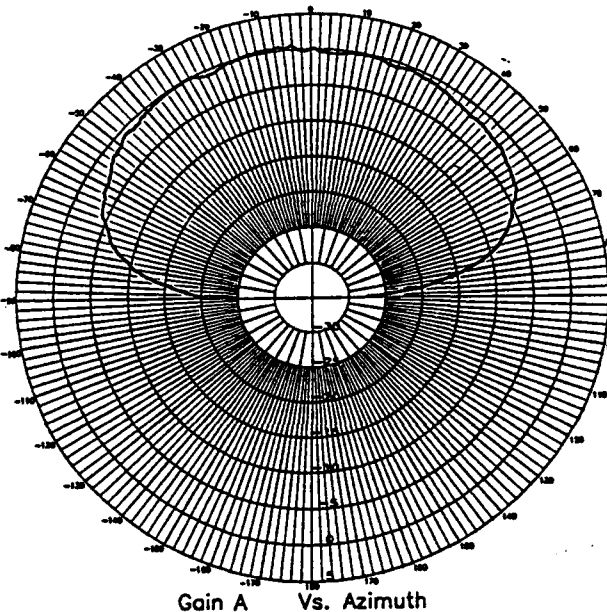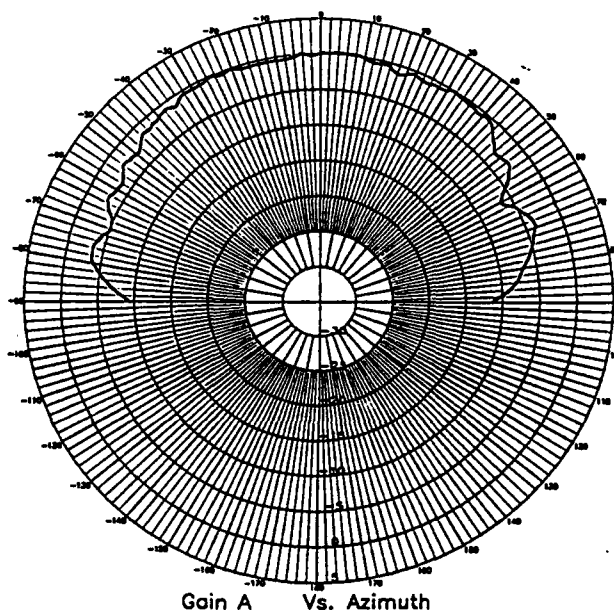
E-plane   H-plane

Figure 17. X-Band Patch Element In-Place Radiation Patterns.

Element to element mutual coupling measurements were performed at both L- and X-band. Coupling was measured from a central element to all of its neighbors. This data was then reduced to active element impedance as a function of beam scan angle. Figure 18 reports the coupling amplitude in dB to L-band element number 8 from its neighbors at 1.35 GHz. Note that the coupling

18

level is relatively low, with the largest value occurring at the immediate neighbor in the E-plane. The return loss for element 8 at this frequency is 19 dB.

The coupling amplitudes at 10.3 GHz to X-band element number 28 from neighboring elements are also very low as evidenced in Figure 19. Figure 20 plots the coupling amplitude trend in the E- and H-planes. Interestingly, the coupling is highest to the first neighbor in the H-plane and then decays rapidly for increasing distance. But in the E-plane, coupling remains relatively constant with almost no decay at increasing distances. The return loss for element 28 is 24 dB.

		1 -36	2 -38		
	3 -44	4 -28	5 -43	6 -39	
	7 -30	8 **-19**	9 -32	10 -44	↑ E-plane
	11 -42	12 -28	13 -41	14 -48	
	15 -48	16 -42	17 -42	18 -61	
		19 -48	20 -50		
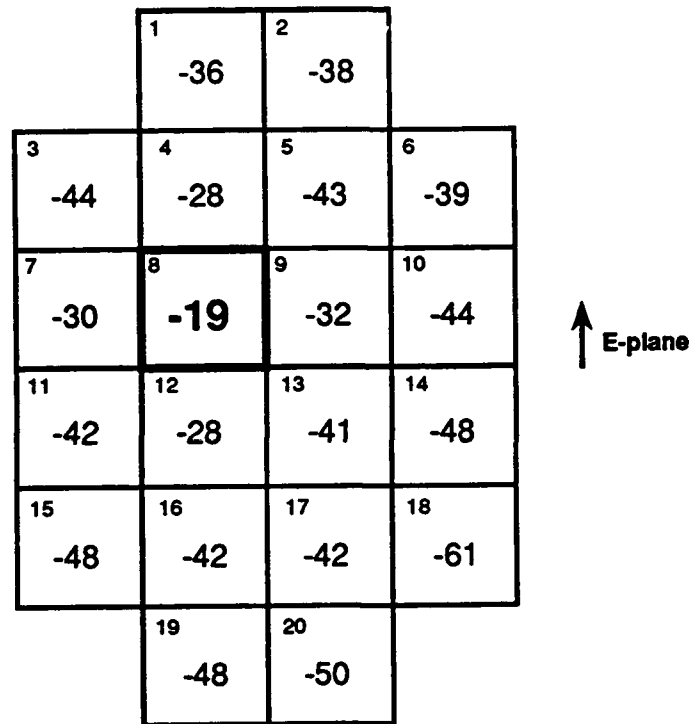
Figure 18. Cavity Backed Multislot Element Mutual Coupling Data at f = 1.35GHz.
Coupling in dB to element #8 from the other 19 elements.

Isolation between an L-band multislot element and an orthogonally polarized X-band stacked patch as a function of frequency was also measured. Figure 21 presents data for a patch that is approximately centered within an L-band element. Isolation is relatively high, being in excess of 50 dB at L-band and approximately 30 dB at X-band. Isolation is even higher for patch locations away from the L-band element's center.
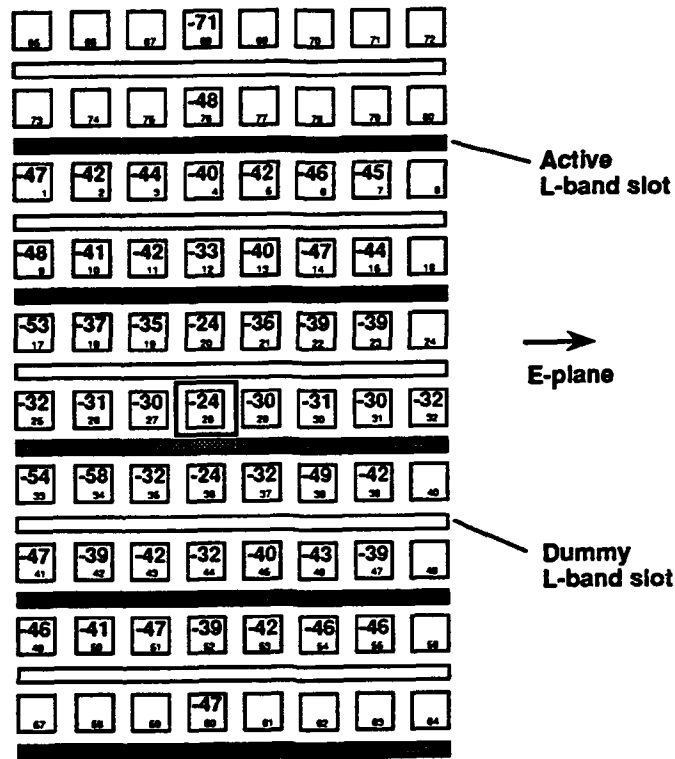
19

Active
L-band slot

E-plane

Dummy
L-band slot

Figure 19. Stacked Patch Mutual Coupling Data at f = 10.3 GHz.
Coupling in dB to element #28 from the neighboring elements.

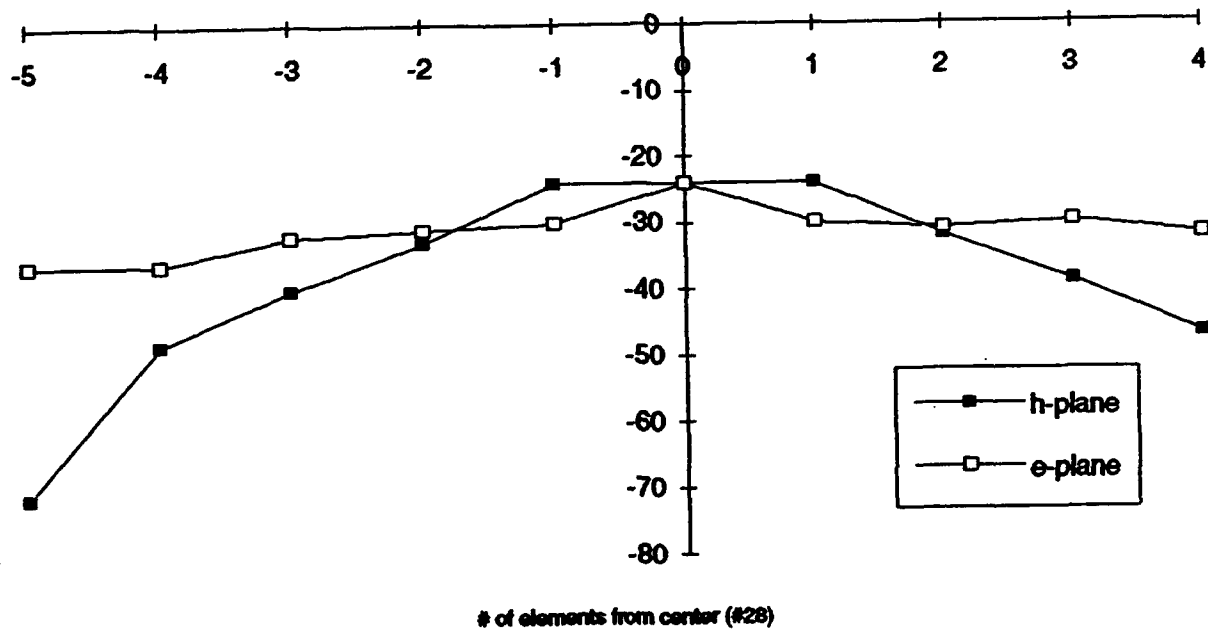# of elements from center (#28)

**Figure 20. E- and H-Plane Mutual Coupling in dB to Patch
Element #28 as a Function of Position.**

20

S21   log MAG
REF 0.0 dB
2   10.0 dB/
▽   -51.045 dB

START   1.000000000 GHz
STOP   11.000000000 GHz
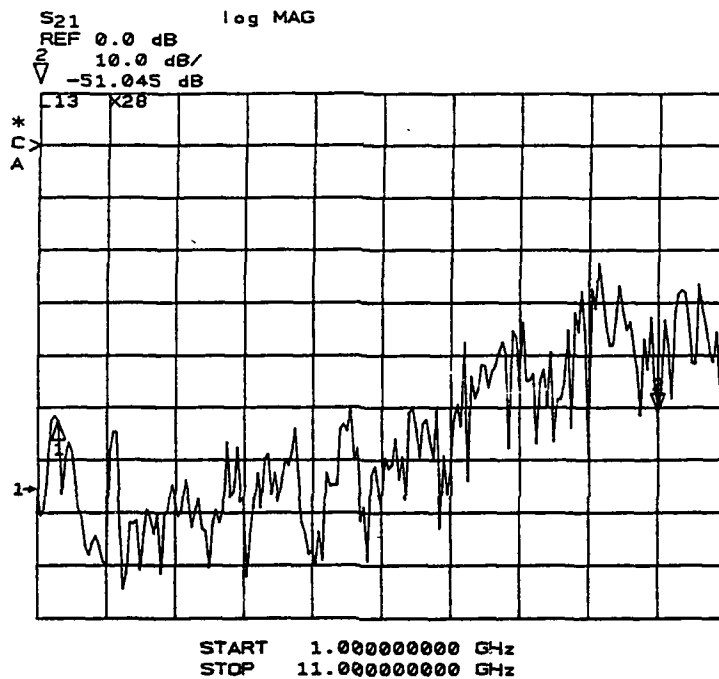
Figure 21. Coupling between an X-Band and an L-Band Element.

The active impedances derived from the mutual coupling data are given in Figures 22 and 23. Impedances are calculated for beam scan from broadside in the H-, E-, and $\phi = 45°$ diagonal planes. At the two frequencies for which this data is calculated, impedance variation with scan is very small. Maximum VSWR is under 1.8:1 – an acceptable value for both transmit and receive active circuitry.

21
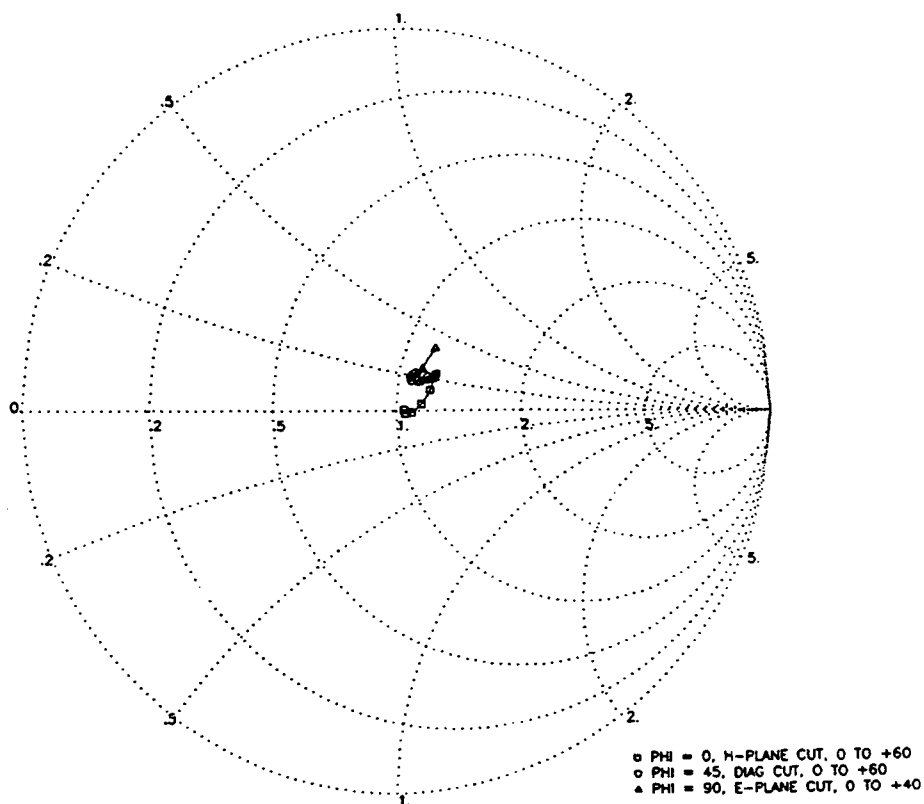
Figure 22. L-Band Multislot Element Active Impedance at 1.35 GHz.
Impedance of element embedded in an operational array as a function of beam scan angle.
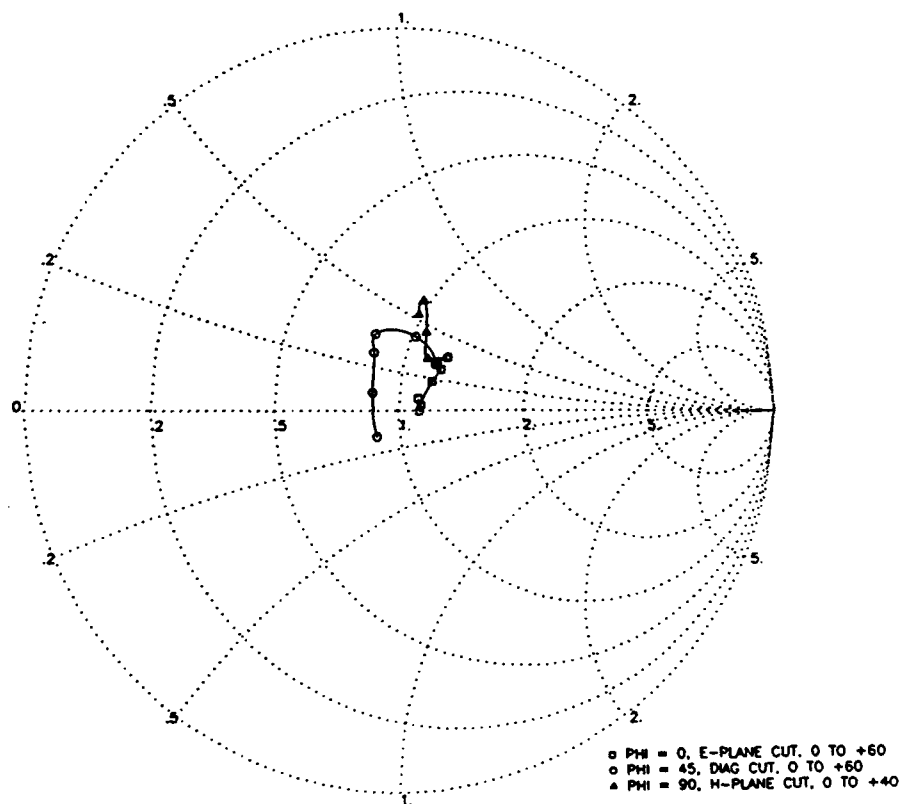

Figure 23. X-Band Stacked Patch Element Active Impedance at 10.3 GHz.
Impedance of element embedded in an operational array as a function of beam scan angle.

22

5.0 ROME LAB OPTICAL BEAMFORMER DEMONSTRATION

On a Cooperative Research agreement, GE's Electronics Laboratory and Rome Lab's Photonics Center will demonstrate the operation of the multiband aperture in conjunction with a unique optical domain beamforming network. Rome Lab is developing a photonic system which spatially integrates a large number of continuously variable microwave signal delay channels [5]. The system finds application to wideband adaptive filtering and phased array beam formation both of which require the generation of independent true time delays on multiple signal paths. Rome Lab is assembling an experimental system with 20 delay channels that will mate with the L-band elements of the multiband aperture for the formation of scanned beams.
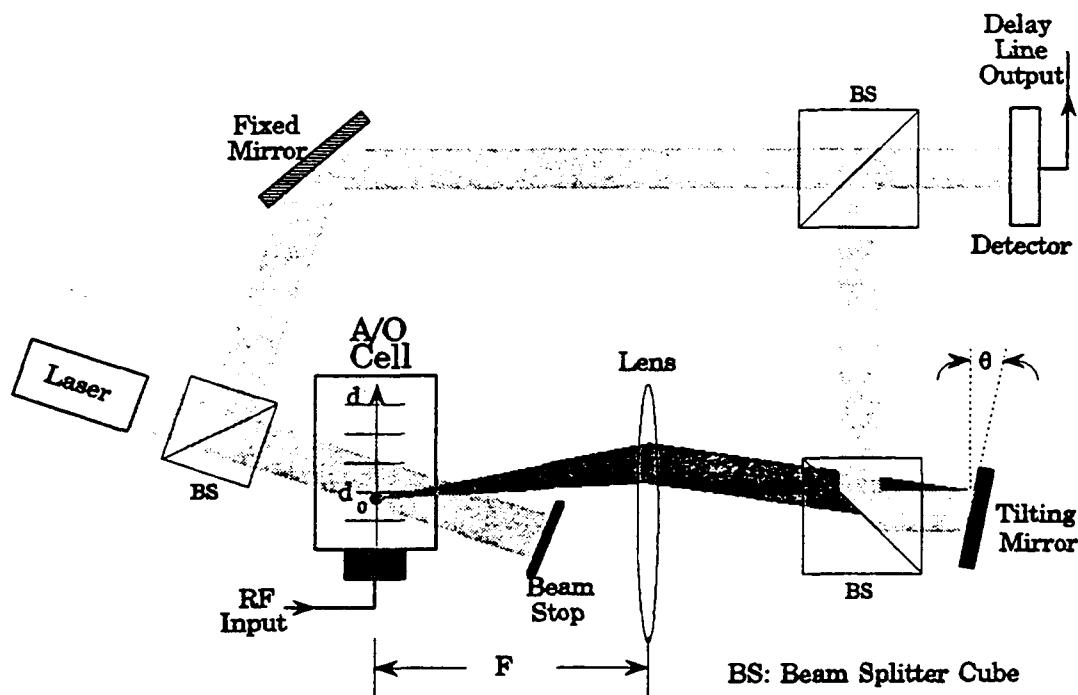

Figure 24. Continuously Variable Time Delay Channel.
The microwave signal traverses an acousto-optic cell and is sampled,
via the tilting mirror, at a point corresponding to the required delay.

The concept of a single continuously variable delay channel is presented in Figure 24. The system incorporates an Acousto-Optic cell (Bragg cell) and a Deformable Mirror Device to respectively time delay and sample the microwave signal. Referring to Figure 24, the laser output splits into two beams – a plane wave local oscillator, which serves as a phase reference, and a second beam that is sent to the acousto-optic cell modulator. The cell operates by applying the microwave signal input to a piezoelectric transducer which efficiently launches an acoustic wave

23

that traverses the cell's medium. The physical length of the cell and the relatively low acoustic velocity of the microwave signal provide for significant time delays. Interaction of the laser beam and the microwave signal lead to modulation products which emerge from the cell at an angle related to the microwave signal's frequency. Using the lensing system, each point along the microwave signal path within the cell generates a ray that is incident on the tiltable mirror. The angle of this ray, as selected by mirror tilt, uniquely corresponds to a spatial coordinate along the path of the acoustic wave in the cell, and hence to a specific time delay. Figure 24 shows a single point along the signal path associated with a specific value of time delay. From the mirror, the ray is focused to a detector where it is heterodyned with the local oscillator phase reference to yield a time delayed microwave signal.

When the microwave signal applied to the acousto-optic cell contains a spectrum of frequencies, the emerging modulated light is dispersed over an angular extent as depicted in Figure 24. The collimating lens system, however, generates a plane wave at the mirror which is then focused to the detector. Again, the mirror tilt selects the spatial coordinate within the cell and therefore the time delay for the wideband signal.

The time delay achieved, T, is the ratio of the distance d (with respect to some zero delay reference point) the microwave signal traverses within the cell, to the velocity v of this signal ($\approx$4000 m/s),

$$T = d/v. \tag{1}$$

For a mirror tilt angle of θ and a lens focal length of F, the point of sampling is

$$d = F \tan(2\theta) \tag{2}$$

where the factor of 2 arises for the total angle between incident and reflected rays about the mirror normal. Combining the above expressions yields the time delay in terms of component parameters

$$T = (F/v)\tan(2\theta). \tag{3}$$

Qualitatively, the delay is determined by the time required for the microwave wavefront in the cell to traverse the width of the laser beam. This acoustic delay provides the reaction time necessary to sustain the optical Fourier components, whose phase have been adjusted by the deformable mirror such that they sum to the desired value. The maximum differential delay is equal to the laser beam diameter divided by the acoustic velocity.

24
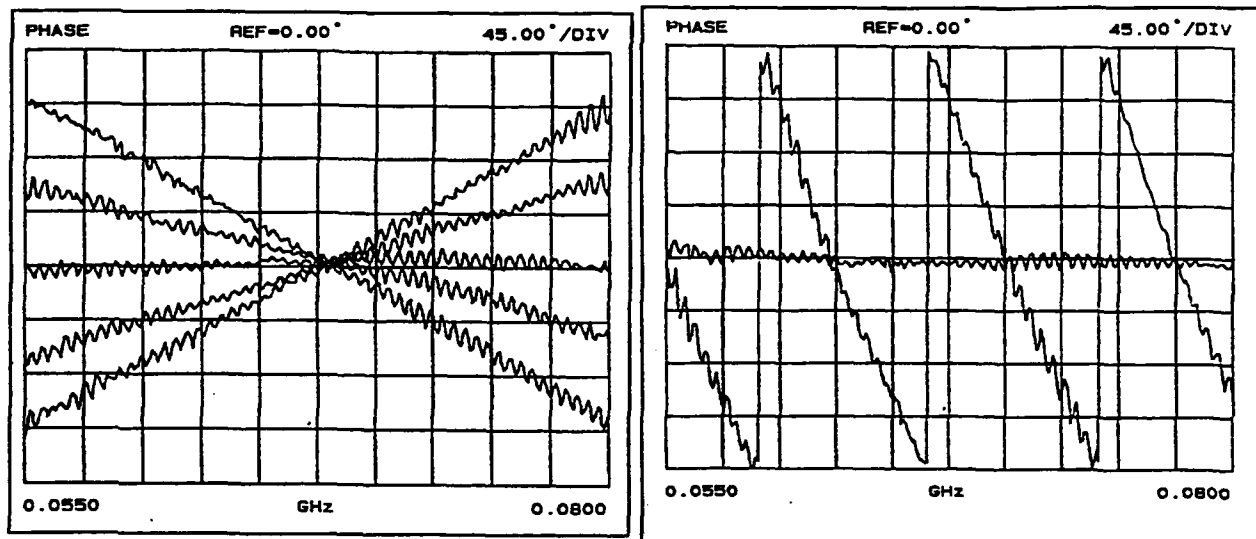
(a) Moderate delay values   (b) Large delay values

**Figure 25. Measured Phase vs Frequency Response
of an Optical Bench Configured Delay Channel.**

A time delay system has been constructed on an optical bench and characterized. Figure 25 reports the electrical phase response of the system as a function of microwave input frequency. Figure 25a shows five moderate values of delay (phase varying linearly with frequency) each representing a different tilt of the mirror. Figure 25b shows that further tilting of the mirror can result in substantial ($>$100 ns) delay. Time domain characterization was also performed and Figure 26 shows the response to a pulse chain for two selected delay values.
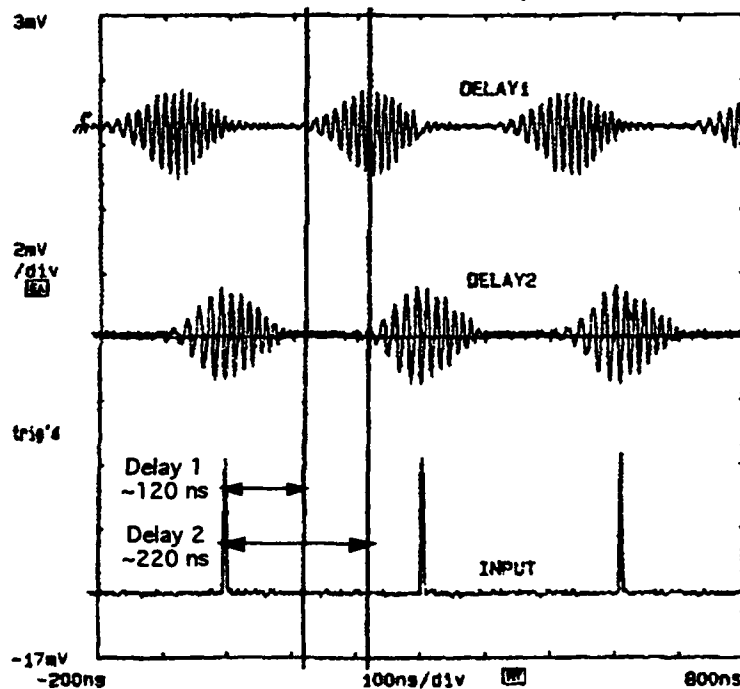

Figure 26. Measured Optical Bench Delay Channel Response to a Pulse Chain Input.

25

The extension to multiple delay channels, as required for phased arrays and adaptive filters, is realized in the spatially integrated optics implementation of Figure 27. This design provides the 20 channels required for the L-band elements of the multiband antenna. The output of the laser is split into two orthogonally polarized beams. One beam is modulated at the acousto-optic cell by the microwave signal and the other serves as a phase reference beam for heterodyning. Beyond the cell, the two beams are summed efficiently by a polarizing cube and sent to a diffractive optic device which produces 20 replicas of the reference beam and all delay information generated in the cell. These 20 beams are in turn sent to a second polarizing cube in order to re-separate reference and modulated beams. The microwave modulated beams are imaged onto a 20 element array of independent deformable mirrors, known as a Segmented Mirror Device. The tilt of each mirror is individually selected to derive the appropriate time delay for that channel. Additional optics are then employed to direct the modulated and reference beams to a lens array aligned with independent output detectors. The detector outputs are the properly delayed microwave signals used to drive the individual antenna elements.
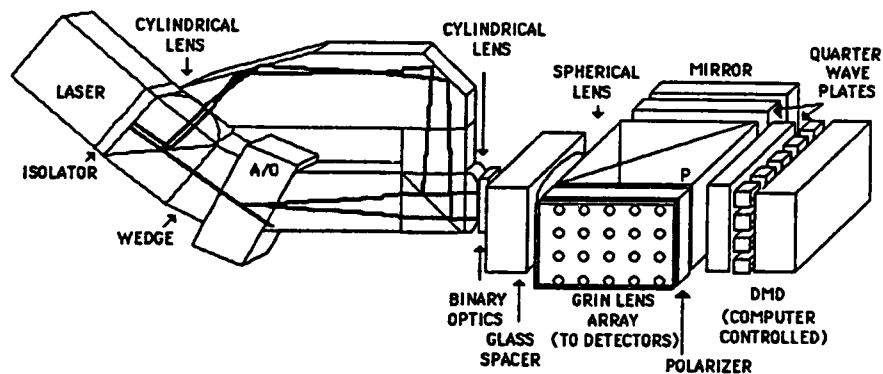

Figure 27. Multiple Channel Variable Time Delay System using a Spatially Integrated Optics Implementation. This optical beamforming network will be mated with the multiband aperture.

26

6.0 CONCLUSION

A multiband active array has been developed that demonstrates the feasibility of a single aperture that operates on two widely separated frequency bands (L and X). While conformal multiband arrays have been previously demonstrated [6], this design addresses the integration of radiating elements, T/R modules, thermal management systems, signal distribution networks, and prime power systems into a common volume without sacrificing performance at either frequency. Low profile radiating element designs have been derived which demonstrate broad radiation patterns as required for array wide angular coverage, and well behaved impedance properties for acceptable interface with active T/R circuitry. The multiband test aperture used for element evaluation accommodates all of the components of the fully active array and may be employed to fully characterize such systems. Demonstration of the multiband test aperture in conjunction with an optical domain beamforming system is proceeding.

27

7.0 ACKNOWLEDGEMENTS

8.0 REFERENCES

1. Sonnet Software, 135 Old Cove Road, Suite 203, Liverpool, NY 13090.

2. Wheeler, H. (1972) A Survey of the Simulator Technique for Designing a Radiating Element in a Phased-Array Antenna, Phased Array Antennas/Proceedings of the 1970 Phased Array Antenna Symposium, Artech House : 132-48.

3. Lee, R., Huynh, T. and Lee K. (1989) Experimental Study of the Cross Polarization Characteristics of Rectangular Patch Antennas, 1989 IEEE Antennas and Propagation Society Symposium : 636-9.

4. Hansen, R.C., Editor. (1985) Microwave Scanning Antennas Vol II, Peninsula Pub., Chapter 3.

5. Zmuda, H. and Toughlian, E. (Feb 1992) Adaptive Microwave Signal Processing: A Photonic Solution, Microwave Journal, Vol. 35, No. 2 : 58-71.

6. Zanel, V.J., et.al. (1986) Dual Band Conformal Element, RADC-TR-85-137. Final Report, Contract F19628-83-C-0006. Boeing Aerospace Co. ADB102494L

DESIGN OF AN INTEGRAL

IFF ARRAY FOR A SLOTTED ANTENNA

G. E. Evans

J. M. Vezmar

Westinghouse Electric Corporation

Electronic Systems Group

Design And Producibility Engineering Division

Baltimore, MD 21203

1

Abstract

Numerous military radar antennas radiate from slotted waveguide faces, and require IFF operation as well. This paper describes the design of an integral slotted array for the beacon, and provides measured data on the components. The beacon array drives the space between the radar sticks to produce sum, difference and reference patterns. It is steered off broadside to account for the radar squint angle, and radiators have been matched in a simulator. Special steps are necessary to avoid affecting the radar pattern and to provide isolation. The feed networks are arranged to lie flat against the back of the radar array. Designs for the AN/TPS-70 have been considered.

2

1. Background

Radar antennas are commonly made using series-fed edge-slotted waveguide sticks. Such arrays are usually horizontally polarized and may squint in azimuth with frequency. In most cases it is a major disadvantage to add a separate antenna for L-band beacon or IFF, since the radome size or wind resistance is significantly increased. The IFF antenna may require a skewed mounting to align the beams with the squint. This paper describes a means of using the space between waveguides to integrate a beacon antenna. It offers many advantages:

1. No radar interaction

2. No added height

3. No rotation

4. Additional gain and reduced beamwidth

5. All beacon beam types (e.g. sum, reference, monopulse)

6. Less than 2" added thickness

7. Uses the radar radome

2. Radiator Design

Figure 1 shows a section of slotted waveguide from a typical radar array face. The polarization is horizontal and the waveguide extrusions are designed to have a trough between rows that suppresses vertical polarization. The Integral L-band beacon signals are vertically polarized, and will radiate through the slot in this region. For the typical S band radar case, the slot and row spacings are smaller than necessary for the 1.03 to 1.09 GHz band, so we can drive every other row at every third slot spacing. The radar array may have very low sidelobes.
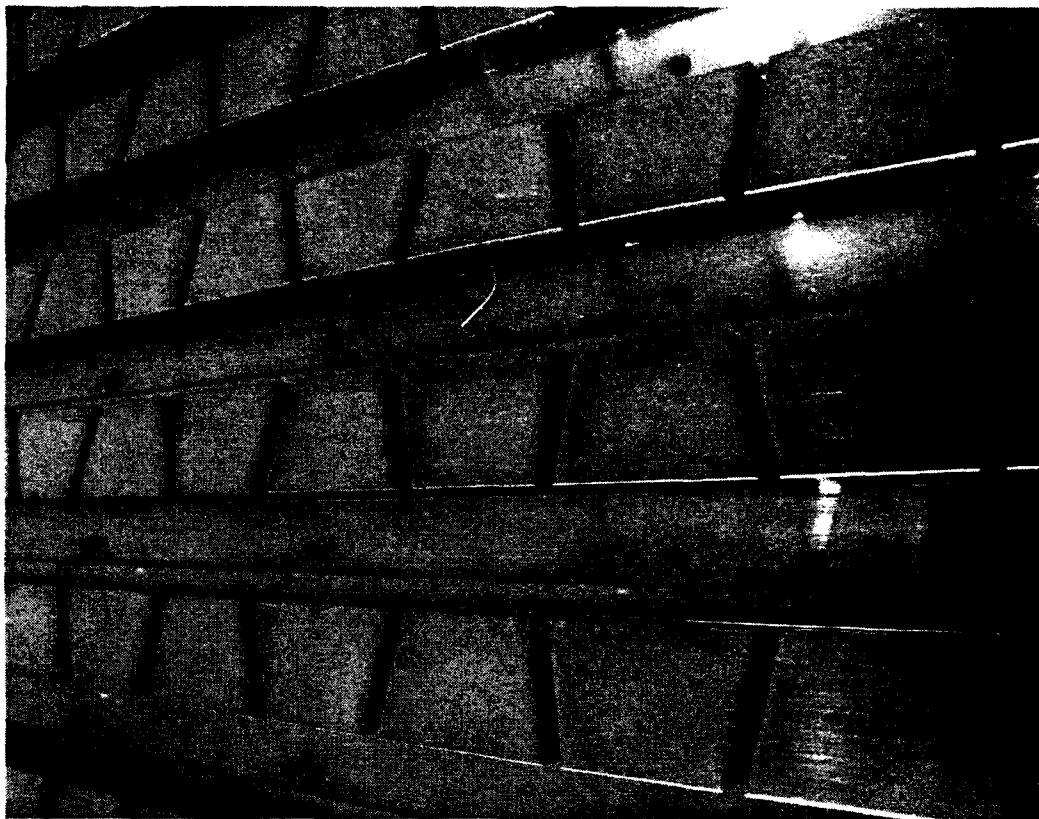
3

Figure 1. Slotted Waveguide Array Face

To avoid grating lobe residues in the radar pattern, we must make the IFF slots invisible to the radar signal with chokes.

Figure 2 shows the design for the TPS-70 system. It is quite difficult to drive high impedance slots from a 50 ohm line over a wide bandwidth in a very limited space. We therefore start by using one long slot without short circuits between elements. Adjacent to every radar slot we require a choke to make the slot appear shorted at S-band. The radiator must transform the impedance of space through the narrow path between waveguides, which tends to add significant capacitance. We therefore add the inductive septum between IFF elements, and drive the gap as close to the aperture as possible.
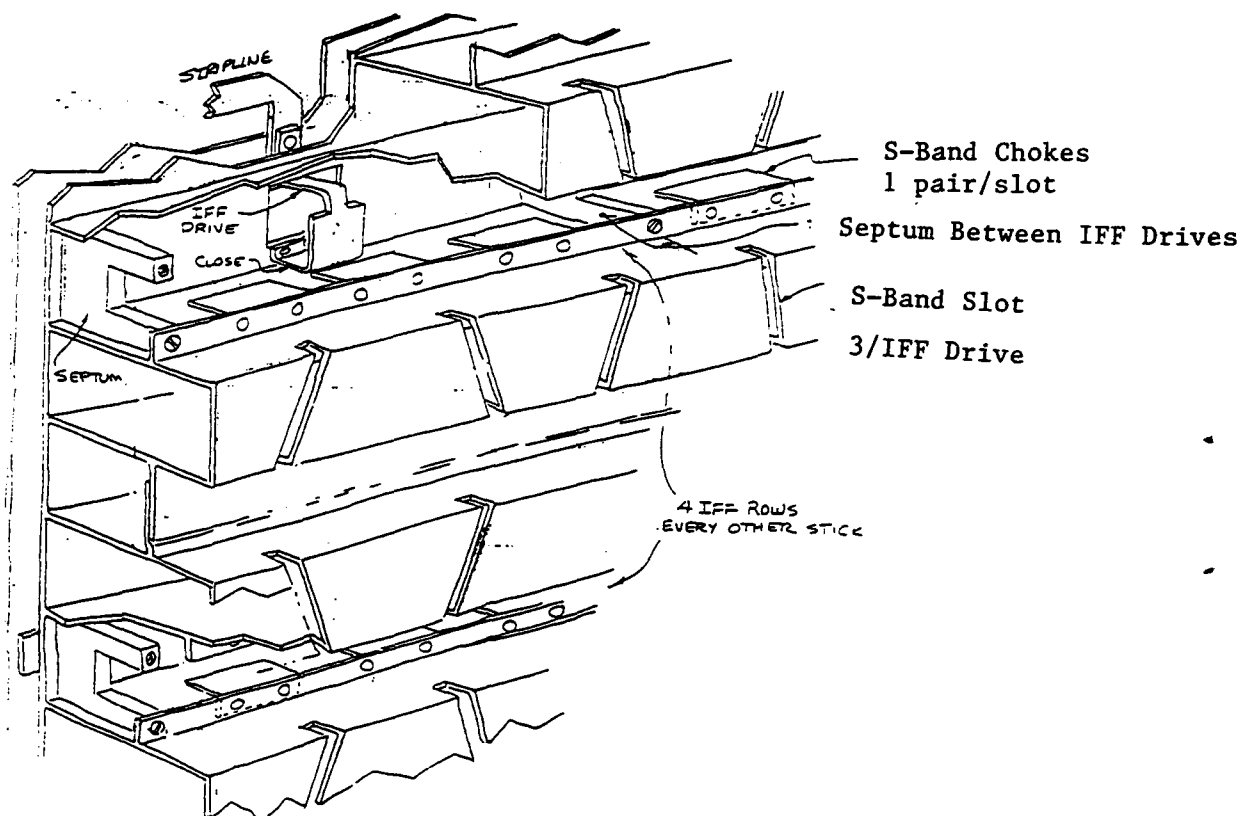
4

Figure 2. Integral IFF Antenna

This allows us to use most of the gap for the unavoidable cavity behind the slot.

The drive is from a stripline feed which is nominally 50 ohms. We choose air-dielectric stripline for low loss. It is essential that the feed be compact enough to lie flat against the back of the array. Therefore the internal matching must fit immediately behind the slots.

A single mode simulator has been designed and breadboarded to match the radiating element. A 1.15:1 maximum VSWR was acheived for the simulator. See Figure 3.

5

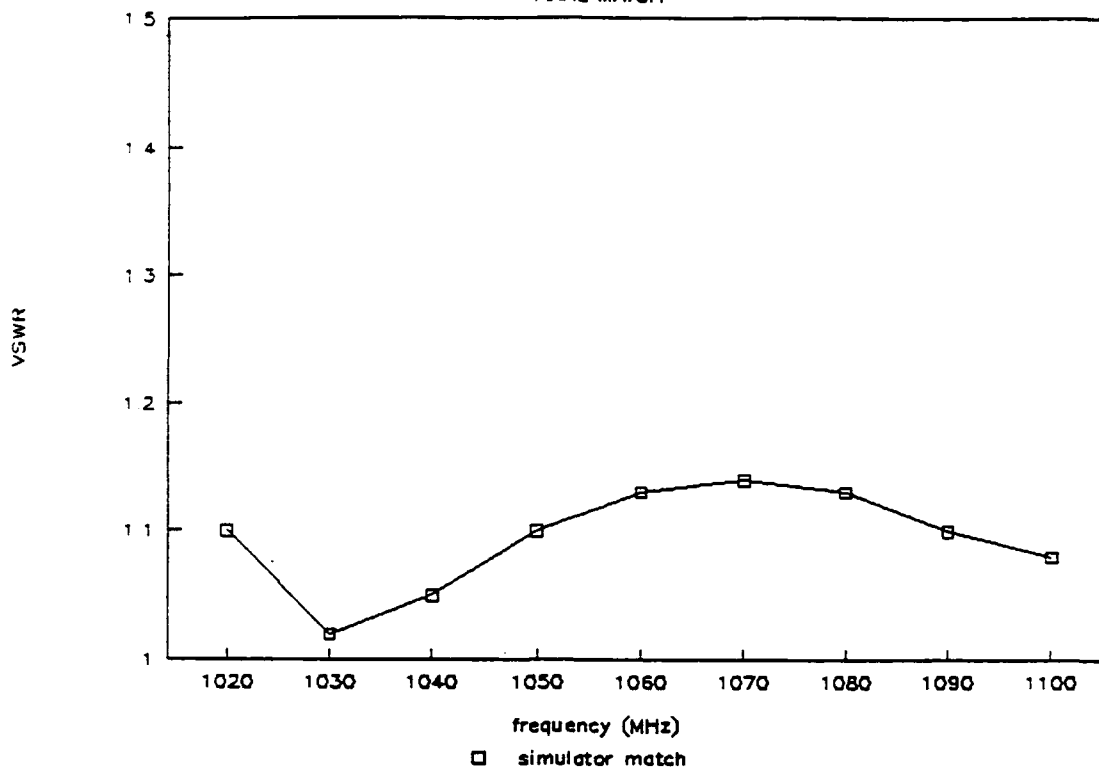# INTEGRAL IFF SIMULATOR

FINAL MATCH

Figure 3. Simulator VSWR

3. Array Description

For the particular beamwidths required for a tactical,
ground-based system, the integral IFF array consists of four rows of
radiators in the elevation plane and thirty-one columns in the
azimuth plane. The elements are spaced to lie between every other
pair of radar antenna sticks. Spacing in azimuth places one IFF
radiator at every third S-band slot. Since the IFF requires
multiple azimuth beams we collect elements first in elevation to
allow a single set of azimuth networks. Thus, the elements are fed
by thirty-one elevation 4:1 dividers which are in turn fed by a
double layer azimuth divider, producing sum, difference and
reference patterns.

6

The entire feed network will be a triple layer 1/2" ground plane spaced air dielectric stripline package.

Figure 4 shows elevation patterns measured with a section of the array eight sticks high in elevation with simulator walls in azimuth. Figure 5 shows computed azimuth patterns. It shows that the large available area allows narrow beams and high gain. Additional work is anticipated to build a full array breadboard so azimuth patterns and gain can be measured.
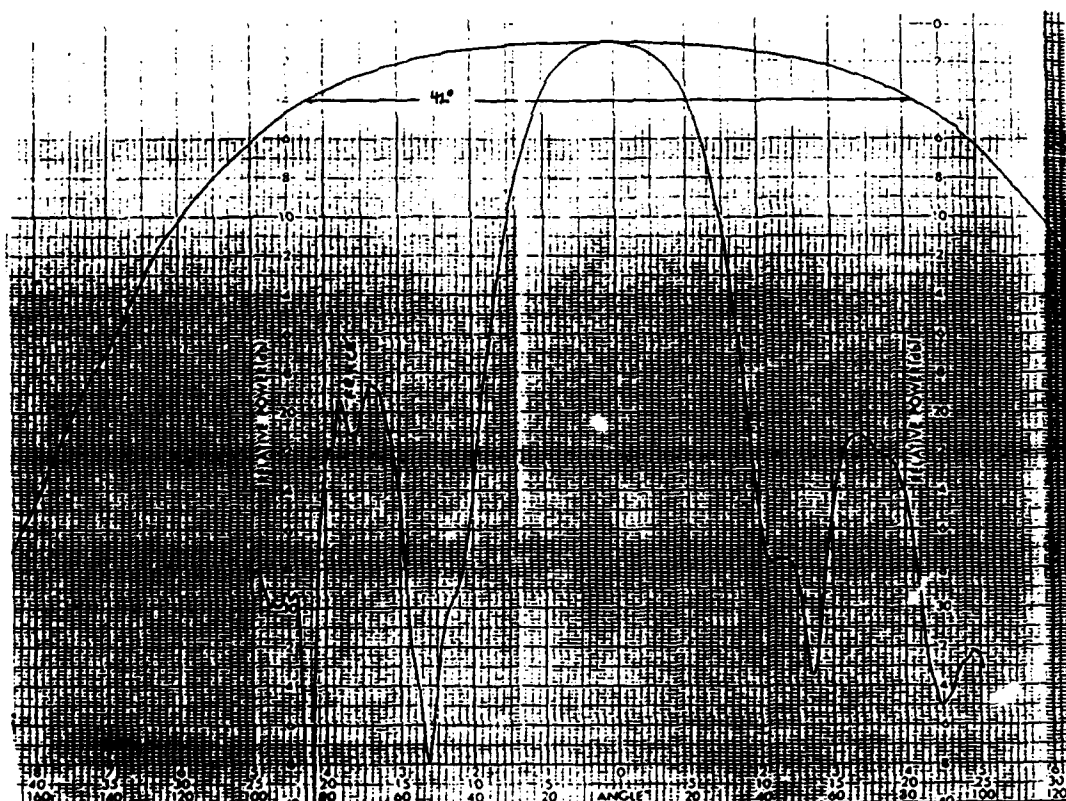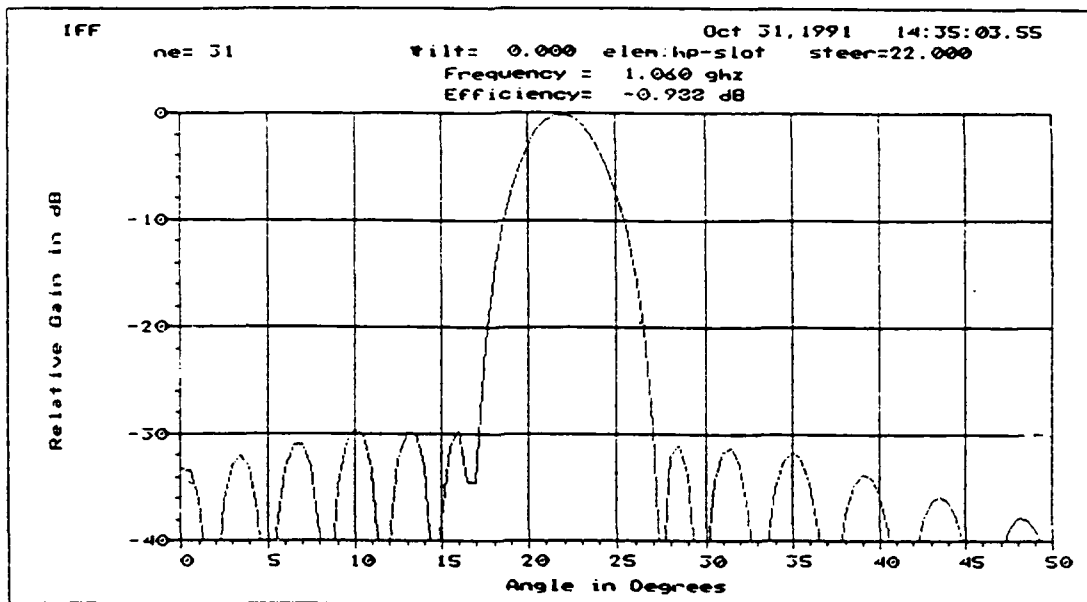

Figure 4. Measured Elevation Pattern, f=1.035 GHz
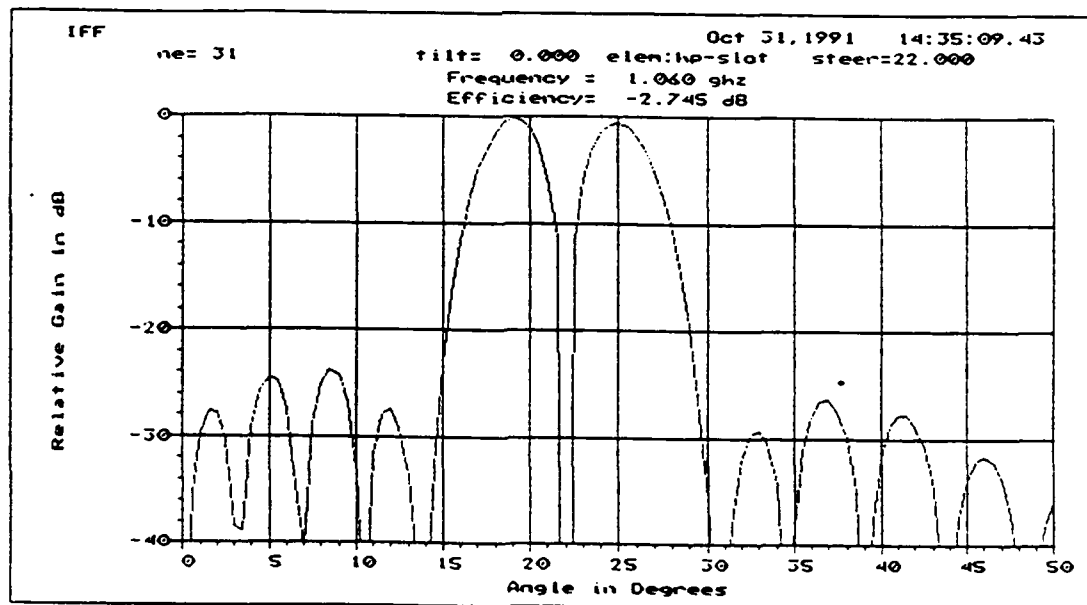
7

Figure 5a. Computed Azimuth Sum Pattern

Figure 5b. Computed Azimuth Difference Pattern

8

4. Conclusion

The improved performance coupled with the compact physical characteristics and simplicity should result in wide application of such an array. It adds negligible depth to the array, and has no discernable effect on radar performance. We anticipate that the added gain, resolution, and pattern options will significantly improve the beacon utility.

9

A Wideband Sub-Array Radiator
for
Advanced Avionics Applications

by
Jerome H. Pozgay
Missile Systems Division, Raytheon Company
Tewksbury, Massachusetts

The wideband requirements of the Air Force's Electronic-Combat Multifunction Radar (EMR) program and the Navy's Airborne Shared Aperture Program (ASAP) have significantly advanced the performance goals for phased array radiators. A new, light weight, well matched radiator for a dual linearly polarized quad notch sub-array has been developed to meet the needs of these future systems. The sub-array radiator has an operating bandwidth exceeding 3:1 as defined by a well-behaved embedded element pattern and better than 2:1 match throughout the frequency/scan coverage volume.

In addition to providing a complete description of radiator performance, this paper will also discuss and compare those unique program requirements which provided the primary impetus for selecting the quad notch.

1.0 Introduction

Requirements for wideband airborne radars are being refined in the Air Force's Electronic-Combat Multifunction Radar program (EMR) and the Navy's Airborne Shared Aperture Program (ASAP). As long range goals, both programs seek to develop radars with wide operational bandwidth, and, as necessary, wide instantaneous bandwidth. At present, however, both programs are concentrating on demonstration of key wideband RF technologies - notably the T/R module, wideband manifolds and wideband radiators. These technology demonstration programs follow preliminary trade-off studies which addressed suitable RF and systems architectures and established performance goals for principal components and subsystems.

A major conclusion of Raytheon's EMR and ASAP contributions is that future systems will require antenna apertures with low radar cross-section and IR signatures for compatibility with stealth platforms. This can be achieved with wideband active antenna apertures when used on a shared aperture basis to serve the functions of radar, electronic warfare and other sensor operations: the single antenna can replace the multiple antennas and eliminate their accompanying radar reflections.

An operational bandwidth on the order of 3:1 and very wide instantaneous bandwidth will be required for future airborne apertures. Shared aperture RF and total systems concepts have been developed for these bandwidth requirements and have been shown to be viable provided the requisite component performance can be achieved. To ensure viability of the systems concepts, Raytheon has contri-

2

buted technology advances under its continuing Wideband Active Array IR&D program for passive wideband components and under several inter-related IR&D programs for development of wideband T/R modules. The present paper discusses the development and performance of the fundamental radiator for the orthogonal pair of collinear radiator pairs known as the quad-notch radiator.

The stripline-fed flared notch radiator has been the dominant wideband radiator for over 20 years. Since its introduction by Lewis, Fassett and Hunt[1,2], variants of this radiator have appeared at the front ends of a large number of wideband array concepts (requiring greater than one octave bandwidth). It has been variously configured for dual linear operation with cophasal and disjoint phase centers, circular polarization with both phase center possibilities and single linear polarization.

Figure 1 shows a sketch of the quad-notch radiator. The radiator consists of two orthogonally polarized, two-radiator sub-arrays. The elemental sub-array radiators are stripline fed flared notch radiators on low
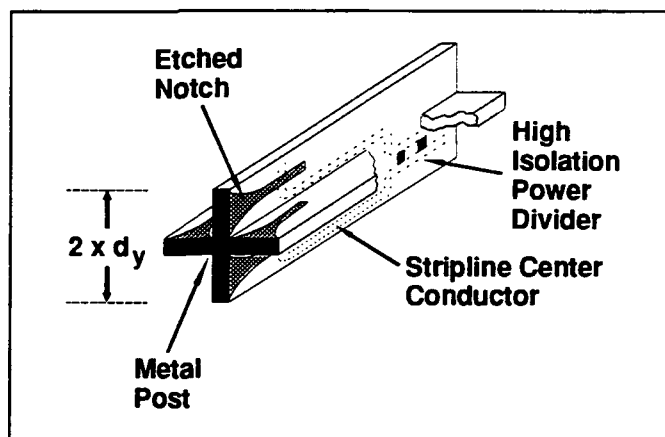

Figure 1. Sketch of a Quad-Notch Radiator

3

loss glass-loaded teflon substrate. Collinear pairs are combined with high isolation, low loss power dividers: high isolation prevents reactive resonance[3] formation and reduces non-specular RCS spikes.

When arrayed, the quad-notch radiator produces a grid which can be viewed as either square or 45 deg triangular. A sketch of the arrayed radiator and grid is shown in Figure 2. The grid dimensions are selected in standard fashion with the
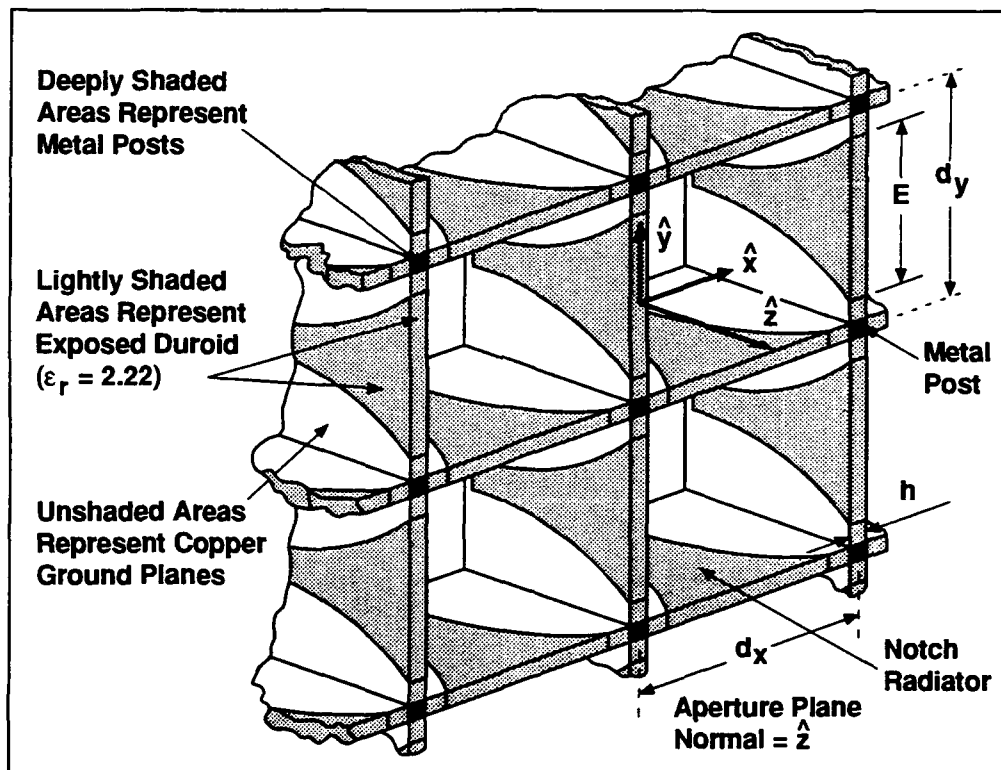

Figure 2. **Sketch of Dual Polarized Notch Radiator Array Segment**

caveat that the sidelobe criteria for the array result in keeping the first grating lobe and its first two sidelobes outside real space throughout the scan/frequency coverage volume. An important aspect of this grid is that the H-plane spacing is

considerably smaller than the fundamental grid. The reason here is that phase center displacement is about the center of the sub-array, at 45 deg to the planes of the radiators. In essence, then, the sub-arrays can be thought of as interleaved, with physical overlap at the boundaries along the cardinal planes of polarization.

Of the many factors leading to the final design configuration of the radiator, the most significant is the tight H-plane spacing of the sub-array radiator that can be achieved with the 45 degree grid. Because of this tight spacing, the present radiator is free of H-plane resonances well beyond the upper operating band edge, yet still packs the aperture efficiently. In addition, the present sub-array radiator is matched to considerably better than 2:1 at broadside and wide angle scan over a 4:1 frequency band and has an element pattern which is very nearly $\cos\Theta$ over a 3:1 frequency band. Further details of sub-array radiator performance will be presented later in this paper.

The remainder of this paper is given to discussions of key requirements for an advanced avionics radiator, some design details and an in-depth examination of sub-array radiator performance.

2.0 Requirements for an Advanced Radiator

Table I presents a summary of principal requirements for an advanced avionics system radiator. In general, these follow from the recognition that future systems will require significant advances in range performance, multifunction capability,

5

Table I
Advanced Radiator Requirements

Parameter	Requirement
RF Architecture	Wideband Active Array
Bandwidth	$\geq 3{:}1$
Scan Coverage	≥ 60 deg 1/2-angle cone
Radiator Size	$0.707d_x \times 0.707d_y$
Radiator Weight	Minimum
Power Handling	> 20 watts CW
Match	$\leq 2.0{:}1$
Efficiency	$> 80\%$ (-1 dB)
Maintainability	Replaceable radiator/module
Polarization	Switched linear

covertness, reliability and target recognition capability. These are, of course, the implied benefits of a wideband active aperture RF architecture. An example of one such system is illustrated in Figure 3.

2.1 *Array Architecture*

This RF system is comprised of a wideband, wide angle scanning, dual polarized aperture of quad-notch radiators, a bank of wideband T/R modules, wideband column distribution networks, and a pair of wideband switched Rotman/Turner lenses. The configuration has both wide operational and instantaneous bandwidths. Wide operational bandwidth is provided by the array of wideband radiators and the associated T/R modules and feeds. Wide instantaneous bandwidth is provided by the Rotman/Turner lenses, the slowly varying properties of the

6

T/R modules and, as needed by the aperture aspect ratio, switched time delay units at the module level.
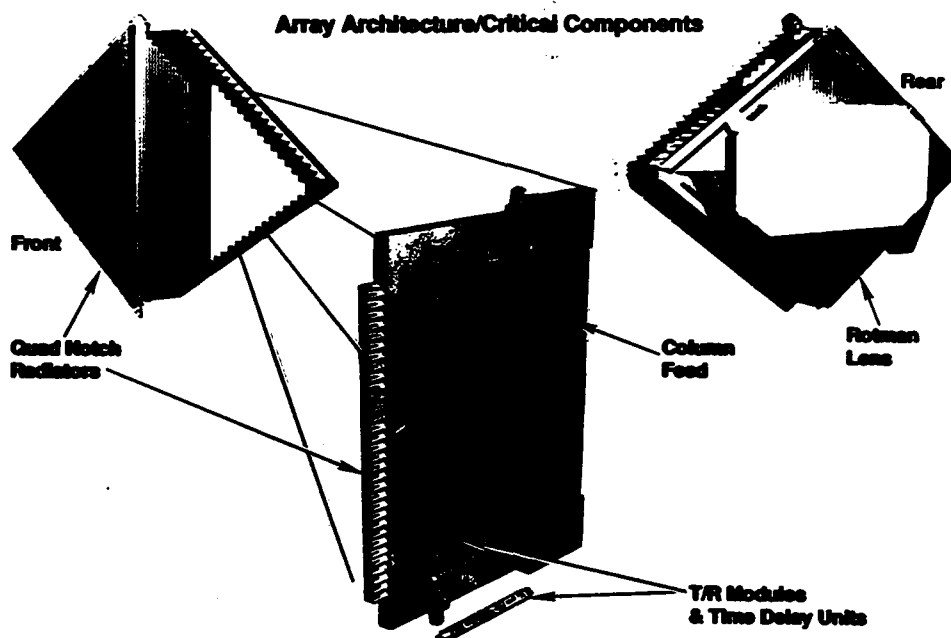

Figure 3. Wideband Active Array Architecture and Major Components

2.2 *Operational Bandwidth*

The selection of 3:1 operational bandwidth addresses most avionics requirements for radar and can support many EW needs. In addition, extreme frequency agil-ity is of itself a useful ECCM technique.

2.3 *Scan Coverage*

Advanced avionics systems will provide 4π steradian coverage for most EW functions and some radar functions. However, in a tactical situation, forward cover-

7

age requires greatest radar range, and it is reasonable to assume that advanced aircraft will continue to carry a powerful forward looking radar. If an electronically scanned array were provided with a mutual coupling free radiator, the gain loss at scan angles greater than 60 to 70 degrees would be still prohibitive. Thus, if wider angle long range coverage is desirable, multiple apertures will be required, perhaps mounted in the aircraft wing roots at some significant angle off the vehicle body axis. Under these circumstances, a requirement for wider than 60 degree ½-angle cone coverage would be reasonable, provided it was understood that both gain and pattern quality degrade rapidly beyond 60 degrees from aperture normal. An interesting, and perhaps exploitable, characteristic of the quad-notch sub-array radiator is the apparently weak dependence of mismatch on scan angle - even at extreme scan angles.

2.4 *Radiator Size*

Selection of radiator or grid size is based on antenna performance criteria and RCS criteria. For a conventional configuration of notches in a wideband architecture, the overriding criterion for grid selection is the elimination of non-specular RCS spikes. The quad-notch radiator, on the other hand, interlaces the sub-array radiators in such a fashion that the aperture plane discontinuities occur on a very small grid, while the phase center discontinuities occur on a much larger grid. The net result is that a poor power combiner in a quad-notch radiator can produce significant reductions in wide angle RCS spikes relative to apertures designed around a single notch per phase center.

8

2.5 *Radiator Weight*

The principal drawback of the quad-notch radiator relative to the single notch or pair of orthogonal notches per phase center is that oversampling is achieved at the expense of an increase in material, and, hence, weight. The design approach here is to select light weight, low relative permittivity materials. Both criteria are satisfied by copper clad, glass loaded teflon.

2.6 *Power Handling*

For an active aperture architecture, power handling issues are related to average, not peak power, even over narrow operating and instantaneous bandwidths. The state of the art in T/R module design is a long way away from producing an output which could conceivably cause break-down internal or external to a stripline fed radiator. But it will be necessary to dump some heat produced by the losses in the stripline/radiator material. Again, the design approach here is to select glass loaded teflon substrates and rolled copper cladding to minimize the loss.

2.7 *Match*

Until recently, state-of-the-art in broadband circulator design had not included a device which was better matched than 2.5:1 over a 3:1 band. The design objective was, therefore, to achieve a radiator match consistent with power amplifier output match requirements as well as to minimize the power lost to the radiation

9

field. But now, the excellent wideband circulator performance which has been obtained substantially removes the first difficulty, and in a sense, relieves the onus on the radiator. Even so, the cost, in terms of system efficiency, to the active aperture architecture remains sufficiently high to warrant continued attention to the issue of radiator efficiency.

2.8 _Efficiency_

Overall radiator efficiency is a function of mismatch and I^2R losses. The objective here is to minimize the ohmic loss in the matching structure. This should not be (and isn't) difficult since a design objective is to create a very low Q circuit.

2.9 _Maintainability_

The maintainance of an active aperture array poses significant design constraints for an aperture comprised of notch or quad-notch radiators. The principal goal here is to develop a means of disassembling and reassembling the aperture of radiators, associated T/R modules, coolant channels, RF feed networks and DC/power distribution networks without disrupting the radiator groundplane continuity. A logical approach is to fully integrate columns consisting of radiators, modules, coolant channels, and DC and RF distribution networks. Columns would then be integrated into the array structure and locked together at the aperture and behind the aperture. At the aperture plane the key is to establish continuity of the stripline ground planes from column to column.

10

2.10 *Polarization*

The battlefield is never benign, and the EMR and ASAP systems will be expected to operate under severe weather conditions. Rain rejection can be effected with use of circular polarization, or with transmission and reception of orthogonal linear polarizations. Overall, there is little performance difference between transmission and reception of orthogonal circulars and orthogonal linears (at least for complex targets in rain clutter). The distinction is in the implementation. It is simply more complex to implement a T/R module which provides dual circulars than one providing time multiplexed dual linears.

3.0 General Radiator Design Principles

3.1 *Grid Selection*

In a wideband aperture, there are too many radiators per square wavelength except at the uppermost frequency. This simply means that the radiator realized gain pattern and directive gain are quite different over the bulk of the operational bandwidth. Lack of equivalence here does not preclude achieving a perfect match over the full scan volume[4]. And we can extend this argument to say that, temporarily setting aside such practical issues as cost and architectural complexity, the natural conclusion of the element-gain paradox is that the optimum aperture condition is to be oversampled - this is the condition of the quad-notch radiator, its elemental sub-array radiators and every successful notch radiator design for an electronically steered phased array.

11

These considerations create a design dilemma. Should the grid be selected to minimize the radiator count, or should the natural oversampling of the wideband system also be allotted to the high end of the operating band in order to _improve_, as it must, at least by inference, performance in that region? Neither situation is really very acceptable, so it is fortunate that they are not mutually exclusive.
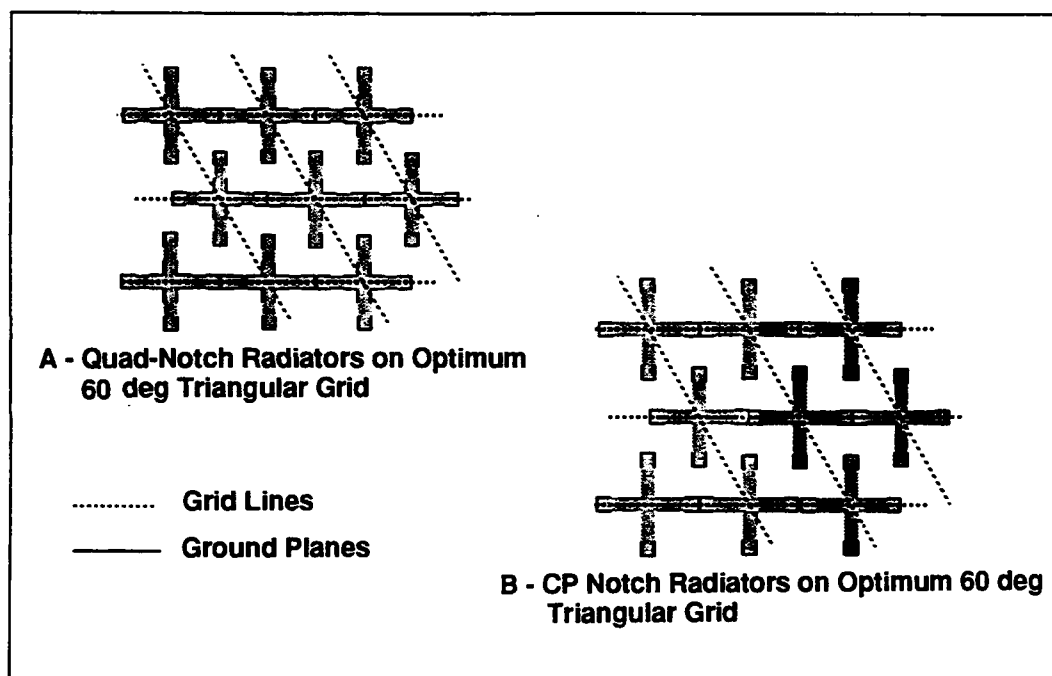
Figures 4 and 5 show the results of arraying circularly or dual linear polarized

Figure 4. 60° Triangular Grids of Notch and Quad-Notch
Radiators

notch and quad-notch radiators on conventional 60° triangular and rectangular grids, respectively. It is obvious from Figure 4 that the optimum triangular grid is not at all optimum for dual linear or circularly polarized radiators for the

12

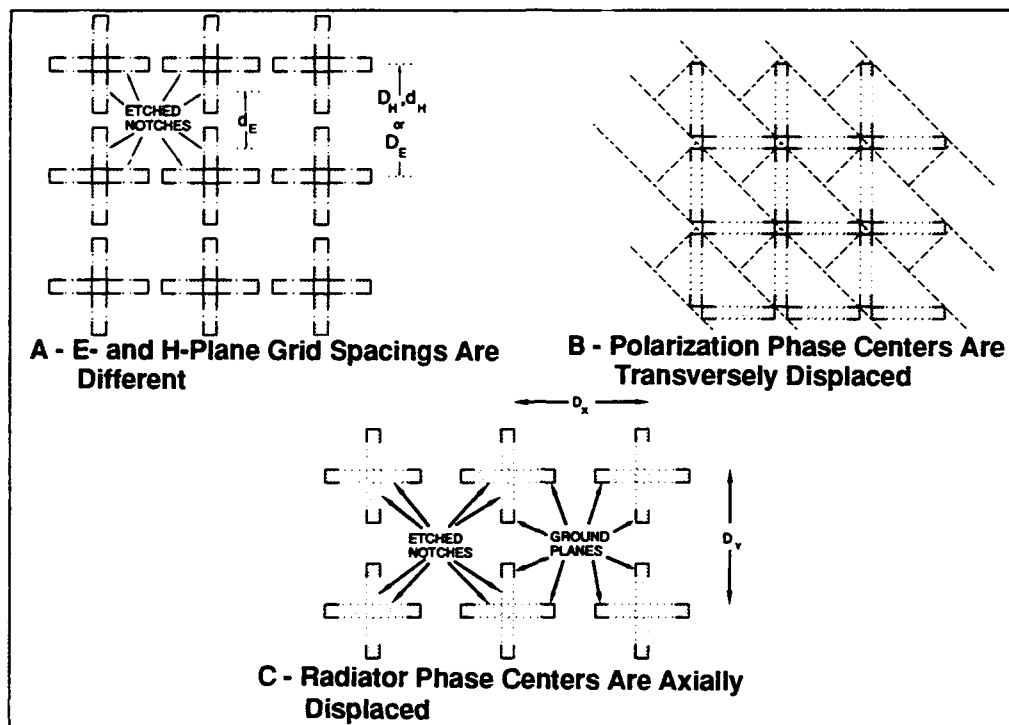simple reason that they have rectangular, not triangular, symmetry. On the other

Figure 5. **Rectangular Grids of Notch and Quad-Notch Radiators**

hand, the quad-notch rectangular configuration in Figure 5a lacks a symmetrical relationship between E- and H-planes: and circularly polarized apertures of notch radiators are realized by phase center displacement in the plane of the aperture (5b) or normal to it (5c).

A truly optimum arrangement for the quad-notch radiator is shown in Figure 6. In this 45° grid orientation, the sub-array is placed on the diagonals of the unit cell, and the spacing between elemental sub-array radiators is half the diagonal

13

length. In this manner, a dual grid is obtained. Elemental radiators form a square grid along the principal polarization axes while phase centers are arrayed along
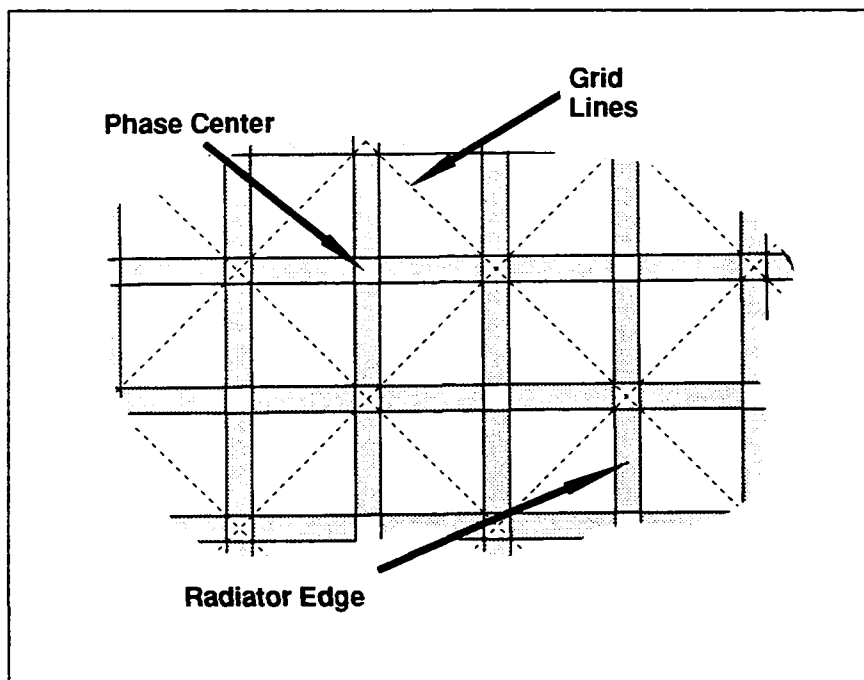

Figure 6. Quad-Notch Radiator on 45° Triangular
Grid

the intercardinal planes. It is obvious from the Figure that the 45° grid arrangment matches the polarization symmetry of the radiator as well as the physical symmetry. There are numerous advantages to this arrangement, but, perhaps the most significant is that phase center spacing can be determined on the basis of antenna coverage requirements rather than ancilliary issues - that is, the number of phase centers can be optimized relative to the maximum operating frequency while maintaining an oversampled, hence optimum by inference, distribution of elemental sub-array radiators. The optimum is, of course, a more dense packing

14

than would be obtained on a 60° triangular grid, increasing phase center density by roughly 12%.

3.2 *Power Divider Selection*

The interleaving of sub-array radiator and phase center grids results in an aperture plane sampling that is on the order of one third wavelength at the maximum operating frequency. This means that the upper edge of the operating band is approximately 33% below the frequency at which the first retrodirective endfire beam can be formed by the aperture face. But it also means that the phase center spacing can support endfire retrodirective beams below the maximum operating frequency. The influence here is on the selection of an appropriate sub-array power divider for the combination of elemental radiators to form the collinear pair sub-arrays. A reactive divider poses several problems with regard to retrodirective beams, and, as shown by Schuss and Hanfling[3], with regard to maintaining a wideband, wide angle scan match at the sub-array input. A reactive power divider has considerably greater power handling capability than, say, a Wilkinson, though matched 3- or 4-port dividers have the distinct advantage of eliminating internal sub-array resonances and can significantly reduce the level of any retrodirective beams which might be generated by the phase center spacing. And, in particular, a matched 4-port divider offers considerable power handling potential.
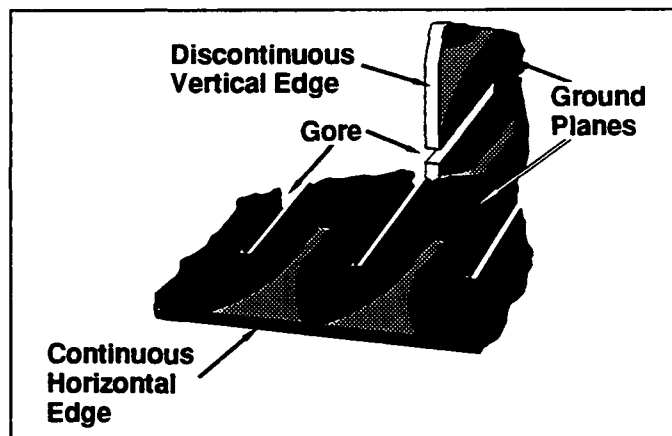
3.3 *Material Selection*

Over the years, the notch radiator has been configured for applications requiring various polarization capabilities. For the most part, the development and produc-

15

tion environments for these applications have encouraged the use of indivual radiators. As we look toward applications wherein the phase center counts will be in the thousands per aperture, it is becoming apparent that cost effective radiator manufacturing methods will play an important role in keeping the overall cost of the active aperture system in check. The examination of this issue has lead to a few surprising requirements for both configuration of the aperture plane and for the selection of appropriate radiator substrates.

In order to reduce manufacturing costs, it was initially convenient to configure developmental dual polarized notch and quad-notch array apertures such that for each polarization, single stripline boards contained entire columns or rows of copolarized radiators or sub-arrays. The boards were gored, as shown in Figure 7, in order to permit interleaving to form a "wine case" structure (often referred to as an "egg crate"). One of these sets

Figure 7. Configuration Producing Assymmetric Resonances

of boards, in this case horizontal boards, has a front edge which is continuous over its length. The other is discontinuous in order to accept the orthogonal sets. It was found, when measuring H-plane patterns of the discontinuous boards that the active notch radiators efficiently coupled to the continuous board parallel plate TEM mode. This mode being reactively terminated, it loaded down the active

16

polarization and produced H-plane resonances at any and all measurement frequencies.

The conclusion drawn here is that the size of the elemental sub-array radiator must be such that the TE_{10} mode of the effective loaded rectangular waveguide is below cut-off. This effective rectangular guide is formed when the aperture plane is gored to prevent excitation of the parallel plate mode for either linear polarization. Since the cut-off frequency of the loaded guide is inversely proportional to the square root of the relative permittivity of the notch radiator substrate, the design rule is more specifically to use the low loss material with the lowest relative permittivity.

3.4 *Sub-Array Matching Structure*

As presented by Lewis and Pozgay[5] and by Lewis *et al*[6], the rudamentary flared notch radiator is double stub tuned. With reference to Figure 8, the two stubs are the length of stripline center conductor which proceeds past the etched notch edge, and the length of etched flared notch which proceeds past the center of the stripline center conductor. The center conductor is substantially terminated in an open circuit, while the notch is substantially terminated in a short.

The operating principle here is to maximize the stripline magnetic field in the slot by establishing an effective short circuit at the slot edge farthest from the stripline generator. Similarly, the reflection of the notch short circuit termination is an open circuit at the reference plane established by the center of the stripline center

17

conductor, at least at operating band center. Once this band center has been established, the design goal is to arrive at a broadband open circuit termination of the stripline center conductor which maintains a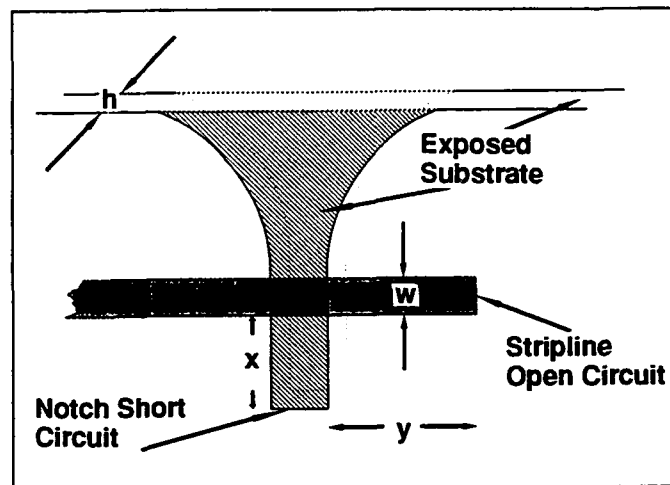n effective short circuit at the far edge of the notch. In the foregoing, it is implied that the aperture plane discontinuity plays a minor role in the design of the matching structure. As a matter of fact, its role is minor, but not negligible. As shown by Lewis and Pozgay[5], the details of notch shape and length in the vicinity of the aperture plane do not have a significant influence on the match of slitted parallel plate modes to the aperture Floquet modes. It has been observed in the laboratory that once a well behaved notch shape is settled on, the design process can concentrate entirely on definition of the stripline center conductor termination and the length of the notch shorting stub.

Figure 8. Anatomy of a Notch Radiator

4.0   Sub-Array Radiator Performance

The many design principles discussed above have been applied to arrive at a sub-array radiator design which meets all coverage and match requirements over a 3:1 frequency band, and has a useful extended range to greater than 4:1. The per-

18

formance was first evaluated in H-plane rectangular waveguide simulators, then in an array aperture consisting of 1799 ind. idual sub-array radiators.

4.1 *Performance in H-Plane Waveguide Simulators*

A set of three waveguide simulators, transitions and calibration kits was developed for the evaluation of the sub-array radiator design. The simulator sets are
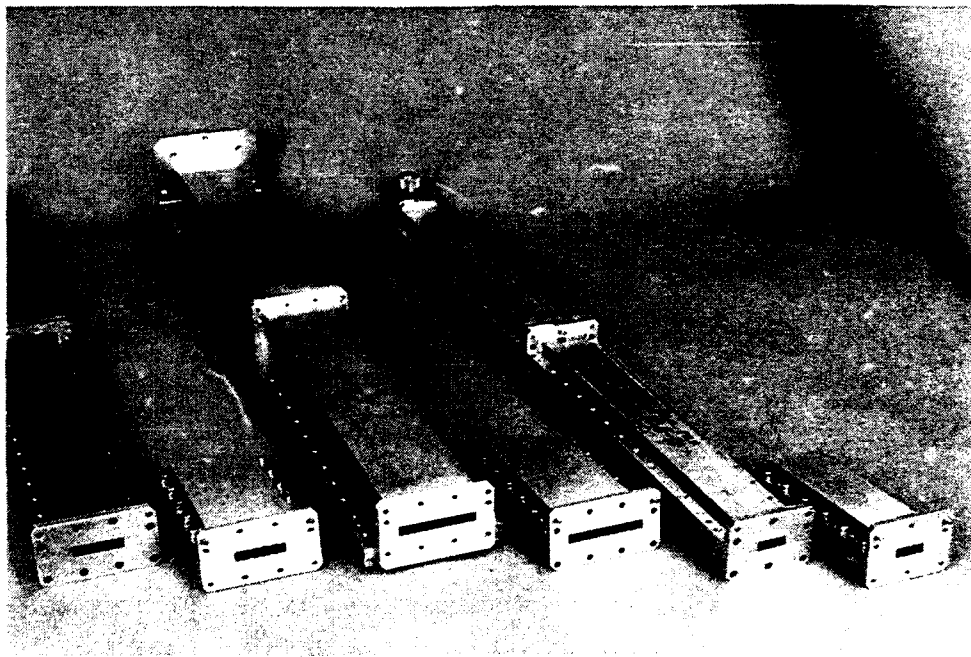

Figure 9. **Waveguide Simulator Sets**

shown in Figure 9. Each set consists of a radiator section, holding 3, 5 or 8 sub-array radiators; a 12 in. long section of straight rectangular waveguide with dimensions $Nd_x \times d_y/2$, where N is the number of sub-array radiators in the radiator section; a doubly tapered transition to a standard waveguide size and a labora-

19

tory quality transition. Alignment pins are provided at all flange interfaces to minimize step discontinuities in the waveguide chain.

An open element section is shown in Figure 10. The section consists of a U-channel, cover and set of radiators. The cover and U-channel have longitudinal pedestals for locating and centering the vertical radiators. Horizontal radiator halves are placed between the pedestals and horizontal radiator quarters are placed between the out-
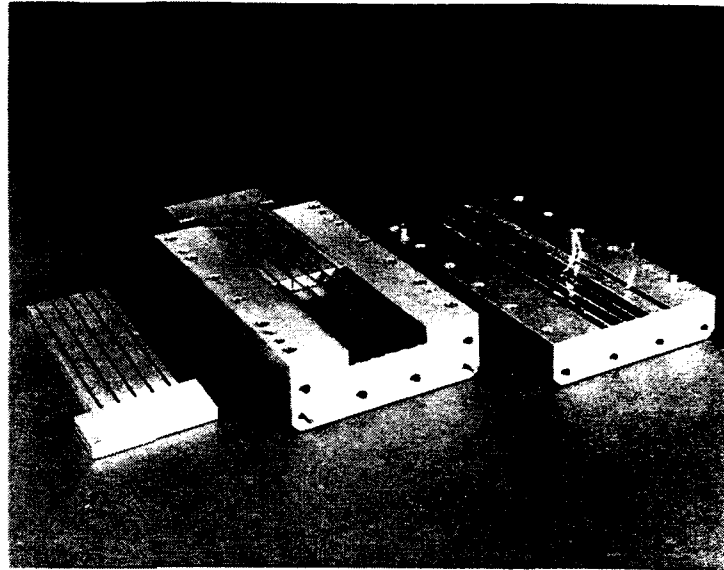

Figure 10. **Disassembled Simulator Element Section**

ermost pedestals and the waveguide walls. All radiators and partial radiators are held in place with double sided copper tape with conductive adhexive (3M product 1182), as shown in Figure 11. All radiators and partial radiators are edge plated.

The assembly of the element sections is aided by forks such as shown in Figure 10. A fully assembled element section is shown in Figure 12. Calibration pieces are shown in Figure 13.

Test results for the three simulator sets are shown in Figure 14. From approxi-
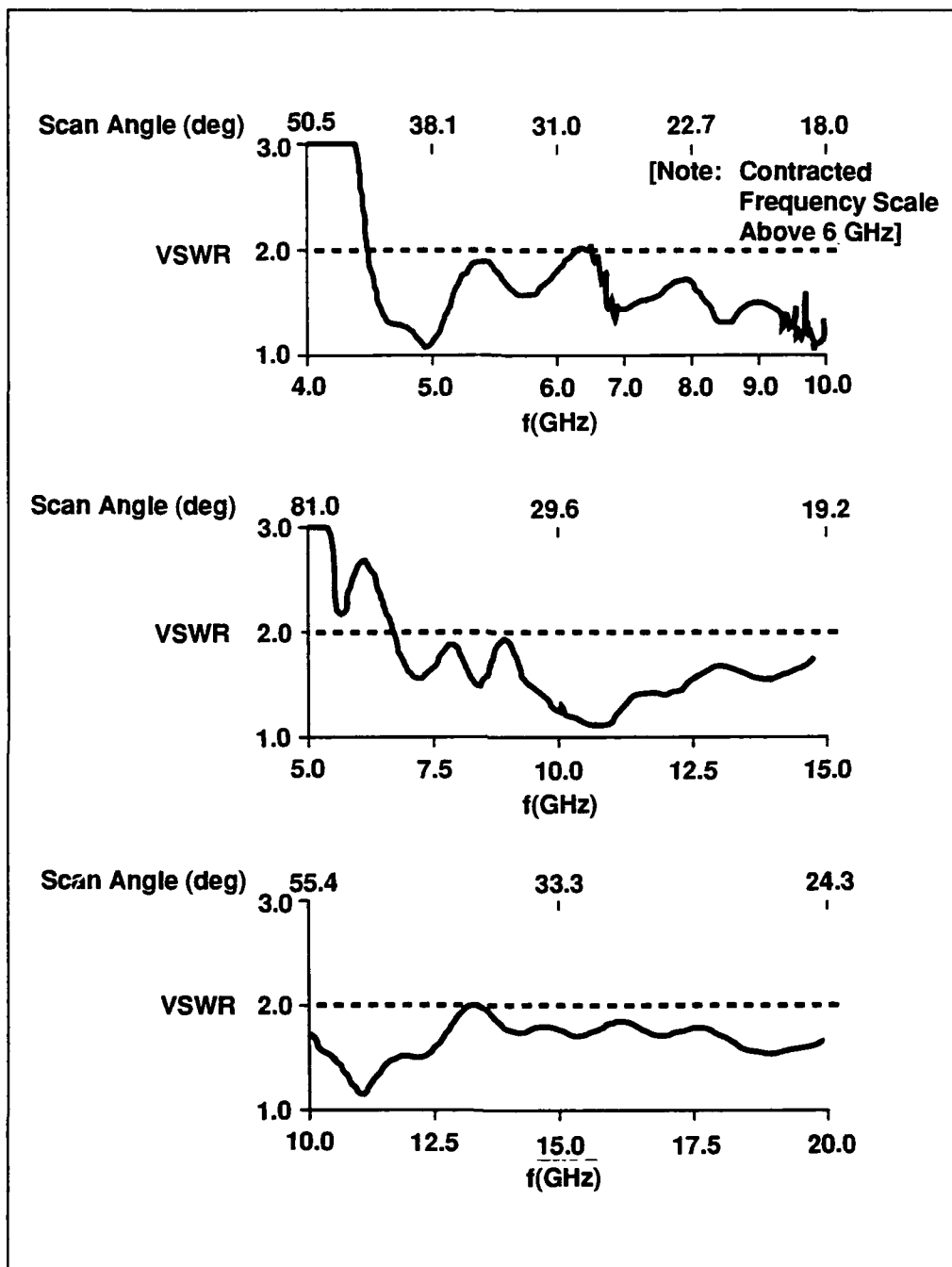
20

Figure 11. Simulator Assembly Technique

mately 4.5 GHz to 20 GHz, the VSWR of the elemental radiator is below 2:1, with the exception of a worst case match of 2.8:1 which occurs at approximately 6.2 GHz. The choice of simulators covers an angle range of 18° to 81°.

Figure 12. Fully Assembled Element Section

Figure 13. Simulator Calibration Set

21

Figure 14. Sub-Array Radiator Performance in H-Plane Simulators

22

4.2 _Embedded Radiator Performance_

Pattern and gain were measured for a single center elemental sub-array radiator embedded in an aperture consisting of 1799 identical radiators. In general, the element pattern showed $\cos\Theta$ shape, at least out to 60° off broadside. There was some deviation due to minor fabrication errors. Figure 15 shows the assembled
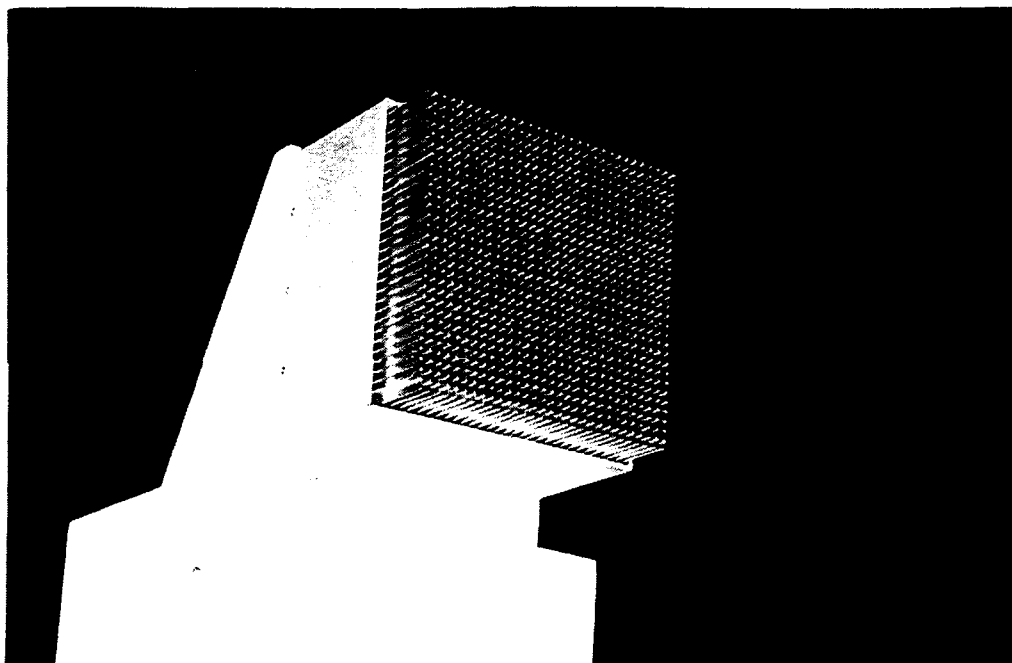

Figure 15. **Array Aperture Installed in Test Chamber**

aperture in the test chamber: the total aperture is approximately 7.25" x 7.25". The test unit has a protective plate jacket to prevent occasional damage to edge radiators. The shield and wooden test stand are covered with wideband absorber during testing.

23

A finer view of the aperture is shown in Figure 16. As is evident from the Figure, radiator placement has been well controlled in the assembly process. Quanti
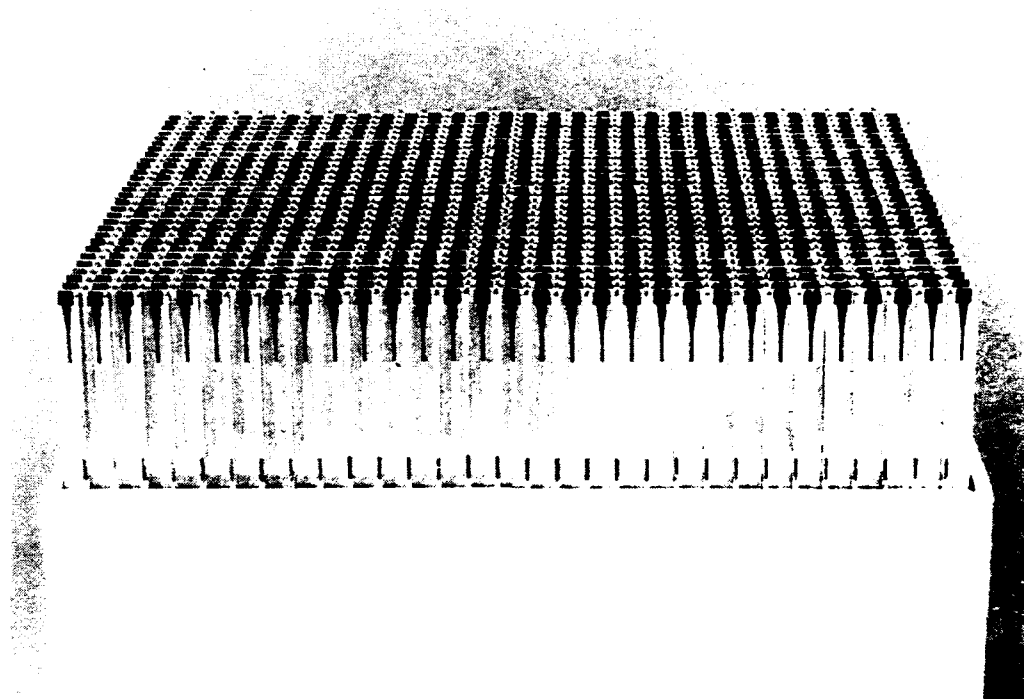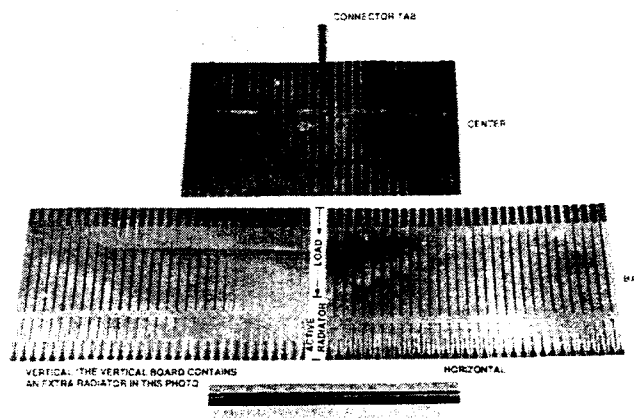

Figure 16. **Close Up of Aperture**

tative data was not collected on the positional accuracy of the radiators except in the vicinity of the center radiator. Transverse error was deemed immeasureable, while there is as much as 0.010" error normal to the aperture plane. The normal error arose from build-up of mechanical resistance in the final aperture integration step. Its effect was to produce some shape distortion in the H-plane patterns.

The aperture is comprised of three stripline board types, an aluminum backplate for mounting to the test stand and a connector. Twenty eight horizontal boards

24

contain 31 elemental sub-array radiators each, as does one center type board which contains the only accessible radiator port. Thirty vertical boards contain 30 elemental sub-array radiators each. The board types are shown in Figure 17. In this photograph, the vertical board contains an extra radiator (which is removed during a later assembly process step). The boards are slotted and edge plated to allow the interlocking arrangement known as "wine case" or "egg crate" construction.

Figure 17. **Stripline Boards for the Aperture**

With the exception of the center element of the center board, all radiators are internally terminated in a tapered metalized mylar load. The incorporation of the internal loads accounts for about 80% of the test board depth - the total elemental sub-array radiator length is about 1".

When the boards are interlocked to form the wine case, the aperture plane appears as shown in Figure 18. Note that the intersection of the slots surrounding the elemental sub-array radiators produces a square channel. As the slots are edge plated, this channel prevents intra-substrate coupling of the elemental radiators and loaded rectangular waveguide. In addition, the plated edges will adhere

25

to a conductive epoxy, thereby providing a means of bonding the boards in position.
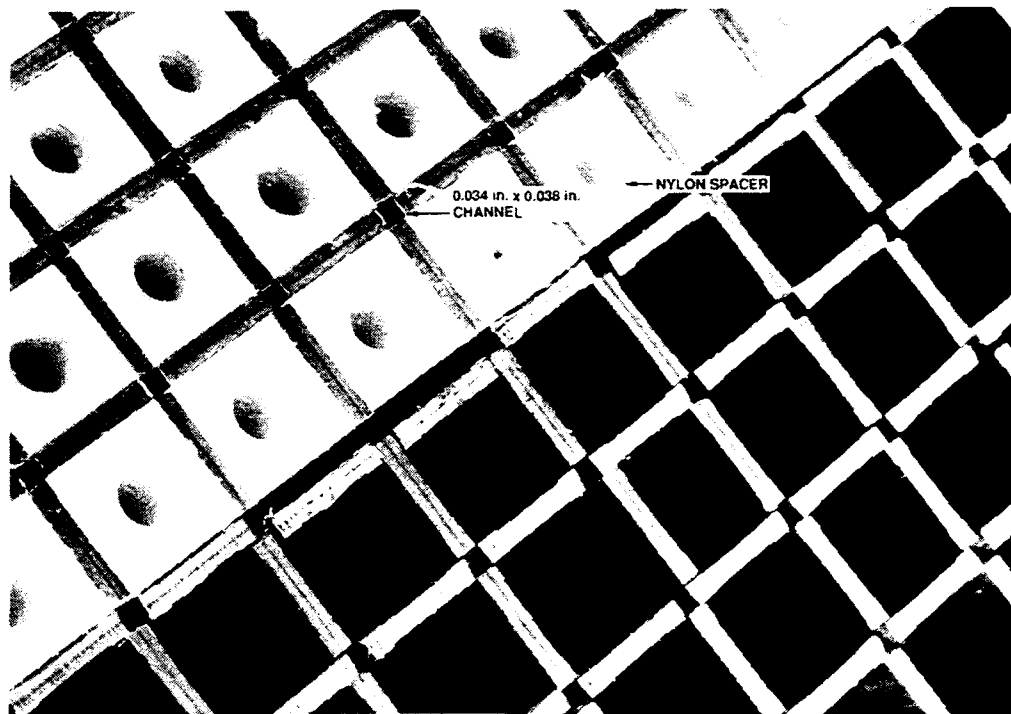

Figure 18. **Aperture Plane During Assembly**

The aperture was exhaustively tested over the full capability of the test range. Both pattern and boresight gain were measured. Figure 19 shows E- and H-plane patterns near measurement extremes. All measured patterns showed similar behavior. A $\cos\Theta$ pattern is superimposed on the measured data as is a replica, reduced by 2 dB. The elemental radiator performance was resonance-free throughout the measurement band.

Elemental sub-array radiator gain was measured at 100 MHz intervals from 4 GHz to 18 GHz. The reduction of gain data to cell efficiency is shown in Figure
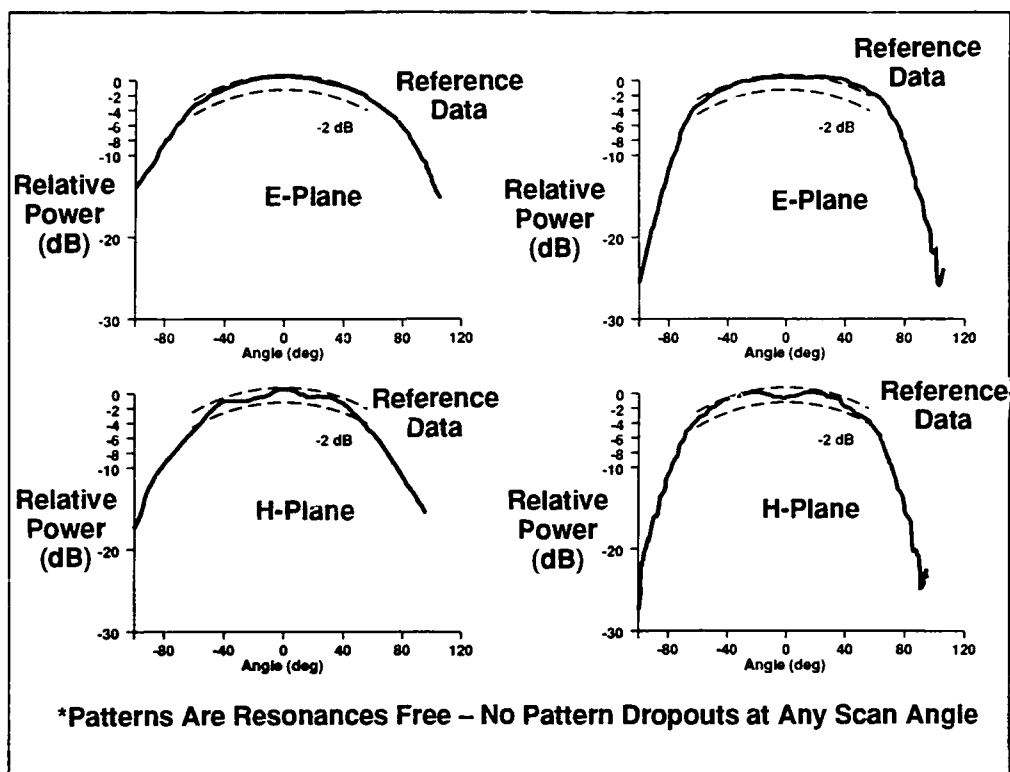
26

*Patterns Are Resonances Free – No Pattern Dropouts at Any Scan Angle

Figure 19. Element Patterns at F_0 (Left) and $3F_0$ (Right)
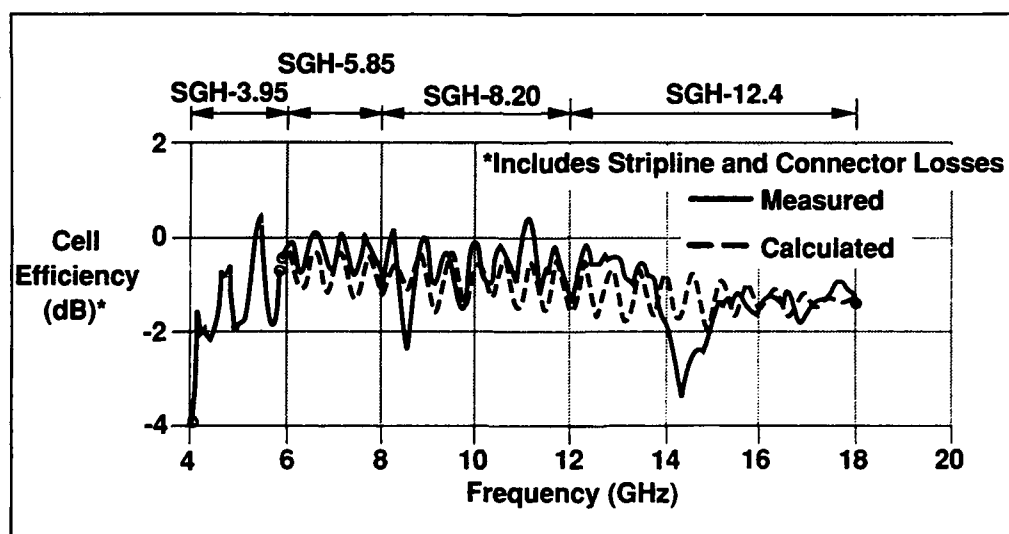

Figure 20. Measured and Calculated Center Element Gain

27

20. The ripple in the data is clearly an interaction between the looking-out impedance of the singly excited elemental sub-array radiator and the test port connector.

To validate the assertion, Figure 19 also shows predicted cell efficiency under the following conditions:

- o deembedded connector characterization
- o assumed active elemental radiator reflection coefficient of zero
- o assumed elemental radiator self-reflection of 0.7
- o an analytically determined stripline loss per unit length

The agreement between experiment and expected cell efficiency is excellent except near 14 GHz where there is a 2 dB fade relative to predicted data. This spectal region was carefully examined - no pattern anomalies were found at any measurement frequency. Furthermore, the dip mimics a similar, but considerably more dramatic fade in the raw power response of the gain standard.

5.0   Conclusions

A wideband sub-array radiator suitable for application in future avionics systems has been developed. The sub-array radiator has demonstrated pattern and VSWR bandwidths exceeding 3:1 and VSWR bandwidth exceeding 4:1. The radiator exhibits no pattern anomalies whatsoever. When integrated with wideband matched

28

3-port or 4-port power divider to form quad-notch radiators, this new sub-array radiator will generate a light-weight array aperture with

- o wide operating bandwidth
- o wide angle scan capability
- o multiple polarization response and
- o intrinsically low radar cross section

Because of the interlacing of polarization aligned and 45° rotated grids, the quad-notch radiator efficiently fills the array aperture at the upper end of the operating band.

6.0 References

1. Lewis, L.R., M. Fassett and J. Hunt, **A Broadband Stripline Array Element**, IEEE International Symposium Digest, Atlanta, GA, 1974.

2. Monser, G., G. Hardie, J. Ehrhardt and T. Smith, **Closely Spaced Orthogonal Dipole Array**, US Pat. No. 3,836,976, assigned to Raytheon. [*n.b.*, the stripline realization of the notch radiator follows from the basic patent claims of Monser *et al*]

3. Schuss, J.J. and J.D. Hanfling, **Nonreciprocity and Scan Blindness in Phased Arrays Using Balanced-Fed Radiators**, Trans. Antennas and Propaga tion, Vol. AP-35, No. 2, February, 1987, pp. 134-138.

4. Hannan, P., **The Element-Gain Paradox for a Phased-Array Antenna**, IEEE Trans. on Antennas and Propagation, Vol. AP-12, No. 4, July, 1964, pp. 423-433.

29

5. Lewis, L.R. and J.H. Pozgay, **Broadband Antenna Study**, Final Report
   AFCRL-TR-75-0178, Contract No. F19628-72-C-0202, March 1975, **ADA014862**

6. Lewis, L.R., J.H. Pozgay and A. Hessel, **Design and Analysis of Broadband
   Notch Antennas and Arrays**, AP-S International Symposium Digest, Amherst,
   MA, 1976, pp. 44-47.

30

WAVEGUIDE EXCITED MICROSTRIP PATCH ANTENNA: THEORY AND EXPERIMENT

M.-H. Ho, K. A. Michalski, and K. Chang

Electromagnetics & Microwave Laboratory
Department of Electrical Engineering
Texas A&M University
College Station, Texas 77843-3128

Abstract

An arbitrarily shaped microstrip patch antenna excited through an arbitrarily shaped iris in the mouth of a rectangular waveguide is investigated theoretically and experimentally. The metallic patch resides on a dielectric substrate grounded by the waveguide flange, and may be covered by a dielectric superstrate. The waveguide may also contain a dielectric plug. Both the substrate (and superstrate, if present) and the dielectric plug consist of one or more planar, homogeneous layers. which may exhibit uniaxial anisotropy. The analysis is based on the space domain integral equation approach. More specifically, the Green's functions for the layered medium and the waveguide are used to formulate a coupled set of integral equations for the patch current and the aperture electric field, and are solved by the method of moments using vector basis functions defined over triangular subdomains. The dominant mode reflection coefficient in the waveguide and the far field radiation patterns are then found from the computed aperture field and patch current distributions. Sample numerical results are presented and are found to be in good agreement with measurements and with published data.

1 Introduction

Microstrip patch antennas. which belong to a large class of printed circuit antennas, are widely used in the microwave frequency range, both as single elements and (more often) in array configurations. Their advantages are well known: low cost, conformity, ease of fabrication and integration, reproducibility, ruggedness, light weight, and low profile [1], [2]. As has been already noted by Kanda et al. [3], the versatility of microstrip patch antennas at microwave frequencies suggests their potential usefulness also at millimeter waves. To a large degree, these antennas can be derived by simply scaling down the counterpart microwave designs. However, the feed structures that operate well at microwave frequencies are not always viable in the millimeterwave range. For example, microstrip line losses become significant and coaxial feed components are not available above approximately 50 GHz, which renders the direct feed techniques impractical in this frequency range. On the other hand, since the waveguide bulkiness becomes less of a factor at higher frequencies, while its losses remain smaller than those of a microstrip line [4], the indirect waveguide feed becomes an attractive option for millimeterwave antennas and antenna arrays [3]. Moreover, in some applications the aluminum waveguide may also serve as a heat sink and support for active devices that may be integrated with the antenna. Also, a planar dielectric plug may be inserted in the waveguide to realize a phase shifter or a multi-section quarter-wave transformer designed to impedance match the antenna to the source [5].

In this paper we present a rigorous integral equation analysis of a waveguide fed microstrip patch antenna. as illustrated in Fig. 1. The arbitrarily shaped microstrip patch is coupled with the rectangular waveguide through an arbitrarily shaped iris. The dielectric medium above the ground plane and the waveguide plug may consist one or more planar. homogeneous lay-
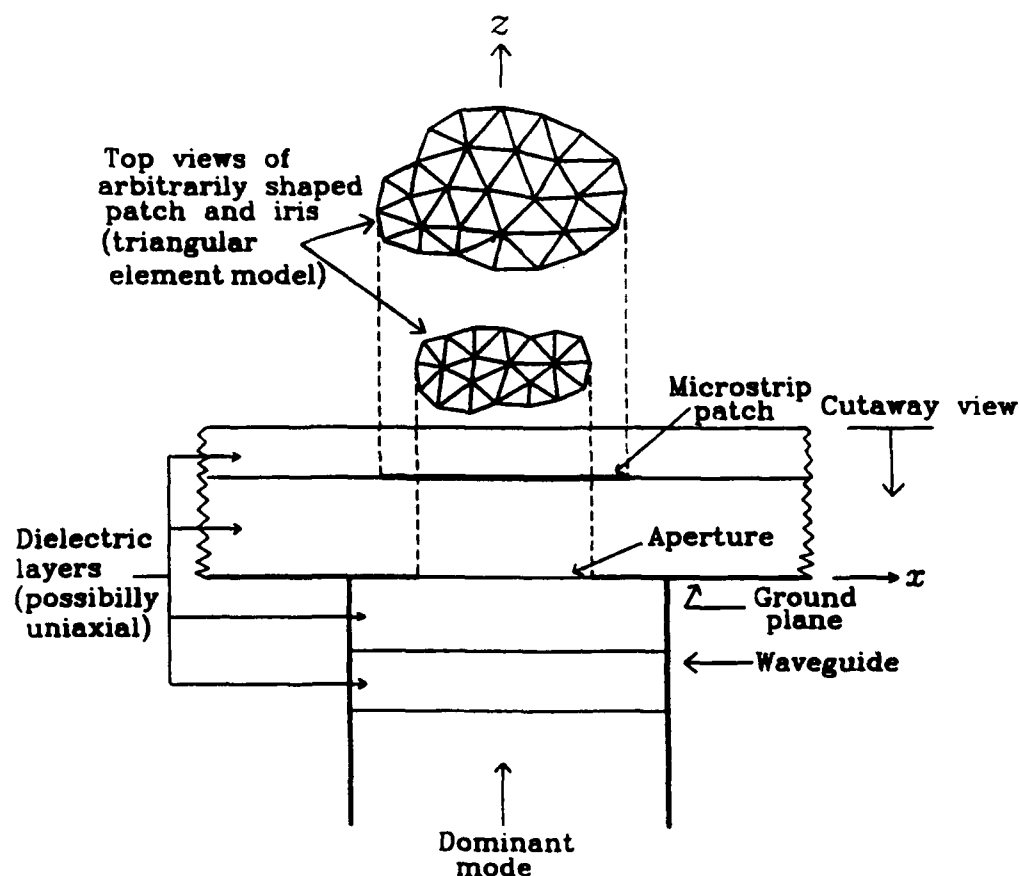
Figure 1: Geometry of a waveguide-fed microstrip patch antenna.

ers. which may exhibit uniaxial anisotropy. The structure is excited by the dominant (TE_{10}) waveguide mode. The primary quantities to be computed are the patch current and iris field distributions. From these. other quantities of interest will be found, including the dominant mode reflection coefficient and the far field radiation patterns. Although attention is limited to a single antenna element. it is expected that the results of this study will also be useful in the analysis, by an approximate technique. of finite waveguide-fed antenna arrays.

3
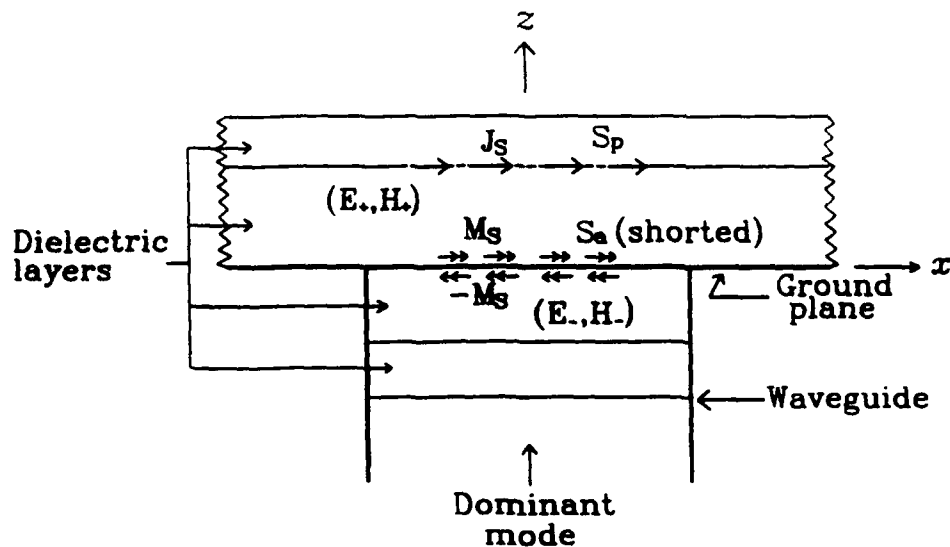
Figure 2: Problem equivalent to that of Fig. 1.

The remainder of this paper is organized as follows. In Sec. 2 we outline the formulation and present the highlights of the *solution procedure*. In Sec. 3 we discuss the experimental validation of the analysis, and in Sec. 4 we present sample computed and measured results. Finally, in Sec. 5 we give the summary and conclusions.

2 Formulation and Solution Procedure

The geometry of the structure under consideration is shown in Fig. 1. To facilitate the analysis, we invoke the equivalence principle [6] to in effect decouple the original problem into two simpler ones, referred to as the 'interior' (inside the shorted waveguide) and 'exterior' (above the ground plane) problems, as illustrated in Fig. 2. This decoupling is achieved by first shorting the aperture S_a through which the two regions interact, and then placing over it an equivalent magnetic surface current M_S, which represents the tangential

l

electric field in the aperture. The negative of M_S is placed on the opposite side of the shorted aperture, thus explicitly enforcing the continuity of the tangential electric field across S_a. In the equivalent problem, the effect of the metallic patch S_p is replaced by an equivalent electric surface current J_S.

The conditions of vanishing tangential electric field on the patch (which is assumed to be perfectly conducting) and continuity of the tangential magnetic field across the aperture may now be stated as

$$\hat{z} \times E_+^s(r) = 0, \quad r \in S_p \tag{1}$$

$$\hat{z} \times H_+^s(r) = \hat{z} \times \left[H_-^s(r) + H_-^i(r) \right], \quad r \in S_a \tag{2}$$

where the subscripts '+' and '−' refer, respectively, to the exterior and the interior regions, $\hat{z}$ is a unit vector in the z direction, r is the position vector, E_+^s and H_+^s are, respectively, the electric and magnetic fields in the exterior region due to J_S and M_S, H_-^s is the magnetic field in the interior region due to $-M_S$, and H_-^i is the magnetic field in the shorted waveguide excited by the incident dominant mode. The 'secondary' fields E_+^s and $H_\pm^s$ may be expressed in terms of the dyadic Green's functions of the two regions as

$$E_+^s(r) = \int_{S_p} \underline{\underline{G}}_+^{EJ}(r \mid r') \cdot J_S(r') \, dS' + \int_{S_a} \underline{\underline{G}}_+^{EM}(r \mid r') \cdot M_S(r') \, dS' \tag{3}$$

$$H_+^s(r) = \int_{S_p} \underline{\underline{G}}_+^{HJ}(r \mid r') \cdot J_S(r') \, dS' + \int_{S_a} \underline{\underline{G}}_+^{HM}(r \mid r') \cdot M_S(r') \, dS' \tag{4}$$

$$H_-^s(r) = - \int_{S_a} \underline{\underline{G}}_-^{HM}(r \mid r') \cdot M_S(r') \, dS' \tag{5}$$

Upon substituting (3)–(5) into (1)–(2), we obtain a coupled set of integral equations for the equivalent currents J_S and M_S. To solve this set of equations, we use the method of moments (MOM) [7], [8] in conjunction with a triangular mesh model of the patch and the aperture (see Fig. 1). The currents J_S and M_S are approximated in terms of vector basis functions with triangular support [9]. Once J_S and M_S are found, it is a relatively simple

5

matter to compute the dominant mode reflection coefficient and the far field radiation patterns. The details of the MOM procedure are rather standard and are omitted here due to lack of space.

For the solution procedure described above to be practical, the dyadic Green's functions in (3)-(5) must be efficiently evaluated. In the exterior region, these Green's functions are expressed in terms of Sommerfeld-type spectral integrals, which are accelerated by asymptotic integrand subtraction and the method of averages [10], [11]. In addition to these techniques, an interpolation and table look-up scheme is implemented to further reduce the computation time [10], [11]. The interior region Green's functions are expressed in terms of series of Floquet modes, and are accelerated by a combination of Kummer and Poisson transformations [12], [13].

3 Measurement Procedure

The experiment was done in X-band, rather than in the millimeterwave range, to reduce the effect of fabrication tolerances on the results. The components of the measured structure are shown in Fig. 3. The measurements were done for a rectangular and a circular patch, each excited through a concentric rectangular iris. as illustrated in Figs. 4a and 4b. respectively. The dimensions of the rectangular patch are $L_p = 7.62$ mm. $W_p = 9.13$ mm, and the diameter of the circular patch is $D_p = 9.3$ mm. The dimensions of the rectangular aperture are $L_a = 5.16$ mm. $W_a = 5.32$ mm. and are the same for the rectangular and circular antennas. Both antennas are on a substrate having a dielectric constant $\varepsilon_r = 2.2$ and thickness $h = 0.787$ mm. The dimensions of the antenna of Fig. 4a have been scaled up from those used by Kanda et al. [3] in their investigation of this antenna configuration in the millimeterwave range. The microstrip antennas were mounted on the waveguide flange using plastic
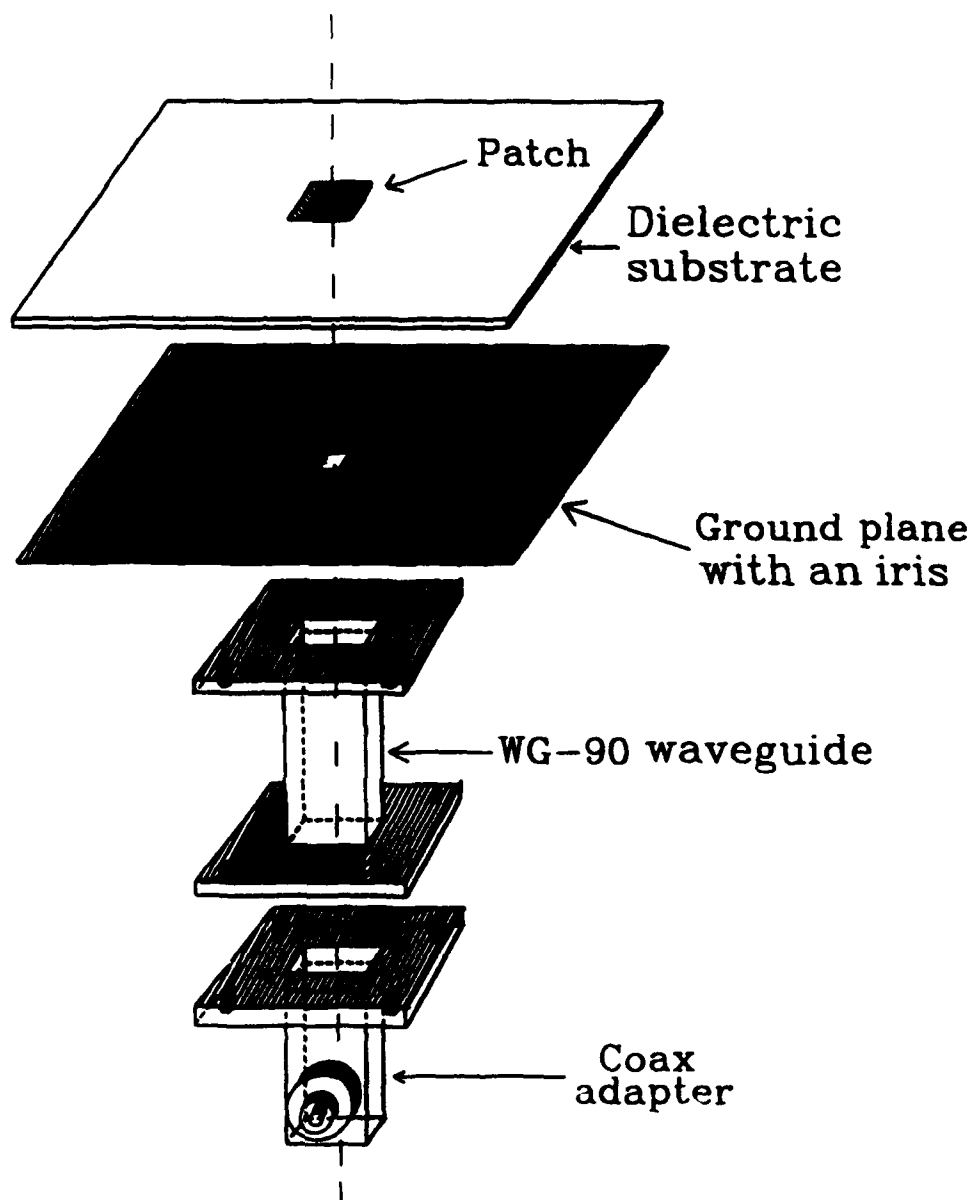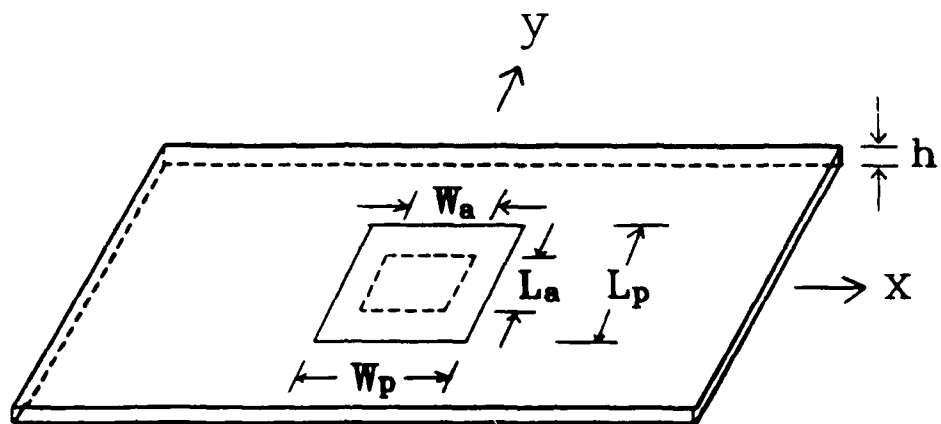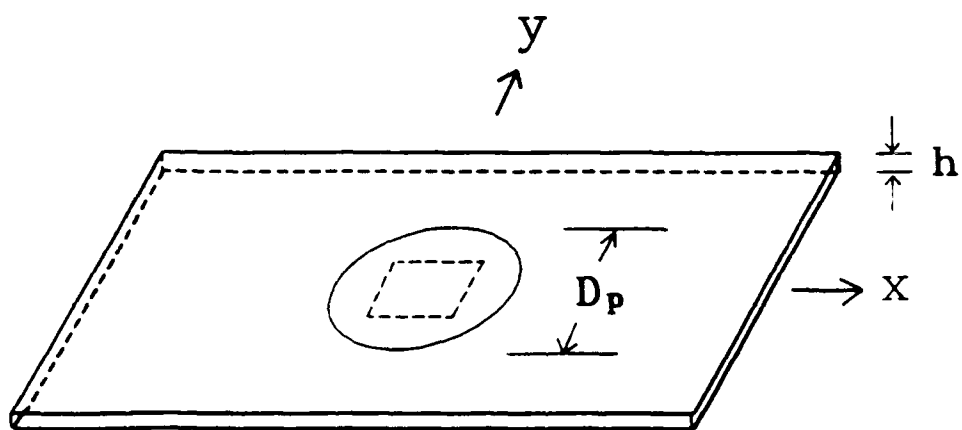
6

Figure 3: Components of the measured structure.

7

Figure 4: (a) Rectangular and (b) circular microstrip patch antennas used in the measurements. Each antenna is fed through a concentric rectangular iris in the ground plane.
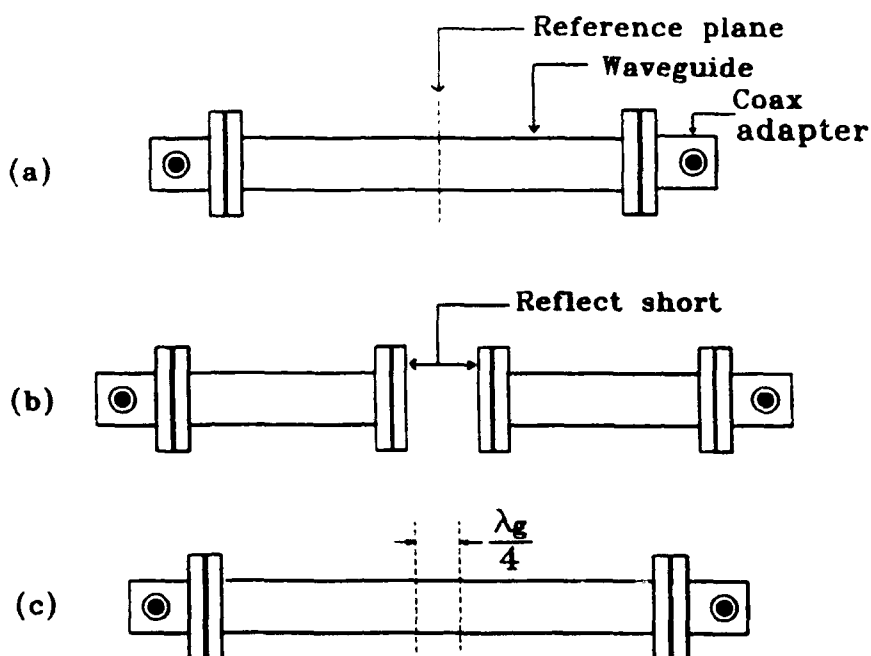
Figure 5: (a) Thru, (b) reflect, and (c) line (delay) standards used in the HP-8510B TRL calibration procedure.

screws (see Fig. 3).

The dominant mode reflection coefficient Γ_{10}, referred to the iris plane. was measured using the HP-8510B network analyzer. Prior to the measurement. the thru-reflect-line (TRL) two-port calibration method [14] was used to eliminate the systematic errors due to the coax-to-waveguide adapter and to establish the measurement reference plane (MRP) at the iris location. In order to implement the TRL calibration procedure. three sets of measurements, referred to as thru, reflect. and line (or delay) were taken. The thru, reflect. and line calibration standards were fabricated from four WG-90 waveguide segments. as illustrated in Fig. 5. The thru was arbitrarily selected to be 84.2 mm long (the length of the thru should be at least two guide wavelengths. to reduce the interference between the coax adapters).

9

293

which resulted in the reflect length of 42.1 mm. A waveguide feed of the same length was used in the actual measurements (see Fig. 3), to ensure that the MRP coincides with the iris plane. Because no two coax adapters are identical, two reflect standards were fabricated and used in the HP-8510B calibration, as indicated in Fig. 5b. The line (delay) was made 9.9 mm longer than the thru. This 9.9 mm length difference between the thru and the line. which at the center frequency $f_c = 10\,\text{GHz}$ is approximately a quarter of the guide wavelength $\lambda_g = 39.7\,\text{mm}$, results in a time delay of 24.94 ps, and this value was keyed into the HP-8510B network analyzer during the TRL calibration procedure.

4 Sample Computed and Measured Results

In this section we present sample results obtained using a computer program implementing the procedures described in Sec. 2. Where possible, the computed results are compared with measured data and with existing published results. All results given here are for a rectangular iris in the mouth of an X-band rectangular waveguide (WG-90) with the dimensions $a = 22.86\,\text{mm}$ and $b = 10.16\,\text{mm}$. excited in the dominant TE_{10} mode, with the characteristic admittance Y_{10}.

In Fig. 6 we plot the normalized input conductance G and susceptance B vs. frequency for a centered iris with dimensions $0.7a \times 0.8b$, which opens into a dielectric slab with the dielectric constant $\varepsilon_r = 2.25$ and $h = 3.201$ mm. There is no patch in this case. Our computed results are seen to agree well with the data computed and measured by Bodnar and Paris [15].

In Fig. 7 we compare the computed and measured (using the procedure of Sec. 3) voltage standing wave ratio (VSWR), phase of the dominant mode reflection coefficient ($\angle \Gamma_{10}$), and input impedance (the latter plotted on a
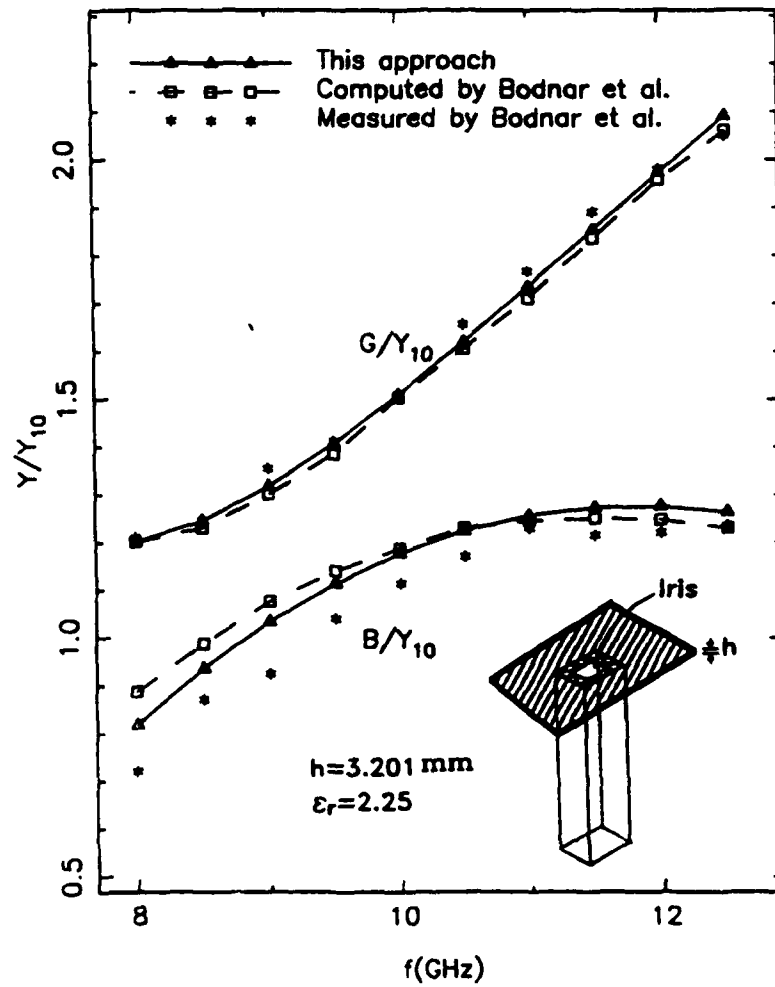
10

Figure 6: Normalized input conductance G and susceptance B of a rectangular waveguide iris open into a dielectric slab.
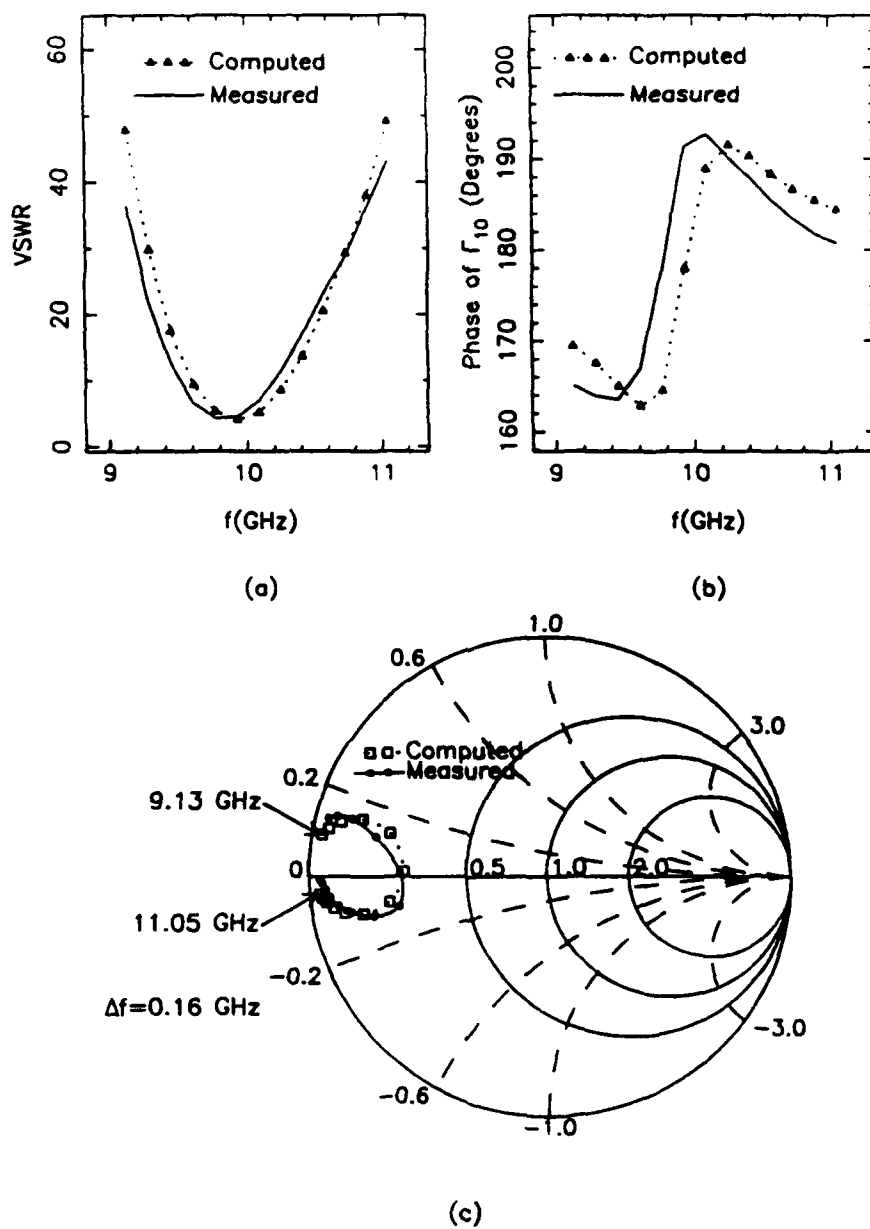
11

Figure 7: Plots of (a) VSWR. (b) phase of Γ_{10}, and (c) input impedance for the rectangular patch antenna of Fig. 4a placed concentrically with the waveguide feed (Antenna 1).

12

Table 1: Minimum values of the VSWR and the corresponding values of the phase of Γ_{10} and frequency f_r.

Antenna	Measured			Computed		
	VSWR	$\angle\,\Gamma_{10}$	f_r(GHz)	VSWR	$\angle\,\Gamma_{10}$	f_r(GHz)
1	3.96	184.1°	9.83	3.95	177.9°	9.93
2	8.11	186.1°	9.86	7.49	178.6°	9.96
3	3.28	177.1°	9.36	3.62	180.1°	9.49

Smith chart) for the rectangular microstrip patch antenna of Fig. 4a placed concentrically with the waveguide (this configuration will be referred to as Antenna 1). The symbols on the Smith chart in Fig. 7c correspond to those in Figs. 7a and 7b. In Fig. 8 we present similar results for the antenna of Fig. 4a shifted (together with the iris) from the centered position a distance of 5.5 mm along the x axis (we will refer to this configuration as Antenna 2). Finally, in Fig. 9 we plot the corresponding results for the circular microstrip patch antenna of Fig. 4b placed concentrically with the waveguide (this configuration will be referred to as Antenna 3). The agreement between the computed and measured results for the three antennas is judged to be very good. except for the small discrepancies (less than 1.5%) in the resonant frequency f_r (the latter being defined as the frequency for which the VSWR is minimum). The measured and computed resonant frequencies for the three antennas. together with the corresponding values of the VSWR and $\angle\,\Gamma_{10}$ are summarized in Table 1. We note that—with the VSWR values in excess of 3—the investigated antennas are far from being matched.

In Figs. 10–11 we present vector plots of the resonant patch and aperture currents for Antennas 1 and 3. respectively. These figures also indicate
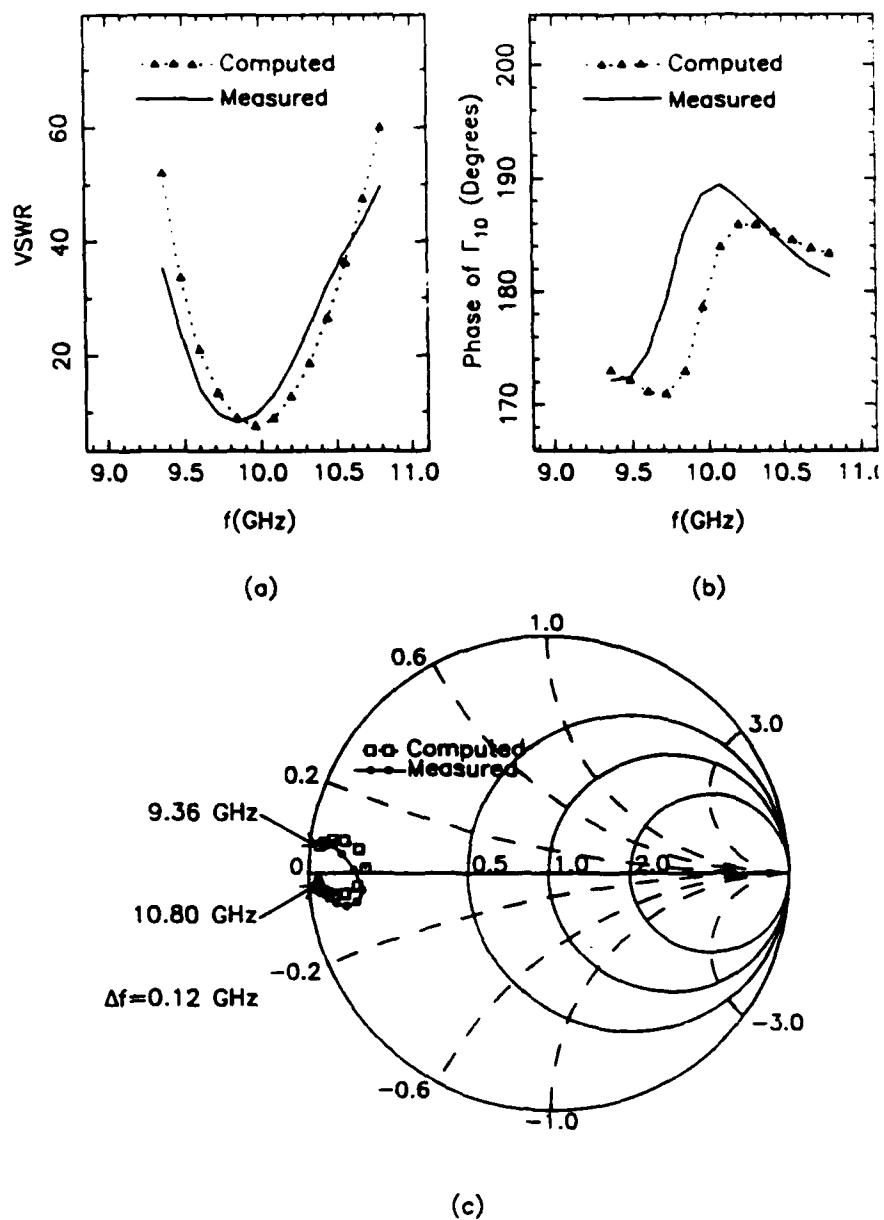
13

Figure 8: Plots of (a) VSWR, (b) phase of Γ_{10}, and (c) input impedance for the rectangular patch antenna of Fig. 4a shifted a distance of 5.5 mm along the x axis with respect to the center of the waveguide feed (Antenna 2).
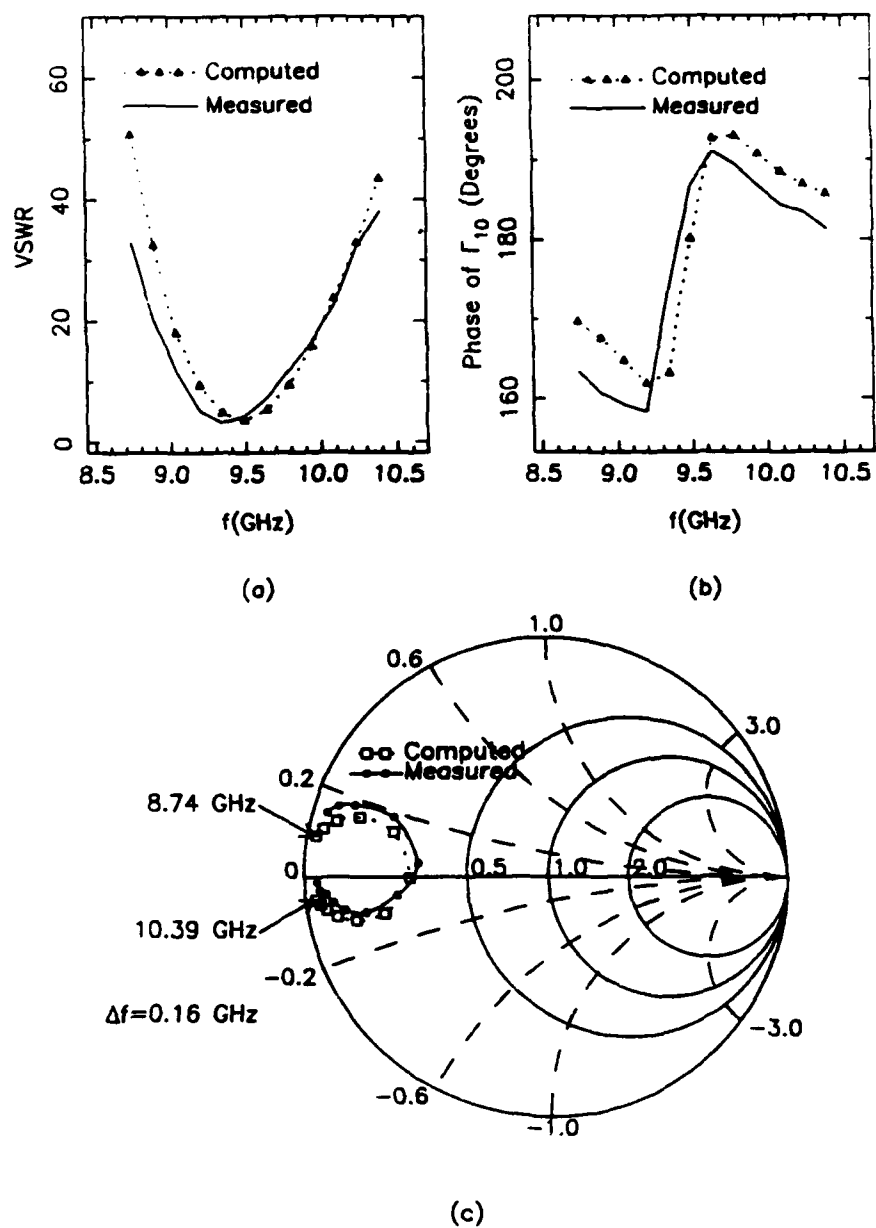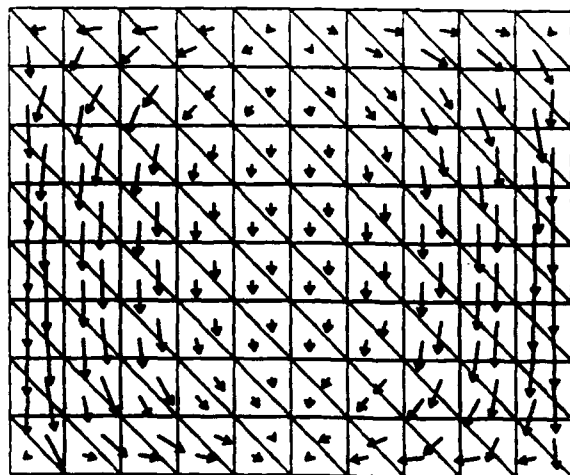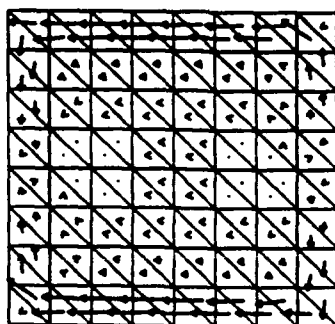
14

Figure 9: Plots of (a) VSWR, (b) phase of Γ_{10}, and (c) input impedance for the circular patch antenna of Fig. 4b placed concentrically with the waveguide feed (Antenna 3).

15

(a)

(b)

Figure 10: Vector plots of (a) the patch electric current and (b) the aperture magnetic current for the antenna of Fig. 4a (Antenna 1) at the resonant frequency $f_r = 9.93\,\text{GHz}$.
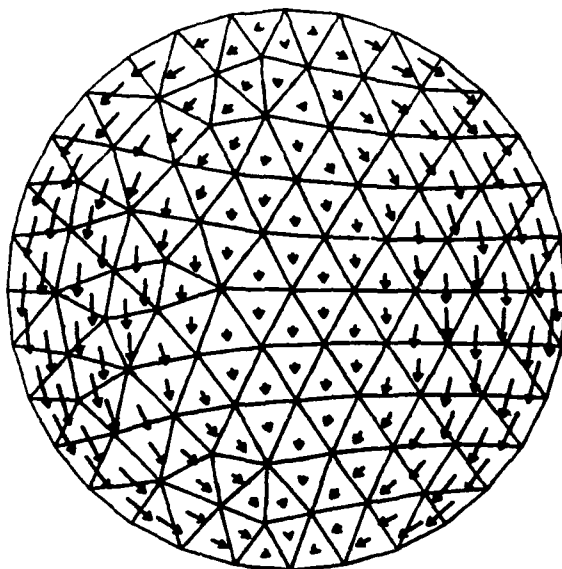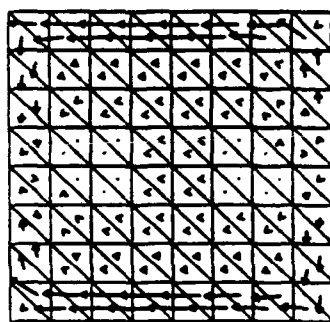
16

(a)

(b)

Figure 11: Vector plots of (a) the patch electric current and (b) the aperture magnetic current for the antenna of Fig. 4b (Antenna 3) at the resonant frequency $f_r = 9.49\,\text{GHz}$.
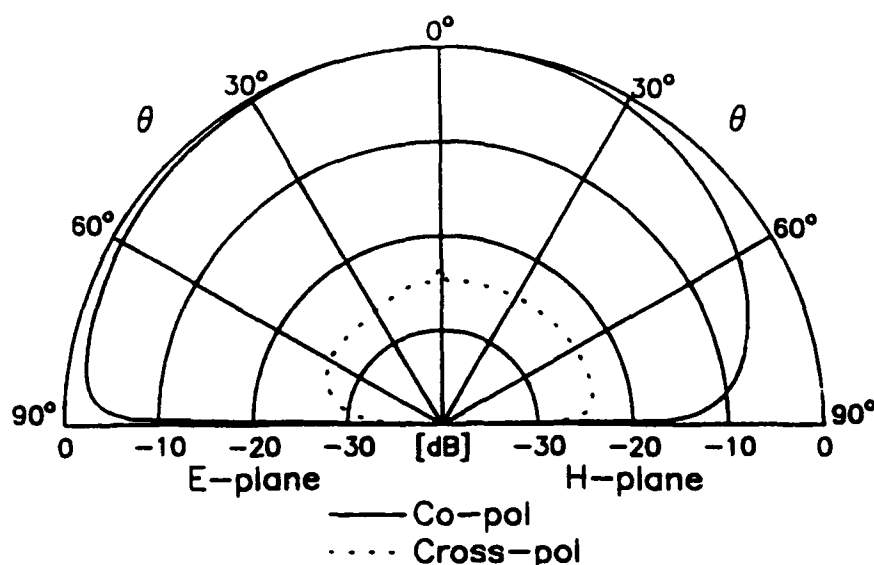
17

Figure 12: Far field patterns of the rectangular microstrip patch antenna of Fig. 4a (Antenna 1) at the resonant frequency 9.93 GHz.

the relative sizes of the microstrip patches and the irises, and illustrate the triangular meshes that were used to model them in the analysis.

Finally, in Figs. 12-13 we plot the computed resonant far field patterns for the rectangular (Antenna 1) and circular (Antenna 3) microstrip patch antennas, respectively. It is noted that the cross-polarization level of Antenna 1 is much lower than that of Antenna 3. This is consistent with the current distributions shown in Figs. 10-11, which clearly indicate that the current flow on the rectangular antenna is predominantly parallel to the E-plane, whereas the current of the circular antenna tends to curve along the edges of the patch.

The CPU time required to analyze the Antennas 1-3 at a single frequency was about 45 minutes on a 12-MIPS computer.
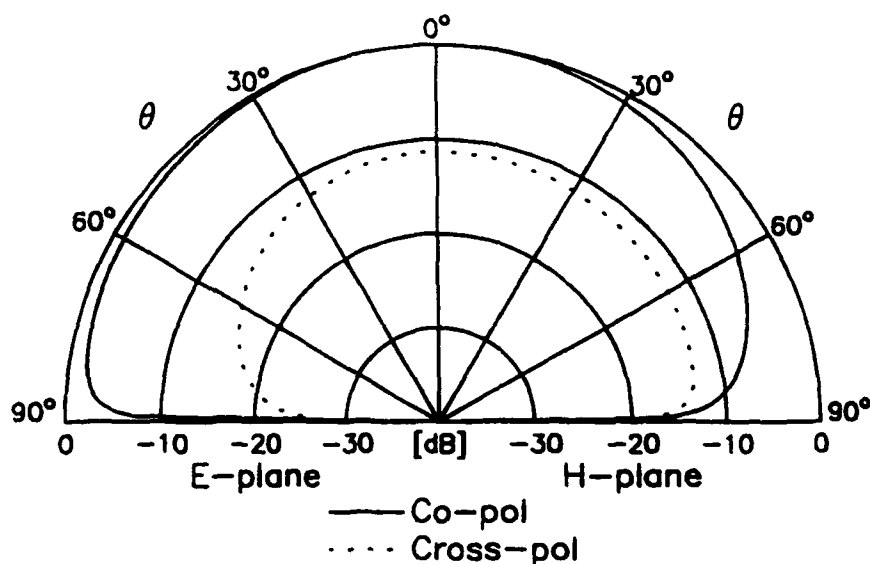
18

Figure 13: Far field patterns of the circular microstrip patch antenna of Fig. 4b (Antenna 3) at the resonant frequency 9.49 GHz.

5 Summary and Conclusions

We have presented a rigorous integral equation analysis of a microstrip patch antenna excited through an iris in the mouth of a rectangular waveguide. The patch may be covered by a dielectric layer and there may also be a dielectric plug in the waveguide. All dielectric layers may be uniaxially anisotropic. The approach incorporates a triangular element model of the patch and the iris. which may both be of arbitrary shape. Hence, microstrip patch antennas of various, possibly irregular shapes, residing in multilayer, possibly uniaxial media. may be analyzed within a single formulation. using the same computer program. The analysis has been validated by an experiment.

An important application of this method will be as an aid in the design of waveguide-fed microstrip patch antenna elements for use in millimeterwave antenna arrays. In particular. the developed computer program will be used

19

to determine the location and size of the waveguide iris that results in an antenna that is impedance matched to the source. It is also anticipated that this program will be useful in deriving accurate equivalent circuit models for the waveguide-to-patch transition, suitable for CAD applications.

Acknowledgments

References

[1] I. J. Bahl and P. Bhartia, *Microstrip Antennas*. Dedham, MA: Artech House, 1980.

[2] J. R. James, P. S. Hall, and C. Wood, *Microstrip Antenna Theory and Design*. London: Peter Peregrinus, 1981.

[3] M. Kanda, D. C. Chang, and D. H. Greenlee. "The characteristics of iris-fed millimeter-wave rectangular microstrip patch antennas." *IEEE Trans. Electromagnet. Compat.*, vol. EMC-27, pp. 212-220. Nov. 1985.

[4] K. C. Gupta, R. Garg, and R. Chadha, *Computer-Aided Design of Microwave Circuits*. Norwood, MA: Artech House, 1981.

[5] R. E. Collin. *Foundations for Microwave Engineering*. New York: McGraw-Hill, 2nd ed.. 1992.

[6] R. F. Harrington. *Time-Harmonic Electromagnetic Field*. New York: McGraw-Hill, 1961.

20

[7] R. F. Harrington. *Field Computation by Moment Methods*. New York: Macmillan, 1968. Reprinted by Krieger Publishing Co.. Melbourne. FL, 1982.

[8] R. C. Hansen, ed., *Moment Methods in Antennas and Scattering*. Norwood, MA· Artech House, 1990.

[9] S. M. Rao, D. R. Wilton, and A. W. Glisson, "Electromagnetic scattering by surfaces of arbitrary shape," *IEEE Trans. Antennas Propagat.*, vol. AP-30, pp. 409–418, May 1982.

[10] J. R. Mosig, "Integral equation technique," in *Numerical Techniques for Microwave and Millimeter-Wave Passive Structures* (T. Itoh, ed.), pp. 133–213, New York: Wiley, 1989.

[11] J. R. Mosig, R. C. Hall, and F. E. Gardiol, "Numerical analysis of microstrip patch antennas," in *Handbook of Microstrip Antennas* (J. R. James and P. S. Hall, eds.), pp. 391–453, London: Peter Peregrinus, 1989.

[12] S. Singh, W. F. Richards, J. R. Zinecker, and D. R. Wilton. "Accelerating the convergence of series representing the free space periodic Green's function." *IEEE Trans. Antennas Propagat.*. vol. 38. pp. 1958–1962. Dec. 1990.

[13] N. W. Montgomery, *Periodic Structures in Stratified Media—A Mixed Potential Formulation*. PhD thesis, University of Houston. Houston. Texas. May 1991.

[14] "Network analysis-applying the HP 8510B TRL calibration for noncoaxial measurements." HP Product Note 8510-8. Palo Alto. CA. Oct. 1987.

21

[15] D. G. Bodnar and D. T. Paris, "New variational principle in electromagnetics." *IEEE Trans. Antennas Propagat.*, vol. AP-18. pp. 216–223. Mar. 1970.

22

A DFT SYNTHESIS METHOD FOR

FINITE ARRAYS OF DIPOLES ON LAYERED MEDIA

Steven M. Wright

Department of Electrical Engineering

Texas A&M University, College Station, TX

ABSTRACT

A method is outlined   which will allow synthesis of near fields of finite phased array antennas.   The method uses an infinite array formulation,   so storage requirements and fill times are largely independent of the number of elements in the array.   However, it includes edge effects and mutual coupling between elements, and can handle arbitrary size arrays.

Fourier coefficient matrices for the fields and scan impedance of the fundamental periodic structure are calculated once for a given periodicity and media.   Once these matrices are obtained,   which typically takes several minutes on a DECstation 5000,   desired near and far field patterns can be synthesized for finite subsets of the infinite array by simple DFT operations. The method is applicable to free or forced excitation of the array.

1. INTRODUCTION

Many applications require the synthesis of a set of array excitations to produce a desired pattern, either near or far field. Standard Fourier synthesis methods can be used to relate far fields to equivalent currents on a convenient aperture or secondary surface. A more difficult problem is relating these equivalent currents, (or near-fields,) to actual element currents on the radiating structure. This requires an analysis of radiation from the structure, including mutual coupling effects. For large arrays, or arrays on layered media, such as microstrip antennas, such an analysis can be computationally intensive.

An efficient synthesis method for finite phased array antennas on planar layered media is described in this paper. The method is applicable to arrays of general elements in essentially arbitrary layered media. The synthesis method is an extension of a finite phased array analysis method reported earlier [1,2]. The analysis method was applied to arrays of microstrip dipoles. In this report, the synthesis method is applied to an array of dipoles in water, simulating a microwave imaging array.

The approach consists of two parts. First, Fourier coefficient matrices for the extended, infinite periodic structure are calculated using infinite array techniques.

2

Computation of these matrices are substantially equivalent to the analysis of an isolated element using the spectral-domain moment-method. Once these matrices have been calculated and stored, which typically takes several minutes on a DECstation 5000, excitations can be calculated to produce near and far field patterns by FFTs.

The method is based on an infinite array formulation, giving fill times and storage requirements of order $(P)^2$ and $(N)^2$, where P is the number of basis functions per element, and N is the total number of elements in the array. This is a significant reduction over standard moment-method approaches. This will allow the analysis of large arrays of general elements. However, the proposed method includes edge effects and can handle arbitrary size arrays with arbitrary excitation. The method is applicable to both forced and free excitation.

2. METHODS

The DFT synthesis method described in this paper is applicable to arrays on planar, layered media. It has been applied to arrays of microstrip dipoles, and arrays of planar dipoles in water. This section begins with an overview of the entire technique. It is then broken down, with each element being discussed individually, starting with the analysis of the infinite array. The DFT analysis of finite arrays is reviewed,

3

2.1.   Overview of Array Analysis Methods

2.1.1.   Spectral-domain moment-method

The analysis of individual microstrip dipoles and patches using the spectral-domain moment-method (SDMM) has been discussed in detail by several authors [3-5]. Microstrip arrays have been analyzed with both the element-by-element approach [6-11] and the infinite array approach [12-15].

Using the element-by-element method, storage and computer time requirements can become prohibitive for the analysis of arrays of more than a few hundred elements, or even moderate sized arrays of general elements. A common alternative approach is to model large periodic structures as infinite. This approach ignores edge effects, but has the advantage that the current is the same in each period or "unit cell" of the array, reducing the problem to the difficulty of a single element problem [16]. Thus, the [Z] matrix is only of order P^2, rather than $(NP)^2$, where P is the number of basis functions per element, and N is the number of elements in the array.

Analysis methods for infinite periodic arrays are well understood and are accurate and efficient. No Sommerfeld integrals are required, and highly efficient acceleration techniques have been developed to compute the doubly infinite summations that arise in their analysis [3,12]. Unfortunately, the cost of such a simple and efficient solution is that the

4

excitation and resultant fields are assumed to be of uniform amplitude with a progressive phase shift from period to period in the array. Thus, edge effects due to the finite size of the array, and element-to-element variations in the active element impedance due to aperiodic excitations are not included.

2.1.2.   Fourier methods

Many researchers have suggested applying Fourier methods to the integral equation solution of large systems.   One approach is to perform the computation of the convolution integrals in the SDMM using FFTs, such as done in the spectral iterative approach [17] or the conjugate gradient-FFT method [18]. These methods can reduce computation time and storage requirements, but the number of unknowns is still of order $(NP)^2$.

Munk and Burrell showed that the impedance of an isolated element can be obtained from integration of the impedance of an infinite array of the same elements over all scan angles [19]. This integration is an inverse Fourier transform of the infinite array active impedance as a function of scan angle.

The aperiodic excitation of infinitely periodic waveguide arrays has been analyzed by Lee using Fourier methods [20]. This was essentially a Fourier series analysis, but the waveguide array remains of infinite extent.   Ishimaru et. al [21] used a Fourier method to determine active impedances of arrays of dipoles over a ground plane with specified excitation currents.

5

The present method is similar to their method, but includes free and forced excitation, arbitrary current distributions on the elements, and synthesis of excitation currents.

2.1.3. DFT synthesis method for finite arrays

A section of a finite, periodic array of m i crostrip dipoles is shown in Figure 1. As described above, one begins by analyzing an infinite array of the same elements and media. Once the infinite array is characterized, finite arrays of arbitrary numbers of elements can be synthesized and analyzed using DFTs.
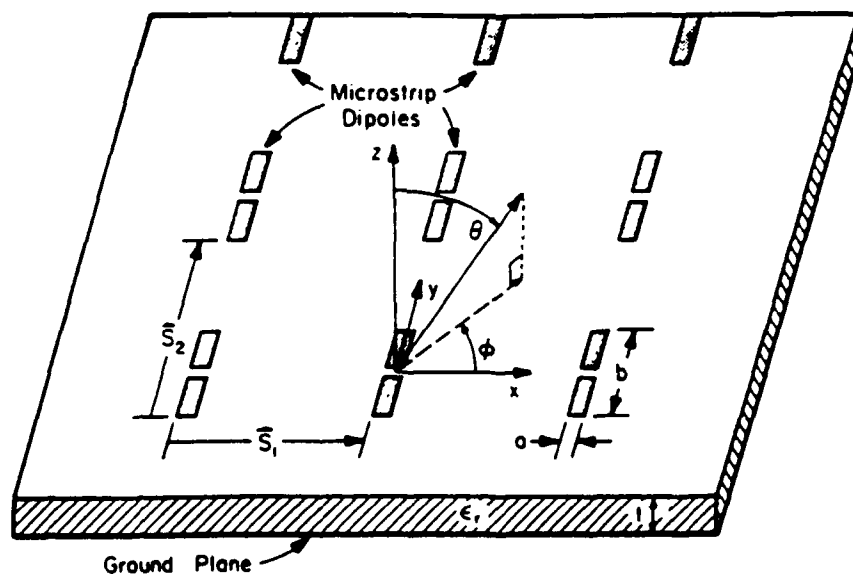

Figure 1. A section of a periodic array of dipoles.

6

Briefly, the steps in the synthesis of a desired near field pattern for a finite array can be summarized as follows.

1) Calculate and store the infinite array active impedance as a function of main beam scan angle.

2) Simultaneously, compute the near field of the infinite array at the desired points above a single unit cell (period) of the infinite array.

3) Compute a set of Fourier coefficients for the desired electric field by DFT of the desired pattern.

4) Compute the necessary excitation currents for a finite array of the desired size.

5) Compute the actual near field produced, and, if desired, compute the element excitation voltages for the free or forced excitation case.

Steps 1 and 2 comprise the majority of the computational effort. The remaining steps simply require DFT operations.In the following sections, each of these steps will be explained in more detail. First, the infinite array method is outlined, then the finite array analysis method is discussed. Finally, the field synthesis method is discussed.

2.1.   Infinite array analysis

2.2.1.   Infinite Array Scan Impedance

The analysis of infinite arrays of microstrip elements is

7

described in detail in [15]. The infinite array can be analyzed using standard spectral domain moment method techniques. One solves an integral equation enforcing the boundary condition on the tangential electric field on the surface of the dipoles:

$$\hat{\underline{n}} \times \left[\underline{E}^i(\underline{r}) + \underline{E}(\underline{r}) \right] = 0, \qquad \underline{r} \in \text{dipole surface} \qquad (1)$$

where $\underline{E}^i(\underline{r})$ is the impressed electric field due to the source, and $\underline{E}(\underline{r})$ is the electric field due to the electric surface currents on the elements. Because of the periodicity of the array, this equation is only enforced on one dipole element.

For brevity, consider an array of y oriented dipoles as shown in Fig. 1, with a single basis function (P = 1). One obtains the infinite array impedance by evaluation of one double summation:

$$\tilde{Z}_{in} = - \frac{1}{A} \sum_m \sum_n \tilde{G}_{yy}(\underline{K}_{mn}) \cdot \tilde{J}_y^2(\underline{K}_{mn}) \qquad (2)$$

where A is the area of one unit cell in the array, $\tilde{G}_{yy}$ is the $\hat{y}\hat{y}$ component of the spectral-domain dyadic periodic Green's function for the problem under consideration, and $\tilde{J}_y$ is the Fourier transform of the basis function. The Green's function for planar, layered media can be easily derived using transmission line methods [5].

8

Equation 2 is a summation of Floquet modes on a periodic lattice in the spectral domain, defined by the vectors $\underline{K}_{mn}$.

$$\underline{K}_{mn} = \underline{\beta}_{mn} + \underline{\beta}_0 \qquad (3a)$$

where:

$$\underline{\beta}_{mn} = m\underline{\beta}_1 + n\underline{\beta}_2 \quad \text{and} \quad \underline{\beta}_0 = m_0\underline{\beta}_1 + n_0\underline{\beta}_2 \qquad (3b)$$

$\underline{\beta}_1$ and $\underline{\beta}_2$ are lattice vectors for the reciprocal or spectral domain lattice, and are obtained from the spatial domain lattice vectors $\underline{S}_1$ and $\underline{S}_2$. For a rectangular array, $\underline{\beta}_1 = 2\pi/\underline{S}_1$ and $\underline{\beta}_2 = 2\pi/\underline{S}_2$. $\underline{\beta}_0$ is an offset of each Floquet mode to allow beam scanning. m_0 and n_0 are essentially the direction cosines. Following the conventions of [15], m_0 and n_0 are given for a rectangular array by:

$$m_0 = -S_1 \sin\theta \cos\phi \qquad (4a)$$

$$n_0 = -S_2 \sin\theta \sin\phi \qquad (4b)$$

The infinite array impedance is periodic in $\underline{\beta}_0$. For each value of the progressive phase shift $\underline{\beta}_0$ of the array excitation, the scan impedance, denoted $Z^\infty(\underline{\beta}_0)$, gives the relation between terminal voltage and current excitation for all elements in the infinite array. Once the array scan impedance $\underline{Z}^\infty(\beta_0)$ is characterized for one period of scan, any number of elements can be analyzed, from an isolated element to thousands of elements.

9

2.2.2. Infinite Array Fields

Once the surface currents on the radiator elements have been determined, the near fields can be easily obtained using standard techniques [5]. For an infinite, periodic array, the fields are also periodic, repeating over each unit cell of the array. One such unit cell is shown in Figure 2. The electric field at the point $\underline{r} = (\underline{\rho} + \hat{\underline{a}}_z z)$ over one unit cell due to the pth basis function (and its infinite repetition), is given by:

$$\underline{E}^{\infty}(\underline{\beta}_0,\underline{r}) = \frac{1}{A} \sum_m \sum_n \tilde{\underline{\underline{G}}}(\underline{K}_{mn},z) \cdot \tilde{\underline{I}}_p(\underline{K}_{mn}) \, e^{j\underline{K}_{mn} \cdot (\underline{\rho}-\underline{\rho}')} \qquad (5)$$

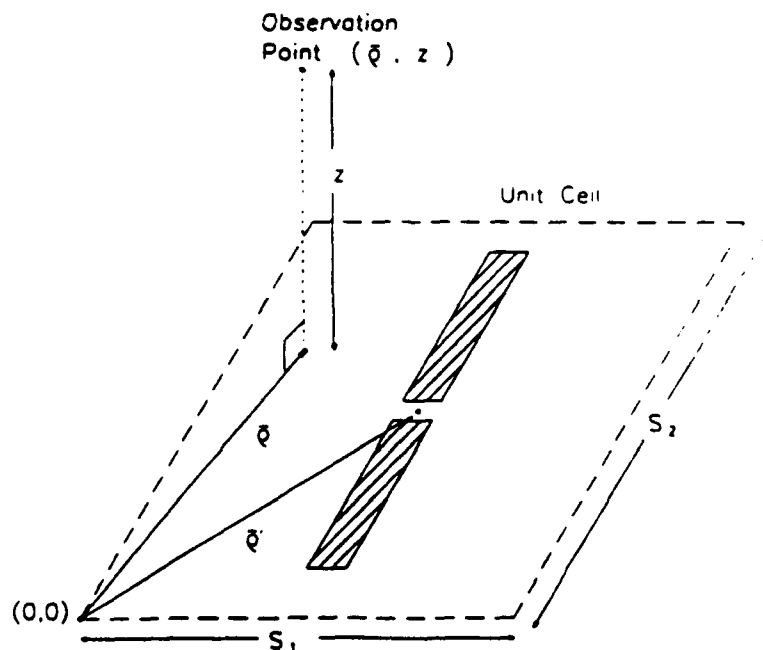where $\underline{\rho}'$ is the location of the basis function in the unit cell.

Figure 2. One unit cell in a periodic array of dipoles.

10

As with the infinite array impedance $Z^\infty(\beta_0)$, $\underline{E}^\infty(\underline{\beta}_0, \underline{r})$ is calculated and stored for a set of scan angles $\underline{\beta}_0$ given below. For most applications, $\underline{r}$ would be chosen to be over the center of the unit cell, with the height chosen depending on the application. represents a set of Fourier coefficients for the array.

2.3. Finite array analysis

2.3.1. Finite array active impedance

To analyze a finite array with aperiodic forced current excitation, one chooses excitation coefficients for each of the $N_x N_y$ elements of the finite array, $I^{ex}(\underline{S}_{mn})$, where $\underline{S}_{mn} = m\underline{S}_1 + n\underline{S}_2$. To use Fourier methods, consider the hypothetical extension of the array to an infinite structure. The goal is to synthesize the excitation of the finite array by a sum of appropriately weighted, uniform periodic excitations of the infinite structure. Those elements with zero current can be considered open-circuited. For resonant length elements, these elements have negligible effect, allowing the finite array to be recovered. For elements for which open-circuiting does not remove their effect, one must enforce zero current at additional points.

Given an excitation function for the finite array, one computes the discrete Fourier transform (DFT) using LK samples of the array excitation:

11

$$\tilde{I}^{ex}(\underline{\beta}_0^{mn}) = DFT\left\{I^{ex}(\underline{S}_{1k})\right\} \qquad (6)$$

where the DFT pair for a discrete, periodic function defined by LK samples on the 2-D lattice defined by $\underline{S}_{1k}$ is given by [22]:

$$\tilde{f}(\underline{\beta}_0^{mn}) = DFT\left\{f(\underline{S}_{1k})\right\} = \sum_{1=0}^{L-1}\sum_{k=0}^{K-1} f(\underline{S}_{1k})\ e^{-j2\pi(ml/L\ +\ nk/K)}$$

$$(7)$$

$$f(\underline{S}_{mn}) = IDFT\left\{f(\underline{\beta}_0^{mn})\right\} = \frac{1}{LK}\sum_{1=0}^{L-1}\sum_{k=0}^{K-1} f(\underline{\beta}_0^{mn})\ e^{j2\pi(ml/L\ +\ nk/K)}$$

where

$$\underline{\beta}_0^{mn} = m\ \underline{\beta}_1/L + n\ \underline{\beta}_2/K \qquad 0 \le m \le L\text{-}1, \quad 0 \le n \le K\text{-}1 \quad (8)$$

and IDFT denotes inverse discrete Fourier transform. LK, the number of sampling points, will typically be much larger than N_xN_y, the number of elements in the array. $I^{ex}(\underline{S}_{1k})$ will be zero for all of the LK samples except the N_xN_y which correspond to elements of the finite array.

The set of Fourier coefficients $\tilde{I}^{ex}(\underline{\beta}_0^{mn})$ represent uniform excitations of the extended infinite periodic structure. For each coefficient, the impedance of the infinite array can be determined using infinite array analysis, as described above. This set of impedances is denoted the $Z(\underline{\beta}_0^{mn})$ matrix. This matrix is independent of the actual excitation, and is pre-calculated

12

and stored for a particular array geometry, to be re-used for different array configurations and excitations.

Once the DFT of the excitation currents is calculated, the DFT of the terminal voltages in the finite array can be determined from:

$$\tilde{V}(\underline{\beta}_0^{mn}) = \tilde{I}^{ex}(\underline{\beta}_0^{mn}) \, Z(\underline{\beta}_0^{mn}) \tag{9}$$

The element voltages, $V(\underline{S}_{mn})$, are obtained by inverse DFT:

$$V(\underline{S}_{mn}) = IDFT \left\{ \tilde{V}(\underline{\beta}_0^{mn}) \right\} \tag{10}$$

This IDFT returns LK unique element voltages, which include the voltages for the original $N_x \times N_y$ array. All other coefficients will be nearly zero. Finally, the input impedance of the element (m,n) in the finite array is:

$$Z(\underline{S}_{mn}) = \frac{V(\underline{S}_{mn})}{I^{ex}(\underline{S}_{mn})} \tag{11}$$

One must use sufficient discretization to avoid aliasing in the DFTs. Preliminary results indicate that good results are obtained with discretizations as small as 128x128.

In addition to the active element impedances across the array, the current distribution on each element can be obtained in a similar manner to determining the impedance by storing the current vector solution for each value of scan angle $\underline{\beta}_0^{mn}$. For

13

P basis functions, this results in a set of P Fourier current coefficient matrices. The current distribution for the finite array is obtained by IDFT of the algebraic product of each matrix with the current coefficient matrix, $\tilde{I}^{ex}(\underline{\beta}_0^{mn})$.

The above method must be modified for the more practical case of free excitation (non-zero generator impedance). Under free excitation, defining zero generator voltage or current does not ensure zero element current. An extension of the above method to include the free excitation case is discussed in [2]. Free excitation can be analyzed by extracting port open-circuit impedance parameters for the finite array from the above method and using conventional N-port analysis. The effect of port networks, such as tuning networks for wide or dual frequency operation, or simple PIN or varactor diodes for tuning and detuning, can easily be included in the analysis.

2.3.2. Finite Array Near Fields

The above technique can also be used to calculate scattered near and far fields for finite arrays from the fields of the infinite structure. Referring to Figure 2, the first step is to calculate and store an $E^\infty(\beta_0^{mn}, \underline{r})$ matrix for the desired field location (or locations) above one unit cell in the infinite array. For a dipole, one can consider each field component separately. For each point $\underline{r}$, a set of Fourier coefficients for the fields of any finite array size and excitation are obtained

14

from the E^∞ matrix and the DFT of the excitation current:

$$\tilde{E}(\underline{\beta}_0^{mn}, \underline{r}) = \tilde{I}(\underline{\beta}_0^{mn}) \, E^\infty(\underline{\beta}_0^{mn}, \underline{r}) \tag{12}$$

Finally, the fields over the finite array are obtained by a second DFT:

$$E(\underline{r} + \underline{S}_{mn}) = \text{IDFT} \left\{ \tilde{I}(\underline{\beta}_0^{mn}) \, E^\infty(\underline{\beta}_0^{mn}, \underline{r}) \right\} \tag{13}$$

Equation 13 returns LK field points on the lattice $(\underline{r} + \underline{S}_{mn})$, spaced by the array periodicity vectors $\underline{S}_1$ and $\underline{S}_2$. If the fields at a number of different distances from the array plane, or at different points in the unit cell are required, E^∞ matrices must be computed for each field point in the unit cell. For most applications, however, only exponential functions change as the observation point is moved. Thus, the other factors can be stored when the impedance matrix is computed. Fields for different locations and currents are then easily computed.

2.4. Synthesis Method

Equation 12 suggests a simple and efficient synthesis technique. An efficient near field synthesis method would be of interest in a number of areas, including microwave hyperthermia, microwave imaging, and magnetic resonance imaging. Following is a 2-D approach for synthesis of a single field component.

15

If one specifies a desired field pattern $E^d(\underline{r})$ in a plane above the array or scatterer, a set of Fourier coefficients for the desired field can be obtained by DFT,

$$E^d(\underline{\beta}_0^{mn},\underline{r}) = DFT\left\{E^d(\underline{S}_{mn},\underline{r})\right\} \tag{14}$$

By inspection of Eq. 12, it is clear that one can obtain a set of excitation currents for an L x K array by a single FFT operation.

$$I(\underline{S}_{mn}) = IDFT\left\{\frac{E^\infty(\underline{\beta}_0^{mn},\underline{r})}{E^d(\underline{S}_{mn},\underline{r})}\right\} \tag{15}$$

Finally, the coefficients of Eq. 15 must be truncated to the elements present in the finite array, as in standard far-field Fourier synthesis methods. The fields realized from the finite array by this set of currents can be calculated from Eq. 13.

2.4.1 Summary of synthesis method

The procedure to synthesize a desired near field pattern can be summarized as follows.

Step 1. Compute Z^∞ and E^∞ matrices, characterizing the fields and active scan impedance of the infinite array.

Step 2. Define a desired near field pattern, $E^d(\underline{S}_{mn},\underline{r})$.

Step 3. Define the excitation currents using Eq. 15.

Step 4. Truncate the synthesized excitation currents.

16

Step 5. Compute the realized pattern using Eq. 13.

Step 6. For free excitation, find the excitation voltages.

3.0 RESULTS

The analysis method has been previously tested by comparison with published results for finite microstrip arrays [2]. In order to test synthesis method a problem of interest in microwave imaging was considered. Following an example given in the literature [23], it was desired to focus a beam at different (x,y) locations on a plane 7 cm in front of a planar, 25 x 25 array of $\hat{y}$ oriented dipoles, as illustrated in Fig. 3. The array was in water, $\varepsilon_r = 77$, $\delta = 0.16$, at f = 3 GHz. The elements were 0.055 λ_0 long, and S_1 and S_2 were $0.0381\lambda_0$ and $0.0635\lambda_0$, respectively. The overall size of the array was approximately 16 cm by 10 cm.
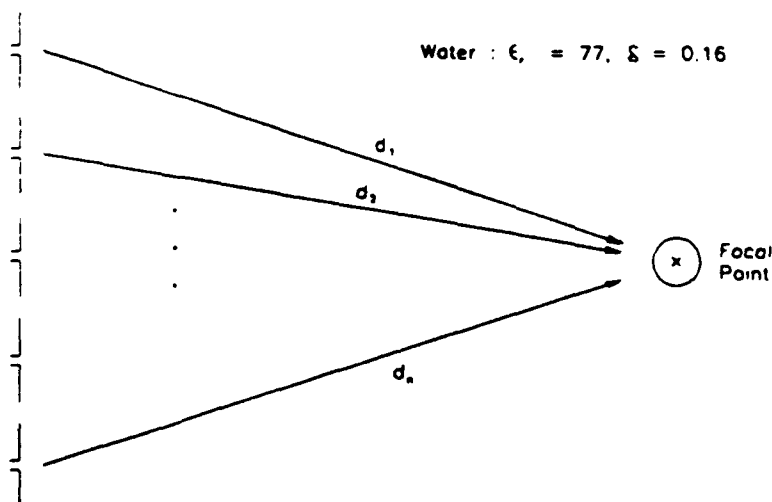

Figure 3. Illustration of array for near field focusing.

17

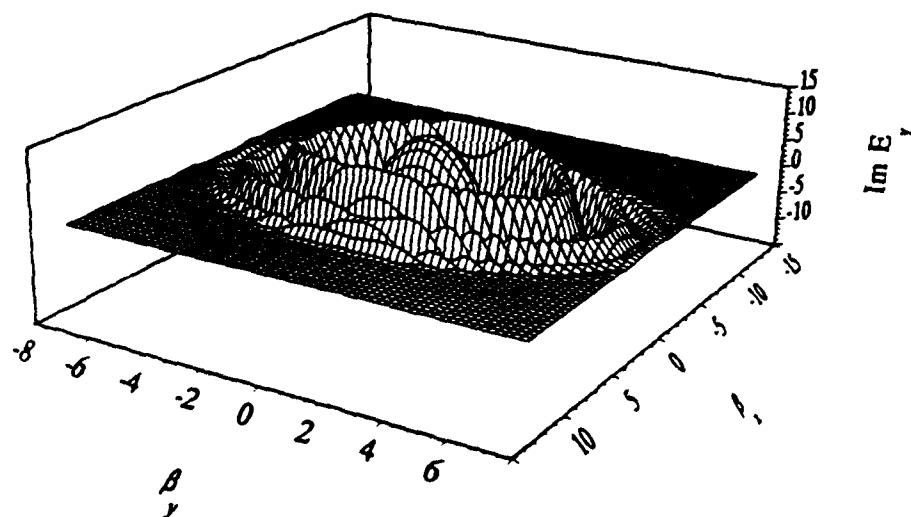## 3.1. Results from conjugate phase and amplitude method

In [23], the conjugate-phase and amplitude method was used to determine element excitations, In this approach, the phase and amplitude of the excitation of each element are set to compensate for different path lengths to the focus point. To test the DFT analysis method, the near fields for this array using conjugate-phase and amplitude excitation.

First, the scan impedance matrix and the field matrix were computed for the extended, infinite array. Figure 4a shows magnitude of the scan impedance matrix $Z^{\infty}(\underline{\beta}_0^{mn})$ for the array. Figure 4b shows the real component of the $E^{\infty}(\underline{\beta}_0^{mn}, \underline{r})$ matrix for $\underline{r} = (0,0,7)$ cm. Figure 5a shows the element excitation amplitudes obtained by conjugate-phase and amplitude for a focus at $\underline{r} = (0,0,7)$ cm, $I^{ex}(\underline{S}_{mn})$. Following the analysis method above, the realized fields for the 25x25 element finite array with these excitations was computed, and is shown in Figure 5b. The focus is well defined in the x-y plane, as desired.

Next, the excitation currents to achieve a focal point at $\underline{r} = (3,4,7)$ cm, near one corner of the array were calculated, again using conjugate-phase and amplitude. These currents are shown in Fig. 6a, and the resultant field pattern in the xy plane over the array is shown in Fig. 6b. While a focus is achieved near the desired point, a second maximum is observed at the opposite corner, due to the combination of the high
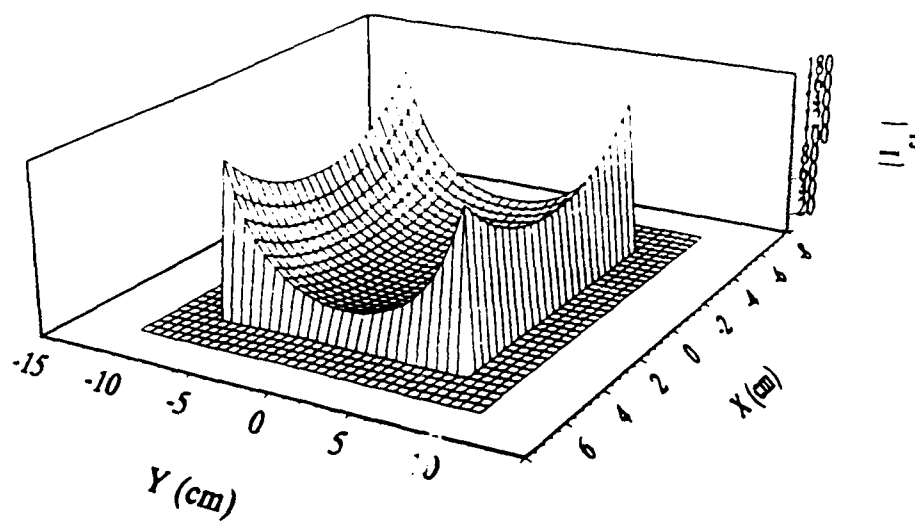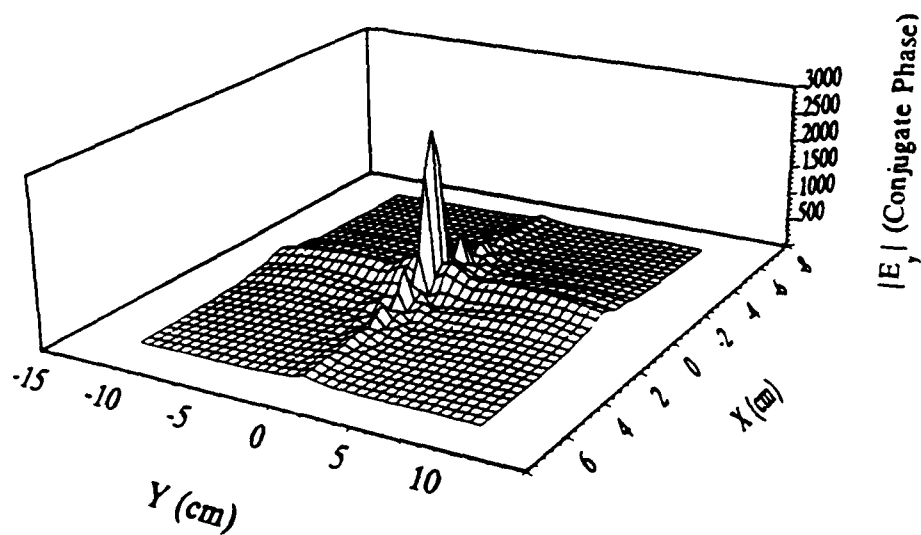
18
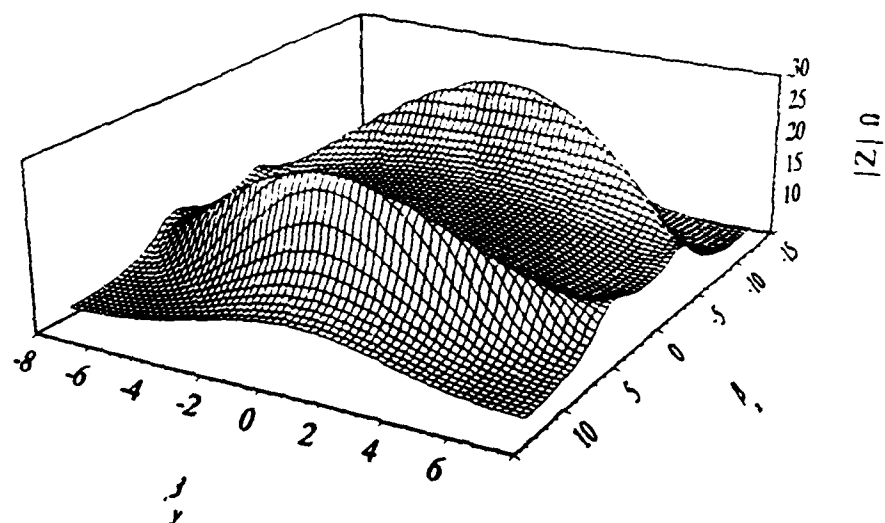
a)

b)

Figure 4. Characteristics of the infinite array of dipoles.

a) Mag. of $Z^{\infty}(\underline{\beta}_0^{mn})$ matrix. b) Imag. comp. of $E_y^{\infty}(\underline{\beta}_0^{mn}, \underline{I})$.
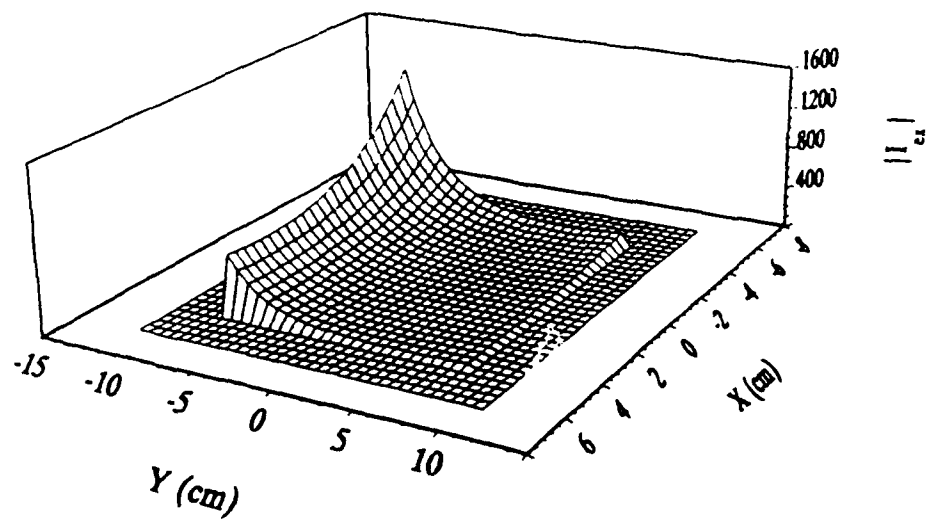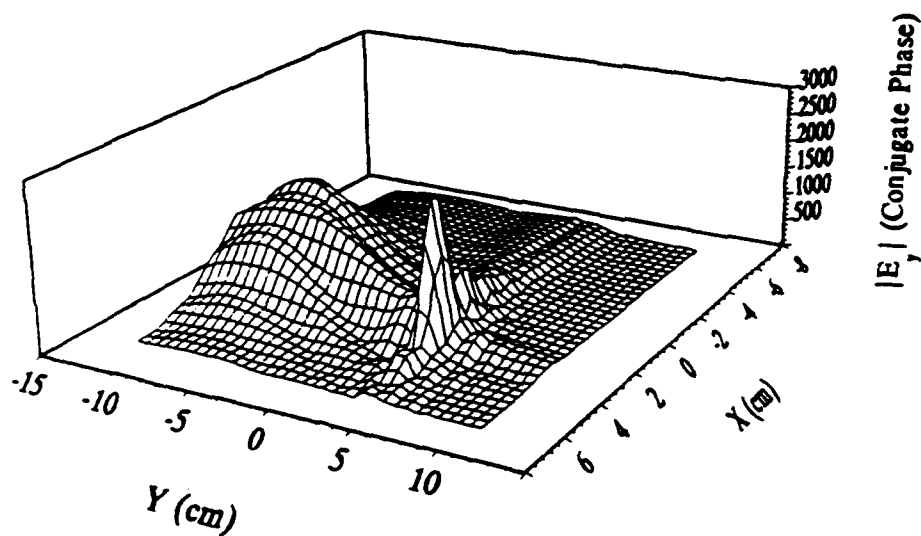
19

a)

b)

Figure 5.   a)   Excitation currents and b) Field pattern from conjugate-phase and amplitude method.   Focus at (0,0,7) cm.

20

a)

b)

Figure 6. a) Excitation currents and b) E_y field pattern from conjugate-phase and amplitude method. Focus at (3,4,7) cm.

21

excitation currents in this vicinity and the high attenuation rate of water. These results compare well to [23], although that study used a hexagonal array.

3.2. Results from the DFT synthesis method

To compare with the conjugate-phase and amplitude method, excitation currents were synthesized to focus the beam at the same two points as above. The $Z^{\infty}(\beta_0^{mn})$ matrix and the $F^{\infty}(\underline{\beta}_0^{mn},\underline{r})$ matrix have been previously calculated, as shown in Fig. 4a and 4b. Note that the same $E^{\infty}(\beta_0^{mn},\underline{r})$ matrix was used for each case. A gaussian beam centered on the desired focal point, with a half-width of 0.75 wavelengths in water, was used as the desired beam pattern, $E^d(\underline{r}+\underline{S}_{mn})$.

The first step in the synthesis method, Eq. 14, is to compute the DFT of the desired beam pattern, $E^d(\underline{\beta}_0^{mn},\underline{r})$. This is also gaussian, and is shown in Figure 7a. The Fourier coefficients of the excitation current are obtained by normalizing the $E^{\infty}(\underline{\beta}_0^{mn},\underline{r})$ matrix in Figure 3b by the $E^d(\underline{\beta}_0^{mn},\underline{r})$ matrix in Figure 7a. These coefficients are shown in Figure 7b. The higher spatial frequencies have been truncated. The calculated excitation currents to synthesize a beam focused at (0,0,7) cm obtained from Equation 14, and truncated to a 25x25 array. These currents are shown in Figure 7c. Finally, the actual beam pattern synthesized by the 25x25 array is calculated using Eqs. 12 and 13, and is shown in Figure 7d.
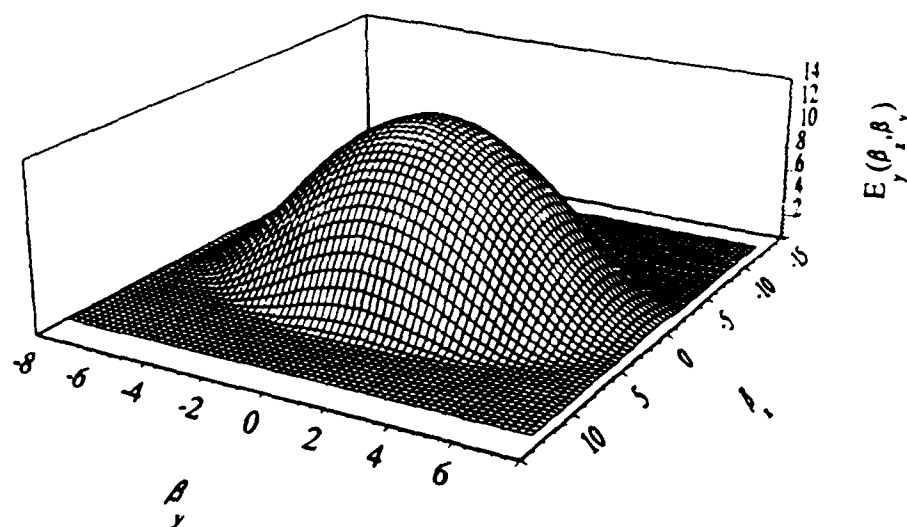
22

Fig 7a. DFT of desired beam pattern, $E^d(\underline{\beta}_0^{mn}, \underline{r})$.
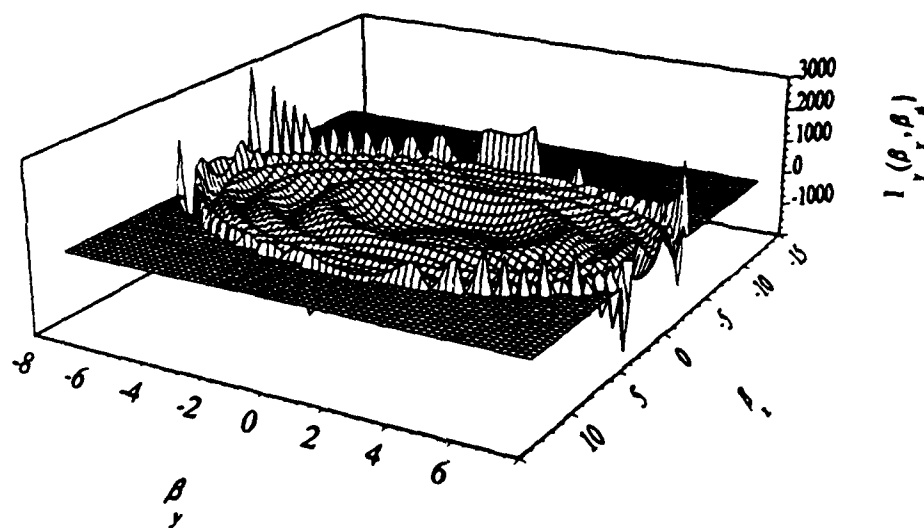

Fig 7b. DFT of excitation currents to synthesize focus at (0,0,7) cm.
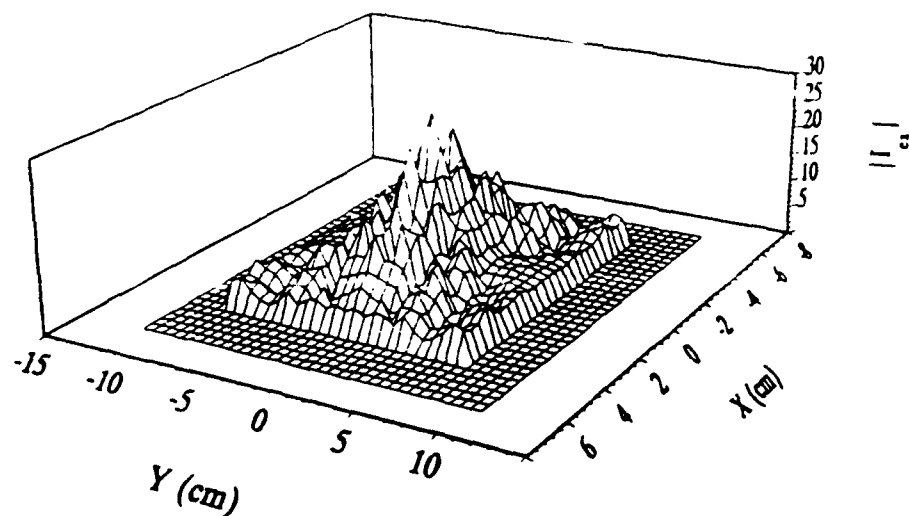
23

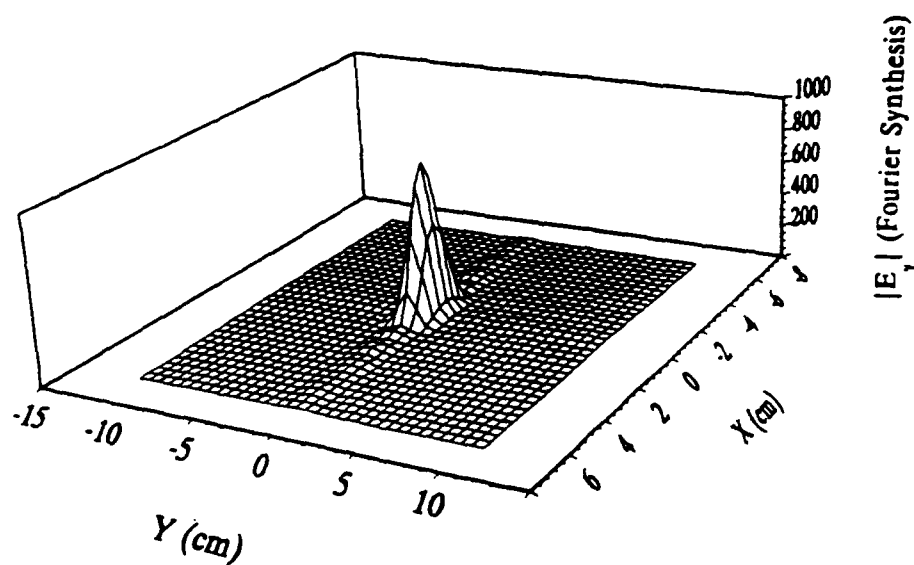Figure 7c. Excitation currents to synthesize focus at (0,0,7) cm.

Fig 7d. Synthesized pattern for focus at (0,0,7) cm.

24

To synthesize a beam at (3,4,7) cm, the above procedure is repeated, but a gaussian centered at (3,4,7) cm is used as the desired field. Using DFT operations only, the excitation currents for a beam at (3,4,7) were calculated, and are shown in Fig. 8a. It is interesting that these excitation currents are substantially different from those obtained from the conjugate phase technique, in Fig. 6a, and that the resultant fields, shown in Fig 8b, do not exhibit a secondary peak.

No attempt was made to optimize the beamwidth in this example. Additionally, filtering in either the spatial or spectral domain would smooth the synthesized current distribution, with some affect on beamwidth.

4.0 CONCLUSION

A Fourier method for the synthesis of near and far field patterns of finite periodic radiators has been presented. The method is based on an efficient infinite array formulation, and therefore reduces the number of unknowns to that of a single element. Nevertheless, edge effects are included, and the method can be used to analyze arrays of arbitrary size and excitation. Most importantly, storage requirements and computational times are essentially independent of the size of the array.

The method was used to synthesize excitations for a near field focusing array. Unlike the conjugate-phase and amplitude
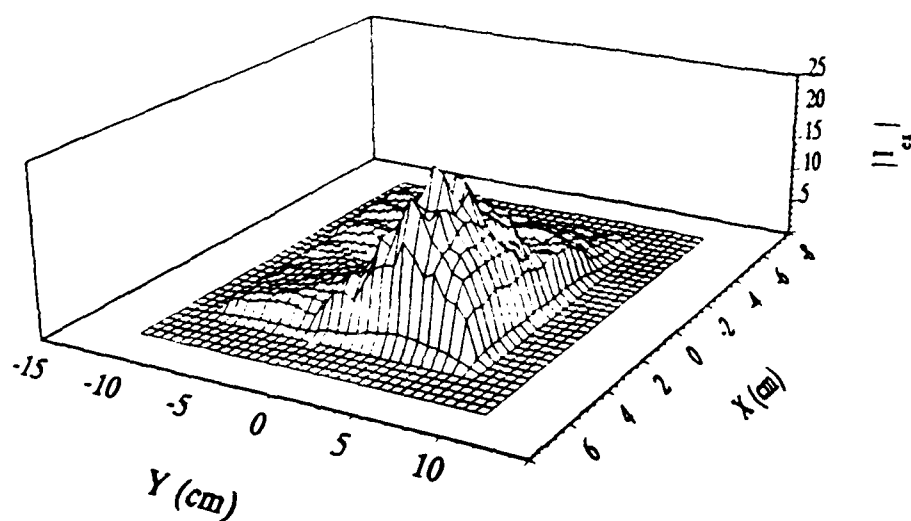
25

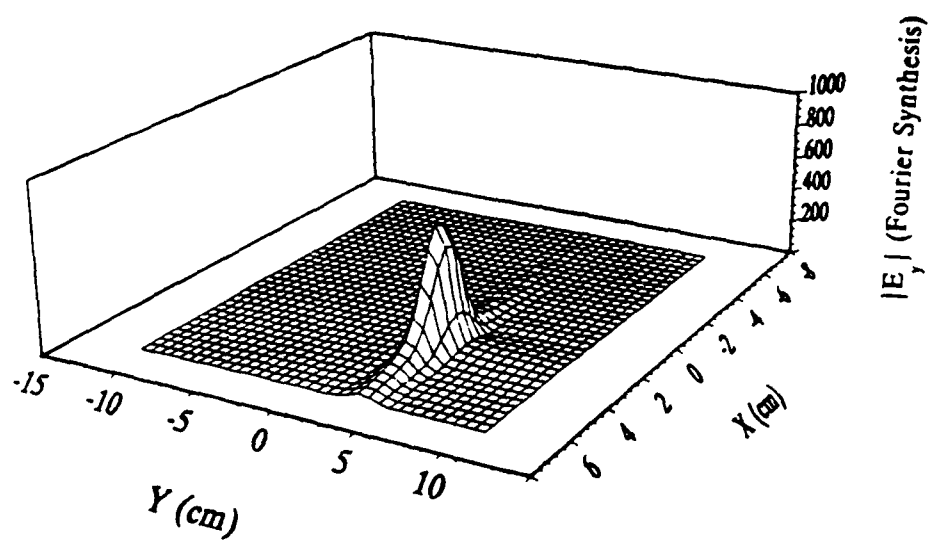Figure 8a. Excitation currents to synthesize focus at (3,4,7) cm.

Fig 8b. Synthesized pattern for focus at (3,4,7) cm.

26

method, the synthesis method does not require the computation of path length losses and phase changes from each element to the target. Assuming the media can reasonably be modeled as homogeneous layers, all media and coupling effects are taken into account.

The analysis method has previously been applied to arrays of microstrip dipoles with good results. It should be applicable to arrays on arbitrary layered media, and includes both forced and free excitation. Because it will allow accurate analysis of larger systems than with existing methods, this technique could find application in a wide variety radiation and scattering problems.

REFERENCES

[1] Wright, S.M. and Twine, D.G., (1990) Improved FFT analysis of finite periodic antenna arrays. *Proc., 1990 Int. APS/URSI Symposium Digest*, p. 1.

[2] Wright, S.M. (1991) Analysis of edge effects in finite phased array antennas. *Proceedings of 1990 Allerton Antenna Applications Symposium*, Technical Report 91-156, Rome Air Force Systems Command, Rome, N.Y., 1991.

[3] Rana, I.E., and Alexopolous, N.G. (1981) Current distribution and input impedance of printed dipoles. *IEEE Trans. Ant. Propag.*, Vol. AP-29, No. 1, pp. 99-106.

27

[4]   Pozar, D.M., (1982) Input impedance and mutual coupling of rectangular microstrip antennas. *IEEE Trans. Ant. Propag.*, Vol. AP-30, No. 6, pp. 1191-1196.

[5]   Itoh, T. (1989) Spectral Domain Approach. in Itoh, T., Ed., *Numerical Techniques for Microwave and Millimeter-Wave Passive Structures.* New York: Wiley. Chpt. 5, pp. 334-380.

[6]   Pozar, D.M. (1985) Analysis of finite phased arrays of printed dipoles. *IEEE Trans. Ant. Propag.*, Vol AP-33, No. 10, pp. 1045-1053.

[7]   Pozar, D.M. (1986) Finite phased arrays of rectangular microstrip patches. *IEEE Trans. Ant. Propag.*, Vol AP-34, No. 5, pp. 658-665.

[8]   Hansen, V., (1987) Finite array of printed dipoles with a dielectric cover. *IEE Proceedings,* Vol 134, Pt. H, No. 3, pp. 261-269.

[9]   Liu, C.C., Hessel, A., and Shmoys, J. (1988) Performance of a probe-fed microstrip-patch element phased arrays. *IEEE Trans. Ant. Propag.*, Vol.   AP-36, No. 11, pp. 1501-1509.

[10]   Lee, K.M. and Chu, R.S., (1988) Analysis of mutual coupling between a finite phased array of dipoles and its feed network. *IEEE Trans. Ant. Propag.*, Vol AP-36, No. 12, pp. 1681-1699.

28

[11] Katebi, P.B., (1989) Mutual coupling between microstrip dipoles in multielement arrays. *IEEE Trans. Ant. Propag.*, Vol. AP-37, No. 3, pp. 275-280.

[12] Wright, S.M. and Lo, Y.T. (1983) Efficient analysis for infinite microstrip dipole array. *Electron. Lett.*, Vol. 19., No. 24, pp. 1043-1045.

[13] Pozar, D.M. and Schaubert, D.H. (1984) Scan blindness in infinite phased arrays of printed dipoles. *IEEE Trans. Antennas Propag.*, Vol., AP-32, pp. 602-610.

[14] Aberle, J.T., and Pozar, D.M. (1989) Analysis of infinite arrays of probe fed rectangular microstrip patches using a rigorous feed model. *IEE Proceedings*, Vol. 136, Pt. H, No. 2, pp. 110-119.

[15] Lo, Y.T., Wright, S.M., and Davidovitz, M. (1989) Microstrip Antennas. in Chang, K. Ed., *Handbook of Microwave and Optical Components*, vol. I. New York: Wiley. Chpt. 13., pp. 764-888.

[16] Hansen, R.C., Ed., (1966) *Microwave Scanning Antennas.* vol. II. Academic Press, New York.

[17] Mittra, R., Ko, W.L. and Rahmat-Samii, Y. (1979) Transform Approach to Electromagnetic Scattering. *Proc. IEEE*, Vol. 67, No. 11, pp. 1486-1503.

29

[18] Volakis, J.L. and Barkeshli, K. (1991) Applications of the Conjugate Gradient FFT Method to Radiation and Scattering. Sarkar, T.K., ed., *PIER 5, Application of Conjugate Gradient Method to Electromagnetics and Signal Analysis*, Elsevier, New York.

[19] Munk, B.A. and Burrell, G.A. (1979) Plane wave expansion for arrays of arbitrarily oriented piecewise linear elements and its application in determining the impedance of a single linear antenna in a lossy half-space. *IEEE Trans. Antennas Propag.*, Vol AP-27, No. 3, pp. 331-343.

[20] Lee, S.W. Radiation from an infinite aperiodic array of parallel-plate waveguides. *IEEE Trans. Ant. Propag.*, Vol. AP-15, pp. 598-606.

[21] Ishimaru, A., Coe, R.J., Miller, G.E. and Geren, W.P. (1985) Finite periodic structure approach to large scanning array problems. *IEEE Trans. Antennas Propag.*, Vol. AP-33, No. 11, pp. 1213-1220.

[22] Dudgeon, D.E. and Mersereau, R.M. (1984) *Multidimensional Digital Signal Processing*. New Jersey: Prentice-Hall.

[23] Guo, T.C., Guo, W.W. and Larsen, L.E. (1984) A Local Field Study of a Water Immersed Microwave Antenna Array for Medical Imagery and Therapy. *IEEE Trans. Microwave Theory and Tech.*, Vol. MTT-32, No. 8, pp. 844-854.

30

MISSION

OF

ROME LABORATORY

Rome Laboratory plans and executes an interdisciplinary program in research, development, test, and technology transition in support of Air Force Command, Control, Communications and Intelligence (C^3I) activities for all Air Force platforms. It also executes selected acquisition programs in several areas of expertise. Technical and engineering support within areas of competence is provided to ESD Program Offices (POs) and other ESD elements to perform effective acquisition of C^3I systems. In addition, Rome Laboratory's technology supports other AFSC Product Divisions, the Air Force user community, and other DOD and non-DOD agencies. Rome Laboratory maintains technical competence and research programs in areas including, but not limited to, communications, command and control, battle management, intelligence information processing, computational sciences and software producibility, wide area surveillance/sensors, signal processing, solid state sciences, photonics, electromagnetic technology, superconductivity, and electronic reliability/maintainability and testability.